A Bubble Is Born: Nucleation and Early Growth of CO2 Bubbles in Polymer Foams

Thesis by
Andrew Samuel Ylitalo

In Partial Fulfillment of the Requirements for the
Degree of
Doctor of Philosophy

Caltech

CALIFORNIA INSTITUTE OF TECHNOLOGY
Pasadena, California

2022
Defended Friday, May 20, 2022

© 2022

Andrew Samuel Ylitalo
ORCID: 0000-0003-4086-3508

Acknowledgments

Why do we acknowledge the support of others? To be kind? To ingratiate ourselves to others? To remind ourselves that the role we play in our own work is a humble fraction of the collective effort that makes it possible? Maybe.

Here, I acknowledge those who helped me so my readers and I can pause to remember that life can, as God declared on the sixth day, "indeed [be] very good."[1] Of course, life can also be not very good. Without those moments of difficulty, despair, and disillusionment, however, I would not have grown into who I am today, for "we also glory in our sufferings, because we know that suffering produces perseverance; perseverance, character; and character, hope."[2] That I grew from those moments instead of receding, emerged hopeful instead of jaded, and look back with joy and not disgust is thanks to all of you.

First, thank you, Julie. I did not know what I sought from my PhD, but I believed that your curiosity, humility, hope, and integrity would lead me to something good; indeed, they did. I aspire to live up to the example you set. And while I regret dismissing your detailed questions that challenged my ideas at first, I know now that those are the questions that shall forever echo in my head, guiding me ever closer to Truth. Zhen-Gang, I have never met anyone who expects such excellence, communicates with such clarity, and seeks understanding with such earnestness as you. I am especially thankful to have seen the meaning of clarity and pedagogy embodied in your lectures and for your encouragement and academic support to pursue my interest in complex coacervation.

I thank the rest of my committee, Profs. Rustem Ismagilov, Richard Flagan, Mitchio Okumura, and John Brady, for taking the time to review my work and advise me on next steps. Rustem, you have taught me how to defend my ideas with professionalism. Rick, you have led me in directions I never would have pursued and that now form an integral part of my thesis. Mitchio, thank you for your kind support. John, thank you for letting me do my demo of beverage foam in class. Thank you also for not letting go of the importance of radial convection—it turned out to be quite important.

I first want to thank my first and forever research advisor, Prof. Andre

---

[1] Book of Genesis, Chapter 1, verse 31, King James Version
[2] St. Paul's Letter to the Romans, ch. 5, v. 3–4, New International Version

Mkhoyan of the University of Minnesota, whose encouragement, recommendation, and guidance brought me to Stanford and then Caltech, and finally to the completion of my PhD. Everyone needs a mentor like Andre. I would also like to thank Prof. Gerry Fuller, my undergrad advisor, for practically twisting my arm to join his lab in 2015, where I grew to love fluid flow, imaging, and image processing that prepared me for this project at Caltech. Last, I thank Prof. John Frostad for mentoring me throughout the Fuller lab and beyond, and for teaching me the simple tenacity of trying things out and seeing what happens. My confidence in myself as a researcher and a programmer is largely due to your years of mentorship.

Thank you to the teams I've worked with at Dow, in person, and remotely: Dr. Tom Fitzgibbons, Dr. Weijun Zhou, Dr. Valeriy Ginzburg, Dr. James Griffith, Dr. Bill Winniford, Dr. Paul Gilles, Marla Gilbert, Dr. Steve Horvath, Dr. Irfan Khan, and Dr. Jacob Crosthwaite. Thank you for investing in the success of this project and supporting my ideas since before I came to Caltech. Yours was my first collaboration, and it set an excellent example for those to come. Grazie assai a Prof. Ernesto Di Maio per ospitarmi nel suo laboratorio per l'estate, e anche ai miei amici napoletani, Vincenzo Il Grande, Vincenzo Il Piccolo, Fabrizio, Antonio, Pepe Scherillo, e Valerio per qualche panini, pizze, tazze di caffè, e conversazioni indimenticabili durante l'ora di pranzo ogni giorno. Mi vita è cambiata nel senso migliore grazie a Napoli e la sua gente imparagonabile.[3] Thank you to Lison, Fulvia, Pepe, Giovanni, Riccardo, and Huidong for making those eternal and error-prone nights in the Death Star (Argonne) bright with laughter and smiles; special thank you to Lison for your persistence in turning the data from those nights into a story worth publishing.

Without the National Science Foundation's Graduate Research Fellowship Proposal and the Dow University Partnership Initiative, this work would not have happened. While the funding provides potential, it is the people who realize it: thank you Tom and Weijun for your consistent feedback throughout my entire PhD and the mentorship you provided as I looked to my next steps. Thank you especially for supporting my research excursions in Naples, Italy, and Lake Jackson, TX, which transformed both the academic and personal experience of my PhD. Thank you also to the Armenian Professional Society for the scholarship that supported the costs of

---

[3]"Thank you very much to Prof. Ernesto Di Maio for hosting me in his lab for the summer, and also to my Neapolitan friends, Vincenzo the Great, Vincenzo the Small, Fabrizio, Antonio, Pepe Scherillo, and Valerio for some unforgettable sandwiches, pizzas, espressos, and conversations during the lunch hour every day. My life has changed in the best way thanks to Naples and its incomparable people." (Italian)

these excursions. Thank you to the cheerful, professional, and supportive staff I had the pleasure to work with: Christine Jary, Abigail McCann, Kate, Allison Kinard, and Kathy Bubash. Thank you Prof. Giapis for taking me on as a TA despite my incomplete chemical engineering background, as well as for the sushi afterward.

Thank you Kriti Chaturvedi for teaching me about the effects of flow on bubbles through her OpenFOAM simulations. Thank you Dr. Justin Bois for teaching me how to manage my data in my first months at Caltech. I would have had no hope of deciphering my past work while writing this thesis were it not for the practices you instilled in me and enthusiasm for clean data analysis in your class. Thank you Dr. Huikuan Chao for not only building the strong platform of theory and modeling on which this thesis was built, but for the time you dedicated to teaching a novice like me not only how to use it, but how to understand it and teach it to others. My academic journey as a theorist began with you.

Thank you Sameer and Harsha for making the upper floor of Steuben a home and the lower floor home to many fond memories of movie nights and dinner over *Rick and Morty*. Thank you Tega for showing me that I can still be fascinated by physics and math as an engineer. Thank you Christoph for teaching me how to fix the bugs in my installation of OpenCV and other C++ problems that had been holding up my image-processing analysis. Grazie mille a Tiziana Di Luccio e la sua famiglia carina, per chi ho un sacco di d'amore.[4] Gracias a Tony por ser un amigo paciente, cómico, y generoso.[5] Gracias también a Leslie por darme un descanso del trabajo con sus historias animadas y por no tener miedo delante de la muerte—todo antes de las 9 en la mañana.[6] Thanks to Brian Wilson for doing a won-won-won-wonderful job making me SMiLE. Thank you immensely to Isaac Swanlund, who turned an aimless walk in the wilderness into a coding project that saved me literally hundreds of hours processing data and taught me enough about programming in teams to get a job. Your impact on my life is understated yet ever-present.

---

[4]"Thanks a thousand to Tiziana Di Luccio and her lovely family, for whom I have lots of love." (Italian)

[5]"Thank you, Tony, for being a patient, funny, and generous friend." (Spanish)

[6]"Thank you also to Leslie for giving me a break from work with your animated stories and for having no fear before death—all before 9:00 a.m." (Spanish)

شكرًا يَا سَامِي لصدَاقتك. أَنَا دَرَستُ العَربية كثيرًا منك.[7]

Huge thank you to the Luys Mens Club (Shaunt, Armen, and Hopar Varag) for good living without hesitation, tossing out nuggets of life wisdom, and giving me an excuse to get good kebab.

Thanks Kyle and Camila for bringing a bit of the vibrancy of our life at Stanford here with us to Pasadena. Deanna, Alice, Scott, Nilo, and Alyssa for being the best physics friends a physicist could have. Mike, Gerardo, Teun, Tamu, and Tynan for reminding me of good times. Mike especially for treating me like an expert and a scientist when I lost sight of what I had to offer academically. Danny for keeping in touch.

Erik. Twenty-seven years says it all. Graham for your indomitable and infectious fascination with science and engineering of all types—nobody else listens with such interest when I ramble about my PhD. Shelby and Nick, Will, Jordan and Yeongseo, Emily and Joe, Lauren and JJ, Toby, Kelsee, Clare, and Chi (who visited twice!) for being Stillwater's finest twenty-some seasons straight.

Mr. Symalla for teaching me about experimental research. Though you told us many times, I doubted that the fourth-quarter project had that much to do with getting a PhD. I was wrong. Thank you for bringing in those two grad students, too. I have often thought back to how they said that the PhD requires you to think about your problem constantly. That scared me at first, but I have come to find joy in this engrossment of late. Mrs. G., the greatest teacher I never had. You were a true friend and support during the first years of my PhD, always ready to catch up and keep in touch. I treasure your creative postcards. Mr. Lindsay, where would my ducks be if not for you? Definitely not in a row—that's for sure.

Thank you Paresh for your eagerness to share your boundless knowledge and earnest wisdom; you have been a great support in both the best and worst times and gave me confidence during my job search with your relentless optimism. Thank you, also, for reading my drafts of this thesis so thoroughly and offering thoughtful comments. Thank you Orland for being my first mentor at Caltech and getting this project off the ground when I was still afraid of the laser cutter. Thank you Rachel for being a great office mate, sounding board, and happy answerer of questions, as well as a great friend. Thank you Red for the most sincere and attentive responses to any question and request for help I ask of you. Thank you Rob for talking shop and

---

[7]"Thank you Sammy for your friendship. I learned a lot of Arabic from you." (Arabic)

making the lab a fun place. Thank you Lealia for your creative suggestions on how to make my presentations pop (and for generally having beautiful presentations) and for making the lab run more like a lab should run. Thank you Jin for fun chats after long days in the lab and making biology understandable to me. Thank you Ben for always having time to help and an eagerness to invest in teaching me the deeper lessons you took from your time at Caltech. You've been a good collaborator and a delightful friend. Thank you Alex for reminding me every day how exciting it is to explore cool science and how to be fearlessly curious. Thank you Hojin for help keeping the lab running. Thank you Priya for the joy of seeing what you're working on and the greater joy of providing explanations that share both your excitement and understanding with me. Thank you Chris for making me feel like Caltech would be a good place to be during the visit and making that true during our time here. And for the best golf of my life. 감사합니다 형주 [8] for pushing me to excel academically in our first year, for earnest friendship, and for pouring hours into teaching me a little bit of Korean. Thank you Sriteja for joining me on the Dow project and helpful discussions. Thank you Chelsea for constantly reminding me that I have what it takes to succeed in academia and teaching me your secrets of success. The 202 has never been the same. Thank you Max for showing me what it means to believe in one's dreams and keep community, as well as for continuing to share your wisdom and kindness even after the 202. Thank you Sunday Nite Dinner for filling my first year and beyond with food and friendship. Thank you Nachi and Gunho for your steady friendship and making every dinner out with you a memorable one.

Widi, I thank the Lord that He placed you in my life through the random roommate process. When I languished, you listened; when I was cynical, you slipped in a sparkle of hope; when I floundered, you were firmly planted. You have helped me, comforted me, and shared a lifetime of the little joys and the big ones with me these past five years. Thanks for boba and pork belly, too. Thank you also for bringing Lena into our friend group, and Lena for always listening and bringing a special sense of quality to time spent together. Albert, thank you for entertaining my curiosities about language and science and for entertaining me with yours. Thank you for your persistent trek forward in life, your limitless fascination, your earnest encouragement of my doubted dreams, and your gentle willingness to teach, all of which have shown me what it means to be a good person. Thank you to the GCFunRunners for making Saturday mornings a weekly joy and for your patience as I learned to listen. Sami, thanks for sketching that picture of me; though just a

---

[8]"Thank you, Hyeongjoo." (Korean)

game, it somehow reminded me of a good piece of myself I had forgotten. Nathan, I would not have run the Rose Bowl half without your encouragement and belief in me. Your leadership of GCF really made my last year at Caltech a special one. Maria for sinners mass and meme mentorship. Hannah for asking all the right questions and listening for the answers. Thank you Rachel for patience and understanding. Thank you Tanner for showing me what it means to live out commitment to your faith, as well as for introducing me to BEMA. You've taught me a lot about myself and how to be a good friend. Mark for saying what needs to be said in the best way possible when everyone else is silent. Thank you to Grace for making micromeetups happen and, through them, community. Also for responding to my ribbing with tea and homecooked meals. Thank you to the SAFE team for showing me that faith can and ought to be part of my scientific self. Thanks to everyone in GCF for putting up with my antics and making Monday nights (and Tuesday tea, and Wednesday prayer lunch, and Friday movie nights, etc.) my favorite time(s) of the week.

Thank you to my students in Caltech's RISE tutoring program, Gael, Seldon, and Chris, who reminded me each week that knowledge's greatest power is the trust it forms when taught. A special thank you to my "two-dimensional person," Engels, whom I have tutored since he started high school: I'm proud to be your tutor. Շնորհակալություն[9] to the AGBU Choir for providing a community for me to be Armenian every week. The special joy of singing Komitas is not possible alone. Barb Catlin, Steve, Richard, Muir, Sophie, Iban, and Daniel, and the rest of the Caltech jazz band; Connor and David for jamming. Barb, thanks especially for believing in me after my hiatus from jazz in college and for teaching me how to be a confident and competent soloist on tenor. In the moments when I was least hopeful, I reminded myself that I would not be playing in a jazz band of this caliber had I not come to Caltech. There's nothing like playing with you all.

Der Sarkis, thank you for teaching me what it means to deeply care for a community by the care you've shown to the St. Gregory community, through happy times and sad. Deacon Aleksan for your persistent confidence in the good and bringing me along to volunteer at Union Station. Deacon Armand for being my first friend in Pasadena. You and your parents made me feel really at home here. Johnathan, John, Hagop, and all the rest for serving on the altar with me. Your growth encourages me. Deacons Hagop, Hagop, Manoug, Kevork, Hovsep, and Carl for your mentorship about church, life, and God. Garo for your inspiring

---

[9]"Gratitude" (Armenian)

dedication. Those at the Upland Church of Christ for reminding me of the beauties of a community small enough for everyone to be friends and look out for each other. David, thank you for getting me out of lab on Friday nights with your randomly timed and delightful phone calls. You never fail to remind me of the incomparable beauty of orthodoxy. Dn. George for opening my mind, heart, and soul to a new level of depth in the Bible and Armenian tradition. What I once ignorantly took for foolishness became a fountain of fascination in your lectures. Thank you to the whole St. Sahag community for your support for and interest in my PhD journey. You will always be my spiritual home and a joy to return to. Thank you especially, Der Tadeos, for making my time at St. Sahag so rejuvenating when I had the opportunity to visit home and for giving me a taste of home while I was away through your podcast, *Podmootiun*.

Thank you Anahid, Hasmik, Hagop, Natasha, and Lucine for your peace and prayer, which dispelled so many of my fears and doubts in my final year. Anahid, while the figures in this thesis—the good ones, at least—bear the mark of your eye for aesthetics, my gratitude for them is nothing compared to my gratitude for your friendship, even if by phone. Յակոբ, եղբայր ջան, thank you for giving me the best moments of the past five years. Thank you Natasha for commiserating about our PhDs over the years and for drawing me back to the things that matter most. My time in Boston with you two last summer left me forever changed. Թոմ ջան, ցավդ տանեմ, ախպեր[10]. Thank you for inspiring me with the beauty of poetry, language, and sincere friendship.

Շատ շնորհակալ եմ քեզի, Թանթ Սոսի, իմ հայերեն ուսուցչուհիս լինելու համար.[11]

Thank you Aunt Kris, Uncle Jerry, Keely (and Scott and Quinn), and Ben for always making times good when we got to see each other. Thank you Aunt Nora, Uncle Akram, Fares, Reena, and Cynthia for filling my time back home with family, even if it was usually cold.

Max, my brother, is the best. Whatever sense of humor and knack for good living I may have is thanks to you.

Thank you, Grandma, for always checking in and bringing simplicity to the complexities I saw in the decisions before me. Thank you, Grandpa, for still keeping an eye on me.

---

[10]"Dear Tommy, let me bear your sorrow, bro." (Armenian)
[11]"I am very grateful to you, Aunt Sossi, for being my Armenian teacher." (Armenian)

Thank you so much, Mom and Dad. I always knew I would do a PhD because I knew I wanted to be like you. You have given me more than I can ever return throughout each year I've spent on this earth. Dad, I would not know excellence if I had not learned it from you, nor would I have known how to approach writing a thesis. If this thesis in any way connects with its audience, it is because you showed me how to communicate why my work matters to others. Mom, thank you for calling and telling me it will be all right if I focus on having a good time in my PhD. I had sought to "fathom all mysteries and all knowledge" in my PhD, but you taught me that if I "do not have love, I am nothing." [12] Thank you for meeting my resistance with love.

Finally, to paraphrase St. Paul, I will "thank my God upon every remembrance of you, always, in every prayer of mine for you all, making request with joy." [13] Գոհանամ զքէն, Տէր Աստուած Մեր. [14]

Abstract

Gas bubble nucleation is a fundamental phenomenon both throughout the natural sciences and in the production of foams for lightweight, functional materials; it is also the basis for many a bubbly beverage. Enhancing bubble nucleation in polyurethane insulating foams used for refrigeration can further reduce their low thermal conductivity without resorting to hazardous blowing agents used in the past. Experimental challenges of measuring the kinetics of the rapid, multiscale process of bubble nucleation pose a roadblock to investigation of suitable processing conditions, as well as the development of theoretical models of bubbles and foams.

Here, using a microfluidic flow-focusing technique developed for measurement of protein and chemical kinetics, we built a microfluidic cell to probe gas bubble nucleation of CO_2 in polyol, a model system for polyurethane insulating foams, at controlled pressure with millisecond resolution over acquisition times sufficient for optical, IR, and X-ray measurements. This technique allows for repeated measurements of bubble nucleation at any degree of supersaturation without the interference of heterogeneous nucleation from surfaces. By extrapolating a model fit to high-speed optical microscopy measurements of bubble growth backward in time, we estimated the degree of supersaturation at nucleation for thousands of bubbles. Estimates of the nucleation rate based on Poisson statistics were consistent with predictions by a string method model based on density functional theory and G-ADSA measurements. This model predicted that the addition of cyclopentane (a common physical blowing agent in polyurethane foams) can dramatically reduce the nucleation energy barrier due to the formation of a liquid-like layer of cyclopentane and CO_2 along the surface of the bubble that reduces the interfacial tension, which previous models have only predicted at significantly higher saturation pressures. This prediction was supported by thermodynamic measurement of a three-phase co-existence under similar conditions, which is a known fingerprint for such nucleation pathways, and measurement of significantly higher bubble nucleation rates upon the addition of cyclopentane. These findings shed light on the possibility of a previously unappreciated role of physical blowing agents like cyclopentane in enhancing bubble nucleation by opening up a qualitatively distinct and more favorable nucleation pathway.

Table of Contents

List of Illustrations

List of Tables

xxiv

Nomenclature

DFT. Classical Density Functional Theory. A framework based on electronic DFT for modeling the spatial variation in the number density of classical particles by minimizing the free energy density functional of the density profile of these particles.

Difunctional. Describes a polyol that has two hydroxyl groups (OH) per polymer chain.

Foam. A gas dispersed in a liquid or solid matrix.

Functionality. Average number of hydroxyl functional groups per polymer chain..

Gravimetry–Axisymmetric Drop Shape Analysis (G-ADSA). A technique that combines precise measurement of the weight of a liquid–gas mixture using a sensitive balance (gravimetry) and image analysis of a pendant drop of the same mixture (axisymmetric drop shape analysis) to measure gas solubility, specific volume, gas diffusivity, and interfacial tension simultaneously.

Harvey Nucleus. A pocket of vapor trapped in the crevice of a solid surface that produces bubbles without nucleation as the pocket of vapor grows large enough for a bubble to detach.

Heterogeneous Nucleation. Nucleation that occurs with the aid of a surface, often in a niche or crack within it. The aid of the surface reduces the supersaturation required for nucleation.

Homogeneous Nucleation. Nucleation that occurs in the bulk phase. Without the aid of a surface, the supersaturation required for nucleation is much greater than for heterogeneous nucleation.

ISCO Pump. A brand of high-pressure syringe pump providing high-precision, pulseless flow. Commonly used in high-pressure microfluidics and super-critical CO_2 applications.

Knudsen Effect. Reduction in the thermal conductivity of a gas as a result of confinement below its mean free path, which effectively shortens the mean free path.

Mother Phase. The medium from which a new phase can nucleate upon supersaturation.

Nucleation. The local formation of a new phase through a first-order phase transition, which requires the system to overcome a free energy barrier.

PC-SAFT. Perturbed Chain–Statistical Associating Fluid Theory, an equation of state published by Gross and Sadowski in *Industrial and Engineering Chemistry Research* (2001).

Physical Blowing Agent (PBA). A volatile, non-reactive compound that vaporizes upon modest heating to generate a foam.

PPG. Polypropylene glycol.

RMSSFE. Root mean signed squared fractional error, the mean of each squared error multiplied by the sign of the error.

RPUF. Rigid Polyurethane Foam, a foam commonly used for thermal insulation in refrigeration units, coolers, and buildings.

Small-Angle X-ray Scattering (SAXS). X-ray scattering technique that detects only X-rays scattered at angles between $0.1°–10°$ from the incident beam axis. These angles correspond to features on the length scale of 1–100 nm.

String Method. A method for identifying the most probable path between two states in a free energy landscape by minimizing the free energy barrier along that path. Often described as the result of a pulling a string taut between the two states.

C h a p t e r   I

Introduction

الحب ومَا يولده.
وَالتمرد ومَا يوجده.
وَالحرية ومَا تنميه.
ثلَاثة مظَاهر من مظَاهر الله.
Love and what generates it.
Rebellion and what creates it.
Liberty and what nourishes it.
Three manifestations of God.

The Vision by Kahlil Gibran,
translation by Juan R. I. Cole

I.1   The Birth of a Bubble

Like our own, the life of each bubble begins with *love*, in this case, the love of its *mother phase*. Unlike other liquids, a mother phase has an abundance of dissolved gas that it selflessly gives away to nourish the birth and growth of bubbles. This condition is called supersaturation—in the case of a bottle of pop[1], the liquid becomes a supersaturated mother phase upon releasing the pressure by opening the cap. Through thermal fluctuations in the density of dissolved gas, some molecules of will cluster and separate from the liquid to form the beginning of a new bubble. Just as a mother does not easily give away her child, neither does the liquid mother phase easily permit this cluster of gas molecules to separate into its own bubble. For a bubble to be born, it must *rebel*. We call this rebellion *nucleation*. Tension arises from this conflict, which resists the separation of the new bubble. All along the surface of the cluster of gas molecules, the liquid molecules of the mother phase are pulling on each other, resulting in a force that resists the rebellion of the bubble aptly named "interfacial tension." This tension not only resists the growth of the bubble but seeks to dissolve it back into the loving embrace of the mother phase. The gas tries in vain to break free from its mother phase on its own, but is often

---

[1]Regional variation on the more common but less fun "soda."

overwhelmed by the cost of independence and dissolves back into the liquid. Those whose rebellions are successful arrive at the third stage: *liberty*. The gas has now become its own bubble and continues to grow in its new life. From this starting point, a bubble may grow to provide life for marine animals, fizz in a can of pop, or one of the many voids in the foam padding you might be sitting on right now. In the case of a bottle of pop, bubbles grow until they ultimately rise and form a foam at the top of the beverage. Note, however, that this growth, while only reached through rebellion, is entirely fueled by the diffusion of dissolved gas that the mother phase lovingly provides.

"Love" Mother Phase	**"Rebellion"** Nucleation	**"Liberty"** Growth
	Cluster of gas molecules	Growing bubble
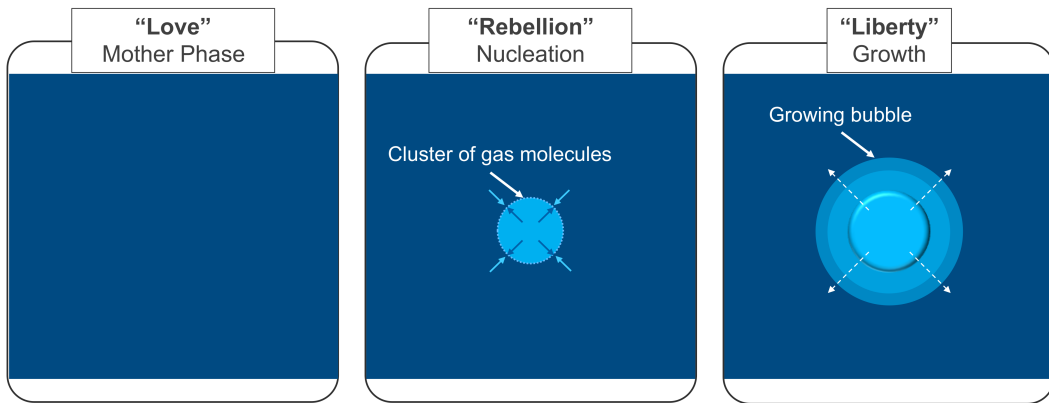
Figure I.1: Schematic of the three stages of a bubble's life. First, the love of the supersaturated mother phase provides fertile ground for the birth of a bubble. Density fluctuations of the dissolved gas lead to temporary clusters of gas that are resisted by the interfacial tension along the interface with the mother phase. If the bubble can overcome the resistance of the mother phase, it reaches the liberty of growth thereafter. Note that, while a bubble must rebel to grow up, its growth is fueled by the abundance of dissolved gas provided by the mother phase.

I.2 The Many Causes of Bubble Nucleation

Bubbles nucleate through a variety of pathways. In each case, the liquid-like mother phase must become supersaturated, meaning that thermodynamics prefers the formation of a vapor-like bubble. The mother phase can always be supersaturated by two changes to state variables of the system: (1) increasing temperature and (2) decreasing pressure. Examples include (1) superheating water and (2) cavitation. In the case of a multicomponent system with dissolved gas, supersaturation can also be reached by increasing the concentration of dissolved gases, such as when mixing baking soda and vinegar produces carbon dioxide bubbles that provide its famous "volcano eruption."

A supersaturated mother phase can produce a bubble in four ways, which have been carefully described in the review by Jones *et al.* [1]. The most similar to the process depicted in Figure I.1 is *homogeneous nucleation*. In this process, thermal fluctuations in the local density of dissolved gas yield a cluster of molecules large enough to overcome the resistance of interfacial tension and continue to grow. This nucleation can occur throughout the mother phase without the assistance of any other component, leading to its name "homogeneous nucleation." A similar process called *heterogeneous nucleation* may occur along a surface, which may reduce the resistance faced by interfacial tension and, therefore, decrease the size of the cluster of gas molecules needed to continue to grow into a bubble.

Most bubbles would agree, however, that assembling a large enough cluster of gas molecules to overcome interfacial tension is a difficult and unlikely process. Its difficulty is why almost every bubble we have ever seen has avoided it entirely. Instead, bubbles we see in daily life generally form from the growth of entrained gas bubbles, such as when pouring a glass of pop, or gas trapped in crevices along rough surfaces, such as along the groove found at the bottom of many champagne flutes [2]. Even bubbles in boiling water come from trapped gas. Such an entrained gas bubble is called a "Harvey nucleus" [3]). Harvey *et al.* reasoned that these pockets of vapor can persist well below saturation because the solvophobicity (hydrophobicity in the case of water) of the surface causes a high enough curvature of the vapor–liquid interface for the interfacial tension to maintain enough pressure to prevent the gas from escaping. Therefore, such pockets of gas are difficult to remove, and due to the ease with which they can grow into bubbles, deplete the available dissolved gas well before true homogeneous or heterogeneous nucleation in the absence of existing bubbles become frequent enough to be observed.

Because nucleation of bubbles from these pockets of gas occurs readily and regularly at specific nucleation sites, it is easy to locate and, therefore, has been measured with greater precision. For example, in Figure I.2, compare the observation of (a) nucleation from a crevice and (b) homogeneous nucleation. While most nucleation from surfaces occurs from trapped pockets of gas rather than the chance clustering of molecules of dissolved gas, we will use the term "heterogeneous bubble nucleation" to refer to both since both occur along surfaces rather than in the bulk of the mother phase.

When homogeneous bubble nucleation does occur, it is more widespread and rapid than heterogeneous bubble nucleation because bubbles can nucleate from any
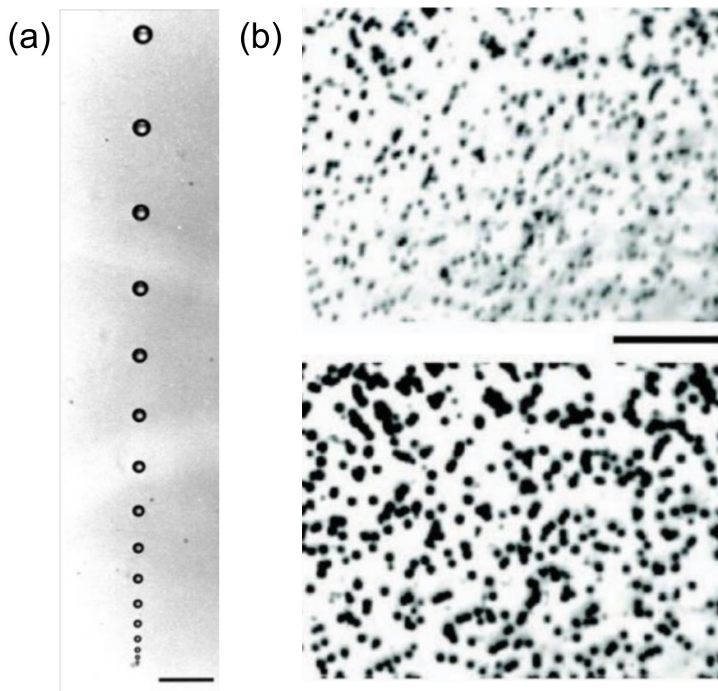
Figure I.2: (a) Observation of nucleation of carbon dioxide bubbles from a pocket of gas trapped in a crevice along the wall of a glass of a champagne (scale bar is 1 mm). Reprinted (adapted) with permission from Gérard Liger-Belair. "The physics and chemistry behind the bubbling properties of champagne and sparkling wines: A state-of-the-art review". In: *Journal of Agricultural and Food Chemistry* 53.8 (2005), pp. 2788–2802. issn: 00218561. doi: 10.1021/jf048259e. Copyright 2005 American Chemical Society. (b) Observation of homogeneous nucleation of carbon dioxide bubbles during the foaming of polystyrene (scale bar 400 μm). Note the regular nucleation of the champagne bubbles from a single nucleation site in comparison to the random nucleation of the bubbles in the polystyrene foam. Reused with permission from John Wiley and Sons [4].

point in the liquid bulk. This process can be catastrophic in the case of contact vapor explosions, in which a liquid is so superheated (often to about 90% of its critical temperature) that it boils homogeneously, creating an explosion of vapor that poses hazards in metallurgy, handling of liquefied natural gas, and nuclear reactors [5]. Nucleating bubbles from pockets of gas may be easier, but shortcuts limit potential. In the context of the present work, however, rapid and widespread bubble nucleation like this can be a boon to producing fine-celled polymer foams, so homogeneous nucleation will be our focus.

I.3 Foams: When Many Bubbles Collide

When enough bubbles nucleate in close proximity, they can form a "foam," a liquid or solid matrix with gas dispersed inside [6]. The pores containing the gas are called "cells," which may form a continuous network (open-cell foam) or may be separated from each other by thin solid films (closed-cell foam). Foams are commonly used as lighter replacements for solid materials, both by humans (structural foams) and nature (bones, wood, etc.). Often, less is more, and foams achieve superior properties over their fully solid counterparts. For example, flexible polyurethane foams provide cushioning to sitters, sleepers, and drivers around the world [7] that solid materials could not. Drinkers may enjoy a foamy head atop their beer [8] or a foamy *collerette* ring about their glasses of champagne [2]. Foam padding in helmets has saved many lives, foam earplugs have protected the hearing of many ears, and foam sugar (marshmallows) has completed many s'mores. Not all foams are beneficial, however. Foams that form over wastewater treatment reservoirs restrict oxygen flow and reduce the amount of biomass needed to clean the water [9]. Whether good or bad, foams and how they form are important for us to understand.

While some foams are produced simply by entraining gas inside the liquid or solid matrix, as in foaming soap dispensers and when whipping egg whites for a foamy meringue, many are produced by nucleating clusters of bubbles by the mechanisms discussed in Section I.2. In all cases, a foam needs to begin with a low enough viscosity to allow cells to form, whether by entrainment of gas or expansion of bubbles. Once the cells have formed, the foam may collapse due to drainage of the liquid and coalescence of the cells if the viscosity is not reduced, as in the case of soapy foams. For this reason, foams are typically cured or vitrified to solidify the cells in place. In a meringue, air is entrained into runny egg whites while the foam is fixed in place by baking. In polymer foams, two methods are used to solidify the polymer. First, in thermoplastic foams, such as polystyrene once used to make insulating cups for hot beverages, the polymer is cooled down below its glass transition temperature T_g ($\approx$ 100–107 °C for M_w > 20 kg/mol [10]) after foaming, causing vitrification of the polymer matrix. Second, in thermoset foams, such as polyurethane used in cushioning, acoustic insulation, and thermal insulation, a chemical reaction crosslinks the polymer reactants.

While the structure of a foam is affected by bubble growth and coarsening, as well as changes in the liquid mother phase like cross-linking or vitrification, bubble nucleation sets much of the structure of polymer foams before these changes take

place. Indeed, the final bubble size distribution is more sensitive to the parameters governing bubble nucleation than those governing bubble growth [11]. The production of a desired foam—or the prevention of an undesirable foam—therefore relies on control of bubble nucleation.

Nucleating More Bubbles for Better Polyurethane Thermal Insulation

Among these types of foams, rigid polyurethane foam (RPUF), a closed-cell thermoset foam used for thermal insulation, poses a unique opportunity for practical application and scientific inquiry. RPUFs are the leading, low-cost thermal insulation material, exceeded only by relatively high-cost aerogels [12]. RPUF's exceptionally low thermal conductivity ($\approx$ 20 mW/(m.K) [12]—see comparison in Figure **??**), ability to cure in place, 30x expansion to form tight seals, and low cost have made it the insulation of choice for refrigeration units, coolers, and even the fuel tanks for the space shuttles [13] (although RPUF was implicated in the tragic explosion of the *Columbia* space shuttle in 2003 [14]). Unfortunately, its low thermal conductivity initially relied on the low thermal conductivity of high-molecular weight volatile compounds like chlorofluorocarbons (CFCs). As discussed in the following section on CO_2-blown foams, these compounds and some of their successors deplete the ozone and contribute to global warming, so regulations have gradually phased them out of production.

Despite the history of environmental hazard caused by RPUFs, they play an essential role in energy conservation by providing a low-cost, easy manufacture, and extremely low thermal conductivity thermal insulation. Retrofitting a building with high-performance thermal insulation like RPUFs can often be the most effective way to reduce the energy consumption of buildings. In some cases, it may even be more economical than investing in solar and wind energy [15]. Given that over 10% of global energy consumption is used to control the temperature of buildings [15], it should not be surprising that RPUFs accounted for $\approx$2% of global plastic production in 2010 [16].

While the seriousness of ozone depletion and global warming demands more environmentally friendly formulations for the production of RPUFs, the importance of high-quality thermal insulation to everyday living motivates investigation into alternative methods of reducing the thermal conductivity of RPUFs. Reducing the thermal conductivity of an insulating foam can focus on any of three major forms of heat transfer: conduction through the solid, conduction through the gas, and

radiation [17] (convection is negligible for foams with cells smaller than 4 mm) [18].

The contribution to the thermal conductivity by the solid is proportional to the solid volume fraction times the thermal conductivity of the solid (refer to equation 2 of [19]). Therefore, reducing conduction through the solid can be achieved by changing the chemistry of the solid matrix to have a lower inherent thermal conductivity or reducing the volume fraction of the solid. Each is difficult to improve upon in RPUFs: changing the chemistry can negatively impact other desirable properties like fast cure time and rigidity and further reduction in the solid fraction of the foam below its current value around 3% [16] may compromise its structural integrity.

The contribution to the thermal conductivity by conduction through the gas is generally proportional to the thermal conductivity of the gas. The thermal conductivity of a simple gas is inversely proportional to the square-root of its molecular weight according to the Chapman–Enskog formula. Therefore, RPUF manufacturers preferred to use the larger CFC molecules over the small CO_2 molecule to keep gas conductivity low (see reduction in gas conductivity in RPUF blown with HCFC–H_2O vs. other blowing agents in Fig. **??**). With increasing regulation of such chemical (see discussion in following subsection on CO_2-blown foams) and flammability concerns with currently used hydrocarbons like cyclopentane, the options for high-molecular-weight blowing agents are decreasing.

Instead, further reduction in gas conductivity may require structural rather than chemical changes to the foam. If the pore size in a foam is on the order of the mean free path of the gas, the effective mean free path of the gas will be reduced. Known as the "Knudsen effect," this reduction in the mean free path reduces the thermal conductivity of the gas. The Knudsen effect has been demonstrated in nanocellular polymer foams [21] (further discussion in following Section on CO_2-blown foams), but nanocellular foams have not become commercially viable yet due to high costs of processing at the high pressures (> 30 MPa [22]) required.

Surprisingly, one of the more viable targets for reducing the thermal conductivity of RPUFs is the radiative heat transfer, *i.e.* the transmission of infrared radiation (IR) through the foam. Thermally insulating foams are produced with low solid fraction (3 % solid or less for polyurethane foams [16]) to minimize weight, material cost, and heat conduction through the solid component. Foams with such a low solid fraction permit a significant amount of radiative heat transfer (up to
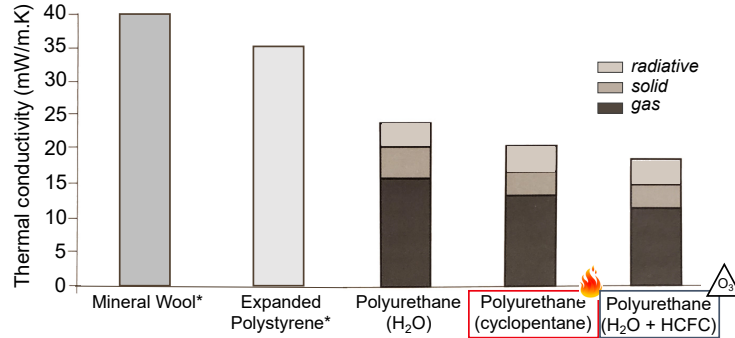
Figure I.3: Comparison of the thermal conductivity at 10 °C of different thermal insulation. The right three foams are polyurethane blown with the blowing agent(s) listed; the flammability hazard of cyclopentane and ozone-depletion hazard of HCFCs (hydrochlorofluorocarbons) is noted. The thermal conductivities of the polyurethane foams are broken down into contributions by heat transfer through radiation (top), solid conduction (middle), and gas conduction (bottom). Estimates of thermal conductivity of mineral wool and expanded polystyrene from Simpson et al. [20]. Figure adapted from Figure 15-5 of *The Polyurethanes Book* edited by David Randall and Steve Lee (2002). Made available by the US EPA Health & Environmental Research Online (HERO) database, HERO ID 4159100.

25 % of the overall heat transfer [17]) because IR radiation is easily transmitted through the gas in the cells and the thin films of polymer that separate them. In polyurethane foams, the struts at the junctions between these thin films (an example is circled in the SEM micrograph in the middle of Figure I.4) constitute 80–90 % of the solid mass [19] and are thick enough to absorb IR radiation and re-radiate it in different directions, which slows radiative heat transfer. Therefore, struts are the key to reducing radiative heat transfer through low-density foams.

Given a foam with a fixed fraction of solid material, the thermal conductivity through radiation can be most reliably decreased by decreasing the cell size, as shown in Figure I.5a. With a fixed solid fraction, decreasing cell size requires a commensurate increase in the number of cells. While the volume of solid in the struts remains the same as the cell size decreases and cell number increases, the surface area of the struts increases, increasing the likelihood that an infrared photon is absorbed and randomly re-radiated. A schematic of this effect is shown in a 2D lattice in Figure I.5b,c. As a result, the rate of radiative heat transfer is lower as the number of cells increases and their size decreases. Moreno derived a quantitative model consistent with this qualitative picture of radiative heat transfer through a foam. Moreno found that for a foam with a fixed solid volume fraction and fixed fraction of solid in the struts, the extinction coefficient is inversely proportional to
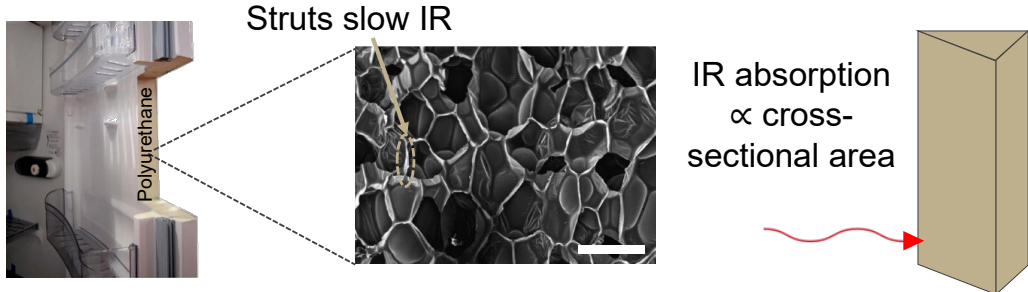
Figure I.4: Left: inside of a refrigerator door reveals polyurethane insulating foam. Center: SEM micrograph of such a foam with the struts at the junction of multiple cells highlighted (scale bar is 500 μm). Adapted with permission from Figure 8 of Xia Cao *et al*. "Polyurethane/clay nanocomposites foams: processing, structure and properties". In: Polymer 46.3 (Jan. 2005), pp. 775–783.©Elsevier 2005 [23]). Right: infrared radiation is mostly absorbed by struts proportional to their cross-sectional area. Therefore, more, smaller struts increases absorption of infrared radiation.

the diameter of the cells (eq 4.10 of [24]). The radiative thermal conductivity is inversely proportional to the extinction coefficient at a fixed temperature (eq 8 of [19]), such that the thermal conductivity would be proportional to the cell diameter according to the model, which is consistent with the empirical result shown in Figure I.5a.

The effectiveness of reducing cell size in reducing the thermal conductivity of RPUFs has typically motivated study on methods for enhancing bubble nucleation [15]. While reducing coalescence and ripening also increases the number density of cells, the desired number density of cells will never be reached without nucleating at least as many bubbles. Bubble nucleation must occur rapidly because each bubble depletes the available dissolved gas in the surrounding medium as it grows. The success of dramatic increases in the nucleation rate in producing foams with more and smaller cells has been demonstrated in nanocellular foams, which are discussed in the next section on CO_2-blown foams. Nanocellular foams have so far only been produced in thermoplastic foams by dissolving blowing agent (typically CO_2) into the polymer at high pressures (up to 30 MPa) and depressurizing quickly to drive rapid nucleation of bubbles [21]. The production of polyurethane foams, however, is far more complex.

The production of polyurethane foam is a finely tuned symphony of chemical reactions, phase changes, volume changes, and rheological changes. Polyurethane foam is produced by mixing two reacting streams. One stream is predominantly
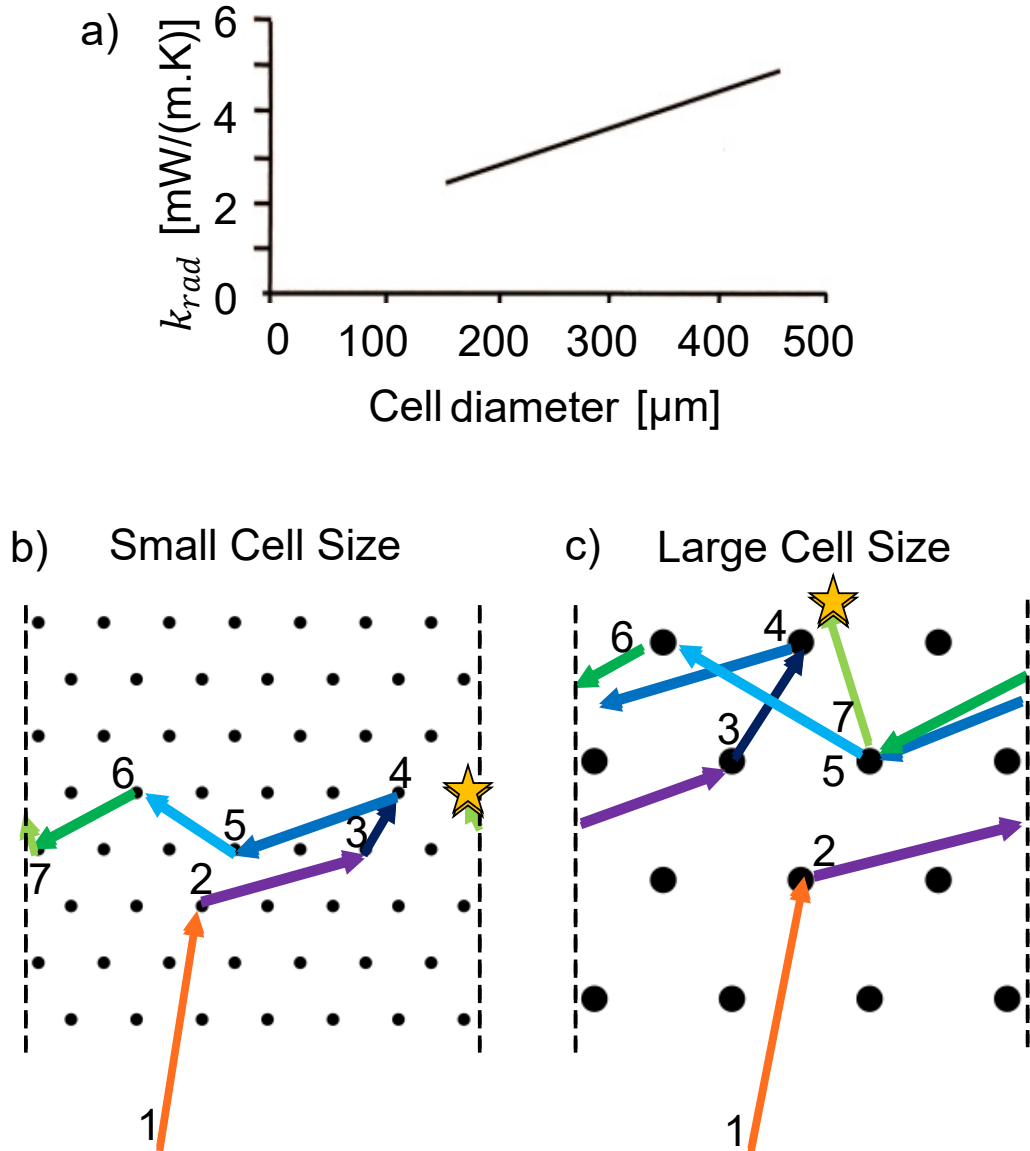
Figure I.5: a) The contribution to the thermal conductivity of a polyurethane foam by radiative heat transfer k_{rad} decreases with the cell size for cells on the order of 100–1000 μm. Adapted from Figure 15-6 of *The Polyurethanes Book* edited by David Randall and Steve Lee (2002). Made available by the US EPA Health & Environmental Research Online (HERO) database, HERO ID 4159100. b) Schematic of a possible path of an infrared photon through a foam, where each dot represents a strut that can absorb the photon and re-radiate it in a random direction. c) Schematic of the same sequence of absorptions and re-radiations of the photon in (b) but in a coarser foam. The larger spacing between struts allows the photon to travel through the foam more quickly, leading to a higher thermal conductivity through radiation.

polyol, a generic term for a polymer with hydroxyl groups at the end. The polyol is mixed with water, a "physical blowing agent" (PBA), surfactants, flame retardant,
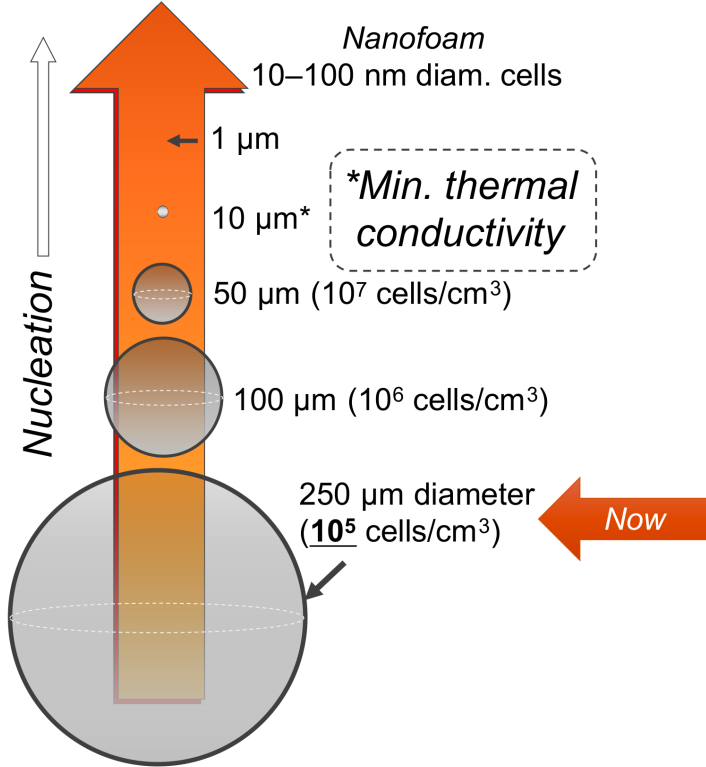
Figure I.6: Schematic of reduction in cell size needed to make significant reductions in the thermal conductivity of polyurethane foams. Current foams have cells of diameter $\sim 250\,\mu$m. By reducing the cell diameter to $50\,\mu$m, the overall contribution to the thermal conductivity could be reduced by half (extrapolate trend in Figure I.5). Reducing the cell size by a factor of 5 requires increasing the number of cells by a factor of 125, which will inherently require more bubble nucleation. Note that further reduction in the cell size to the nanoscale would cause radiative heat transfer to increase, but would limit gas conduction by entering the Knudsen diffusion regime.

and catalysts [25]. These components can be mixed together because they are not particularly reactive. The other stream is made purely of isocyanate; nothing is mixed with it due to its highly reactive cyanate end groups. The two streams are mixed at high pressure due to their high viscosities (up to ~ 1 Pa.s). For a discussion of the components of a polyurethane rigid foam, see the patent application by Golini and Guandalini [26].

Once mixed, these two streams undergo two chemical reactions (Figure I.9). The highly reactive cyanate end groups of the isocyanate attack the hydroxyl (-OH) end groups of the polyol to form polyurethane cross-links. The cyanate end groups also react with the hydroxyl groups in the water, which produces carbon dioxide

and an amine that then reacts with an isocyanate group to form a urea cross-link. This liberated CO_2 drives early blowing of the foam. Later, the heat released from these two exothermic reactions vaporizes the volatile PBA, typically a hydrocarbon like cyclopentane or, historically an HCFC (see discussion on their discontinued use in the next section on CO_2-blown foams). For example, the boiling point for cyclopentane, a PBA commonly used in RPUFs, is about 49 °C, while the PU foam can reach 120 °C [25] to 190 °C [7] during curing, lasting minutes to hours. The nucleation of bubbles therefore is driven by an increase in the concentration of gas (CO_2 and vaporized cyclopentane) and decreased solubility in the polymer matrix, due to both the rising temperature and curing. Surfactants reduce the interfacial tension of bubbles, decreasing the nucleation barrier (see discussion of the role of interfacial tension in Section I.4) and reducing the driving force for coarsening through coalescence and ripening. The selection of surfactant can mean the difference between an open-cell and a closed-cell foam. Catalysts accelerate the polyurethane synthesis reaction so the foam cures fast enough to prevent collapse, but slowly enough to allow for expansion [7].

When first ejected from the nozzle, the mixture of polyol and isocyanate is still translucent because it has not yet reacted and few bubbles have nucleated. After about 10 seconds, enough bubbles nucleate and grow to micron size that the mixture becomes opaque and has a yellowish, creamy appearance; this point in time is known as the "cream time." After about 1 minute, the foam becomes sticky, such that inserting and removing a probe (*e.g.*, wooden tongue depressor) leaves a string of foam stuck to the end; this time is known as the "gel time." Finally, after a few minutes the surface of the foam is no longer tacky, such that a probe does not stick when tapped on the surface; this time is known as the "tack-free time." Nevertheless, the reaction may continue for hours thereafter [7]. The height and temperature of the foam is plotted over time in Figure I.7.

With so many components interacting simultaneously during the production of an RPUF, identifying the effects of each component on bubble nucleation is challenging. Many studies have focused on the effect of adding micro- or nano-particles to provide more sites for heterogeneous bubble nucleation [15].

Others have focused on dissolving more blowing agent into the polymer to increase bubble nucleation. Depressurization will then induce a greater supersaturation, reducing the nucleation barrier (see discussion of the effect of supersaturation on the nucleation barrier in Section I.4) and increasing the nucleation rate. By
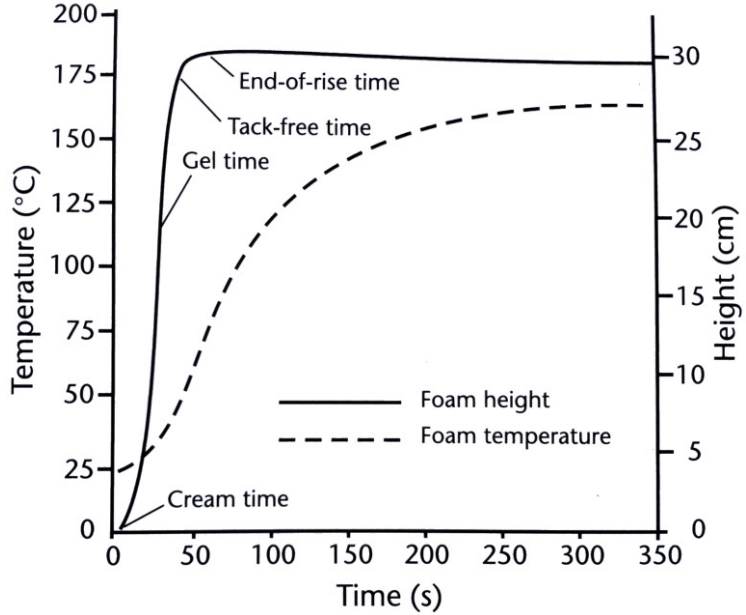
Figure I.7: Polyurethane foam temperature (dashed line, left vertical axis) and rise height (solid line, right vertical axis) over time. The cream time (when the foam becomes opaque), gel time (when the foam becomes sticky and elastic upon poking with a wooden stick), tack-free time (when the foam does not leave a tacky residue upon poking with a wooden stick), and end-of-rise time (when the foam stops rising) are marked. Adapted from Figure 15-1 of *The Polyurethanes Book* edited by David Randall and Steve Lee (2002). Made available by the US EPA Health & Environmental Research Online (HERO) database, HERO ID 4159100.

dramatically increasing the solubility of CO_2 in poly(methylmethacrylate) (PMMA) by reducing the saturation temperature to as low as -30 °C [27] or increasing the saturation pressure as high as 30 MPa [22], the average cell size of the resulting foam after a pressure quench can be made as low as 200 nm [22, 28]. Other techniques for enhancing bubble nucleation in polymer foams changes the pressure during the chemical reaction. Simply dropping the pressure more rapidly can increase the nucleation rate of CO_2-blown polymer foams by an order of magnitude [29].

Increasing bubble nucleation in reactive foams, such as polyurethane, can be more challenging than in thermoplastic foams due to the dynamic changes in the viscosity and modulus of the polymer during the reaction. Two groups have demonstrated that changing the pressure in specific ways during the chemical reaction can significantly increase bubble nucleation rates. Yang *et al.* described a two-step pressurization process in which the reactants are first saturated with CO_2 before the reaction, and then, while the reaction is occurring, the pressure is further increased and held before a rapid depressurization drives foam formation. They found that

the curing reaction reduced the solubility of CO_2 in the polymer matrix, causing premature bubble nucleation before the pressure quench. By increasing the CO_2 pressure during the curing reaction, they found that the resulting foam had micron-sized cells of uniform distribution, which they believe resulted from the suppression of premature bubble nucleation during curing by the higher pressure [30]. Brondi *et al.* described a processing protocol in which the reactants are first saturated with CO_2 and the pressure is suddenly quenched partially when the reaction begins. This initial partial pressure quench nucleates many small bubbles but prevents them from growing while the foam is not cured. As the reaction proceeds and the polyurethane foam cures, the pressure is gradually decreased, such that the toughening of the solid matrix matches the added stress from the expanding bubbles to produce a fine-celled foam with minimal coalescence [31].

Due to the difficulty of observing foaming *in situ*, these studies tend to focus on the correlation between the particles added and the foam produced. In this thesis, we seek to address the challenge of direct observation of bubble nucleation in RPUFs. Relative to thermoplastic foams (see Section III.1), observing bubble nucleation in RPUFs is more challenging due to the opacity that arises during the initial mixing of polyol and isocyanate. Direct observation of bubble nucleation during polyurethane foaming has consequently not yet been demonstrated in the literature. Nevertheless, several researchers have made impressive contributions to the understanding of the effects of the compounds and processes involved in polyurethane foaming on bubble nucleation and growth in the last two decades. Minogue is recognized as having published the first live images of bubble growth in polyurethane foam in 2000 [32]. To observe bubbles under a microscope, Minogue first mixed the components of polyurethane with a turbine mixer, then placed a droplet of the mixture on a microscope slide with a spatula and covered it with a coverslip. Despite the potential for inconsistencies in the sample preparation, Minogue repeated each experiment 10 times, which was sufficient to show statistically significant differences between bubble nucleation and growth rates upon the addition of various components of polyurethane, including surfactants, catalysts, and different blowing agents, specifically, cyclopentane and perfluorohexane. The images acquired by this technique are limited in three important ways, however. First, clear images cannot be acquired until about 30 seconds after mixing due to cloudiness resulting from the poor miscibility of polyol and isocyanate. Second, optical microscopy cannot directly observe bubble nucleation because bubble nuclei are smaller than the diffraction limit of light (about 1 μm). Third, the microscope is focused on the

inner surface of the coverslip, so only bubbles that nucleate and grow along this surface are in focus.

Reignier *et al.* [33] overcame these challenges by observing snapshots of bubble growth in PU with cryo-SEM. After mixing the components in a rotating mixer at 2500 RPM, they poured the sample at the desired time into an SEM specimen holder kept cold enough to cryogenically freeze the foam. The morphology of the frozen foam could then be analyzed with SEM. With this freezing technique, they showed the structure of the foam as early as 13 seconds after mixing. Additionally, because the resolution of SEM is much smaller than optical microscopy (order tens of nanometers) due to the shorter wavelength of electrons than optical photons, they could resolve bubbles smaller than 1 μm. Finally, they could section the frozen sample to examine bubbles that were not affected by the walls of the foaming container. Their unique approach to observing bubbles in the production of RPUFs revealed nanodroplets (14–71 nm in diameter) composed of their PBA (isopentane) dispersed throughout the polymer matrix, which they attributed to emulsification by the surfactant (polysiloxane-ether). They did not observe these nanodomains of PBA in foams frozen more than 24 seconds after mixing, when the temperature had only reached 31.5 °C, while the boiling point of isopentane is only slightly lower (27.8 °C). At this stage of foaming, the number of cells observed was the same as the number of air bubbles entrained during the initial mixing (air bubbles could be clearly distinguished from nanodomains of PBA by their significantly larger size). This observation led them to conclude that the cells they could observe in the final foam were produced by entraining air and not homogeneous bubble nucleation. Their conclusion highlighted the importance of preventing the entrainment of air for the measurement of homogeneous bubble nucleation.

Brondi *et al.* provide a possible explanation for the limited role of CO_2 and the PBA in driving bubble nucleation observed by Reignier *et al.* They analyzed bubble growth along an optically clear window inserted into the wall of the foaming container following a procedure similar to the standard cup-foaming procedure (ASTM D7487 [34]). While their observations were limited to bubbles that grew along the optically clear window, they could draw qualitative comparisons between the effects of different processing conditions on the overall nucleation and growth rates of bubbles. They first observed that the number of bubbles decreased in foams produced by mixing at rates fast enough to entrain air bubbles (1000 RPM), suggesting that no new bubbles nucleated while some air bubbles merged. This

observation is consistent with the observation of Reignier *et al.* that new bubbles do not nucleate during polyurethane foaming in the presence of entrained air bubbles [33]. When they mixed the foam at a rate slow enough *not* to entrain air bubbles (50 RPM), however, they saw bubbles nucleate. Industrial mixers used for polyurethane are designed not to entrain air, which is a quality that we sought to replicate in our apparatus given the significant effect of entrained air observed in this work by Brondi *et al.* (see Section III.2). This observation suggests that, at least in the presence of a surfactant, liberated CO_2 or vaporized hydrocarbon PBA can nucleate bubbles, contrary to the conclusion of Reignier *et al.* [33]. They also observed that foams with cyclopentane (hydrocarbon PBA) in addition to water produced more, larger bubbles than foams without cyclopentane. Minogue also observed that polyurethane foams blown with cyclopentane increased cell size, attributing the improved mixing due to the lower viscosity as the cause [32].

All the previous studies but that of Reignier *et al.* were limited to observation of bubbles that grew along a solid surface. While Reignier *et al.* were limited to interior bubbles frozen at specific times during foaming, Perez-Tamarit *et al.* achieved live imaging of interior bubbles using X-ray tomography [35]. By focusing their observation on bubbles that nucleated in the bulk rather than on those that nucleated heterogeneously on the surface of the container walls, they could more precisely investigate the effect of adding nanoparticles on bubble nucleation. With a time resolution of 156 ms, they showed that adding 3 % by weight of fumed silica nanoparticles (10–40 nm diameter at a density of 60 g/L, or approximately 10^{17} particles/cm^3) increased the number of bubbles by two orders of magnitude. A similar effect has been observed in a CO_2-blown polystyrene foam upon the addition of 10^9/cm^3 talc microparticles (1.8 μm diameter) to the polystyrene [29]. Nevertheless, published industrial formulations do not include any solid particles [26], suggesting that other disadvantages of adding solid particles might outweigh the advantage of increasing bubble nucleation.

Roberts *et al.* observed foaming in a transparent column after injection of the mixed polyurethane components with a syringe [36]. They observed the foam with three techniques: (1) optical microscopy, (2) SEM, and (3) diffusing wave spectroscopy (DWS). Optical microscopy provided live measurements of the bubble size distribution, but was limited to bubbles that grew along the observation window, as in many of the previous studies discussed above. They referred to this region of the foam as the "skin." SEM provided a high-resolution measurement of the

final bulk foam morphology. They noted that the bubbles in the skin observed with optical microscopy had a significantly different size distribution than bubbles in the bulk observed with SEM. To provide live measurements of the bubble size in the bulk, they developed an apparatus to probe the bulk of the foam with a laser and perform DWS on the signal to estimate the average bubble size. Unlike the optical measurements of bubbles along the skin, the DWS measurement of the average size of bubbles in the bulk was consistent with SEM measurements of the final size distribution, providing further evidence of the difference in growth of bubbles along the skin and in the bulk.

A striking visual depiction of this difference is shown for the foaming of polystyrene with CO_2 and N_2 gas in Figure I.8 [37]. Images are shown before (first image) and after depressurization, with the time since beginning depressurization listed below each image. The region outside the ring is in contact with a surface while the region inside is only exposed to gas, so the bubbles observed within the ring are far more likely to have nucleated in the bulk. Bubbles along the skin are more numerous and larger than bubbles in the bulk.
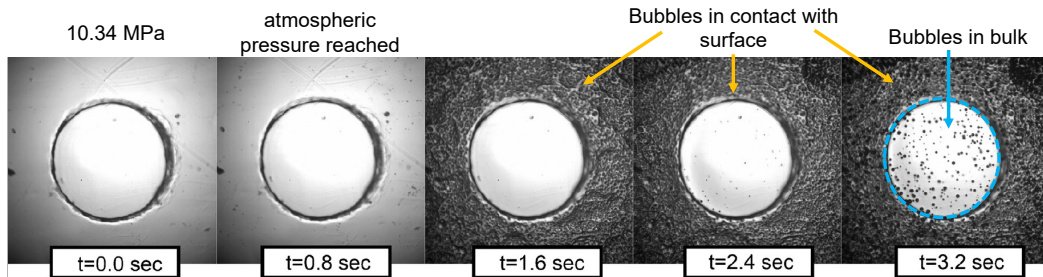
Figure I.8: Nucleation of bubbles in polystyrene blown with a blend of dissolved CO_2 and N_2 is significantly greater where the polystyrene is in contact with a solid surface than where it is only in contact with the atmosphere (inside blue dashed circle in rightmost image). Adapted with permission from Anson Wong *et al.* "The synergy of supercritical CO2 and supercritical N2 in foaming of polystyrene for cell nucleation". In: *Journal of Supercritical Fluids* 90 (2014), pp. 35–43. ©Elsevier 2014 [37].

Each of the studies discussed above has made a significant contribution to the general understanding of bubble nucleation and growth in polyurethane foams. The instruments used in each have distinct features, the most important of which are summarized in Table I.1. In entering this field, we identified three features missing from all previous studies, performing a continuous foaming process and imaging within 100 ms from the start of foaming, and producing foam from a high-pressure nozzle, which are written in bold in the Table. The first, continuous foaming, is

important because much more data can be collected from a continuous process than a batch process. The second, imaging within 100 ms from the start of foaming, is important because the initial degree of mixing of the polyol and isocyanate has been shown to affect the foam structure. The third, producing the foam from a high-pressure nozzle, is important for making a more direct comparison to industrial foaming, where RPUFs are produced from nozzles at pressures exceeding 8 MPa [16]. In many extruded foams, bubbles may nucleate within the nozzle because the pressure will decrease below the saturation pressure of the dissolved gas. If too many bubbles form in the nozzle, they may expand too rapidly as a result of the large decrease in pressure upon exiting the nozzle and lead to some collapse of the foam [38], but bubble nucleation in a nozzle has not yet been reported in the literature. We therefore designed the instrument for the present study to provide these features (see Chapter III).

Feature	[32]	[35]	[33]	[39]	[36]	This work
Can measure bubbles in the bulk		✓	✓		✓	✓
Live imaging	✓	✓		✓	✓	✓
Sub-micron imaging			✓		✓	
3D imaging		✓				
Images bubbles 1–90 s after mixing	✓	✓	✓	✓	✓	
Images bubbles > 90 s after mixing	✓			✓	✓	
Prevents entrainment of air	✓			✓		✓
Continuous process						✓
Images within 100 ms from start of foaming						✓
Foam produced in high-pressure nozzle						✓

Table I.1: Compares key features of studies of polyurethane foaming by previous research groups with the present work. Unique features of the experimental method described in the present thesis are bolded. Studies are listed by reference number in the table. Author list and year for each study are listed here: [32] Minogue (2000), [35] Perez-Tamarit *et al.* (2019), [33] Reignier *et al.* (2019), [39] Brondi *et al.* (2021), [36] Roberts *et al.* (2022).

In addition to developing an instrument capable of achieving those three features, the present work aimed to elucidate the specific role of the many components of the polyurethane formulation. Therefore, rather than study a full formulation, we
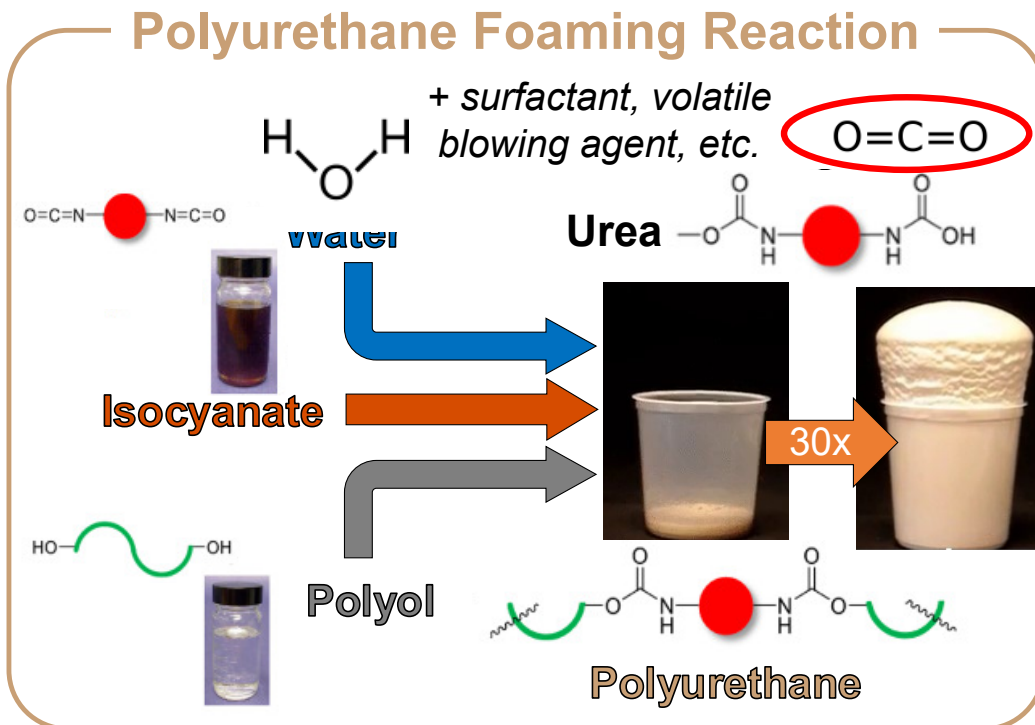
Figure I.9: Schematic of the polyurethane reaction, focusing on the main chemical reactions (polyol + isocyanate to form polyurethane and isocyanate + water to form CO_2 and urea). The foam also usually has surfactants and volatile blowing agents (*e.g.*, cyclopentane) mixed in the polyol formulation. The polyurethane foam can grow in volume by a factor of 30, as shown schematically by the beginning and end of a cup foaming experiment shown in the center (to expand by a factor of 30, foam must be produced in a high-pressure nozzle). Molecular structures and macroscale pictures of chemicals used with permission from Dr. Chris Letko of Dow, Inc. Original source for cup foaming experiment unknown.

began with the simplest model system for polyurethane, polyol and CO_2, shown in Figure I.10. Polyol and CO_2 were selected to be the model system given their ability to produce a foam with a similar expansion ratio and viscosity (prior to curing) as polyurethane. Due to the technical difficulty of generating carbon dioxide *in situ*, we study bubble nucleation from carbon dioxide dissolved in the polyol inside a high-pressure reactor. This mixture is then transferred under pressure to a high-pressure syringe pump for use in our experimental apparatus (presented in Chapter III). While this method of bubble nucleation is more similar to CO_2-blown foams like polystyrene (see discussion of these foams in the next subsection) than foams with CO_2 produced *in situ* like polyurethaen, we believe that its study will provide a foundation for individually studying the effects of each of the key components in a polyurethane formulation: PBA, surfactant, isocyanate, heat, water, and catalyst.

Due to the complexity of the experiment, we have only just begun investigation into the effects of adding either cyclopentane (PBA) or surfactant, as discussed in Chapter VII.
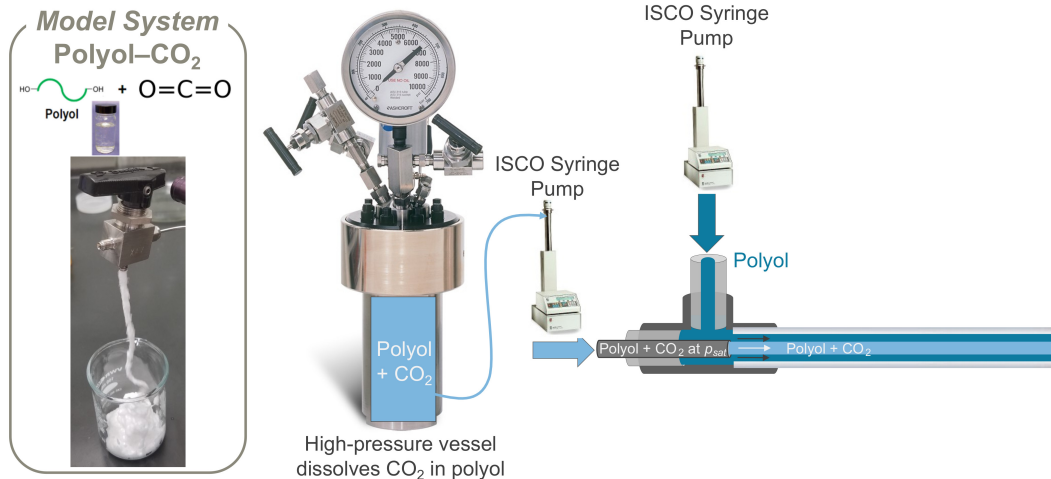
Figure I.10: Schematic of model system of the fewest components required to make a convincing foam: polyol and CO_2. Experimental procedure shown to the right. Because of the absence of isocyanate and water, CO_2 is not produced in the model system, so it is instead dissolved into polyol under high pressures in a Parr reactor. The mixture is then transferred under high pressure to an ISCO syringe pump, which pumps it into the inner stream of the microfluidic channel used to study bubble nucleation (discussed in Chapter III—see Figure III.1). Additional components can be added in sequentially to understand their effect on bubble nucleation and growth. Molecular structures and macroscale pictures of chemicals used with permission from Dr. Chris Letko of Dow, Inc. Original source for cup foaming experiment unknown.

Polyols used in polyurethane are typically either polyether polyols or polyester polyols. In general, polyether polyols are chosen for thermally insulating polyurethane foams because of their hydrolytic stability [40], easier processability (liquid at room temperature), and highly customizable architecture relative to polyester polyols [40]. Most RPUFs are produced with polyether polyols of high functionality, meaning a high number of hydroxyl functional groups per polymer chain, which yields a greater number of cross-links for a more rigid foam [7]. For these reasons, we will focus on polyether polyols in the present work, using higher functionality polyols where possible.

In Chapter VII, we explore the effects of adding other ingredients in the polyurethane formulation, specifically, cyclopentane (physical blowing agent) and silicone surfactant. While most who have worked with polyurethane observe that

the properties of polyurethane cannot be extrapolated based on the individual effects of each component, we hope that by carefully measuring the effects of individual components on bubble nucleation and comparing to theoretical models, we provide useful insights into the roles played by each component in achieving the remarkable properties of polyurethane insulating foams.

Carbon Dioxide: The Green Option for Blowing Foams

Foams blown with CO_2 are valuable for their lower impact on the environment. In the late 1950s, manufacturers discovered that they could produce polyurethane foams with unprecedented low thermal conductivity by blowing with chlorofluorocarbons (CFCs) in addition to the CO_2 produced from the reaction of isocyanate and water. CFCs have half the thermal conductivity of CO_2 (7.4 mW/(m.K) for CFC-11 (CCl_3F) vs. 15.3 mW/(m.K) for CO_2 at 10 °C) due to their slower diffusivity resulting from their higher molecular weights (137.4 g/mol for CFC-11 (CCl_3F) vs. 44 g/mol for CO_2), as shown in Figure I.11 [7]. CFCs also deplete the ozone and were phased out over a decade ago according to the 1987 Montreal Protocol [7].
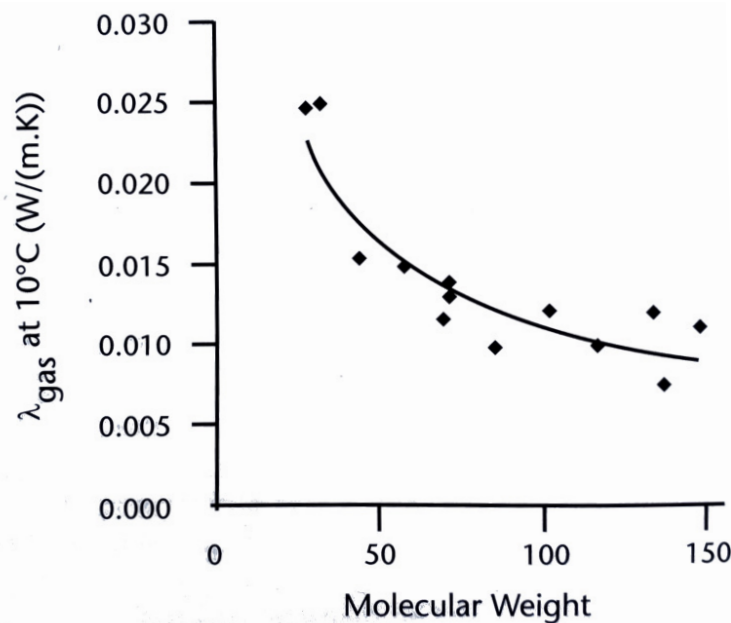
Figure I.11: Thermal conductivity contribution from gas conduction λ_{gas} plotted as a function of the molecular weight of different physical blowing agents. Data are plotted as diamonds and a curve is drawn to guide the eye. Reproduced from Figure 15-8 of *The Polyurethanes Book* edited by David Randall and Steve Lee (2002). Made available by the US EPA Health & Environmental Research Online (HERO) database, HERO ID 4159100.

Following the adoption of the Montreal Protocol, hydrochlorofluorocarbons (HCFCs) were introduced as alternatives to CFCs due to their significantly lower ozone depletion potential, but because they nevertheless deplete the ozone and typically have a global warming potential one thousand times larger than that of CO_2, they are planned to be phased out by 2040 according to the 1992 Copenhagen amendment to the Montreal Protocol [7]. Hydrofluorocarbons (HFCs) are currently used as alternatives to CFCs and HCFCs because their lack of chlorine means that they do not deplete the ozone and research suggests that they do not contribute to smog [7]. They nevertheless have a global warming potential of about a thousand times more than CO_2 (1600 for HFC-134a vs. 1 for CO_2), but are targeted for phasing out by the Paris Climate Agreement (2015) and the Kigali amendment to the Montreal Protocol (2016) [41]. Hydrocarbons, particularly isopentane and cyclopentane, emerged as alternative physical blowing agents in the late 1980s with the development of technology for safe handling of these flammable compounds during manufacturing [7]. Nonetheless, foams blown with hydrocarbons pose a high risk of flammability to customers, even with the addition of flame retardants [42]. Perfluorocarbons (*e.g.*, C_5F_{12}) are non-flammable alternatives to hydrocarbons, but due to their high global warming potential, they have not been used in commercial polyurethane foams [7].

In contrast, CO_2 poses none of the hazards caused by the blowing agents listed above: it does not deplete the ozone, it is not flammable, and it has a negligible global warming potential because the CO_2 feedstock often comes from industrial waste streams that would otherwise end up in the atmosphere. Nitrogen gas N_2 is also a sustainable blowing agent, but it is less commonly used due to lower solubility in many polymers [43, 44] and higher interfacial tension [44], which may hinder nucleation. It is worth noting, however, that a 75:25 mixture of supercritical CO_2 and supercritical N_2 can yield a higher cell number density in polystyrene foaming as compared to either pure gas in its supercritical state [37].

Were blowing high-quality foams easier with CO_2 than CFCs, we never would have gone through the trouble of synthesizing CFCs. CFCs, however, are highly soluble in a variety of polymers at atmospheric pressure, while CO_2 requires several MPa of pressure to reach even 10% solubility (see Chapter II). Closed-cell foams filled with CFCs also have lower thermal conductivity, due to both the lower thermal conductivity of CFC than CO_2 mentioned above and the lower diffusivity of CFCs, which slows the rate that the blowing agent diffuses out of the foam [45]. Due

to the higher thermal conductivity of CO_2 gas resulting from its lower molecular weight, thermal conductivity must be reduced through structural improvements, in particular, increasing cell density and expansion ratio. Previous studies have shown that both of these properties increase with the amount of dissolved CO_2 [22, 28, 46]. Furthermore, the accessibility of the supercritical regime of CO_2 (> 7.39 MPa, > 31.6 °C [47]) made possible the development of microcellular foams due to its low interfacial tension that promotes bubble nucleation [30] (see discussion of role of interfacial tension in nucleation in Section I.4). CO_2 also acts as a plasticizer that can allow for easier processability and extrusion [48].

Foams blown with CO_2 are produced in two stages. First, CO_2 must be dissolved into the glassy polymer by pressurizing the atmosphere with CO_2 to several MPa, making it easier to process by lowering the glass transition temperature T_g below the processing temperature. Second, the foam is expanded. The polymer is initially expanded by reducing the pressure, but glassier polymers with higher T_g may be subsequently heated for further expansion. The resulting foam ultimately solidifies as the polymer cools and loses dissolved CO_2, returning it to its glassy state [49].

Often, foams blown with CO_2 are lower in performance and more challenging to produce than foams blown with other blowing agents. The production of CO_2-blown foams with properties competitive with other commercial foams requires that the foam be made microcellular, meaning that the cell size must be on the order of 1–100 μm [50]. Producing microcellular foams requires a large enhancement in nucleation only possible with supercritical or liquid CO_2, due to the reduction in interfacial tension along the surface of bubble nuclei (see Section I.4 for a discussion of the role of the interfacial tension in the nucleation rate). The high pressures needed to use supercritical and liquid CO_2 require more robust equipment and additional safety protocols, which add to the cost. Furthermore, before blowing a foam with CO_2, the CO_2 must be dissolved into the polymer, which may take on the order of days even for a 1.5 mm-thick sample [51]. Consequently, few CO_2 blown foams exist commercially, although they are replacing the more hazardous and environmentally harmful blowing agents listed above in some foams, such as polystyrene coffee cups and meat trays. More often, CO_2 is effective as a co-blowing agent, as in the case of polyurethane and structural polystyrene foams, where CO_2 is mixed with volatile hydrocarbons [45].

Should the cost of blowing polymer foams with supercritical CO_2 be made

economical, it may provide a feasible route to the production of nanocellular foams. Nanocellular foams are foams with cells that are significantly smaller than 1 μm, often with the goal of producing cells smaller than 100 nm to reach a new regime of thermal, dielectric, mechanical, and optical properties [52]. They require substantially more bubble nucleation, which is made possible by (1) dissolving high concentrations of CO_2 (> 25%) into the polymer, often requiring high pressure (*e.g.*, > 20 MPa) and low temperature, (2) quenching the pressure fast enough that the CO_2 remains supercritical and avoids the high nucleation barrier of the liquid–vapor equilibrium, and (3) adding nanoparticles to act as nucleation sites [53]. Nanocellular foams are particularly relevant to primary application of the present work, the reduction of the thermal conductivity of insulating foams, having a cell size smaller than the mean free path of air. When gas molecules are confined to dimensions smaller than their mean free path, they no longer conduct heat as efficiently, being frequently interrupted by the confining structure. This reduction in heat conduction is known as the "Knudsen effect," and is the same mechanism by which aerogels have such low thermal conductivity as well [52].

Every nanofoam relies on a substantial increase in bubble nucleation relative to microfoams because the number density of cells grows as the inverse third power of the cell size. While many techniques have been shown to enhance bubble nucleation enough to produce reliable nanofoams, from applying a stress to reduce the nucleation barrier energy [54] to inducing nanoscopic phase separation with block copolymers [55], nanofoams still have a relatively lower porosity (maximum 85% [52]) than commerical polyurethane foams [7]. Therefore, while the gas component of nanofoams may have a lower thermal conductivity than polyurethane foams, its solid component conducts significantly more heat. Greater porosity is necessary to make nanofoams commercially viable.

I.4 Bubble Nucleation: Many Models, Few Measurements

Bubble nucleation inherently takes place out of equilibrium when a liquid is brought to a metastable state in which a vapor phase is more thermodynamically stable. Therefore, a rigorous treatment of bubble nucleation would employ a kinetic model [56]. A proper kinetic model of bubble nucleation considers bubble embryos consisting of 1, 2, 3,..., N particles, where N is some number much larger than the smallest stable nucleus, defined by the critical radius. A particle may enter an embryo, increasing its size by 1, or it may leave, decreasing its size by 1, with the rate of each depending on the nucleus size and supersaturation. Most embryos are

unstable and dissolve back into solution, but those that reach a critical size continue to grow according to the transport properties of the medium. Modeling this kinetic process therefore requires both (1) molecular precision to resolve absorption and desorption of single molecules and (2) long simulation times for representative statistics of the frequency of successful bubble nucleation. Molecular dynamics simulations have successfully estimated homogeneous bubble nucleation rates in single-component vapors under high supersaturation, for which the critical embryo size is small and nucleation rate is high [57].

To identify the "onset" of nucleation, *i.e.* the supersaturation at which bubbles nucleate within a time scale relevant for experimental observation (typically seconds), a more efficient calculation is required. In these cases, the supersaturation is small, such that the critical size of the bubble embryo is large enough to be treated as a uniform thermodynamic phase. Furthermore, bubble nucleation is rare enough that it is limited by the reversible work ΔG^* required to form a bubble embryo of the critical size. Therefore, if we assume a well-defined interface and constant temperature during nucleation—which are not guaranteed for the nucleation of a vapor in a liquid—the nucleation of a bubble can be approximated as a quasi-equilibrium process where the rate of nucleation J is proportional to the Boltzmann factor corresponding to the critical embryo size

$$J \propto e^{-\Delta G^*/k_B T} \tag{I.1}$$

This Arrhenius-like model for bubble nucleation was first proposed by Volmer and Weber [58] using the thermodynamic principles of Gibbs and Boltzmann [59]. The full development of the thermodynamic model of bubble nucleation into a formalized theory, known as "classical nucleation theory" (CNT), including the derivation of the prefactor for the exponential term based on the conditions of the system and deviations from equilibrium, are credited to Farkas [60], Kaischew and Stranski [61], Becker and Döring [62], Zeldovich [63], and Kagan [64]. Their work showed that the thermodynamic picture of bubble nucleation that is the hallmark of CNT emerges from the application of constraints to the kinetic model. Assuming that the metastable state is stable enough for the sizes of bubble embryos to reach an equilibrium distribution and that the rates at which particles are absorbed into and released from the embryo are independent of time and embryo size and occur one at a time (*i.e.* no merging or splitting of embryos), the rate at which embryos of $n-1$ particles gain a particle and grow to size n is equal to the rate at which embryos of

n particles lose a particle and shrink to size $n-1$ by microscopic reversibility. This assumption is the key to reaching a thermodynamic model from a kinetic framework because it allows the use of Boltzmann factors to estimate the number density of embryos of different sizes. The Boltzmann factor, $e^{-\Delta G(n)/k_B T}$ requires the calculation of the reversible work $\Delta G(n)$ to form an embryo of *n* particles. Due to the small size of the embryos, the application of thermodynamics is not always appropriate because it models each phase as a homogeneous bulk. In cases where the critical embryo size is large enough to be described as a bulk thermodynamic phase and the interfacial tension along the surface of the embryo can be well approximated by the planar surface tension, treating the embryo as a uniform thermodynamic phase and its surface as an infinitesimal boundary is reasonable [65].

In this thermodynamic picture, the dominant contributions to the reversible work to form an embryo of size *n* are the lower chemical potential of the embryo, which is the driving force for nucleation resulting from supersaturation, and the energy penalty for creating a surface between the embryo and the mother phase, which drives the dissolution of the embryo. The first is proportional to the volume and the second to the area.

In the case of a single-component mixture, this thermodynamic picture results in the following equation for the reversible work of embryo formation,

$$\Delta G(n) = (\mu_{bub} - \mu_{bulk})n + F(n)\gamma \tag{I.2}$$

where μ_{bub} is the chemical potential of the bubble embryo, μ_{bulk} is the chemical potential of the bulk mother phase, $F(n)$ gives the surface area of an embryo of *n* particles, and γ is the interfacial tension along the surface of the embryo. If we assume that the embryo is a sphere of radius R, then $n = \frac{4\pi}{3}R^3 v$ where v is the volume of one particle, and $F(n) = 4\pi R^2$. Letting $\Delta\mu \equiv \mu_{bulk} - \mu_{bub}$, which must be greater than 0 for bubble nucleation, we can rewrite equation I.2 as

$$\Delta G(R) = -\frac{4\pi}{3}R^3 v(\Delta\mu) + 4\pi R^2 \gamma \tag{I.3}$$

This expression for the reversible work to form a bubble embryo of radius R is plotted in Figure I.12. Based on this model, the reversible work peaks at a critical radius R^*: the drive to lower energy will cause smaller bubble embryos to shrink and larger bubble embryos to grow.
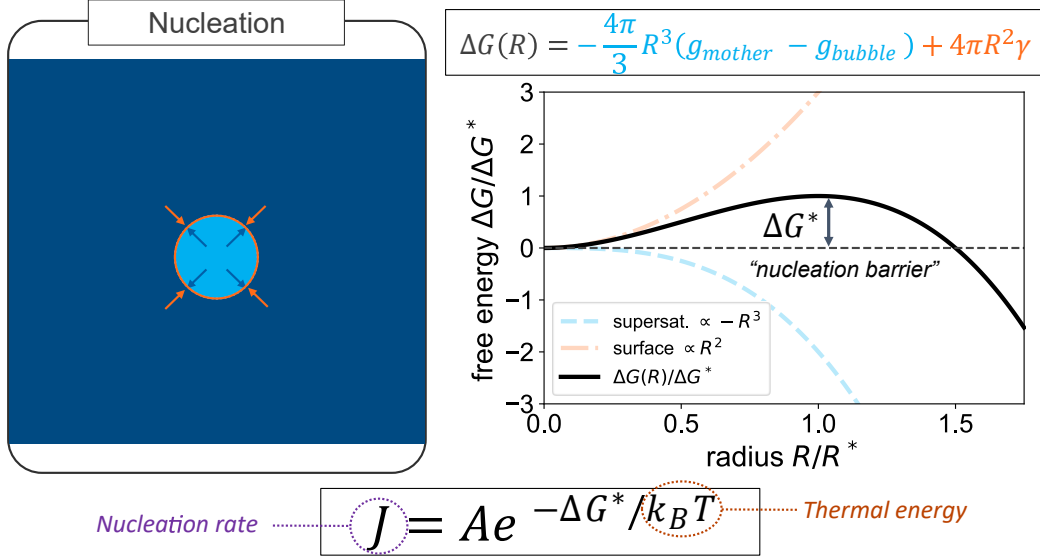
Figure I.12: The reversible work to form a bubble embryo of radius R is plotted (black solid line) alongside the energy gain due to supersaturation proportional to the volume (red dashed line) and the energy penalty due to the formation of an interface proportional to the surface area (blue dot-dash line). The radius R is scaled by the critical radius R^* and the reversible work $\Delta G(R)$ is scaled by the value at the critical radius $\Delta G^* \equiv \Delta G(R^*)$. The maximum value or "nucleation barrier" is indicated with an arrow as ΔG^*.

By maximizing $\Delta G(R)$ with respect to R in equation I.3, the critical radius is found to be

$$R^* = \frac{2\gamma}{v(-\Delta\mu)} \tag{I.4}$$

and the corresponding critical energy, known as the "nucleation energy barrier," is

$$\Delta G^* = \frac{16\pi}{3} \frac{\gamma^3}{v^2(\Delta\mu)^2} \tag{I.5}$$

although for an incompressible bubble assumed to be in equilibrium with the surrounding fluid, the following more convenient and experimentally tractable form of the nucleation barrier can be used [66]:

$$\Delta G^* = \frac{16\pi}{3} \frac{\gamma^3}{(\Delta p)^2} \tag{I.6}$$

where $\Delta p = p_{sat} - p$ with p_{sat} that pressure at which the gas was saturated in the mother phase. While more applicable to the condensation of liquid droplets (the

subject of Kalikmanov's review), the formula provides a tractable formula for rough calculations.

Because we have assumed that the size distribution of bubble embryos is given by the equilibrium distribution, which is proportional to the Boltzmann factor for each size $e^{-\Delta G(n)/k_B T}$, there are exponentially fewer bubble embryos of sizes near the critical size with radius R^*. This minimum in the bubble population creates a bottleneck in the kinetic picture: there are so few bubbles of this size that the rate of bubble nucleation is almost entirely determined by the rates of growth of bubbles of similar size. In the mathematical derivation, this feature allows an integral (which is used to approximate a summation to high accuracy) to be approximated by the quadratic expansion about the peak at $R = R^*$, which yields an expression for the nucleation rate of the following form

$$J = j(R^*)Z \left[N_{tot} \exp\left(-\frac{\Delta G^*}{k_B T} \right) \right] \tag{I.7}$$

where $j(R^*)$ is the product of the rate at which particles are absorbed into the embryo per unit area and the surface area of the critical nucleus $4\pi(R^*)^2$, originally suggested by Farkas [60], Z is the Zeldovich factor [63], which is proportional to the square-root of the second derivative of the reversible work at the peak $R = R^*$ and gives the deviation of the distribution of embryo sizes from the equilibrium distribution given by the Boltzmann factors [5], and N_{tot} is the total number density of bubble embryos which, when scaled by the Boltzmann factor, gives the rough number of critical bubble embryos. This model ignores the limitations of diffusion, viscosity, and inertia in the bulk fluid. While these aspects of the mother phase do not affect the exponential term, they can affect the form of the prefactor [5]. For further details of the mathematical derivation of this formula from the kinetic picture, see the review articles by Blander and Katz [5] and Oxtoby [67], and the books by Skripov [68], Debenedetti [56], and Kalikmanov [66].

For the experimentalist, the most significant feature of the model for the nucleation rate given in equation I.7 is the strong dependence of the exponential term on the supersaturation, quantified by the difference in chemical potential between the nucleating phase and the mother phase $\Delta\mu$. Because the prefactor tends to have a much weaker dependence on the supersaturation, it can generally be ignored in identifying the onset of bubble nucleation [5]. Therefore, a precise estimate of the

nucleation energy barrier ΔG^* may be sufficient to identify the supersaturation at which bubble nucleation becomes observable.

Because the measurement of the chemical potential is not straightforward, the expression for the nucleation energy barrier given in equation I.5 is often further simplified by making one of the following two assumptions: (1) the fluid is ideal, or (2) the fluid is incompressible. These yield the approximations for $\Delta \mu$ of (1) $\Delta \mu \approx \Delta p$, where Δp is the difference in the saturation pressure and the ambient pressure, and (2) $\Delta \mu \approx \log S$, where $S = \frac{p_{sat}}{p_{amb}}$ is the supersaturation ratio of saturation to ambient pressure.

These approximate models can yield reasonable agreement with experimental measurements. The most rigorous validation of classical nucleation theory (CNT) for homogeneous nucleation comes from studies of the superheating of liquids. Skripov reports a variety of early works in which the measured onset temperature of bubble nucleation in superheating liquids differed from the prediction by the appropriate form of CNT by less than 2 °C, which was often within the experimental error of the time [68]. He reasoned that the high sensitivity of the exponential term to temperature yielded a very sharply defined onset. The advantage of superheating water for testing CNT was more recently demonstrated by Ando *et al.*, who utilized a laser to superheat small regions of the bulk of a container of water, such that all nucleation was homogeneous due to the isolation from the container walls. They found that even the onset of bubble nucleation in water can be reasonably described by CNT [69]. Most notably in the field of polymer foaming, Goel and Parks demonstrated reasonable agreement between not just the onset of nucleation but also the nucleation rates observed in foams of poly(methyl methacrylate) (PMMA) and supercritical CO_2 [70]. In general, however, CNT tends to perform better for the precipitation of larger molecules, such as polymers in poor solvents, where "even a single chain takes the form of a spherical globule with a fairly uniform core when the chain is long enough" [71].

Nevertheless, CNT has generally faced considerable challenges in modeling nucleation in multicomponent mixtures. While the theory has been extended successfully to multiple components [56, 72], two of the fundamental assumptions of the theory often fail in multicomponent mixtures. First, the concentration profile of the components can be highly non-uniform, violating the assumption by CNT that each phase is homogeneous. In particular, when a volatile compound is dissolved in a liquid, as in the case of polymer foaming that is the focus of the present work,

the volatile component tends to aggregate along the surfaces of bubbles due to the gain in attractive energy, as shown by Talanquer and Oxtoby using classical density functional theory (DFT) [65]. This aggregation significantly affects the interfacial tension, which they found to result in errors in the prediction of the nucleation rate by CNT of factors up to 10^{20}. Xu *et al.* likewise found that the assumption of a infinitesimal interface by CNT yields an incorrect interfacial tension [73]. Second, multicomponent mixtures may nucleate in more than one step, while CNT assumes nucleation is completely defined by the overcoming of a single nucleation energy barrier ΔG^*. This behavior results from the Gibbs phase rule, according to which multicomponent mixtures can access more phases than pure substances. While there are exceptional cases in which CNT provides an accurate model for two-stage nucleation, it generally fails [74]. For example, in some mixtures of liquid and volatile fluid, the critical embryo size is small enough that the aggregation of volatile fluid along the surface may extend deep inside the embryo, such that the density of the embryo is more liquid-like than vapor-like. Consequently, the driving force of supersaturation is much smaller than the difference in chemical potential between the vapor bubble phase and the liquid mother phase assumed by CNT [65].

Both of these problems arise in the case of polymer foams. Due to the high pressures at which blowing agents like CO_2 are dissolved in the polymer melt before foaming, the concentration of CO_2 in the mixture is high. Furthermore, under fast depressurization, the concentration may be high enough to form a liquid-like bubble before vaporizing. Xu *et al.* predicted such a pathway to bubble nucleation in the case of poly(methyl methacrylate) (PMMA) blown with CO_2 [73]. They first corrected the interfacial tension in the CNT model to account for the first issue arising from aggregation of CO_2 along the interface, which raised the predicted nucleation barrier. When they fully accounted for the non-uniform, liquid-like concentration profile of CO_2 in the bubble using DFT, they predicted a significantly higher nucleation energy barrier than predicted by CNT, even with the corrected interfacial tension. When modeling bubble nucleation in polymer foams, CNT also introduces errors by neglecting the change in conformational entropy of polymer chains along the surface of small, high-curvature bubbles [75]. This error leads to a significant *over*estimate of the nucleation energy barrier. CNT also fails to account for variations in polymer architecture unless they change the bulk properties [76].

CNT tends to fail near the spinodal at high supersaturations, as well. While the CNT formula for the nucleation energy barrier in equation I.5 reaches a plateau

as the supersaturation reaches its maximum value (when the chemical potential of the nucleating phase reaches its minimum), the nucleation energy barrier actually drops below the thermal energy $k_B T$ and approaches zero. A more appropriate model of nucleation is given by Cahn and Hilliard [77], which accurately captures the vanishing of the nucleation energy barrier. This model tends to fail for nucleation energy barriers greater than the thermal energy $k_B T$ (see [78]), which are the most relevant to physical polymer foaming processes.

In the intermediate regime between the binodal and spinodal where CNT and Cahn–Hilliard theory fail, more sophisticated models like density functional theory or self-consistent field theory are required [78]. Although molecular dynamics simulations could provide high accuracy estimates of the bubble nucleation rate [57], the computational requirements limit them to short times, so they are more useful for high degrees of supersaturation than for determining the onset of nucleation. Instead, we adopt the approach of Xu *et al.* [73, 79] and model the non-uniform concentration profile of both polymer and dissolved gas using DFT, as first demonstrated by Talanquer and Oxtoby [65]. We then employ the "string method" as a tool to identify the pathway that requires the least addition of free energy [80, 81]. By considering the free energy along the entire path, the string method can identify multi-step nucleation pathways that require less energy than the single-step pathways to which CNT is limited. The string method is still limited in its application because it assumes a quasi-equilibrium is reached at each point along the pathway, which is only valid when nucleation is rare enough that bubble embryos may explore many pathways before nucleating. While the string method has made predictions consistent with experiments in other systems, such as membrane fusion [82], its predictions of bubble nucleation (see [73, 79]) have not been compared against experiments (see Section III.1 for a review measurements of bubble nucleation). In particular, the prediction of two-stage nucleation starting with a liquid–liquid phase separation has not been verified. The present work intends to provide the foundation for such verification. The importance of validating models of bubble nucleation against experimental measurements was underscored in the review by Di Maio and Kiran in 2018, in which they noted that "the current lack of [nucleation's] full understanding presents the main actual limitation to modeling the foaming process" [83]. This lack of understanding motivated the beginning of the present work and has remained throughout its course. In 2022, Roberts *et al.* noted that "models that include the effects of bubble growth have also been developed for PU foams but suffer from a dearth of bubble-scale data" [36]. There are many models, but few

measurements. The present work provides a few more.

I.5   Summary of Contents

This thesis is organized along the lifetime of a bubble. We begin by discussing the source of all bubbles, the mother phase, in Chapter II. Specifically, we present measurements of the thermophysical properties of the polyol–CO_2 mixtures prepared as sources of bubble nucleation for the experiments discussed in the rest of the thesis. The measurements were taken using the G-ADSA technique developed by Prof. Ernesto Di Maio at the University of Naples. We also explore the effects of polyol architecture on the solubility of CO_2, noting a non-monotonic dependence on the molecular weight. We then describe the microfluidic flow-focusing apparatus through which we flow the mother phase to drive local, reproducible, and continuous bubble nucleation for observation with high-speed microscopy in Chapter III. The image-processing algorithms for analyzing the high-speed microscopy videos are discussed in Chapter IV.

Having described the experimental setup, we present experimental measurements of bubble growth in Chapter V. Because high-speed microscopy cannot directly detect bubble nucleation, we estimate the time of nucleation by fitting a model of bubble growth to measurements and extrapolating its predicted dynamics backward to the critical nucleus size. We compare two models for bubble growth and find that both yield reasonable agreement. We then analyze the statistical distribution of predicted nucleation times through two approaches to demonstrate that the nucleation behaves like homogeneous nucleation, which we then compare to models of homogeneous bubble nucleation in Chapter VI. First, we show that a quantity related to the time between nucleation events at the same degree of supersaturation along the length of the microfulidic channel follows an exponential decay characteristic of a random Poisson process, from which we can estimate a nucleation rate. Second, we count the number of events per time at a particular degree of supersaturation and divide by the volume and time over which the nucleation events were counted, which revealed that the nucleation rate was sensitive to the supersaturation. Both methods measured similar nucleation rates, so we compared their measurements to predictions by a model based on the string method and classical nucleation theory, finding that the string method model could describe the data while the classical nucleation theory could not. Having demonstrated our proposed method for estimating the nucleation rate with supersaturation, we show that adding cyclopentane to a mixture of polyol and CO_2 dramatically enhances bubble nucleation in Chapter VII. Using

the string method model and measurements of phase behavior, we provide evidence that the cause of the enhanced bubble nucleation is the opening up of a two-stage nucleation pathway with a significantly lower nucleation energy barrier upon the addition of cyclopentane. We also discuss future work for studying the effects of other additives from a full polyurethane foaming reaction missing from our model system. Finally, we present a survey of observations of what happens after bubbles grow too large for the nucleation analysis in Chapter VIII, exploring the dynamics of bubbles when they grow so large that they elongate, ripening and coalescence of bubbles, and flow instabilities.

Throughout the thesis, we complement theory and experiment to arrive at a deeper understanding of bubble nucleation. The roadmap we followed to arrive there is shown in Figure I.13.
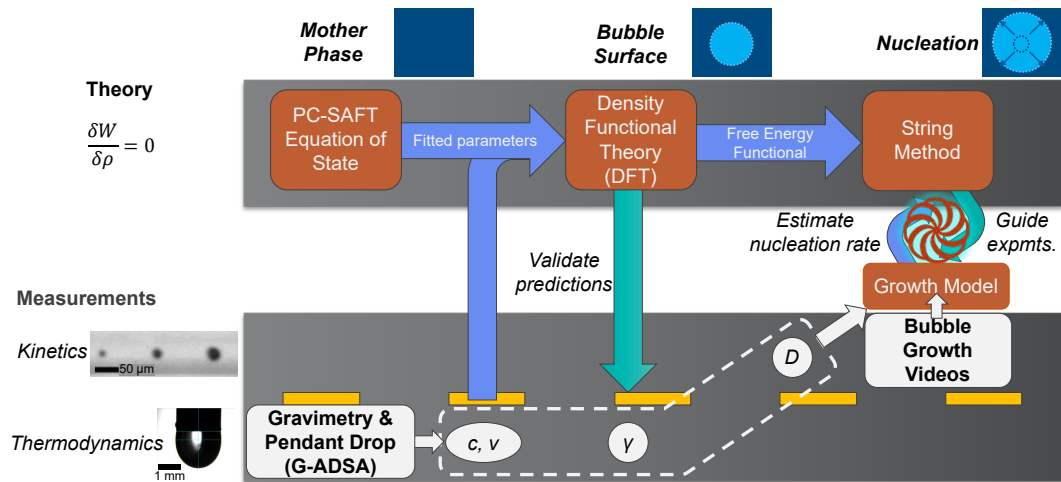
Figure I.13: Roadmap of the cooperation between experiments and theory to understand bubble nucleation. The top track shows the theoretical methods employed, which were largely developed by our collaborator Dr. Huikuan Chao. The bottom two tracks show the experimental methods employed, with kinetic measurements along the top lane and thermodynamic measurements along the bottom lane. The two tracks interact at each level of sophistication of the model: mother phase, bubble surface, and bubble nucleation. The ultimate goal is a synergy between theory and experiment to understand bubble nucleation, with theory guiding experiments toward interesting conditions and experiments testing the predictions of theory, as shown by the Armenian symbol of eternity between the string method and bubble growth model.

References

1. Jones, S., Evans, G. & Galvin, K. Bubble nucleation from gas cavities a review. *Advances in Colloid and Interface Science* **80,** 27–50. ISSN: 00018686. https://linkinghub.elsevier.com/retrieve/pii/S0001868698000748 (Feb. 1999).

2. Liger-Belair, G. The physics and chemistry behind the bubbling properties of champagne and sparkling wines: A state-of-the-art review. *Journal of Agricultural and Food Chemistry* **53,** 2788–2802. ISSN: 00218561 (2005).

3. Harvey, E. N. *et al.* Bubble formation in animals. I. Physical factors. *Journal of Cellular and Comparative Physiology* **24,** 1–22. ISSN: 0095-9898. https://onlinelibrary.wiley.com/doi/10.1002/jcp.1030240102 (Aug. 1944).

4. Guo, Z. *et al.* CO2 bubble nucleation in polystyrene: Experimental and modeling studies. *Journal of Applied Polymer Science* **125,** 2170–2186. ISSN: 00218995. https://onlinelibrary.wiley.com/doi/10.1002/app.36422 (Aug. 2012).

5. Blander, M. & Katz, J. L. Bubble nucleation in liquids. *AIChE Journal* **21,** 833–848. ISSN: 15475905 (1975).

6. Kraynik, A. M. Foam Flows. *Annual Review of Fluid Mechanics* **20,** 325–357. ISSN: 0066-4189. https://www.annualreviews.org/doi/10.1146/annurev.fl.20.010188.001545 (Jan. 1988).

7. *The Polyurethanes Book* (eds Randall, D. & Lee, S.) ISBN: 0470850418 (Huntsman International LLC, Polyurethanes business, 2002).

8. Zenit, R. & Rodríguez-Rodríguez, J. The fluid mechanics of bubbly drinks. *Physics Today* **71,** 44–50. ISSN: 0031-9228. http://physicstoday.scitation.org/doi/10.1063/PT.3.4069 (Nov. 2018).

9. Collivignarelli, M. C. *et al.* Foams in Wastewater Treatment Plants: From Causes to Control Methods. *Applied Sciences* **10,** 2716. ISSN: 2076-3417. https://www.mdpi.com/2076-3417/10/8/2716 (Apr. 2020).

10. Claudy, P., Létoffé, J. M., Camberlain, Y. & Pascault, J. P. Glass Transition of Polystyrene Versus Molecular Weight. *Polymer Bulletin* **9,** 208–215 (1983).

11. Shafi, M. A., Joshi, K. & Flumerfelt, R. W. Bubble size distributions in freely expanded polymer foams. *Chemical Engineering Science* **52,** 635–644. ISSN: 00092509 (1997).

12. Schiavoni, S., D'Alessandro, F., Bianchi, F. & Asdrubali, F. Insulation materials for the building sector: A review and comparative analysis. *Renewable and Sustainable Energy Reviews* **62,** 988–1011. ISSN: 13640321. https://linkinghub.elsevier.com/retrieve/pii/S1364032116301551 (Sept. 2016).

13. Stirna, U., Beverte, I., Yakushin, V. & Cabulis, U. *Polyurethane and poly-isocyanurate foams in external tank cryogenic insulation* 203–244. ISBN: 9783642353352 (2013).

14. Ivashov, S., Razevig, V., Vasiliev, I., Bechtel, T. & Capineri, L. Holographic subsurface radar for diagnostics of cryogenic fuel tank thermal insulation of space vehicles. *NDT and E International* **69,** 48–54. ISSN: 09638695. http://dx.doi.org/10.1016/j.ndteint.2014.10.002 (2015).

15. Burgaz, E. *Polyurethane Insulation Foams for Energy and Sustainability* 1–26. ISBN: 9783030195588 (Springer, Cham, 2019).

16. Szycher, M. *Szycher's handbook of Polyurethanes* 2nd ed., 1–1192. ISBN: 9781439863138 (CRC Press, Boca Raton, FL, 2012).

17. Glicksman, L. R. in *Low Density Cellular Plastics: Physical Basis of Behavior* 104–151 (1994).

18. Booth, L. Radiation Contribution as an Element of Thermal Conductivity. *Journal of Thermal Insulation* **12,** 153–166. ISSN: 0148-8287. http://journals.sagepub.com/doi/10.1177/109719638801200207 (Oct. 1988).

19. Schuetz, M. & Glicksman, L. A Basic Study of Heat Transfer Through Foam Insulation. *Journal of Cellular Plastics* **20,** 114–121. ISSN: 0021-955X. http://journals.sagepub.com/doi/10.1177/0021955X8402000203 (Mar. 1984).

20. Simpson, A., Rattigan, I., Kalavsky, E. & Parr, G. Thermal conductivity and conditioning of grey expanded polystyrene foams. *Cellular Polymers* **39,** 238–262. ISSN: 0262-4893. http://journals.sagepub.com/doi/10.1177/0262489320934263 (Nov. 2020).

21. Notario, B. *et al.* Experimental validation of the Knudsen effect in nanocellular polymeric foams. *Polymer* **56,** 57–67. ISSN: 00323861. https://linkinghub.elsevier.com/retrieve/pii/S0032386114009021 (Jan. 2015).

22. Notario, B., Pinto, J. & Rodríguez-Pérez, M. A. Towards a new generation of polymeric foams: PMMA nanocellular foams with enhanced physical properties. *Polymer* **63,** 116–126. ISSN: 00323861 (2015).

23. Cao, X., James Lee, L., Widya, T. & Macosko, C. Polyurethane/clay nanocomposites foams: processing, structure and properties. *Polymer* **46,** 775–783. ISSN: 0032-3861. https://www.sciencedirect.com/science/article/pii/S0032386104011322 (Jan. 2005).

24. Moreno, J. D. *Radiative transfer and thermal performance levels in foam insulation boardstocks* PhD thesis (Massachusetts Institute of Technology, 1991). https://dspace.mit.edu/handle/1721.1/28004.

25. Tesser, R., Di Serio, M., Sclafani, A. & Santacesaria, E. Modeling of polyurethane foam formation. *Journal of Applied Polymer Science* **92,** 1875–1886. ISSN: 0021-8995. https://onlinelibrary.wiley.com/doi/pdf/10.1002/app.20170%20https://onlinelibrary.wiley.com/doi/10.1002/app.20170 (May 2004).

26. Golini, P. & Guandalini, M. *Polyurethane Rigid Foams* 2013. https://patents.google.com/patent/WO2013030101A1/en.

27. Guo, H. & Kumar, V. Solid-state poly(methyl methacrylate) (PMMA) nanofoams. Part I: Low-temperature CO2 sorption, diffusion, and the depression in PMMA glass transition. *Polymer* **57,** 157–163. ISSN: 00323861. http://dx.doi.org/10.1016/j.polymer.2014.12.029 (2015).

28. Guo, H., Nicolae, A. & Kumar, V. Solid-state poly(methyl methacrylate) (PMMA) nanofoams. Part II: Low-temperature solid-state process space using CO2 and the resulting morphologies. *Polymer* **70,** 231–241. ISSN: 00323861. http://dx.doi.org/10.1016/j.polymer.2015.06.031 (2015).

29. Tammaro, D., Astarita, A., Di Maio, E. & Iannace, S. Polystyrene Foaming at High Pressure Drop Rates. *Industrial and Engineering Chemistry Research* **55,** 5696–5701. ISSN: 15205045 (2016).

30. Yang, Z., Hu, D., Liu, T., Xu, Z. & Zhao, L. Strategy for preparation of microcellular rigid polyurethane foams with uniform fine cells and high expansion ratio using supercritical CO2 as blowing agent. *The Journal of Supercritical Fluids* **153,** 104601. ISSN: 1359-0286. http://dx.doi.org/10.1016/j.cossms.2010.07.001 (2019).

31. Brondi, C. *et al.* Thermosetting polyurethane foams by physical blowing agents: Chasing the synthesis reaction with the pressure. *The Journal of Supercritical Fluids* **154,** 104630. ISSN: 08968446. https://linkinghub.elsevier.com/retrieve/pii/S0896844619302323 (Dec. 2019).

32. Minogue, E. *An in-situ study of the nucleation process of polyurethane rigid foam formation* PhD thesis (Dublin City University, 2000), 1–194. http://doras.dcu.ie/19076/.

33. Reignier, J., Alcouffe, P., Méchin, F. & Fenouillot, F. The morphology of rigid polyurethane foam matrix and its evolution with time during foaming – New insight by cryogenic scanning electron microscopy. *Journal of Colloid and Interface Science* **552,** 153–165. ISSN: 00219797. https://linkinghub.elsevier.com/retrieve/pii/S0021979719305764 (Sept. 2019).

34. ASTM. *Standard Practice for Polyurethane Raw Materials: Polyurethane Foam Cup Test* 2021. https://www-astm-org.caltech.idm.oclc.org/d7487-18.html.

35. Pérez-Tamarit, S., Solórzano, E., Mokso, R. & Rodríguez-Pérez, M. In-situ understanding of pore nucleation and growth in polyurethane foams by using real-time synchrotron X-ray tomography. *Polymer* **166,** 50–54. ISSN: 0032-3861. https://www.sciencedirect.com/science/article/pii/S0032386119300618 (Mar. 2019).

36. Roberts, C. *et al.* Bubblescale observations of polyurethane foam expansion. *AIChE Journal* **68,** e17595. ISSN: 0001-1541. https://onlinelibrary.wiley.com/doi/10.1002/aic.17595 (May 2022).

37. Wong, A., Mark, L. H., Hasan, M. M. & Park, C. B. The synergy of supercritical CO2 and supercritical N2 in foaming of polystyrene for cell nucleation. *Journal of Supercritical Fluids* **90,** 35–43. ISSN: 08968446. http://dx.doi.org/10.1016/j.supflu.2014.03.001 (2014).

38. Leung, S. N. S. *Mechanisms of Cell Nucleation, Growth, and Coarsening in Plastic Foaming: Theory, Simulation, and Experiment* PhD thesis (University of Toronto, 2009), 1–214.

39. Brondi, C., Di Maio, E., Bertucelli, L., Parenti, V. & Mosciatti, T. Competing bubble formation mechanisms in rigid polyurethane foaming. *Polymer* **228,** 123877. ISSN: 00323861. https://doi.org/10.1016/j.polymer.2021.123877%20https://linkinghub.elsevier.com/retrieve/pii/S0032386121005000 (July 2021).

40. Ionescu, M. *Chemistry and Technology of Polyols for Polyurethanes , 2nd Edition Chemistry and Technology of Polyols for Polyurethanes* 2nd ed., 1–548. ISBN: 9781910242988 (iSmithers Rapra Publishing, 2005).

41. Purohit, P., Borgford-Parnell, N., Klimont, Z. & Höglund-Isaksson, L. Achieving Paris climate goals calls for increasing ambition of the Kigali Amendment. *Nature Climate Change.* ISSN: 1758-678X (2022).

42. Akdogan, E., Erdem, M., Ureyen, M. E. & Kaya, M. Rigid polyurethane foams with halogen-free flame retardants: Thermal insulation, mechanical, and flame retardant properties. *Journal of Applied Polymer Science* **137,** 1–14 (2019).

43. Kazarian, S. G. Polymer Processing with Supercritical Fluids. *Polymer Science, Ser. C* **42,** 78–101 (2000).

44. Primel, A. *et al.* Solubility and interfacial tension of thermoplastic polyurethane melt in supercritical carbon dioxide and nitrogen. *Journal of Supercritical Fluids* **122,** 52–57. ISSN: 08968446. http://dx.doi.org/10.1016/j.supflu.2016.11.016 (2017).

45. Tomasko, D. L. *et al.* Development of CO2 for polymer foam applications. *The Journal of Supercritical Fluids* **47,** 493–499. ISSN: 0896-8446. https://www.sciencedirect.com/science/article/pii/S0896844608003586 (Jan. 2009).

46. Arora, K. A., Lesser, A. J. & Mccarthy, T. J. Preparation and Characterization of Microcellular Polystyrene Foams Processed in Supercritical Carbon Dioxide. *Macromolecules* **31,** 4614–4620. https://pubs.acs.org/sharingguidelines (1998).

47. NIST. *NIST Standard Reference Database Number 69* 2022. https://webbook.nist.gov/chemistry/ (2022).

48. Sauceau, M., Fages, J., Common, A., Nikitine, C. & Rodier, E. New challenges in polymer foaming: A review of extrusion processes assisted by supercritical carbon dioxide. *Progress in Polymer Science* **36,** 749–766. ISSN: 00796700. http://dx.doi.org/10.1016/j.progpolymsci.2010.12.004%20https://linkinghub.elsevier.com/retrieve/pii/S0079670010001280%20https://pubs.acs.org/doi/10.1021/la0266381 (June 2011).

49. Jacobs, L. J., Kemmere, M. F. & Keurentjes, J. T. Sustainable polymer foaming using high pressure carbon dioxide: A review on fundamentals, processes and applications. *Green Chemistry* **10,** 731–73. ISSN: 14639270 (2008).

50. Forest, C., Chaumont, P., Cassagnau, P., Swoboda, B. & Sonntag, P. Polymer nano-foams for insulating applications prepared from CO2 foaming. *Progress in Polymer Science* **41,** 122–145. ISSN: 00796700. https://www.sciencedirect.com/science/article/pii/S0079670014000689%20https://linkinghub.elsevier.com/retrieve/pii/S0079670014000689 (Feb. 2015).

51. Miller, D., Chatchaisucha, P. & Kumar, V. Microcellular and nanocellular solid-state polyetherimide (PEI) foams using sub-critical carbon dioxide I. Processing and structure. *Polymer* **50,** 5576–5584. ISSN: 00323861. http://dx.doi.org/10.1016/j.polymer.2009.09.020 (2009).

52. Costeux, S. CO2-blown nanocellular foams. *Journal of Applied Polymer Science* **131,** 41293. http://doi.wiley.com/10.1002/app.41293 (Dec. 2014).

53. Costeux, S. & Zhu, L. Low density thermoplastic nanofoams nucleated by nanoparticles. *Polymer* **54,** 2785–2795. ISSN: 0032-3861. https://www.sciencedirect.com/science/article/pii/S0032386113002711 (May 2013).

54. Zhao, J., Wang, G., Zhang, A., Zhao, G. & Park, C. B. Nanocellular TPU composite foams achieved by stretch-assisted microcellular foaming with low-pressure gaseous CO2 as blowing agent. *Journal of CO2 Utilization* **53,** 101708 (Nov. 2021).

55. Yokoyama, H. & Sugiyama, K. Nanocellular structures in block copolymers with CO2-philic blocks using CO2 as a blowing agent: Crossover from micro-to nanocellular structures with depressurization temperature. *Macromolecules*

38, 10516–10522. ISSN: 00249297. https://pubs.acs.org/doi/10.1021/ma051757j (Dec. 2005).

56. Debenedetti, P. G. *Metastable Liquids* 147–176. ISBN: 0-691-08595-1 (Princeton University Press, Princeton, NJ, 1996).

57. Diemand, J., Angélil, R., Tanaka, K. K. & Tanaka, H. Large scale molecular dynamics simulations of homogeneous nucleation. *The Journal of Chemical Physics* **139,** 074309. ISSN: 0021-9606. arXiv: 1308.0972. http://aip.scitation.org/doi/10.1063/1.4818639 (Aug. 2013).

58. Volmer, M. & Weber, Keimbildung in übersättigten Gebilden. *Zeitschrift für Physikalische Chemie* **119U,** 277–301. ISSN: 2196-7156. https://www.degruyter.com/document/doi/10.1515/zpch-1926-11927/html (Jan. 1926).

59. Gibbs, J. W. *The Scientific Papers of JW Gibbs* (Dover, 1961).

60. Farkas, L. Nucleation Rates in Supersaturated Vapours. *Z. Phys. Chem.* **125,** 236 (1927).

61. Kaischew, R. & Stranski, I. N. Zur kinetischen Ableitung der Keimbildungsgeschwindigkeit. *Zeitschrift für Physikalische Chemie* **26B,** 317–326. ISSN: 2196-7156. https://www.degruyter.com/document/doi/10.1515/zpch-1934-2628/html (June 1934).

62. Becker, R. & Döring, W. Kinetische Behandlung der Keimbildung in übersättigten Dämpfen. *Annalen der Physik* **416,** 719–752. ISSN: 00033804. https://onlinelibrary.wiley.com/doi/10.1002/andp.19354160806 (1935).

63. Zeldovich, J. Theory of Nucleation and Condensation. *Sov. Phys. JETP* **12,** 525 (1942).

64. Kagan, Y. The Kinetics of Boiling of a Pure Liquid. *Russ. J. Phys. Chem.* **34** (1960).

65. Talanquer, V. & Oxtoby, D. W. Nucleation of bubbles in binary fluids. *The Journal of Chemical Physics* **102,** 2156–2164. ISSN: 0021-9606. http://aip.scitation.org/toc/jcp/102/5%20http://aip.scitation.org/doi/10.1063/1.468737 (Feb. 1995).

66. Kalikmanov, V. I. in *Lecture Notes in Physics* 1–331 (2013). ISBN: 9789048136421.

67. Oxtoby, D. W. Homogeneous nucleation: theory and experiment. *Journal of Physics: Condensed Matter* **4,** 7627–7650. ISSN: 0953-8984. https://iopscience.iop.org/article/10.1088/0953-8984/4/38/001 (Sept. 1992).

68. Skripov, V. P. *Metastable Liquids* 1–264. ISBN: 0-470-79546-8 (Halsted Press, New York, NY, 1974).

69. Ando, K., Liu, A. Q. & Ohl, C. D. Homogeneous nucleation in water in microfluidic channels. *Physical Review Letters* **109,** 044501. ISSN: 00319007 (2012).

70. Goel, S. K. & Beckman, E. J. Generation of microcellular polymeric foams using supercritical. *Polymer Engineering and Science* **34,** 1137–1147 (1994).

71. Wang, R. & Wang, Z. G. Theory of polymers in poor solvent: Phase equilibrium and nucleation behavior. *Macromolecules* **45,** 6266–6271. ISSN: 00249297 (2012).

72. Flagan, R. C. A thermodynamically consistent kinetic framework for binary nucleation. *Journal of Chemical Physics* **127,** 1–7. ISSN: 00219606 (2007).

73. Xu, X., Cristancho, D. E., Costeux, S. & Wang, Z.-G. Bubble nucleation in polymer–CO2 mixtures. *Soft Matter* **9,** 9675. ISSN: 1744-683X. www.rsc.org/softmatter%20http://xlink.rsc.org/?DOI=c3sm51477c (2013).

74. Sleutel, M., Lutsko, J., Van Driessche, A. E., Durán-Olivencia, M. A. & Maes, D. Observing classical nucleation theory at work by monitoring phase transitions with molecular precision. *Nature Communications* **5.** ISSN: 20411723 (2014).

75. Kim, Y., Park, C. B., Chen, P. & Thompson, R. B. Origins of the failure of classical nucleation theory for nanocellular polymer foams. *Soft Matter* **7,** 7351–7358. ISSN: 1744683X (Aug. 2011).

76. Costeux, S., Khan, I., Bunker, S. P. & Jeon, H. K. Experimental study and modeling of nanofoams formation from single phase acrylic copolymers. *Journal of Cellular Plastics* **51,** 197–221 (2015).

77. Cahn, J. W. & Hilliard, J. E. Free Energy of a Nonuniform System. III. Nucleation in a TwoComponent Incompressible Fluid. *The Journal of Chemical Physics* **31,** 688–699. ISSN: 0021-9606. http://aip.scitation.org/doi/10.1063/1.1730447 (Sept. 1959).

78. Müller, M., MacDowell, L. G., Virnau, P. & Binder, K. Interface properties and bubble nucleation in compressible mixtures containing polymers. *The Journal of Chemical Physics* **117,** 5480–5496. ISSN: 0021-9606. http://aip.scitation.org/doi/10.1063/1.1497636 (Sept. 2002).

79. Xu, X., Cristancho, D. E., Costeux, S. & Wang, Z.-G. Discontinuous Bubble Nucleation Due to a Metastable Condensation Transition in Polymer–CO2 Mixtures. *The Journal of Physical Chemistry Letters* **4,** 1639–1643. http://pubs.acs.org/doi/10.1021/jz4005575 (May 2013).

80. E, W., Ren, W. & Vanden-Eijnden, E. String method for the study of rare events. *Physical Review B* **66,** 052301. ISSN: 0163-1829. https://link.aps.org/doi/10.1103/PhysRevB.66.052301 (Aug. 2002).

81. E, W., Ren, W. & Vanden-Eijnden, E. Simplified and improved string method for computing the minimum energy paths in barrier-crossing events. *The Journal of Chemical Physics* **126,** 164103. ISSN: 0021-9606. http://jcp.aip.org/jcp/copyright.jsp%20http://aip.scitation.org/doi/10.1063/1.2720838 (Apr. 2007).

82. Zhang, C. Z. & Wang, Z. G. Nucleation of membrane adhesions. *Physical Review E* **77,** 021906. ISSN: 15393755 (2008).

83. Di Maio, E. & Kiran, E. Foaming of polymers with supercritical fluids and perspectives on the current knowledge gaps and challenges. *The Journal of Supercritical Fluids* **134,** 157–166. ISSN: 08968446. https://www.sciencedirect.com/science/article/pii/S0896844617307593 (Apr. 2018).

Chapter II

Know Mother Best: Measurement and Modeling of the Properties of the Mother Phase Relevant to Bubble Nucleation

> If we want to understand the birth and growth of the baby, we ought to get to know its mother.

———————————

Prof. Julie Kornfield

A.Y. and Prof. Ernesto Di Maio measured polyol–CO_2 properties with G-ADSA in the Di Maio lab at the University of Naples Federico II with initial help from Dr. Maria Rosaria Di Caprio. Dr. Jacob Crosthwaite measured the solubility of VORANOL 360 at Dow, Inc., Midland, MI. Dr. Huikuan Chao developed the theoretical models, which A.Y. fit to the data.

Try as a bubble might to be independent, it will always depend on its mother phase, the medium from which it nucleates. A bubble cannot exist unless its mother phase has a sufficient excess of dissolved gas to give it birth. A bubble cannot survive unless it overcomes the tension along the interface dividing it from its mother phase. A bubble cannot grow unless it receives gas by diffusion from its mother phase.

Any prediction of a bubble's life in a polymer foam requires knowledge of the gas solubility, interfacial tension, and gas diffusivity in the polymer component of its mother phase. In this CHAPTER, we describe a method to measure these key physical properties for our polyurethane model system, carbon dioxide in a polyether polyol. We close by fitting a thermodynamic model of the polyol–CO_2 mother phase to the measured properties.

Because these properties are interdependent, they must be measured simultaneously. The simultaneous measurement of these properties for binary gas–polymer mixtures is possible with gravimetry–axisymmetric drop shape analysis (G-ADSA)[1], a technique pioneered by Prof. Ernesto Di Maio, who permitted the use of his custom instrument at the University of Naples Federico II for the present work. We describe the method and analysis in Section II.1.

Because a high supersaturation of CO_2 is necessary to observe homogeneous bubble nucleation in our microfluidic channel, we pay specific attention to the types of polymer architectures that maximize the CO_2 solubility in Section II.3. The solubility of CO_2 in polyol has additional applications in the foaming industry. While CO_2 in polyurethane foams is typically produced *in situ* by chemical blowing, the equilibrium CO_2 solubility can still affect foaming [2]. Additionally, a high equilibrium CO_2 solubility is required in alternative polyurethane foaming processes that utilize pre-dissolved CO_2 in the polyol and isocyanate to achieve desired structures and minimize polyurea formation inherent in foams wherein CO_2 is formed through water-blowing, which can compromise strength, stiffness and processability [3–5]. Previous studies have suggested that maximal solubility of polyol in CO_2 balances the entropic penalty of a longer molecular weight with the enthalpic gain of a higher ratio of ether to hydroxyl end groups [4], but this trend has not been demonstrated for CO_2 solubility in polyether polyols, the focus of the present work. This trend is important to guide the selection of the structure of polyols used in polyurethane foaming to achieve desired structural characteristics and, ultimately, desired thermal and mechanical properties in CO_2-based polyurethane foams.

Currently, the effect of the molecular structure of the polyol on CO_2 solubility remains unclear due to conflicting trends reported as a function of molecular weight and hydroxyl functionality. We reconcile these conflicting reports of CO_2 solubility in polyether polyols through experiments that isolate the effects of molecular weight and hydroxyl functionality. We show that CO_2 solubility decreases with molecular weight above 1000 g/mol due to reduced mixing entropy and decreases with hydroxyl functionality due to increased concentration of CO_2-phobic, self-preferential hydrogen bonds. The competition between these trends explains the increase in CO_2 solubility with molecular weight for short polyols (less than 1000 g/mol), validated by the available literature. Due to the importance of hydrogen bonds in governing CO_2 solubility, below 1000 g/mol, an accurate PC-SAFT model will likely need to account for the associative hydrogen-bonding interactions among the hydroxyl groups. These results led us to select polyether polyols with 2–3 hydroxyl groups per polymer and an intermediate molecular weight (1000 g/mol) for maximal CO_2 solubility.

We further use the measurements from G-ADSA to fit parameters of a thermodynamic model of these mixtures based on the perturbed chain–statistical associating fluid theory (PC-SAFT) described in Section II.4. This model serves

two purposes: first, it allows us to estimate the properties of polyol–CO_2 mixtures that we produce in the lab and, second, it serves as the foundation of additional models of the interface, bubble growth, and bubble nucleation. We briefly describe the use of a classical density functional theory (DFT) based on the PC-SAFT model for modeling the interface between the polyol-rich and CO_2-rich phases in Section II.4. We explore the role of these models in the prediction of bubble growth in Chapter V and of nucleation in Chapter VI.

II.1 Gravimetry–Axisymmetric Drop Shape Analysis (G-ADSA) Measures Physical Properties of Polyol–CO_2 Mixtures

Gravimetry–Axisymmetric Drop Shape Analysis (G-ADSA) [1] is a technique for simultaneous measurement of the properties of liquid–gas mixtures that combines weight measurements using a magnetic suspension balance (gravimetry) with pendant drop analysis (axisymmetric drop shape analysis). Its measurements can be used to estimate gas solubility, specific volume, gas diffusivity, and interfacial tension. In the present work, we employed this technique to measure these properties for mixtures of CO_2 and polyether polyols of various molecular weights and functionalities (see Table II.1) in the range of 0–8 MPa at 30 °C and 60 °C. Here, we briefly describe the apparatus and technique. For a more thorough discussion, we refer the reader to the original publication of this method by Pastore Carbone *et al.* [1].

Name	M_n (g/mol)	f	ρ (g/mL)	η (mPa.s)	Supplier
1k2f	1000	2	1.02	160	Dow, Inc.
1k3f	1000	3	1.02	290	Dow, Inc.
1k5f	728	4.7	1.084	4820	Dow, Inc.
3k2f	2700	2	1.004	740	MilliporeSigma

Table II.1: Table of properties of the polyols used in this study (M_n = number-averaged molecular weight, f = functionality or number of hydroxyl groups per chain, ρ = density, η = viscosity). Values reported are averages. Molecular weights, functionalities, and densities supplied by manufacturers. Viscosities measured using ARES shear rheometer. Density and viscosity measurements measured at 25 °C. Polydispersities are not known.

Apparatus

Briefly, a magnetic suspension balance (MSB, Rubotherm Prazisionsmesstechnik GmbH, Germany) holds a Pyrex crucible with an inner diameter of 1.82 cm that contains the polyol sample. The crucible is suspended from the MSB by hooks with

a volume of 2.26735 mL, as measured in a helium atmosphere by Dr. Maria Rosaria Di Caprio of the Di Maio lab [1]. A Teflon rod with a diameter of 2.05 mm is fitted snugly into a slot in the apparatus to hold the pendant drop. The MSB is encased in a steel high-pressure cell, which is sealed around the MSB with a rubber O-ring. Two sapphire windows of a few centimeters in diameter machined in the cell provide a clear view of the pendant drop to a video camera with a convex objective lens.

Method

Before each measurement, an analytical balance was tared with the crucible. 1 mL of the desired polyol was then slowly poured into the crucible, taking care not to entrain any bubbles, and the weight of the sample under normal temperature and pressure was measured with the MSB. Next, to prepare the pendant drop, a drop of polyol was first deposited onto the corner of a clean glass slide. The corner of the slide was then tilted over the upward-facing tip of the Teflon rod until a small drop (3–5 μL) dripped off and formed a hemisphere atop the tip of the rod. The rod was then inverted carefully to prevent loss of the drop and inserted into a slot in the MSB. The high-pressure steel encasement was then sealed around the MSB gently enough that the pendant drop would not fall. The high-pressure cell was enveloped in a second stainless steel jacket, which contained oil that was heated with a heating circulator (Julabo F25) to control the temperature of the sample. Once sealed, the pressure of CO_2 inside the high-pressure cell was controlled using a Belsorp system. During the first stage of each experiment, moisture was removed from the polyol sample and the pendant drop by pulling a vacuum until the sample weight stopped decreasing. If the sample weight did not stop decreasing within 15–20 minutes, we assumed that the additional mass loss resulted from the loss of the polyol, which could contain some polymer chains small enough to be slightly volatile. At this point, the weight of the pure polyol sample and the volume of the pure polyol pendant drop were measured.

The measurement of the pure polyol sample was followed by several measurements after pressurization with CO_2. Pressurization was performed using the Belsorp system to slowly inject CO_2 into the chamber. Above 5500 kPa, the Belsorp could not supply sufficient CO_2 pressure to pressurize the chamber further, so we used an ISCO pump to pressurize the CO_2 first before injecting it manually. Throughout each measurement, the MSB recorded the changing mass of the crucible as CO_2 was absorbed into the polyol. The pressure was kept constant (within 20 kPa) until the mass did not change by more than 30 μg in five minutes. At this point,

we considered the system to be sufficiently close to equilibrium for the error to be negligible. Upon reaching equilibrium, the MSB lowered the crucible until it rested on an overhanging platform, allowing the MSB to take three measurements of the tare weight. At the same time, a video camera captured images of the pendant drop as it swelled from absorption of CO_2, which were taken every few minutes. The Teflon rod swelled as well, as shown in Figure II.S1 of the Supporting Information (SI). These measurements were repeated at ever higher pressures until reaching the maximum pressure for the experiment between 5–8 MPa. At this point, we depressurized the system in steps by releasing CO_2 through an automated ball valve from the high-pressure cell, taking measurements at each step. The release of CO_2 was performed slowly enough that no nucleation of bubbles was observed in the pendant drop. Overall, we took measurements at 10–20 pressure values over the course of 1 week for each set of conditions.

Compute Gas Solubility, Specific Volume, Gas Diffusivity, and Interfacial Tension from G-ADSA Measurements

The G-ADSA technique only directly measures an image of the drop shape, the total apparent weight of the crucible, attaching hooks, and sample, and the apparent weight of the tare. The specific volume of the polyol–CO_2 mixture, solubility of CO_2 in the polyol, diffusivity of CO_2 in the polyol, and interfacial tension between the polyol-rich and CO_2-rich phases must therefore be calculated from these raw data. These calculations were performed with custom methods using open-souce Python packages, including jupyter[6], matplotlib [7], numpy [8], pandas [9], and scipy [10]. The corresponding notebooks and libraries can be found in the GitHub repository `andylitalo/g-adsa` [11].

The general scheme of these calculations is summarized here. For further detail, we refer the reader to the Supporting Information (SI).

We first estimated the equilibrium volume of the pendant drop from the shape of the pendant drop using the commercial software FTA32 (First Ten Angstroms). We then estimate the sample volume by assuming that its volume changes proportionally to the equilibrium volume of the drop. Next, we estimated the equilibrium sample mass using the MSB. The balance only directly measures the apparent weight and the tare weight. The difference between these measurements gives the sum of the masses of the sample, the crucible, and the supporting hooks minus the effect of the buoyant force, which must be accounted for due to the precision of these

measurements. To compute the buoyant force, we multiply the density of CO_2 at the given pressure and temperature (available on the NIST Chemistry WebBook [12]) by the total volume of weighed objects, which includes the volumes of the crucible, the supporting hooks, and the sample. The volume of the crucible and hooks was previously measured by Dr. Maria Rosaria Di Caprio in a helium atmosphere [1]. After correcting for buoyancy effects, the difference between the balance readings for the apparent weight and tare weight at zero pressure gives the mass of dissolved gas. We then estimated the dry mass of the polyol by pulling a vacuum to remove dissolved vapor and moisture. The CO_2 solubility is then the mass of dissolved gas divided by the total sample mass, equal to the sum of the mass of dissolved gas and the dry mass of the polyol. The specific volume of the sample can then be calculated by dividing the sample volume by the total sample mass.

To estimate the diffusivity, we followed the model derived by Crank for diffusion into a slab [13] and described in Section II.S1. The model considers an infinite slab of fluid with a concentration-dependent diffusivity and a gas atmosphere on both sides. In our case, the polyol sample is only open to the CO_2 atmosphere on one side. The situation is nevertheless analogous if we map the midpoint of the slab to the base of the crucible because there is no flux through either surface.

With this model, we can estimate the diffusivity of CO_2 as a function of the saturation pressure in the sample in two ways: (1) fit a square root function to the mass of dissolved gas over time at early times, and (2) fit an exponential function to the mass of dissolved gas over time upon approaching equilibrium. While we used both to estimate the diffusivity, we generally used the first method (square root) due to better fitting of the data and lower sensitivity to noise. In practice, because the concentration changes during the measurement of gas diffusivity, we can only measure an upper and lower bound at a given concentration. Our measurement of diffusivity after pressurizing provides the upper bound because the CO_2 concentration begins lower than the equilibrium value, and our measurement after depressurizing provides the lower bound because the CO_2 concentration begins higher than the equilibrium value.

Finally, we estimate the interfacial tension at a given pressure using axisymmetric drop shape analysis (ADSA) performed with the commercial software First Ten Angstroms 32 (FTA32). This software automatically detects the edge of the drop and fits the contour predicted for a pendant drop predicted to its shape. When provided the density of the drop (reciprocal of the specific volume) and the density of

the CO_2-rich atmosphere (estimated using the pvT data for pure CO_2 available from NIST [12]), the software computes the interfacial tension. To learn more about the pendant drop method and its estimation of interfacial tension, see the work of Song and Springer [14]. Because ADSA was performed using a camera separate from the Rubotherm MSB used for gravimetry, the two sets of measurements were synchronized to a common start time, thereby providing simultaneous measurements of each parameter. See Section II.S1 of the SI for further experimental details, analysis, and discussion of sources of error.

II.2   G-ADSA Measurements: Effects of Pressure and Temperature

Here, I will describe the effects of pressure and temperature on CO_2 solubility, specific volume of a polyol–CO_2 mixture, the interfacial tension between the polyol-rich and CO_2-rich phases, and the diffusivity of CO_2.

One key aspect governing the properties of polyol-CO_2 mixtures is whether the CO_2 is subcritical to supercritical. To explore this aspect, we show the solubility of CO_2 in polyol (difunctional, 1000 g/mol, supplied by Dow, Inc.) as a function of pressure for subcritical and supercritical temperatures in Figure II.1. In this figure, we combine data measured with G-ADSA in the Di Maio lab and data measured with a magnetic suspension balance (MSB) by Dr. Jacob Crosthwaite at Dow, Inc. (Midland, MI). The agreement between adsorption (○) and desorption (×) measurements with G-ADSA and the agreement between G-ADSA in the Di Maio lab and MSB at Dow, Inc. at 60 °C testifies to the consistency of these measurement techniques. Therefore, although time limited the repetition of these week-long experiments, we believe their results are reproducible.

From the data, we see that the CO_2 solubility grows roughly linearly with pressure at low pressures (below 2000 kPa), as expected from Henry's law. As the pressure increases, the effect of temperature becomes more pronounced. If the temperature is subcritical (< 31 °C), the CO_2 solubility increases superlinearly, as observed for the data measured at 25 °C and at 30.5 °C. At high enough pressure, the CO_2 atmosphere eventually condenses into a liquid phase (> 6430 kPa at 25 °C [12]). This liquid atmosphere may dissolve a non-negligible amount of polyol and violate our assumption of a fixed polyol mass (see Section II.1), so measurements were not taken above 6000 kPa. At the supercritical temperature of 60 °C, however, the CO_2 solubility increases roughly linearly well above the critical pressure (7.38 MPa [12]), which is qualitatively consistent with solubility measurements for CO_2
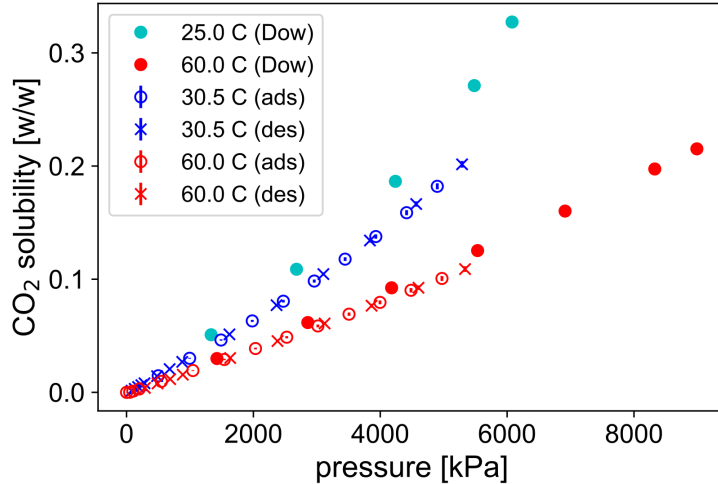
Figure II.1: CO_2 solubility in difunctional (two hydroxyls per chain), 1000 g/mol polyol as a function of pressure for different temperatures (indicated by color). Data are combined from G-ADSA measurements made with Prof. Ernesto Di Maio at the University of Naples Federico II (adsorption ∘ and desorption ×) and measurements made with an MSB at Dow, Inc. (Midland, MI) by Dr. Jacob Crosthwaite (●). Error bars are shown, but are sometimes smaller than the marker.

in polyols in the literature [2, 5, 15]. We expect the slope to decrease at a high enough pressure as observed above 10 MPa for CO_2 in PMMA [16].

We will return to CO_2 solubility to discuss the effects of polymer architecture in Section II.3, but now we turn to the effects of pressure and temperature on the other thermophysical properties measured by G-ADSA (specific volume, interfacial tension, and CO_2 diffusivity). Because the Julabo temperature controller available in the Di Maio lab for G-ADSA could only heat and not chill its silicone oil bath, its minimum temperature was limited to 30.5 °C by the ambient temperature (> 25 °C in the Naples summer) and the viscous heating caused by flow, so we could not directly repeat the measurements performed at Dow at 25 °C. Additionally, this temperature is within experimental uncertainty (0.5 °C) of the critical temperature for CO_2, 31 °C, so we cannot guarantee that the CO_2 at the lower temperature did not become supercritical during these measurements. To increase reproducibility, we will present data for a commercially available poly(propylene glycol) (average $M_n \approx 2700$ g/mol, MilliporeSigma, CAS 25322-69-4). In each dataset, data from two measurements performed at 60 °C are shown. They are indistinguishable from each other beyond statistical uncertainty, further demonstrating the reproducibility of the G-ADSA measurements.
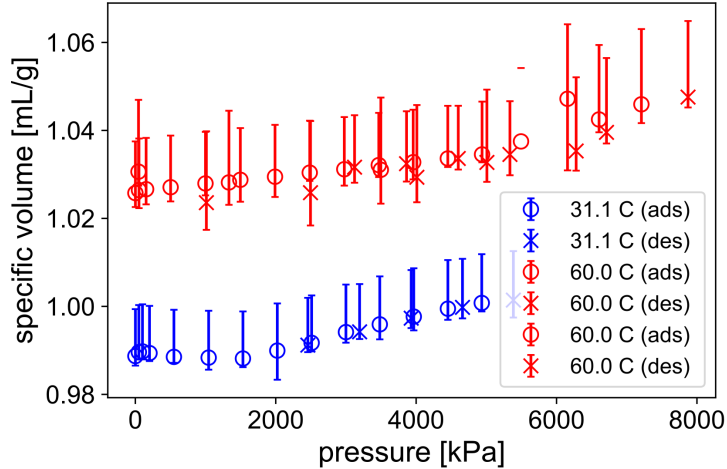
Figure II.2: The specific volume of a mixture of poly(propylene glycol) (PPG) of molecular weight 2700 g/mol and CO_2 as a function of pressure, measured with G-ADSA. Measurements were taken during both adsorption (∘) and desorption (×) of CO_2 with agreement within uncertainty. Upper error bars indicate systematic error and lower error bars indicate statistical error. Data are shown at 31 °C (blue) and 60 °C (red). Data were collected in the lab of Prof. Ernesto Di Maio at the University of Naples Federico II.

The specific volume (reciprocal of the density) of the PPG–CO_2 mixture generally increased with pressure and temperature but exhibited a unique, non-monotonic behavior at low pressure and temperature. This behavior is shown in Figure II.2, where the specific volume at 31.1 °C slightly decreases with pressure from 0–1000 kPa before increasing steadily with further increase in pressure. While this small variation in the specific volume is much smaller than the systematic error (upper error bars), it is slightly larger than the statistical error (lower error bars), suggesting that it is not the result of noise. The Di Maio group has previously reported a similar non-monotonic dependence of the specific volume on pressure from measurements with G-ADSA for a formulation of polyether polyols [2] and for poly(caprolactone) (PCL) [17]. They further demonstrated that this behavior is the result of different packing densities of CO_2 in the polymer matrix at different pressures using evidence from Raman spectroscopy [18–20].

The interfacial tension between the polyol-rich and CO_2-rich phases decreased with pressure and decreased with temperature when the concentration of dissolved CO_2 was fixed. These two behaviors are shown in Figures II.3a and II.3b. The decrease in the interfacial tension with pressure seen in Figure II.3a is expected given that the CO_2-rich atmosphere becomes more similar in density to

(a) Interfacial tension vs. pressure

(b) Interfacial tension vs. solubility
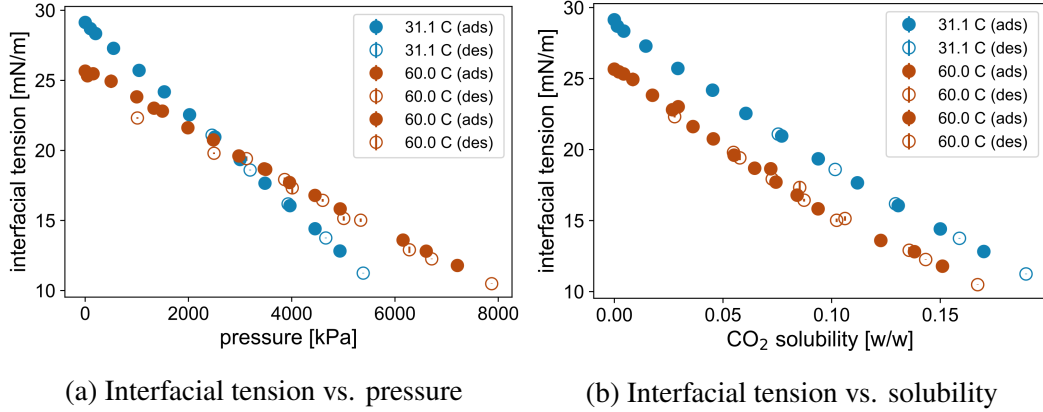
Figure II.3: Interfacial tension of a mixture of PPG and CO_2 between the polyol-rich and CO_2-rich phases G-ADSA. Measurements were taken during both pressurization (filled circles) and depressurization (empty circles) of CO_2 with agreement within uncertainty. Error bars shown but may be smaller than glyph for some data points. Data are shown at 31 °C (blue) and 60 °C (red). Data were collected in the lab of Prof. Ernesto Di Maio at the University of Naples Federico II.

the polyol-rich phase as the pressure increases, consistent with previous G-ADSA measurements from the Di Maio group for a formulation of polyether polyol [2] and PCL [17] and by Yang *et al.* for various polyols [5]. From this figure, we see that the effect of temperature depends on the pressure: at low pressure, interfacial tension decreases with temperature, but at high pressure, interfacial tension increases with temperature. The reason for this non-monotonic effect of temperature at different pressures is more clearly seen in Figure II.3b, where the interfacial tension is plotted as a function of the weight fraction of dissolved CO_2. Here, increasing the temperature decreases the interfacial tension, as is observed for pure liquids due to the increased entropic driving force for mixing. At a fixed pressure, however, increasing the temperature decreases the amount of dissolved CO_2, and the amount by which it decreases is greater at higher pressure (see Figure II.1). Because the interfacial tension decreases with the amount of dissolved CO_2 (due to the increased similarity of the polyol–CO_2 mixture to the CO_2 atmosphere), the reduction in dissolved CO_2 with temperature can increase the interfacial tension more than raising the temperature alone decreases it. The result is the increase in the interfacial tension with temperature at pressures above 3000 kPa. To our knowledge, measurements distinctly demonstrating this crossover in the interfacial tension with temperature have not been reported in the literature.

We observed that the diffusivity of CO_2 in polyol increased with pressure and temperature, consistent with previous measurements in other polyols [2, 5].

(a) Square-root fit method (b) Exponential fit method
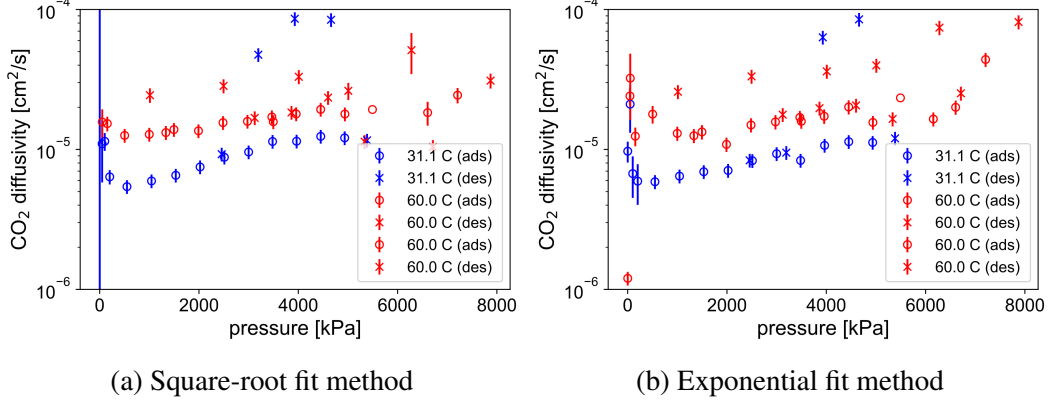
Figure II.4: The diffusivity of CO_2 in poly(propylene glycol) (PPG) of molecular weight 2700 g/mol estimated with the square-root fit (see Section II.1) as a function of pressure of CO_2 headspace, measured with G-ADSA. Measurements were taken during both adsorption (∘) and desorption (×) of CO_2 with agreement within uncertainty. Error bars may be smaller than glyphs of some data points. Data are shown at 31 °C (blue) and 60 °C (red). Data were collected in the lab of Prof. Ernesto Di Maio at the University of Naples Federico II.

Our estimation of the diffusivity from G-ADSA measurements is shown in Figure II.4 for the square-root fit method (II.4a) and the exponential fit method (II.4b) (see Section II.1 for details of these methods). While we expect a higher estimate of the diffusivity during desorption than adsorption, the difference should not be much larger than the difference in diffusivity over a similar pressure range. Our estimates yielded significantly higher diffusivities from desorption measurements, however, which we believe may be the result of depressurizing too quickly. Although increasing the temperature reduces the weight fraction of dissolved CO_2 (Figure II.1), which we observe decreases the diffusivity, the greater thermal energy conferred to the mixture at higher temperature appears to dominate that effect, leading to a monotonic increase in diffusivity with temperature, unlike the effect of temperature on interfacial tension (Figure II.3).

Finally, we compared our measurements with G-ADSA to measurements performed with other techniques. While our measurements with G-ADSA quantitatively agreed with those of the MSB reported by Dow, they significantly disagreed quantitatively with others reported in the literature [5, 15]. For a discussion of these comparisons, see Section II.S3 in the SI.

II.3 Discussion: Competition Between CO_2-philicity and Mixing Entropy Underlies CO_2 Solubility Maximum in Polyether Polyols

Because the solubility of CO_2 in a polymer profoundly shapes the structure and, consequently, the physical properties of CO_2-blown polymer foams, we direct specific attention to its dependence on polymer architecture in this section. The effect of the architecture of the polyol has not been systematically studied in full. Parks and Beckman provided useful intuition for the effect of polyol architecture on CO_2–polyol interactions in their study of the solubility of polyol in CO_2 [4]. They noted that because the carbon in CO_2 has a lower electron density, it has a strong attraction to the relatively electron-rich ether groups along the polyol backbone, which has since been demonstrated with quantum mechanical calculations [21]. In contrast, they reasoned that the CO_2-phobicity hydroxyl groups, caused by their preference for self-interaction by hydrogen bonding [21], would significantly decrease the solubility of short-chain polyols in CO_2, such as those used in polyurethane synthesis, due to the high proportion of hydroxyl end groups to ether groups along the backbone [4]. They ultimately found that the solubility of polyol in CO_2 increases with molecular weight for short chains, but decreases with molecular weight for longer chains as the decrease in the entropy of mixing with molecular weight dominates the enthalpic gain of a higher ratio of ether to hydroxyl end groups.

Indeed, Daneshvar *et al.* [22] and Li *et al.* [23] showed that the solubility of CO_2 in poly(ethylene glycol) (PEG) increases with molecular weight for short chains (150–1000 g/mol), as did Yang *et al.* for various polyether polyols in the range of 255–1000 g/mol [5]. Weidner *et al.* and Wiesmet *et al.* published measurements of CO_2 solubility in longer PEG chains of 1500–8000 g/mol at temperatures between 50–100 °C, but observed no statistically significant effect of molecular weight. Based on the work of Parks and Beckman and intuition from the Flory–Huggins model, we hypothesize that the solubility of CO_2 should decrease with molecular weight for long chains due to the decreased entropic gain from mixing. This effect will become more pronounced at lower temperatures and may be discernible with more precise measurements made possible with G-ADSA. To our knowledge, however, this trend has not been demonstrated with experimental measurements in the literature.

The effect of the number of hydroxyl groups per chain, known as the "functionality," was investigated by Yang *et al.*, who reported maximal CO_2 solubility in polyether polyols with 3 hydroxyl groups per chain [5]. This finding conflicts with the reasoning of Beckman and Parks that a higher concentration of hydroxyl

groups should reduce the attraction of CO_2 to polyol, so further study is in order. Uncovering these trends is important to guide the selection of the structure of polyols used in polyurethane foaming to optimize CO_2 solubility and achieve the desired thermal and mechanical properties in CO_2-blown polyurethane foams.

In the present study, we systematically investigate the effect of molecular weight and hydroxyl groups per chain on the solubility of CO_2 in polyether polyols. We measure the solubility of CO_2 using gravimetry–axisymetric drop-shape analysis (G-ADSA), which measures the change in mass of a sample upon absorption of CO_2 using a magnetic suspension balance while simultaneously measuring the specific volume for precise accounting of the buoyant force. Given the abundance of previous measurements of CO_2 solubility in polyols with a molecular weight smaller than 1000 g/mol, we selected longer polyols of 1000 and 2700 g/mol. Rather than observe the CO_2 solubility increase further with molecular weight, as reported in the literature for shorter polyols, we hypothesized that we would observe a decrease in CO_2 solubility with molecular weight, consistent with the observations of Parks and Beckman for the solubility of polyol in CO_2 [4]. We also systematically varied the average number of hydroxyl groups per chain from 2 to 4.7. Combined with the literature, these measurements reveal a non-monotonic dependence of the CO_2 solubility on molecular weight, peaking around 1000 g/mol, and a monotonic decrease with hydroxyl groups per chain.

We further use the measurements from G-ADSA to fit parameters of a thermodynamic model of these mixtures based on perturbed chain–statistical associating fluid theory (PC-SAFT) described in Section II.4. This model serves two purposes: first, it provides a general method for estimating the properties of polyol–CO_2 mixtures and, second, it can provide the foundation of additional models of the interface, bubble growth, and bubble nucleation. In the same section, we also briefly describe the use of a classical density functional theory (DFT) based on the free energy of the PC-SAFT model for modeling the interface between the polyol-rich and CO_2-rich phases, which we validate against interfacial tension measurements provided by G-ADSA. While the models accurately capture the CO_2 solubility and interfacial tension, the PC-SAFT model significantly underestimates the specific volume of the polyol-rich phase, likely because it does not account for associative interactions like hydrogen bonding. For polyols smaller than 1000 g/mol, an accurate PC-SAFT model even of CO_2 solubility may likewise require accounting for hydrogen bonding through associative interactions. Nevertheless, this study shows that CO_2 is most

soluble in polyether polyols of 1000 g/mol with as few hydroxyl groups as possible.

To explore the effect of polymer architecture on the amount of CO_2 it can dissolve, we separately studied the effects of hydroxyls per chain and the molecular weight, starting with the hydroxyls per chain. To our knowledge, investigation of the effect of the hydroxyl number per chain with a fixed molecular weight has not been previously reported in the literature. We considered the solubility of CO_2 of two polyols and a blend of polyol with a molecular weight of 1000 g/mol and different average numbers of hydroxyls per chain in Figure II.5. At low pressures, the difference in solubility is within the experimental uncertainty. At the higher temperature (60 °C, lower cluster of measurements) and at pressures above 3000 kPa, we can see that the polyol blend with the higher average number of hydroxyls per chain (4.7) has a significantly lower solubility of CO_2 than the other polyols; above 4000 kPa, the polyol with the middle average number of hydroxyls per chain (3) has a significantly lower solubility than the polyol with the fewest (2). This observation suggests that increasing the number of hydroxyls per chain decreases the solubility, with the difference becoming more apparent at higher pressures. This difference is less clear at the lower temperature data (upper cluster of measurements), in part because the CO_2 solubility in the polyol blend with an average of 4.7 hydroxyls per chain was measured at a lower temperature (25 °C) than the others (30.5 °C), yielding a higher solubility. While we cannot make this conclusion without measuring the CO_2 solubility at 30.5 °C and showing significantly lower values, we expect this to be the case based on a rough estimation of the effects of lower molecular weight and lower temperature on the solubility of CO_2, whose details are presented in Section II.S2 of the SI. Our observation of decreased CO_2 solubility with hydroxyl number per chain is consistent with the favorability of CO_2–ether interactions over CO_2–hydroxyl interactions [4, 21].

Next, we considered the effect of molecular weight on CO_2 solubility at a fixed hydroxyl number per chain of 2. We performed G-ADSA measurements of CO_2 solubility in two such polyols, one of 1000 g/mol and the other of 2700 g/mol, as shown in Figure II.6. The difference in solubility was not statistically significant at the higher temperature (60 °C, lower cluster of data), but the solubility was slightly lower for the longer polyol at the lower temperature (30.5–31.1 °C, upper cluster of data). The solubility of the longer polyol, however, was measured at a slightly higher temperature than that of the shorter polyol (31.1 °C for the longer vs. 30.5 °C for the shorter), which could have also led to the lower measurement of solubility.
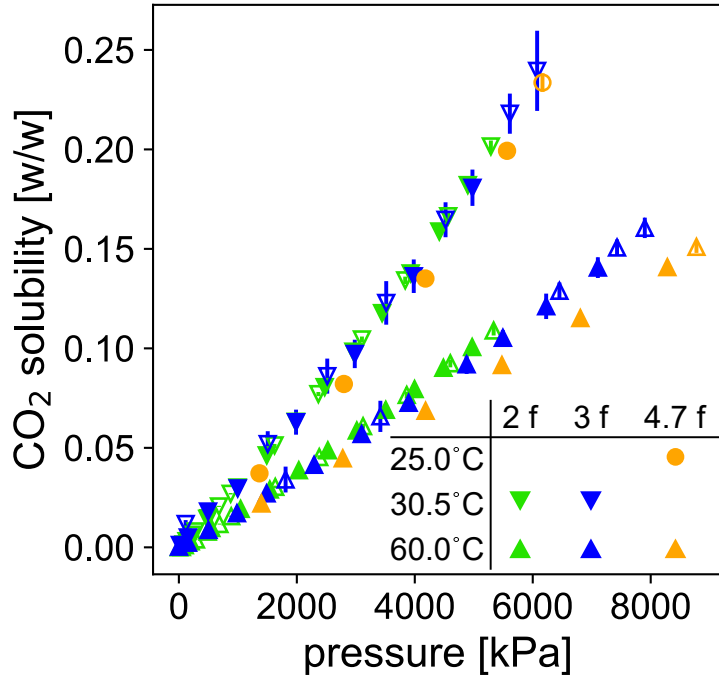
Figure II.5: The solubility of CO_2 in polyol as a function of pressure (measured with G-ADSA) is shown for polyols of three functionalities (average number of hydroxyl groups per chain): 2 (green), 3 (blue), and 4.7 (yellow) (labeled as "#f" in the legend). Each polyol has an average molecular weight of 1000 g/mol, except for the polyol with a functionality of 4.7, which has an average molecular weight of 728 g/mol (this effect is roughly cancelled out by the lower temperature). Measurements were taken during both pressurization (filled symbols) and depressurization (open symbols) of CO_2 with agreement within uncertainty. Error bars may be smaller than glyphs of some data points. Data are shown in two temperature clusters: the upper cluster contains data measured at 30.5 °C (downward triangle) for 2f and 3f but 25 °C (circle) for 4.7f; the lower cluster contains data measured at 60 °C (upward triangle).

Because our measurements are not sufficient to draw a clear conclusion about the effect of molecular weight on CO_2 solubility, we turn to the literature to augment our dataset. In particular, we combine our measurements with those of Gui *et al.* [24] for monomers ethylene glycol and propylene glycol and Li *et al.* [23] for oligomers of poly(ethylene glycol) (PEG). While our measurements were taken of PPG-like polyols, which have an additional methyl group on each monomer when compared to PEG, we do not expect this difference to have a significant effect on the enthalpy of CO_2 solubility due to the distance from the methyl group in PPG and the ether linkage where CO_2 tends to associate [21].

To compare the CO_2 solubility more clearly among measurements from the
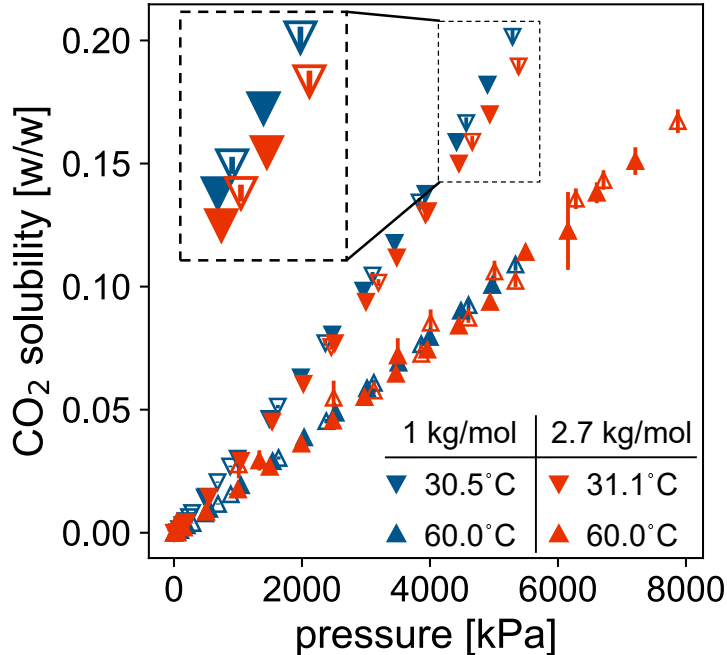
Figure II.6: The solubility of CO_2 in polyol as a function of pressure (measured with G-ADSA) is shown for difunctional polyols of two number-averaged molecular weights M_n: 1 kg/mol (blue) and 2.7 kg/mol (red). Measurements were taken during both pressurization (filled symbols) and depressurization (open symbols) of CO_2 with agreement within uncertainty. Error bars may be smaller than glyphs of some data points. Data are shown in two temperature clusters: the upper cluster contains data measured at 30.5 °C for 1000 g/mol and 31.1 °C for 2700 g/mol (downward triangles); the lower cluster contains data measured at 60 °C (upward triangles).

literature, we compared Henry's constant, the rate at which the solubility increases with pressure. We computed Henry's constant by fitting the slope of a line passing through the origin to measurements of CO_2 solubility at pressures below 1 MPa based on our observation in Figure II.5 that the solubility vs. pressure increases superlinearly at higher pressures, deviating from Henry's law. We report Henry's constant in terms of weight fraction of CO_2 per Pa [w/(w.MPa)] for comparison to other plots in this section. The only published measurements of polyether polyols that report solubility at pressures below 1 MPa were taken of difunctional polyols (two hydroxyl OH groups per chain) [23, 24]. Other measurements of CO_2 solubility available in the literature either only report solubility at pressures well above 1 MPa [5, 15, 22, 25–28] or do not report a sufficiently precise experimental uncertainty for meaningful comparison [29, 30]. Henry's constant for the CO_2 solubility in difunctional (two hydroxyl OH groups per chain) polyether polyols is shown in Figure II.7. We can see that Henry's constant increases with molecular weight

below ≈ 1000 g/mol but decreases with molecular weight above ≈ 1000 g/mol for a range of temperatures from 30 °C to 60 °C.
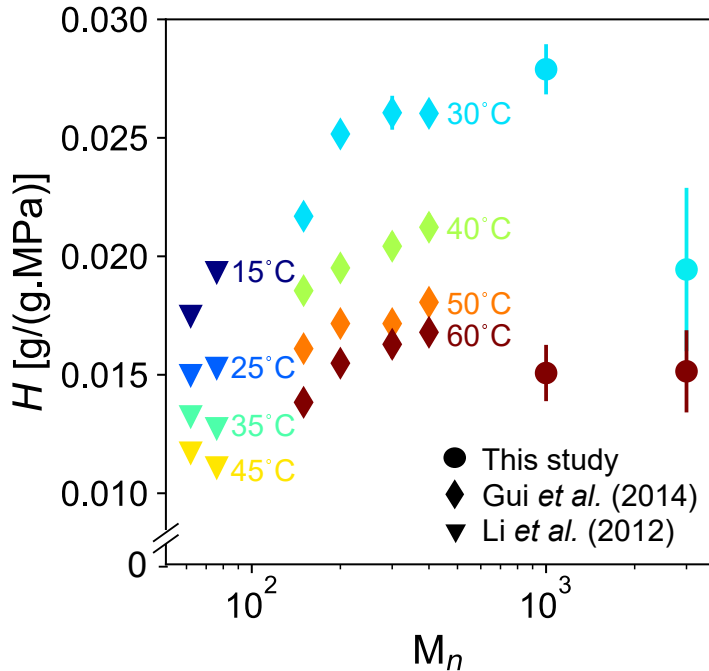
Figure II.7: Henry's constant for CO_2 solubility in difunctional polyols (two hydroxyls per chain) is plotted as a function of the average molecular weight. Both the data measured with G-ADSA in this study and literature data are provided. Error bars may be smaller than glyphs of some data points. Data are shown at different temperatures indicated by the color as defined in the legend.

Our finding of maximal CO_2 solubility in polyether polyols with a molecular weight near 1000 g/mol is consistent with the findings of Parks and Beckman for the opposite situation, the solubility of polyether polyols in CO_2 [4]. Although they made measurements at a lower temperature (25 °C) and higher pressures (tens of MPa), they also reported a maximum in the solubility of difunctional polyols at a molecular weight of 1000 g/mol. Along with other groups who have explored this question [21, 24, 31], we agree with their explanation of this non-monotonic trend based on the competition between decreasing concentration of CO_2-phobic hydroxyl groups (relative to ether linkages [21]) and decreasing mixing entropy with molecular weight. We also note that we might expect the optimal molecular weight for CO_2 solubility to decrease with temperature due to the increased importance of entropy, which favors shorter chains. Our collection of data in Figure II.7 appears to be consistent with this hypothesis at 60 °C, where the optimal molecular

weight appears to be below 1000 g/mol, but further measurements are necessary to demonstrate this behavior robustly.

II.4 Thermophysical Measurements Provide the Basis for Fitting Empirical Parameters of Thermodynamic Models

Because a single set of G-ADSA measurements (one polyol, one temperature) can last over a week, measuring the properties for all temperatures and pressures is not feasible. Instead, we turn to a thermodynamic model to estimate some of the properties (solubility, specific volume) under conditions for which we lack measurements. We chose the perturbed chain–statistical associating fluid theory (PC-SAFT) model [32] based on its success in modeling the solubility of CO_2 in polystyrene and poly(methyl methacrylate) [33]. PC-SAFT also formed a suitable basis for the development of a classical density functional theory (DFT) for modeling the interfacial tension [33], which will be discussed later in this section, as well as for an estimation of the energy barrier for bubble nucleation using the string method [34, 35], which will be discussed in Chapter VI. The application of PC-SAFT to ternary mixtures will be explored as well in Chapter VII.
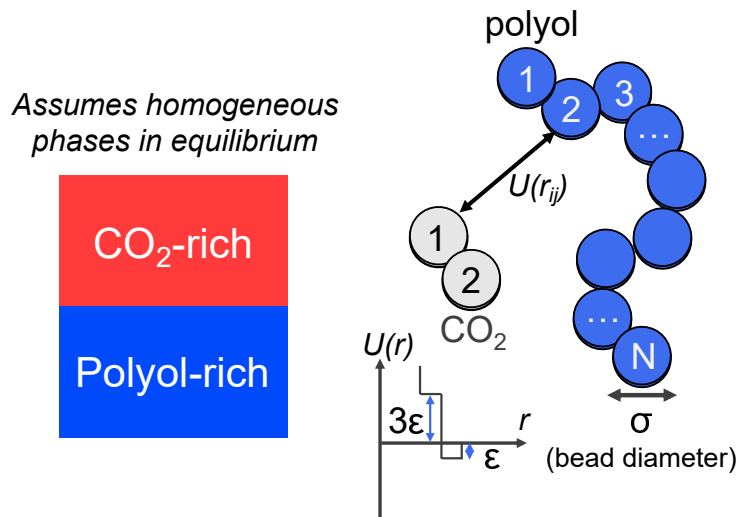
Figure II.8: A schematic of the PC-SAFT model for binary mixtures of polyol and CO_2. The model considers the polyol-rich and CO_2-rich phases as uniform and separated by an infinitesimal interface (left schematic). Both components are modeled as chains of hard-sphere beads of diameter σ (right schematic) with an attractive, radial interaction potential $U(r_{ij})$ scaled by energy parameter ε, which is plotted at the bottom of the Figure. Polyol is modeled as N beads while CO_2 is modeled as 2 beads as in [33]. Schematic adapted with permission from the unpublished work of Dr. Huikuan Chao.

The PC-SAFT model of the equation of state provides a thermodynamic model for both pure components and mixtures. It improves upon previous "SAFT" models of fluid compounds by applying a perturbation theory to a reference state of fluid of chains of purely repulsive beads, leading to the prefix "perturbed chain." A schematic of the PC-SAFT model is shown in Figure II.8. This particular application of the perturbation theory combined with the fitting of some empirical parameters to measured properties of real polymers allows PC-SAFT to model the properties of polymer mixtures better than other SAFTs (*e.g.*, PR-SAFT [33]). Due to our focus on experimental measurements, we provide only a brief, conceptual description of the PC-SAFT model sufficient to introduce the parameters to be fitted; for a detailed mathematical description of the model, see the work of Xu *et al.* [33]. The model is a mean-field theory with a free energy composed of four contributions: ideal, hard-sphere, association, and dispersion. The ideal contribution is the free energy of an ideal gas (non-interacting point particles). The hard-chain contribution is model use the Boublik–Mansoori–Carnahan–Starling–Leland (BMCSL) theory for mixtures of hard spheres with diameter σ [36, 37]. The association contribution accounts for the connectivity of the N_i beads in a chain of species i based on the bead diameter σ and density. Finally, the dispersion contribution provides an empirical model of the interactions of the molecules, which are scaled by an energy scale ε_{ij} between two species i and j. This energy scale is computed using an energy parameter ε_i for a single species i and a correction $k_{ij} = AT + B$ for fit parameters A and B and temperature T (in Kelvin) to account for differences in the interactions between two different species i and j.

Species	N (beads)	σ [Å]	ε [k_B]	k
CO_2	2	2.79	170.5	$10^{-4}(2.7T - 820)$
PPG (2700 g/mol)	123	3.01	228.5	$10^{-4}(2.7T - 820)$

Table II.2: The parameters N (number of beads per chain), σ (bead diameter in Angstroms), ε (interaction energy parameter in units of Boltzmann's constant), and k (cross-interaction parameter between the two species, unitless with T representing the temperature in Kelvin; identical for both species) that fit the solubility data for PPG (2700 g/mol) are listed. The corresponding model and experimental data are shown in Figure II.9.

Therefore, a complete PC-SAFT model of polyol and CO_2 is described by eight parameters: two chain lengths N_{CO2} and N_{polyol}, two bead diameter σ_{CO2} and σ_{polyol}, two energy parameters ε_{CO2} and ε_{polyol}, and the two parameters A and B defining the cross interaction correction term $k_{CO2,polyol} = AT + B$. Thanks to

previous work on polyol–CO$_2$ mixtures by Xu *et al.* [33], the parameters specific to CO$_2$ had already been fit to the pure-component equation of state data and were validated against NIST data [12]. The parameters for the polyol and the cross interaction were fit by Dr. Huikuan Chao through trial and error until the PC-SAFT accurately modeled the CO$_2$ solubility in that polyol measured with G-ADSA. Note that existing software packages that automatically fit thermodynamic model parameters are commercial, but a team from Imperial College London is extending their open-source `ypaul21/Clapeyron.jl` package [38] in `julia` for equation-of-state modeling to provide parameter estimation as well at the time of this writing [39]. As is often the case for PC-SAFT models of vapor-liquid equilibria, an infinite set of degenerate parameters for the polyol can model the CO$_2$ solubility. To break this degeneracy, we begin by guessing parameters based on those predicted using the group contribution method, a common method for estimating PC-SAFT parameters based on the functional groups present in the compounds [40]. These parameters result in a model that does not fit the data well, so we adjusted them manually until a fit was achieved. The PC-SAFT parameters for CO$_2$ and PPG (2700 g/mol) are listed in Table II.2. The CO$_2$ solubility predicted using these parameters is compared to the corresponding G-ADSA measurements in Figure II.9.

PC-SAFT Fits Solubility Measurements
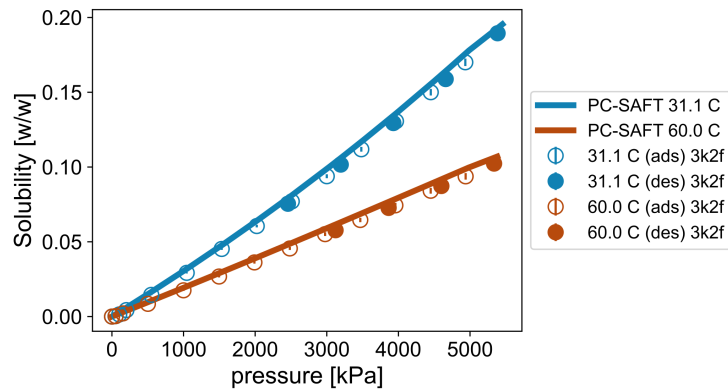
Figure II.9: CO$_2$ solubility in PPG of 2700 g/mol as function of pressure. Measurements from G-ADSA are shown in circular glyphs (empty indicates adsorption measurement and filled indicates desorption measurement); error bars may be smaller than the glyphs of some data points. Data were collected in the lab of Prof. Ernesto Di Maio at the University of Naples Federico II. Predicted solubility from PC-SAFT is shown in solid lines. Model was developed by Dr. Huikuan Chao in the group of Prof. Zhen-Gang Wang. Data are plotted for 31.1 °C (blue) and 60 °C (dark orange).

Because we fit the PC-SAFT parameters through trial and error, we cannot provide confidence intervals on our parameters. Instead, to demonstrate the precision of our estimate, we show the sensitivity of our predictions of different properties to ±5% variations in the σ, ε, and N parameters for PPG in Figure II.S12 of the SI. This figure shows the sensitivity of the PC-SAFT predictions of CO_2 solubility and specific volume (discussed later) and of the DFT predictions (discussed later) of interfacial tension.

DFT Model Based on PC-SAFT Models Interfacial Tension with PC-SAFT Parameters Fitted to Solubility
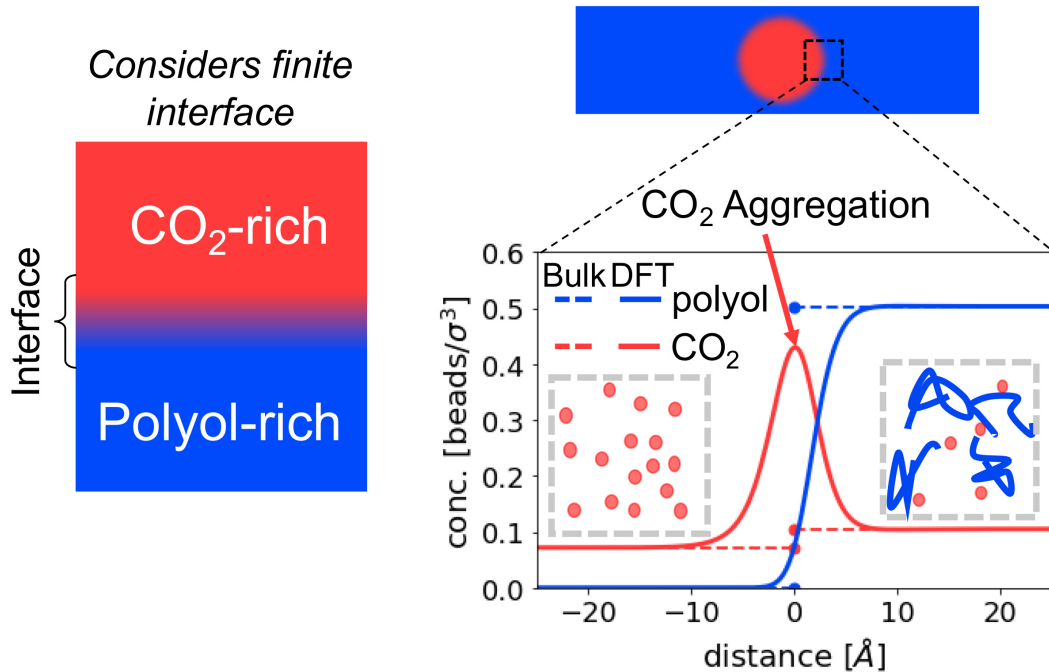
Figure II.10: Schematic of the density functional theory model of the interface between CO_2-rich and polyol-rich phases. On the left is a schematic of how DFT takes into account the non-uniformities along the finite interface. On the right is an example plot of the concentration of polyol (blue) and CO_2 (red) in the CO_2-rich phase (left), the polyol-rich phase (right), and along the interface (center) between a CO_2-rich bubble and a polyol-rich mother phase (depicted in schematic above the plot). This plot reveals an accumulation of CO_2 along the interface (indicated by red arrow; see Section II.S5 for further discussion) and other discrepancies between the DFT (solid lines) and the bulk phase concentrations predicted by PC-SAFT (dashed lines). Plot generated from the calculations of Dr. Huikuan Chao.

Based on the PC-SAFT model described above, Dr. Huikuan Chao developed a model of the interface between the polyol-rich and CO_2-rich phases with classical density functional theory (DFT) following the method described in Xu *et*

al. [33]. A schematic of the DFT model used is shown in Figure II.10. The result is a model that takes the PC-SAFT parameters fitted to experimental CO_2 solubility data as input and predicts the equilibrium concentration profile of each species and the resulting interfacial tension at an interface between two phases. An example of the equilibrium concentration profile of CO_2 and PPG is shown in Figure II.S14 of the SI; here, we will focus on the predicted interfacial tension. This value is not fitted in any way to the values of interfacial tension measured with G-ADSA; therefore, we can test the validity of this model by comparing its blind prediction to the experimental data, following the method described by Xu *et al.* [33]. The prediction of the interfacial tension between the CO_2-rich and polyol-rich phases of a mixture of CO_2 and PPG (2700 g/mol) is shown in Figure II.11. We see that the DFT model not only predicts the qualitative trends observed in the experimental measurements, such as decreasing interfacial tension with temperature at low pressure and increasing interfacial tension with temperature at high pressure, but also achieves reasonable, though not perfect, quantitative accuracy. This agreement between model and measurement supports our use of the DFT model for predictions of interfacial properties and provides our justification for using this model as the basis of our string method predictions of the energy barrier for bubble nucleation discussed in Chapter VI.
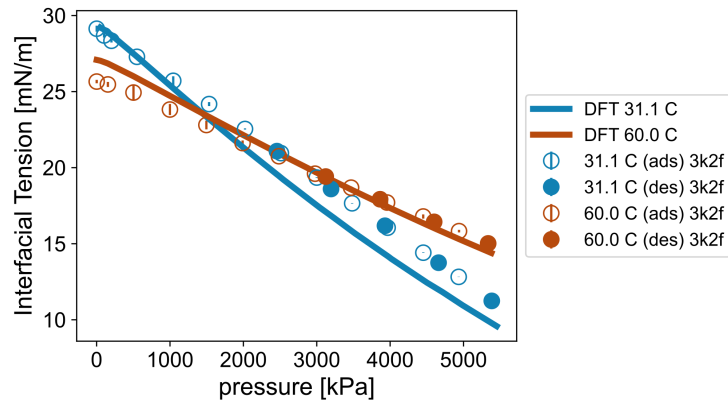
Figure II.11: Interfacial tension between polyol-rich and CO_2-rich phases of a mixture of CO_2 and PPG (2700 g/mol) predicted by DFT model based on parameters from fitting PC-SAFT model to solubility data (see Fig. II.9) shown in solid lines compared to measurements from G-ADSA shown in circular glyphs (empty indicates adsorption measurement and filled indicates desorption measurement). Error bars may be smaller than the glyphs of some data points. Data are plotted for 31.1 °C (blue) and 60 °C (dark orange). Data were collected in the lab of Prof. Ernesto Di Maio at the University of Naples Federico II. Model was developed by Dr. Huikuan Chao in the group of Prof. Zhen-Gang Wang.

PC-SAFT Fails to Model Specific Volume

Despite the success of PC-SAFT in modeling CO_2 solubility and DFT in modeling interfacial tension for polyol–CO_2 mixtures, it fails to model the specific volume. While there is an infinite set of degenerate PC-SAFT parameters for which the PC-SAFT model accurately describes the measured CO_2 solubility and the DFT model accurately describes the measured interfacial tension, no group of parameters in that set yields an accurate PC-SAFT model of the specific volume. The disagreement between the specific volume measured with G-ADSA and the predictions of PC-SAFT model based on the parameters in Table II.2 is shown in Figure II.12. Qualitatively, while the PC-SAFT model accurately captures the effect of temperature and high pressure on specific volume, it fails to capture the non-monotonic dependence of the specific volume on pressure at low pressures and temperatures. This failure of PC-SAFT's coarse-grained beads to capture this behavior is not surprising given that it arises due to the molecular structure [18–20]. Quantitatively, however, PC-SAFT underestimates the specific volume (overestimates the density) by over 10%. For the sake of providing model predictions to compare to experimental measurements, we accept the failure of our PC-SAFT model to predict the specific volume accurately and ignore the association of the hydroxyl end groups.
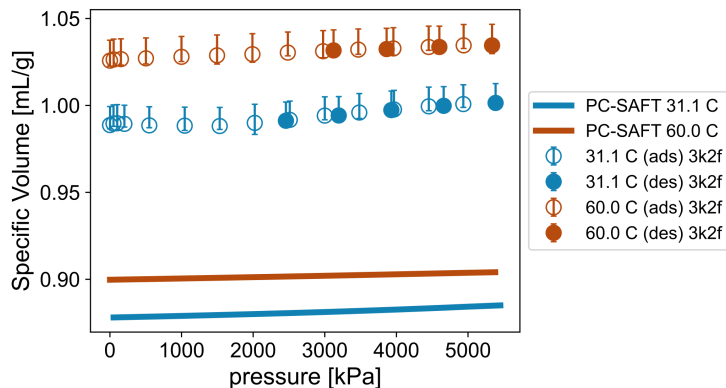
Figure II.12: The specific volume of a mixture of CO_2 and PPG (2700 g/mol) as a function of pressure predicted by PC-SAFT (solid lines) and measured with G-ADSA (circular glyphs: empty indicates adsorption measurement and filled indicates desorption measurement). Error bars may be smaller than the glyphs of some data points. Data are plotted for 31.1 °C (blue) and 60 °C (dark orange). Upper error bars indicate systematic error and lower error bars indicate statistical error. Data are shown at 31 °C (blue) and 60 °C (red). Data were collected in the lab of Prof. Ernesto Di Maio at the University of Naples Federico II. Model was developed by Dr. Huikuan Chao in the group of Prof. Zhen-Gang Wang.

II.5   Recommendation for Future Work

Based on the conclusion of Parks and Beckman that "a complete description of the phase behavior of these CO_2–polyol mixtures may require a more rigorous model of hydrogen bonding" [4], we are hopeful that the proper incorporation of the association of the hydroxyl end groups of the polyol can yield an accurate model for both CO_2 solubility and specific volume. The incorporation of the association of the end groups was explored with some success by Dr. Huikuan Chao, but the extension of such a model to DFT and, ultimately, to the string method would be a colossal task.

References

1. Pastore Carbone, M. G., Di Maio, E., Iannace, S. & Mensitieri, G. Simultaneous experimental evaluation of solubility, diffusivity, interfacial tension and specific volume of polymer/gas solutions. *Polymer Testing* **30,** 303–309. ISSN: 01429418. https://linkinghub.elsevier.com/retrieve/pii/S0142941811000067 (May 2011).

2. Di Caprio, M. R. *et al.* Polyether polyol/CO2 solutions: Solubility, mutual diffusivity, specific volume and interfacial tension by coupled gravimetry-Axisymmetric Drop Shape Analysis. *Fluid Phase Equilibria* **425,** 342–350. ISSN: 03783812. https://linkinghub.elsevier.com/retrieve/pii/S0378381216302990 (Oct. 2016).

3. Di Caprio, M. R. *et al. Thermosetting polyurethane foams by supercritical CO 2 as physical blowing agent* tech. rep. (University of Naples Federico II, Naples, 2017).

4. Parks, K. L. & Beckman, E. J. Generation of microcellular polyurethane foams via polymerization in carbon dioxide. I: Phase behavior of polyurethane precursors. *Polymer Engineering & Science* **36,** 2404–2416. ISSN: 0032-3888. https://onlinelibrary.wiley.com/doi/10.1002/pen.10639 (Oct. 1996).

5. Yang, Z. *et al.* Effect of the properties of polyether polyol on sorption behaviour and interfacial tension of polyol/CO2 solutions under high pressure condition. *The Journal of Chemical Thermodynamics* **133,** 29–36. ISSN: 00219614. https://linkinghub.elsevier.com/retrieve/pii/S0021961419300643 (June 2019).

6. Kluyver, T. *et al.* in *Positioning and Power in Academic Publishing: Players, Agents and Agendas* (eds Loizides, F. & Schmidt, B.) 87–90 (IOS Press, 2016). ISBN: 9781614996484. https://ebooks.iospress.nl/ISBN/978-1-61499-648-4.

7. Hunter, J. D. Matplotlib: A 2D Graphics Environment. *Computing in Science & Engineering* **9,** 90–95. ISSN: 1521-9615. http://ieeexplore.ieee.org/document/4160265/ (2007).

8. Harris, C. R. *et al.* Array programming with NumPy. *Nature* **585,** 357–362. ISSN: 0028-0836. arXiv: 2006.10256. https://www.nature.com/articles/s41586-020-2649-2 (Sept. 2020).

9. Reback, J. *et al. pandas-dev/pandas: Pandas 1.0.1* 2022. 10.5281/zenodo.5893288.

10. Virtanen, P. *et al.* SciPy 1.0: fundamental algorithms for scientific computing in Python. *Nature Methods* **17,** 261–272. ISSN: 1548-7091. arXiv: 1907.10121. http://www.nature.com/articles/s41592-019-0686-2 (Mar. 2020).

11. Ylitalo, A. S. *andylitalo/g-adsa: v0.1.0* 2022. https://github.com/andylitalo/g-adsa (2022).

12. NIST. *NIST Standard Reference Database Number 69* 2022. https://webbook.nist.gov/chemistry/ (2022).

13. Crank, J. *The Mathematics of Diffusion* 2nd Ed., 1–352 (Oxford University Press, London, 1975).

14. Song, B. & Springer, J. Determination of interfacial tension from the profile of a pendant drop using computer-aided image processing. *Journal of Colloid and Interface Science* **184,** 64–76. ISSN: 00219797 (1996).

15. Guadagno, T. & Kazarian, S. G. High-Pressure CO 2 -Expanded Solvents: Simultaneous Measurement of CO 2 Sorption and Swelling of Liquid Polymers with in-Situ Near-IR Spectroscopy. *The Journal of Physical Chemistry B* **108,** 13995–13999. ISSN: 1520-6106. https://pubs.acs.org/doi/abs/10.1021/jp0481097%20https://pubs.acs.org/doi/10.1021/jp0481097 (Sept. 2004).

16. Rajendran, A. *et al.* Simultaneous measurement of swelling and sorption in a supercritical CO2-poly(methyl methacrylate) system. *Industrial and Engineering Chemistry Research* **44,** 2549–2560. ISSN: 08885885 (Apr. 2005).

17. Carbone, M. G. P., Di Maio, E., Scherillo, G., Mensitieri, G. & Iannace, S. Solubility, mutual diffusivity, specific volume and interfacial tension of molten PCL/CO2 solutions by a fully experimental procedure: effect of pressure and temperature. *The Journal of Supercritical Fluids* **67,** 131–138. http://dx.doi.org/10.1016/j.supflu.2012.04.001 (2012).

18. Pastore Carbone, M. G., Di Maio, E., Musto, P., Braeuer, A. & Mensitieri, G. On the unexpected non-monotonic profile of specific volume observed in PCL/CO2 solutions. *Polymer* **56,** 252–255. ISSN: 00323861. https://linkinghub.elsevier.com/retrieve/pii/S0032386114010568 (Jan. 2015).

19. Carbone, M. G. P. *et al.* Raman Line Imaging of Poly(e-caprolactone)/Carbon Dioxide Solutions at High Pressures: A Combined Experimental and Computational Study for Interpreting Intermolecular Interactions and Free-Volume Effects. *Journal of Physical Chemistry B* **120,** 9115–9131. ISSN: 15205207. https://pubs.acs.org/sharingguidelines (Sept. 2016).

20. Mensitieri, G., Scherillo, G., Panayiotou, C. & Musto, P. Towards a predictive thermodynamic description of sorption processes in polymers: The synergy between theoretical EoS models and vibrational spectroscopy. *Materials Science and Engineering: R: Reports* **140,** 100525. ISSN: 0927796X. https://linkinghub.elsevier.com/retrieve/pii/S0927796X19301275 (Apr. 2020).

21. Kilic, S. *et al. Phase behavior of oxygen-containing polymers in CO2* in *Macromolecules* **40** (American Chemical Society, Feb. 2007), 1332–1341. https://pubs.acs.org/sharingguidelines.

22. Daneshvar, M., Kim, S. & Gulari, E. High-pressure phase equilibria of polyethylene glycol-carbon dioxide systems. *The Journal of Physical Chemistry* **94,** 2124–2128. ISSN: 0022-3654. https://pubs.acs.org/doi/10.1021/j100368a071 (Mar. 1990).

23. Li, J., Ye, Y., Chen, L. & Qi, Z. Solubilities of CO 2 in poly(ethylene glycols) from (303.15 to 333.15) K. *Journal of Chemical and Engineering Data* **57,** 610–616. ISSN: 00219568. https://pubs.acs.org/sharingguidelines (Feb. 2012).

24. Gui, X., Tang, Z. & Fei, W. Solubility of CO2 in alcohols, glycols, ethers, and ketones at high pressures from (288.15 to 318.15) K. *Journal of Chemical and Engineering Data* **56,** 2420–2429. ISSN: 00219568. https://pubs.acs.org/sharingguidelines (May 2011).

25. Weidner, E., Wiesmet, V., Knez, Ž. & Škerget, M. Phase equilibrium (solid-liquid-gas) in polyethyleneglycol-carbon dioxide systems. *The Journal of Supercritical Fluids* **10,** 139–147. ISSN: 08968446. https://linkinghub.elsevier.com/retrieve/pii/S0896844697000168 (Aug. 1997).

26. Aionicesei, E., Škerget, M. & Knez, Ž. Measurement and modeling of the CO2 solubility in polyethylene glycol of different molecular weights. *Journal of Chemical and Engineering Data* **53,** 185–188. ISSN: 00219568. https://pubs.acs.org/sharingguidelines (Jan. 2008).

27. Medina-Gonzalez, Y. *et al.* Phase equilibrium of the CO2/glycerol system: Experimental data by in situ FT-IR spectroscopy and thermodynamic modeling. *The Journal of Supercritical Fluids* **73,** 97–107. https://hal.archives-ouvertes.fr/hal-00877680/document (2013).

28. Nunes, A. V., Carrera, G. V., Najdanovic-Visak, V. & Nunes da Ponte, M. Solubility of CO2 in glycerol at high pressures. *Fluid Phase Equilibria* **358,**

105–107. ISSN: 0378-3812. https://www.sciencedirect.com/science/article/pii/S0378381213004172 (Nov. 2013).

29. Aschenbrenner, O. & Styring, P. Comparative study of solvent properties for carbon dioxide absorption. *Energy Environ. Sci.* **3,** 1106–1113. www.rsc.org/ees (2010).

30. Wiesmet, V., Weidner, E., Behme, S., Sadowski, G. & Arlt, W. Measurement and modelling of high-pressure phase equilibria in the systems polyethyleneglycol (PEG)–propane, PEG–nitrogen and PEG–carbon dioxide. *The Journal of Supercritical Fluids* **17,** 1–12. ISSN: 08968446 (Feb. 2000).

31. Girard, E., Tassaing, T., Marty, J.-D. & Destarac, M. Structure–Property Relationships in CO 2 -philic (Co)polymers: Phase Behavior, Self-Assembly, and Stabilization of Water/CO 2 Emulsions. *Chemical Reviews* **116,** 4125–4169. ISSN: 0009-2665. https://pubs.acs.org/doi/10.1021/acs.chemrev.5b00420 (Apr. 2016).

32. Gross, J. & Sadowski, G. Perturbed-Chain SAFT: An Equation of State Based on a Perturbation Theory for Chain Molecules. *Ind. Eng. Chem. Res.* **40,** 1244–1260. https://pubs.acs.org/doi/abs/10.1021/ie0003887 (2001).

33. Xu, X., Cristancho, D. E., Costeux, S. & Wang, Z.-G. Density-functional theory for polymer-carbon dioxide mixtures: A perturbed-chain SAFT approach. *The Journal of Chemical Physics* **137,** 054902. ISSN: 0021-9606. http://aip.scitation.org/doi/10.1063/1.4742346 (Aug. 2012).

34. Xu, X., Cristancho, D. E., Costeux, S. & Wang, Z.-G. Discontinuous Bubble Nucleation Due to a Metastable Condensation Transition in Polymer–CO2 Mixtures. *The Journal of Physical Chemistry Letters* **4,** 1639–1643. http://pubs.acs.org/doi/10.1021/jz4005575 (May 2013).

35. Xu, X., Cristancho, D. E., Costeux, S. & Wang, Z.-G. Bubble nucleation in polymer–CO2 mixtures. *Soft Matter* **9,** 9675. ISSN: 1744-683X. www.rsc.org/softmatter%20http://xlink.rsc.org/?DOI=c3sm51477c (2013).

36. Boublík, T. Hard - Sphere Equation of State. *The Journal of Chemical Physics* **53,** 471–472. ISSN: 0021-9606. http://aip.scitation.org/doi/10.1063/1.1673824 (July 1970).

37. Mansoori, G. A., Carnahan, N. F., Starling, K. E. & Leland, T. W. Equilibrium thermodynamic properties of the mixture of hard spheres. *The Journal of Chemical Physics* **54,** 1523–1526. ISSN: 00219606 (1971).

38. Riedemann, A. *et al. ypaul21/Clapeyron.jl: v0.3.5* 2022. https://github.com/ypaul21/Clapeyron.jl.

39. Walker, P. J., Yew, H.-W. & Riedemann, A. Clapeyron.jl: An extensible, open-source fluid-thermodynamics toolkit, 1–67. arXiv: 2201.08927. http://arxiv.org/abs/2201.08927 (2022).

40. Tihic, A., Kontogeorgis, G. M., von Solms, N., Michelsen, M. L. & Constanti-nou, L. A Predictive Group-Contribution Simplified PC-SAFT Equation of State: Application to Polymer Systems. *Industrial & Engineering Chemistry Research* **47,** 5092–5101. ISSN: 0888-5885. https://pubs.acs.org/doi/10.1021/ie0710768 (Aug. 2008).

II.S1   Gravimetry–Axisymmetric Drop Shape Analysis (G-ADSA)

Apparatus

As described in Section II.1, the Teflon rod swelled as a result of absorbing CO_2 as the pressure increased. This swelling is depicted in Figure II.S1. An image of the interior of the G-ADSA apparatus is shown in panel (a) as well for reference, with the Teflon rod marked by a box.
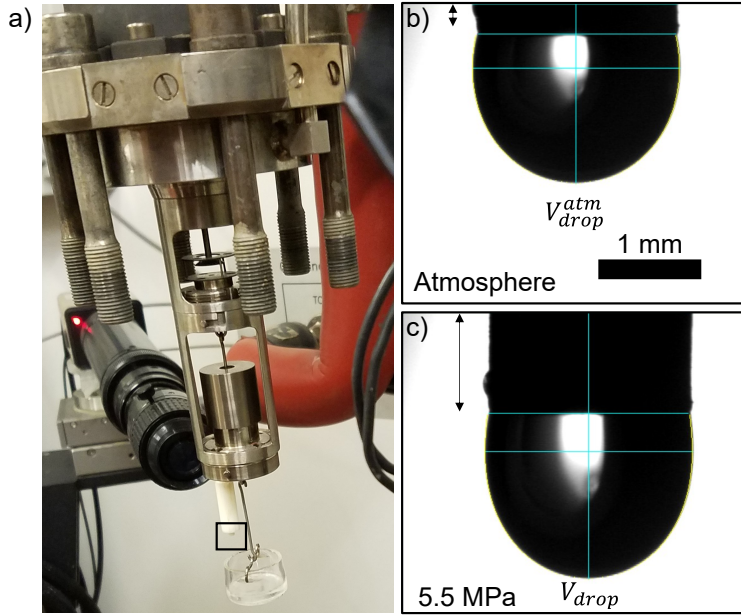
Figure II.S1: Swelling of Teflon rod for suspending pendant drop in G-ADSA due to absorption of CO_2. a) Interior of G-ADSA setup with tip of Teflon rod outlined in a black square. Images of the Teflon rod are recorded with the camera seen behind the rod. b) Image of Teflon rod under atmospheric pressure. c) Image of Teflon rod camera under 5.5 MPa of CO_2. Note that the tip of the Teflon rod has descended due to the swelling of the rod from absorption of CO_2.

Data Analysis

Having briefly described the methods for estimating CO_2 solubility, specific volume, interfacial tension, and CO_2 diffusivity for polyol–CO_2 mixtures using G-ADSA measurements, we now describe the analysis in greater depth and mathematical detail below. This analysis is encoded in the GitHub repository `andylitalo/g-adsa` [1].

We begin by estimating the equilibrium volume of the pendant drop from the image of the drop shape using the commercial software FTA32 developed by First Ten Angstroms. The software only requires that we click the leftmost and rightmost points of contact between the pendant drop and the Teflon rod and provide a length

scale for the pixels in the image. To determine the length scale, we divide the known width of the tip of the rod (measured with calipers) by its width in pixels in the image taken under vacuum—at higher pressures, the Teflon rod swells. Finally, the software estimates the equilibrium drop volume V_{drop} by assuming axisymmetry. We assume that the equilibrium drop volume $V_{drop}(p)$ grows with pressure p in proportion to the equilibrium sample volume $V_{samp}(p)$,

$$V_{samp}(p) = \frac{V_{drop}(p)}{V_{drop}(0)} V_{samp}(0) \tag{II.1}$$

Next, we estimate the equilibrium sample mass. In this Section, we will use the letter B to indicate a direct measurement of force by the Rubotherm balance in the G-ADSA apparatus (scaled by the gravitational acceleration g to be in units of mass), m to indicate mass, $\tilde{m}$ to indicate a force on the balance (buoyancy) scaled to be in units of mass, and w to indicate a mass fraction (kg/kg). The balance provides us readings of the apparent weight $B_{app}(p)$ and the tare weight $B_{tare}(p)$ at the given pressure. Because these weights are scaled by the gravitational acceleration, they correspond to the mass of the components of the scale minus the buoyant force from the surrounding atmosphere. Thus, the difference between these measurements $\Delta B(p) \equiv B_{app}(p) - B_{tare}(p)$ is equivalent to the sum of the mass of the sample at the equilibrium pressure $m_{samp}(p)$, the mass of the crucible m_{cruc}, and the mass of the hooks m_{hook} minus the buoyant force scaled by gravitational acceleration $\tilde{m}_{buoy}(p)$ at the equilibrium pressure (note that the buoyant force must be accounted for due to the precision of these measurements),

$$\Delta B(p) = m_{samp}(p) + m_{cruc} + m_{hook} - \tilde{m}_{buoy}(p) \tag{II.2}$$

When the pressure $p = 0$, the mass of the sample is the dry mass of the polyol $m_{samp}(p = 0) \equiv m_{poly}$ (assumed to be constant, *i.e.* negligible vaporization of polyol) and there is no buoyant force ($\tilde{m}_{buoy}(p = 0) = 0$). Thus, the difference in balance readings at zero pressure is

$$\Delta B(p = 0) = m_{poly} + m_{cruc} + m_{hook} \tag{II.3}$$

Subtracting equation II.3 from equation II.2 gives

$$\Delta B(p) - \Delta B(p = 0) = m_{samp} - m_{poly} - m_{buoy}(p)$$

The sample mass m_{samp} is composed of the mass of the dry polyol m_{poly} and the mass of the gas m_{gas}, such that the equation above can be solved for the mass of the gas,

$$m_{gas}(p) = \Delta B(p) - \Delta B(p = 0) + m_{buoy}(p) \tag{II.4}$$

We now only require the effect of the buoyant force on the balance reading $\tilde{m}_{buoy}(p)$ to compute the mass of dissolved gas. When scaled by gravitational acceleration, the buoyant force on the balance reading is the density of the CO_2 atmosphere at the given pressure and temperature T, $\rho_{CO2}(p, T)$ (available on the NIST Chemistry WebBook[2]), multiplied by the total volume of weighed objects V_{tot}. The total volume of weighed objects includes the volumes of the crucible V_{cruc}, the supporting hooks V_{hook}, and the sample $V_{samp}(p)$. Thus, the buoyant force is

$$\tilde{m}_{buoy}(p) = \rho_{CO2}(p)[V_{cruc} + V_{hook} + V_{samp}(p)] \tag{II.5}$$

The volume of the crucible and hooks $V_{cruc} + V_{hook}$ was measured to be 2.2675 mL by Dr. Maria Rosaria Di Caprio in a helium atmosphere before performing experiments, as described in previous work [3]. The volume of the sample at the given pressure $V_{samp}(p)$ can be calculated with equation II.1.

The mass of dissolved gas can thus be computed by plugging the result of equation II.5 into equation II.4. To compute the solubility of CO_2 in the polyol, we also need the dry mass polyol, m_{poly}. While we measured the polyol mass in the atmosphere beforehand, we expect that the polyol had absorbed some of the moisture from the humid, Neapolitan summertime atmosphere. We therefore solve equation II.3 for m_{poly}

$$m_{poly} = \Delta B(p = 0) - (m_{cruc} + m_{hook}) \tag{II.6}$$

and plug in the known difference in balance readings at zero pressure $\Delta B(p = 0)$ and mass of the crucible and supporting hooks $m_{cruc} + m_{hook}$ to compute the dry

polyol mass. Having computed the gas mass at the given pressure $m_{gas}(p)$ and dry polyol mass m_{poly}, we compute the solubility by mass of CO_2 in the polyol,

$$w_{CO2}(p) = \frac{m_{gas}(p)}{m_{gas}(p) + m_{poly}} \tag{II.7}$$

Next, we compute the specific volume of the sample, which is the sample volume $V_{samp}(p)$ divided by the sample mass $m_{samp}(p)$. Noting that the sum of the gas mass and dry polyol mass gives the sample mass $m_{samp}(p) = m_{gas}(p) + m_{poly}$, the specific volume is

$$v(p) = \frac{V_{samp}(p)}{m_{samp}(p)} \tag{II.8}$$

To estimate the diffusivity, we followed the model derived by Crank for diffusion into a slab [4]. The model considers an infinite slab of fluid with a concentration dependent diffusivity with thickness $2l$ and a gas atmosphere on both sides, as shown in Figure II.S2. In our case, the polyol sample is only open to the CO_2 atmosphere on one side. The situation is nevertheless analogous if we map the midpoint of the slab ($x = 0$) to the base of the crucible because there is no flux through either surface. We can therefore treat the top half of the slab in the model as our sample in the crucible, where the parameter $l = h_{samp}$, the height of our sample.
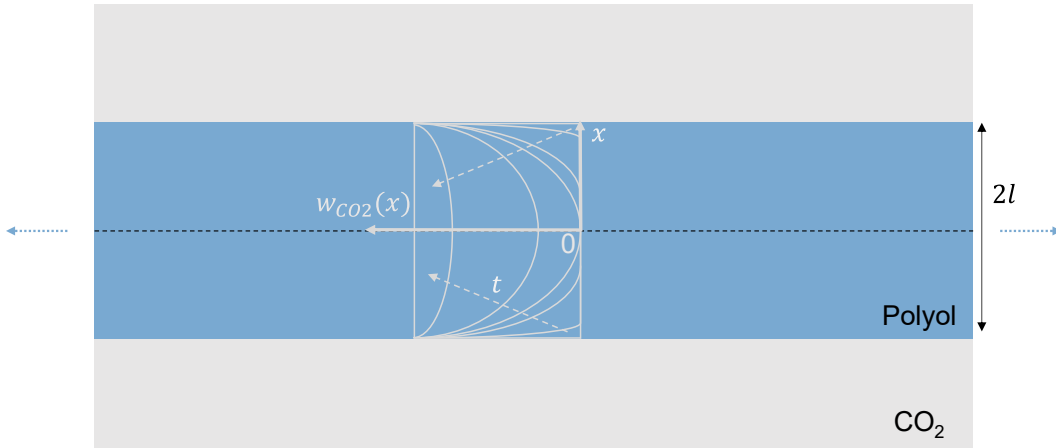
Figure II.S2: Schematic of diffusion of CO_2 (gray) into a slab of polyol (blue) with width l and infinite horizontal extent.

With this model, we can estimate the diffusivity of CO_2 as a function of the saturation pressure $\mathcal{D}(p)$ in the sample in two ways: (1) fit a square-root function to the mass of dissolved gas over time $m_{gas}(t)$ at early times and (2) fit an

exponential function to the mass of dissolved gas over time $m_{gas}(t)$ upon approaching equilibrium. While we used both to estimate the diffusivity, we generally used the first method (square root) due to better fitting of the data and lower sensitivity to noise. We begin by deriving the diffusivity from an early-time square-root fit. In the book *The Mathematics of Diffusion*, Crank derives the mass of dissolved gas over time at short times (see equation 4.20 on p. 48 of [4]). We adapt the notation of the equation below, where $m(t)$ corresponds to $m_{gas}(t)$, its value at infinity $m(t \to \infty)$ is the equilibrium value of the mass of dissolved gas, $m_{gas}(p)$, the diffusivity D is the diffusivity of CO_2 at the equilibrium pressure $\mathcal{D}(p)$, and the size parameter corresponds to the height of our sample $l = h_{samp}$, as mentioned earlier,

$$\frac{m_{gas}(t)}{m_{gas}(p)} = 2 \left(\frac{\mathcal{D}(p)t}{h_{samp}^2} \right)^{1/2} \left\{ \pi^{-1/2} + 2 \sum_{n=1}^{\infty} (-1)^n \operatorname{ierfc}\left(\frac{nh_{samp}}{\sqrt{\mathcal{D}(p)t}} \right) \right\} \tag{II.9}$$

where ierfc is the integral of the complementary error function and $\mathcal{D}$ is an average diffusivity in the material. Due to the complexity of deriving an accurate formula to average the diffusivity within the sample, we will keep the changes in pressure between measurements small enough so the diffusivity throughout the sample will be close to the diffusivity at equilibrium for the given pressure $\mathcal{D}(p)$. The results of this assumption are seen in Figure II.4, where the estimated diffusivity is larger during depressurization $\mathcal{D}_{dp}(p)$, when the diffusivity in the sample starts higher than the equilibrium value, than during pressurization $\mathcal{D}_p(p)$, when diffusivity in the sample starts lower than the equilibrium, *i.e.* $\mathcal{D}_p(p) < \mathcal{D}(p) < \mathcal{D}_{dp}(p)$. The errors incurred by applying large changes in pressure, especially during depressurization, can also be seen.

At short times $t \ll \frac{l^2}{\mathcal{D}}$, the terms in the summation are negligible, and we can simplify this equation to

$$\frac{m_{gas}(t)}{m_{gas}(p)} = \frac{2}{\sqrt{\pi}} \left(\frac{\mathcal{D}t}{l^2} \right)^{1/2} \tag{II.10}$$

If we assume that the swelling of the sample is negligible at short times, then the initial gradient of the mass of dissolved gas with respect to the square root of time $\frac{d}{d\sqrt{t}} \left(\frac{m_{gas}(t)}{m_{gas}(p)} \right) \Big|_{t=t_0} = \frac{2}{\sqrt{\pi}} \left(\frac{\mathcal{D}}{l^2} \right)^{1/2}$, where t_0 is the time at which the concentration of gas in the surrounding atmosphere is changed. Thus, the diffusivity of CO_2 at pressure p is

$$\mathcal{D}(p) = \frac{\pi h_{samp}^2}{4} \left[\frac{\mathrm{d}}{\mathrm{d}\sqrt{t}} \left(\frac{m_{gas}(t)}{m_{gas}(p)} \right) \Bigg|_{t=t_0} \right]^2 \qquad (\text{II.11})$$

Knowing that the mass of dissolved gas $m_{gas}(t)$ will grow as $t^{1/2}$ from equation II.10, we fit the measurement of dissolved gas over time, $m_{gas}(t)$, which can be calculated by noting that $m_{gas}(t)$ is $m_{gas}(p)$ computed at a moment in time rather than at the equilibrium pressure. Thus, we can compute $m_{gas}(t)$ using equation II.4 where measurements taken at the equilibrium pressure p are replaced measurements at a particular time t,

$$m_{gas}(t) = \Delta B(t) - \Delta B(p = 0) + \tilde{m}_{buoy}(t) \qquad (\text{II.12})$$

We fit $m_{gas}(t)$ to the function

$$m_{gas}(t) = a\sqrt{t - t_0} + m_{gas}(p_{prev}) \qquad (\text{II.13})$$

for positive real constants a, t_0, where $m_{gas}(p_{prev})$ is the mass of gas measured at the previous equilibrium pressure. We compared the quality of fit to the data of this function to three other fit functions: (1) equation II.13 where t_0 was specified as the time when the pressure was changed, (2) equation II.13 where t_0 was specified as in (1) but $m_{gas}(p_{prev})$ was a fitted parameter, and (3) equation II.13 where both t_0 and $m_{gas}(p_{prev})$ were fitted parameters. The form shown in equation II.13 yielded the best fits to the data, so we used it for fitting. An example fit to the transient sample mass is shown in Figure II.S3.

By fitting $m_{gas}(t)$ to a square-root growth in time, we find that the derivative we must compute in equation II.11 is $\frac{\mathrm{d}}{\mathrm{d}\sqrt{t}} m_{gas}(t) = a$, one of the fitting parameters in equation II.13. Therefore, our estimation for the diffusivity at a given pressure based on a square-root fit is

$$\mathcal{D}(p) = \frac{\pi h_{samp}^2}{4} \left(\frac{a}{m_{gas}(p)} \right)^2 \qquad (\text{II.14})$$

In some cases, we also use the exponential-fit method to estimate the diffusivity, such as when comparing to an estimate based on an exponential fit in the literature in Figure II.S10. Below, we describe the derivation of this estimation

method. This estimation method considers the latest stages of diffusion as the system approaches equilibrium. Crank demonstrates that the mass of a sample in an atmosphere of diffusing gas obeys the following equation (equation 10.168) [4],

$$\frac{\mathrm{d}}{\mathrm{d}t}\left[\log(m(t) - m(t \to \infty))\right] = -\frac{\mathcal{D}\pi^2}{4h_{samp}^2} \tag{II.15}$$

where we have substituted $2h_{samp}$ for the length scale l, which is the full width of the slab (rather than half the width) in this section of Crank's book. At late enough times, the concentration is close enough to the equilibrium value that the effect of the changing concentration in the system on the diffusion coefficient $\mathcal{D}(p)$ is negligible. Therefore, in this model, we assume that $\mathcal{D}(p)$ is constant and corresponds to the diffusion coefficient at the equilibrium concentration.

We then integrate equation II.15 to arrive at the following functional form for the mass of the sample,

$$m(t) - m(t \to \infty) = [m(t = 0) - m(t \to \infty)] \exp\left[-\frac{\mathcal{D}\pi^2}{4h_{samp}^2}t\right]$$

$$\frac{m(t \to \infty) - m(t)}{m(t \to \infty) - m(t = 0)} = \exp\left[-\frac{\mathcal{D}\pi^2}{4h_{samp}^2}t\right]$$

Note that, as opposed to the case for the $t^{1/2}$ fit, $m(t = 0)$ is the mass of the sample at the beginning of the exponential behavior (which we define as $t = 0$). We can then perform a fit of the mass of absorbed gas to the following functional form,

$$m(t) = A \exp\left[Bt\right] + C$$

where A, B, and C are fitting parameters. An example fit to the transient sample mass is shown in Figure II.S3. Then C is the equilibrium mass of absorbed gas $m(t \to \infty)$ and B can be related to the diffusion constant $\mathcal{D}$ by the following equation,

$$\mathcal{D} = -\frac{4h_{samp}^2}{\pi^2}B \tag{II.16}$$

giving the exponential-fit estimate of the diffusivity $\mathcal{D}$. Note that the change in h_{samp} during the course of a pressure step is negligible relative to the error in the fitted parameter B (at most 2%).

In practice, we only measure a range for $\mathcal{D}(p)$, with the measurement taken upon pressurization $\mathcal{D}_p(p)$ providing the lower bound and the measurement taken upon depressurization $\mathcal{D}_{dp}(p)$ providing the upper bound.
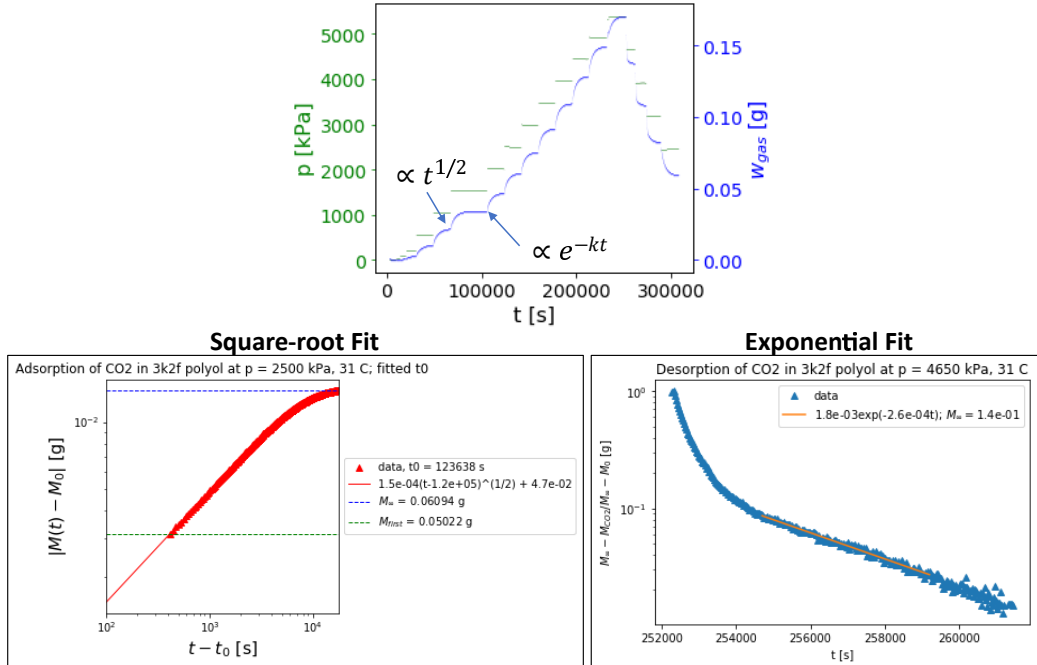
Figure II.S3: Plots of the transient mass absorption and desorption from the polyol–CO_2 sample over time. Polyol is PPG 2700 g/mol measured at 31.1 °C. Top: pressure (green, left vertical axis) and dissolved weight fraction of CO_2 (w_{gas}, blue, right vertical axis) as a function of time for a full G-ADSA experiment. Note that the initial transient of the weight fraction goes as the square root of time while the end of the transient nearing equilibrium goes as exponential decay. Lower left: an example fit of square-root function to the initial transient dissolved mass of CO_2 measured relative to the initial mass upon changing the pressure. Lower right: an example fit of exponential decay to the final transient dissolved mass of CO_2 measured relative to the estimated equilibrium mass. Fit parameters shown in legend.

Finally, we estimate the interfacial tension at a given pressure $\gamma(p)$ using axisymmetric drop shape analysis (ADSA) performed with the commercial software First Ten Angstroms 32 (FTA32). This software automatically detects the edge

of the drop and fits a contour consistent with the predictions for a pendant drop to the detected edge. When provided the density of the drop (reciprocal of the specific volume $1/v(p)$) and the density of the CO_2-rich atmosphere (estimated using the p-v-T data for pure CO_2 available from NIST[2]), the software computes the interfacial tension. To learn more about the pendant drop method and its estimation of interfacial tension, see the work of Song and Springer [5]. Because ADSA was performed using a camera separate from the Rubotherm MSB used for gravimetry, the two sets of measurements were synchronized to a common start time, thereby providing simultaneous measurements of each parameter.

Propagating Uncertainty in G-ADSA Measurements

To estimate the error bars shown in the plots of G-ADSA measurements, we propagated the uncertainty from all known sources of error through the analysis equations. These formulas are encoded in the `errprop.py` library of functions within the `andylitalo/g-adsa` GitHub repository [1].

Reproducibility of Results

In addition to being precise, measurements with G-ADSA are reproducible. We demonstrate their reproducibility in two ways. First, we show that the measurements made while pressurizing the system are generally statistically indistinguishable from those made while depressurizing the system—which may take place days later—with few exceptions. Second, we show that measurements from two separate experiments run under the same conditions are also generally statistically indistinguishable. We demonstrate this reproducibility using PPG (2700 g/mol) at $60\,^\circ$C in Figure II.S4 for the solubility of CO_2 (a), interfacial tension (b), and specific volume of the polyol-rich phase (c). For each property, the measurements made during pressurization (filled symbols) are statistically indistinguishable from those made during depressurization (open symbols), indicating that the measurements were taken near equilibrium, as desired. The one exception is the measurement of the interfacial tension at low pressures in trial 2, which was significantly lower during depressurization than during pressurization. The cause is most likely residual CO_2 because we depressurized the system in larger steps than those with which we pressurized the system, and the CO_2 solubility is slightly higher as well. Therefore, reaching equilibrium would take longer, but due to limited time, we could not always wait to reach equilibrium. The measurements from the two experiments (blue and magenta) are generally indistinguishable, especially those of the specific volume (c).

The primary exception is that the CO_2 solubility was measured to be slightly higher in trial 2 than in trial 1 at pressures above 2000 kPa, which may have resulted in slight variations in the preparation of the sample that were not accounted for in the uncertainty analysis.

II.S2 Estimate Effects of Temperature and Molecular Weight on CO_2 Solubility in 4.7-functional Polyol

In Figure II.5, the solubility of CO_2 in three polyols of similar molecular weight and different functionality is compared. While the CO_2 solubility appears to decrease with increased functionality (from 2f to 3f to 4.7f), the parameters of the measurement for the 4.7-functional polyol are not exactly the same, so a precise comparison cannot be made. Specifically, the 4.7-functional polyol is 25 % shorter than the others, having an average molecular weight of 728 g/mol rather than 1000 g/mol according to the manufacturer (Dow, Inc.). Additionally, the low-temperature measurement of the 4.7-functional polyol was performed at a lower temperature (25 °C) than was that of the other polyols (30.5 °C).

To distinguish the effect of functionality more clearly, we estimated the effects of molecular weight and temperature in this measurement, as shown in Figure II.5. The effect of temperature can be estimated using a PC-SAFT model, which was developed to model the branched structure of the 4.7-functional polyol. In this branched model, a new species is added to represent the hydroxyl end groups. These are given a high value of the ϵ parameter ($_{OH}$ = 265 k_B) than the backbone ϵ_{bb} = 259 k_B) to model the greater affinity of CO_2 to the backbone than the end groups noted in literature [6]. After fitting the model to the measurements of CO_2 solubility for the 4.7-functional polyol shown in Figure II.5, we used the model to estimate the solubility at 30.5 °C (yellow dashed line in Figure II.S5), which was lower than the solubility measured at 25 °C (yellow circles in Figure II.S5).

To estimate the effect of increasing the molecular weight of the 4.7-functional polyol from the true average value of 728 g/mol to the average value of the 2-functional and 3-functional polyols of 1000 g/mol, we could not use the PC-SAFT model because it does not account for the association of the hydroxyl end groups that leads to the non-monotonic dependence of CO_2 solubility on the molecular weight. Instead, we estimated the effect by extrapolating from the measured increase in Henry's constant based on the data for 2-functional polyols in Figure 3 of the main text, which is reproduced for convenience in Figure II.S6. In the Figure, Henry's
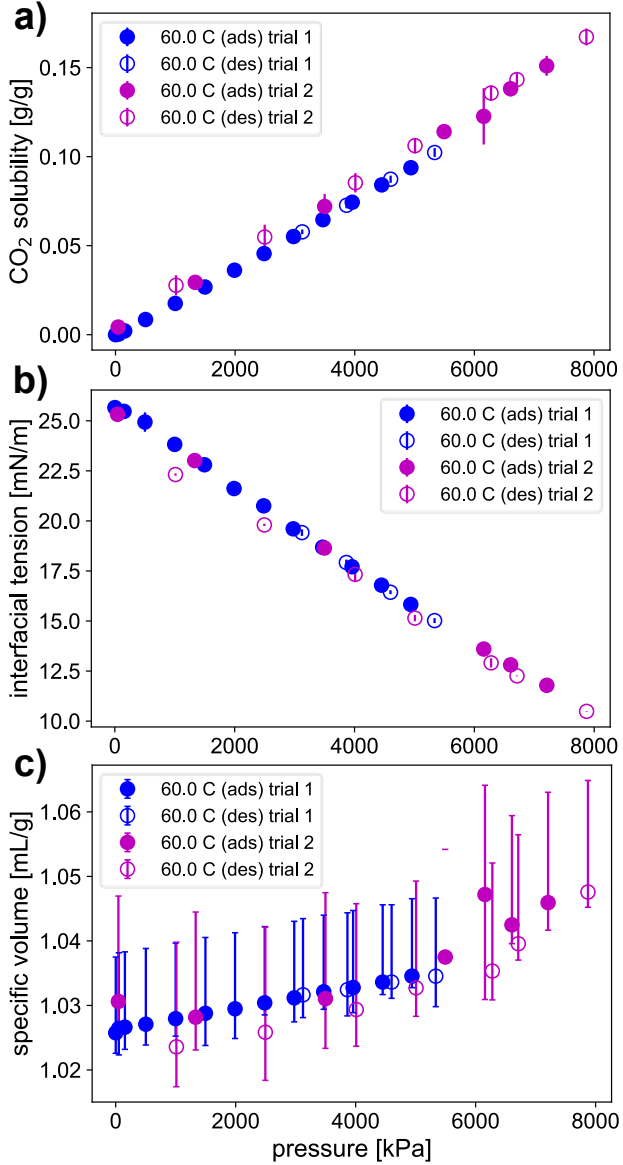
Figure II.S4: Measurements from two experiments of (a) the solubility of CO_2, (b) the interfacial tension, and (c) the specific volume of the polyol-rich phase for a mixture of CO_2 and PPG (2700 g/mol) at 60 °C. Measurements taken during pressurization (adsorption of CO_2) are shown with filled circles while those taken during depressurization (desorption of CO_2) are shown with open circle. The measurements taken from the first trial of the experiment are shown in blue and those taken from the second trial are shown in magenta. Error bars are shown, though they may be smaller than the symbol. In (c), the top error bar represents the systematic error of the experiment while the bottom error bar represents the statistical error of that particular measurement. Measurements are generally statistically indistinguishable, except for the solubility at high pressures and the interfacial tension at lower pressures between experiments.
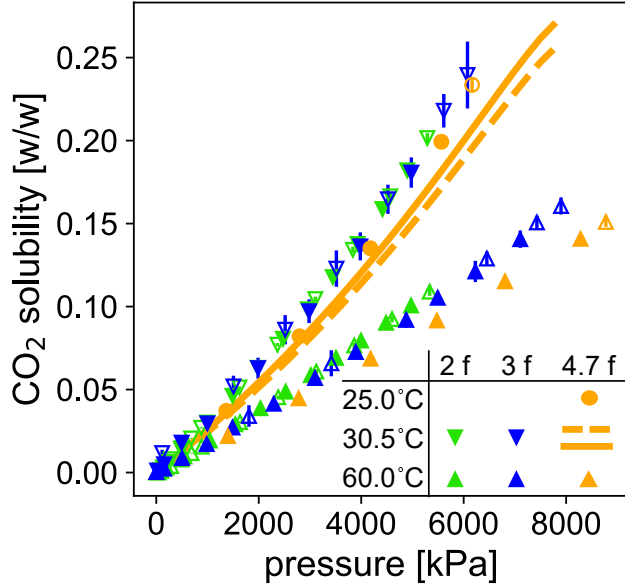
Figure II.S5: Reproduction of Figure II.5 from the main text showing the effect of functionality on the solubility of CO_2 in polyol, here with two estimates of the solubility in a 4.7-functional polyol. The first estimate uses a PC-SAFT model to estimate the effect of increasing the temperature from 25 °C (measurement shown in yellow circles) to 30.5 °C to match the temperature of the low-temperature measurements for the 2-functional and 3-functional polyols (yellow dashed line). The second estimate uses the effect of molecular weight on Henry's constant to estimate the effect of increasing the molecular weight from 728 g/mol (true value) to 1000 g/mol (value for the 2-functional and 3-functional polyols) on Henry's constant at 30 °C, as shown in Figure II.S6, and assumes that the CO_2 solubility would increase by the same fraction (solid yellow line).

constant increases from 0.0260 ± 0.0005 (w/w)/MPa at 400 g/mol to 0.028 ± 0.001 (w/w)/MPa at 1000 g/mol. While a linear interpolation may not be accurate due to the non-monotonicity, the downward concavity of the trendline means that any non-monotonicity would only reduce the increase in Henry's constant with molecular weight from 728 g/mol to 1000 g/mol because Henry's constant at 728 g/mol would be higher.

Therefore, to estimate the largest increase in Henry's constant with molecular weight consistent with the reported measurements, we use a linear interpolation from the lower end of the uncertainty in the measurement at 400 g/mol (0.0255 (w/w)/MPa) to the upper end of the uncertainty in the measurement at 1000 g/mol (0.029 (w/w)/MPa) to estimate a Henry's constant of 0.0274 (w/w)/MPa at 728 g/mol. This linear interpolation is shown in the zoomed-in section of the plot shown in the top of Figure II.S6. The increase in Henry's constant from 728 g/mol to 1000
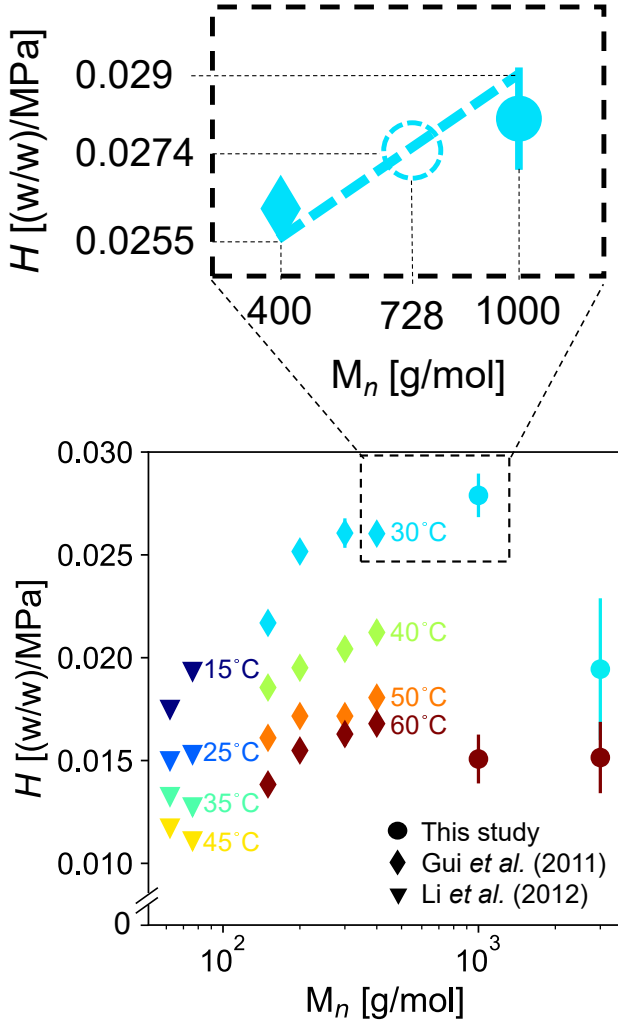
Figure II.S6: Figure II.7 is reproduced at the bottom, showing Henry's constant H in weight fraction of dissolved CO_2 per MPa as a function of number-averaged molecular weight M_n [g/mol]. At the top, the section of the plot used to estimate the effect of molecular weight on Henry's constant at 30 °C between 400 g/mol and 1000 g/mol is shown. As an upper bound on the estimate, the greatest slope within the experimental uncertainty is assumed (dashed blue line). The estimated Henry's constant at 728 g/mol, the molecular weight of the 1k5f polyol, is shown (blue dashed circle). The fractional increase in Henry's constant from 728 g/mol to 1000 g/mol for these 2-functional polyols is used as a rough estimate of the increase in the CO_2 solubility in the 1k5f polyol if its molecular weight were increased from its true value of 728 g/mol to 1000 g/mol. The coordinates of each point on the interpolation line are indicated by thin dashed gray lines.

g/mol would then at most be 0.0274 (w/w)/MPa to 0.029 (w/w)/MPa, which is an increase of 5.8 %. In Figure II.S5, we increased the solubility of CO_2 estimated by the PC-SAFT model at 30.5 °C (yellow dashed line) by 5.8 % as an estimate of

the solubility of CO_2 in a hypothetical 4.7-functional polyol of molecular weight 1000 g/mol at 30.5 °C. These are the identical temperature and molecular weight of the low-temperature measurements of CO_2 solubility in the 2-functional and 3-functional polyols. Even after accounting for the effects of the discrepancy in these parameters in the original measurements shown in Figure 1, we show that our observation that the solubility of CO_2 decrease with functionality still holds.

At 60 °C, the measurements in Figure 3 of the main text show that Henry's constant either stays constant or decreases with molecular weight between 400 g/mol and 1000 g/mol. Therefore, our observation that the solubility of CO_2 decreases with functionality at 60 °C is also still true after accounting for the discrepancy in the molecular weight.

II.S3 Comparison of G-ADSA Measurements to Literature

Here, we show measurements from G-ADSA alongside measurements of the same properties for the same polyols reported in the literature. In Figure II.S7, we compare the measurement of the CO_2 solubility of PPG (2700 g/mol) measured by G-ADSA in the present work and by Near-infrared (NIR) in the work of Guadagno and Kazarian [7]. We note that the solubilities measured with NIR are significantly lower than those measured by G-ADSA, despite the difference in temperature. We expect less statistical error from G-ADSA due to the higher number of measurements at each temperature and the agreement of two repeated experiments (the 60 °C data are combined from two indistinguishable sets of measurements), but we cannot comment on the possibility of unknown sources of systematic error between G-ADSA and the NIR method reported in the literature. Given that Guadagno and Kazarian declare their solubility measurements to be "consistent" with previously published values 30% higher than theirs, we assume that their experimental uncertainty is on the order of 30%. Within this uncertainty, our results are likewise consistent with theirs.

In Figure II.S8, we compare measurements of the solubility of CO_2 in a polyol (three hydroxyls per chain, 1000 g/mol, labeled SD301 in [8]) by G-ADSA from the present work and by a similar method reported by Yang *et al.* [8]. The discrepancy in these measurements is large, with G-ADSA measuring a significantly lower CO_2 solubility at 30.5 °C than Yang *et al.* measured at 35 °C, contrary to our expectation that solubility should decrease with temperature. Both methods use a magnetic suspension balance (Rubotherm) to measure weight and a pendant
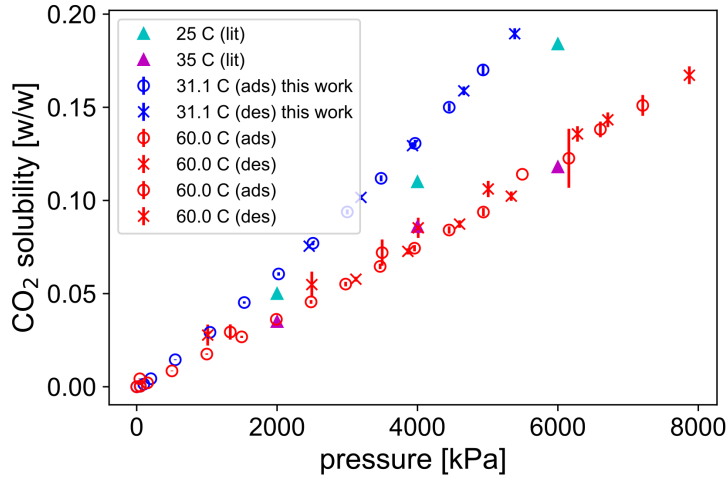
Figure II.S7: Solubility of CO_2 in PPG (2700 g/mol) measured by G-ADSA (○ - adsorption, × - desorption, labeled "this work" in the legend) at 31.1 °C (blue) and 60°C (red) and by FTIR at 25 °C (teal) and 35 °C (purple) by Guadagno and Kazarian [7] (filled triangles, labeled "lit" in the legend).

to measure the interfacial tension. They differ in their estimation of the swelling of the polyol: G-ADSA estimates the swelling by the change in the volume of the pendant drop (assuming axisymmetry) while the method by Yang *et al.* estimates the swelling by the change in the height of the polyol sample in a glass tube (ID = 5 mm). Yang *et al.* repeated their measurements three times, although they applied a much larger change in pressure (2 MPa) between measurements than was used in G-ADSA ($\approx$ 0.5 MPa) and did not perform measurements during depressurization. While Yang *et al.* reported their measurements of solubility in weight of CO_2 per weight of polyol [8], we have converted them to weight of CO_2 per weight of sample for comparison to our measurements. We cannot determine the cause for the significant discrepancy in our results.

We also compared our G-ADSA measurements of the specific volume of this polyol–CO_2 mixture. In this case, the specific volume reported by Yang *et al.* is over 15% higher than the values measured with G-ADSA in the present work. They did not provide a measurement at zero pressure, however, which could have been compared to the value reported in the chemical technical data sheet from Dow (specific gravity of 1.02 at 25 °C, *i.e.* specific volume of 0.98 mL/g). This reported value is consistent with our measurement of a specific volume near 1.00 mL/g at 30.5 °C given that the specific volume increases slightly with temperature. The values reported in the literature at 35 °C exceeded the higher specific volume measured at 60 °C by G-ADSA as well. While each study used a different method to measure
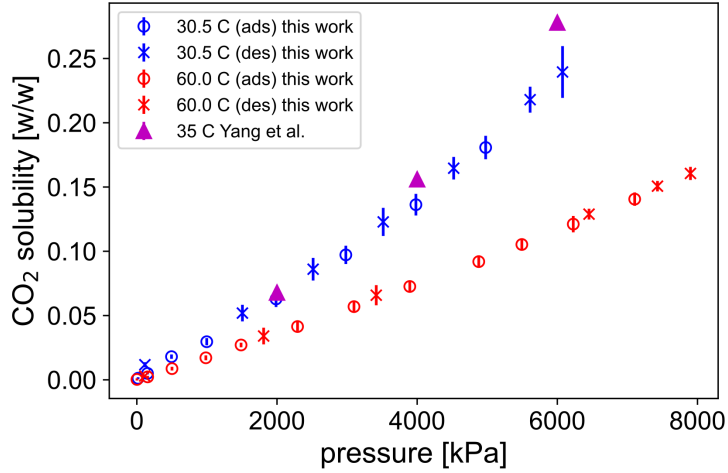
Figure II.S8: Solubility of CO_2 in polyol (three hydroxyls per chain, 1000 g/mol) as a function of pressure measured by G-ADSA and by a similar method reported by Yang *et al.* [8]. G-ADSA data were measured at 30.5 °C (blue) and 60 °C (red). Both adsorption (∘) and desorption (×) measurements are shown. Data from Yang *et al.* were measured at 35 °C (cyan filled triangles). Error bars are plotted but may be smaller than glyphs for some data points.

the volume of the sample, we cannot provide an explanation for their significant discrepancy.
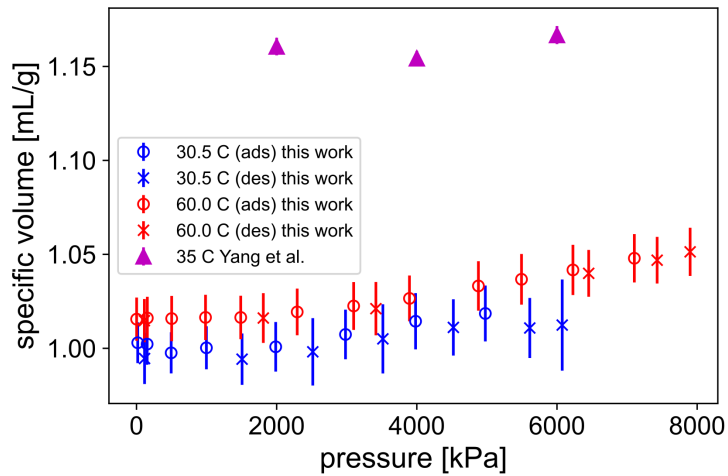
Figure II.S9: Specific volume of a mixture of CO_2 and polyol (three hydroxyls per chain, 1000 g/mol) as a function of pressure measured by G-ADSA and by a similar method reported by Yang *et al.* [8]. G-ADSA data were measured at 30.5 °C (blue) and 60 °C (red). Both adsorption (∘) and desorption (×) measurements are shown. Data from Yang *et al.* were measured at 35 °C (cyan filled triangles). Error bars are plotted but may be smaller than glyphs for some data points.

Next we compared our measurements of the diffusivity of CO_2 in this polyol

with G-ADSA to the measurement reported by Yang *et al.* Yang *et al.* estimated the diffusivity using an exponential fit, which we found to be consistent within uncertainty with the square-root fit method (for details on the fit methods, see Section II.S1). Both measurements report a similar power-law increase in diffusivity with pressure. Yang *et al.*, however, report a diffusivity about ten times larger than measured with G-ADSA. While their measurement was performed at a higher temperature (35 °C vs. 30.5 °C with G-ADSA), these diffusivities exceed even those measured at 60 °C by G-ADSA. Nevertheless, we see that an outlier of the G-ADSA data matches the literature data, but we have not explored the cause for this chance agreement.
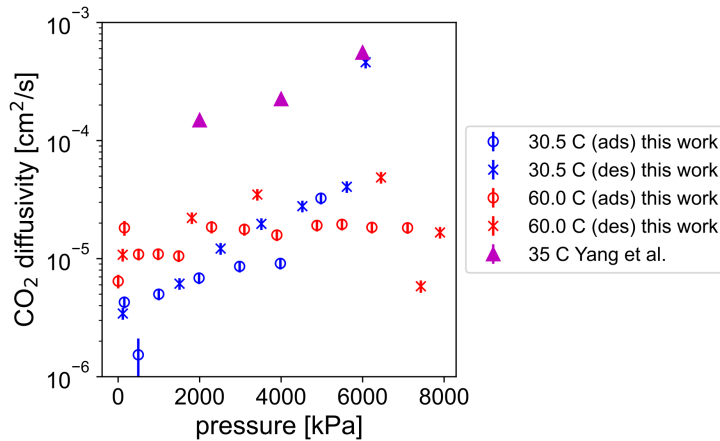
Figure II.S10: Diffusivity of CO_2 in polyol (three hydroxyls per chain, 1000 g/mol) as a function of pressure measured by G-ADSA and by a similar method reported by Yang *et al.* [8]. Both methods fit the transient mass of dissolved gas to an exponential function. G-ADSA data were measured at 30.5 °C (blue) and 60 °C (red). Both adsorption (○) and desorption (×) measurements are shown. Data from Yang *et al.* were measured at 35 °C (cyan filled triangles). Error bars are plotted but may be smaller than glyphs for some data points.

Last, we compare Henry's constant measured with G-ADSA to measurements for a variety of polyether polyols available in the literature in Figure II.S11. While the data have not been neatly collapsed, a general increase in Henry's constant with molecular weight is observed for $M_n <$ 1000 g/mol followed by a general decrease for $M_n >$ 1000 g/mol. In some studies, solubility data were not provided at low pressures (below 1000 kPa), so we estimated Henry's constant by the slope from the origin to solubility measurement at the lowest pressure.
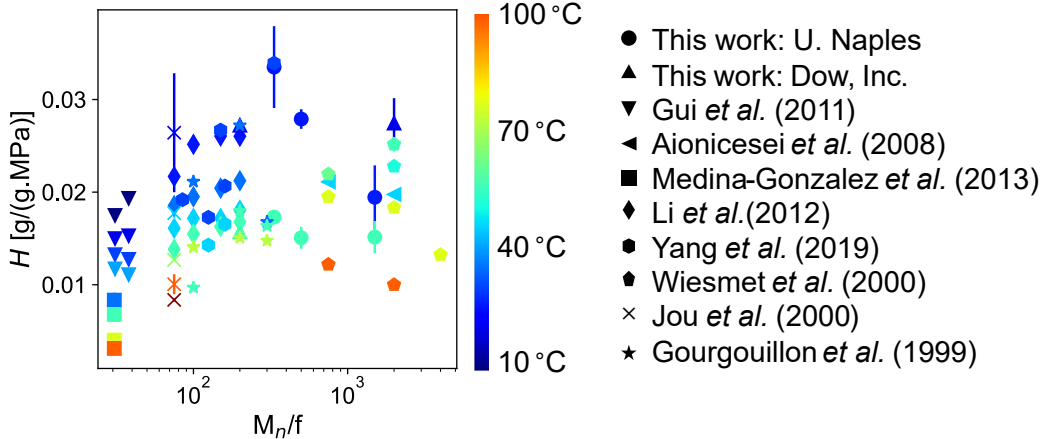
Figure II.S11: Henry's constant for CO_2 solubility in polyether polyols is plotted as a function of the average molecular weight. Both the data measured with G-ADSA in this study and literature data are provided. Error bars may be smaller than glyphs of some data points. Data are shown at different temperatures indicated by the color as defined in the legend.

II.S4   Sensitivity of PC-SAFT and DFT Models to Variations in Parameters

In Section II.4 of the main text, parameters of a PC-SAFT thermodynamic model of the equation of state of a binary mixture of CO_2 and PPG (2700 g/mol) were fit to CO_2 solubility measurements (see Figure II.9). These fitted parameters are reported in Table II.2. Because we fit these parameters through trial and error, we did not compute confidence intervals. Instead, we show the effect of ±5% variations in each of these parameters on the predictions of different properties made by the PC-SAFT (for specific volume and solubility) and corresponding DFT (for interfacial tension) models in Figure II.S12.

The properties of the polyol–CO_2 mixture are most sensitive to the polyol bead size σ, as seen in the left column of Figure II.S12. CO_2 solubility increases with bead size while interfacial tension decreases, in large part due to the increased concentration of dissolved CO_2. The specific volume increases with bead size since the molecular weight of each bead is kept the same, but interestingly the effect of pressure on the specific volume reverses. For small bead size (σ = 2.86 Å, blue line), the specific volume increases with pressure, while at large bead size (σ = 3.16 Å, red line), the specific volume decreases with pressure. Interestingly, the best quantitative agreement with the G-ADSA measurements is achieved with the large bead size, while the best qualitative agreement with the general increase in specific volume with pressure is achieved with the small bead size. We expect that a different model is needed to achieve both quantitative and qualitative agreement, likely one
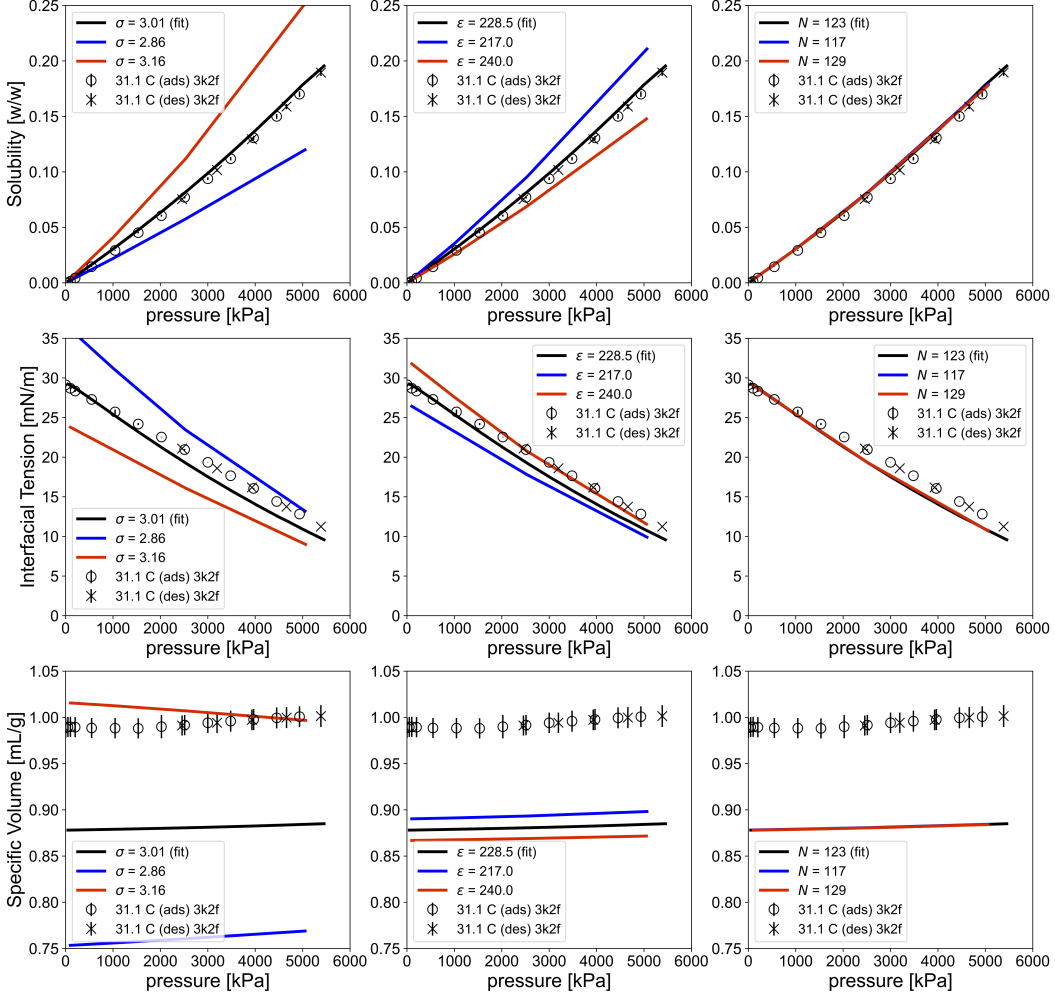
Figure II.S12: The sensitivity of the predictions of our PC-SAFT and DFT models to the polyol parameters σ (bead size, Angstroms, first column), ε (energy parameter, k_B, second column), and N (number of beads, third column) to +5% (red) and -5% (blue) variations about the fitted value (black) are plotted for the solubility of CO_2 (first row, PC-SAFT), interfacial tension (second row, DFT), and specific volume (third row, PC-SAFT) of a mixture of CO_2 and PPG (2700 g/mol). The G-ADSA data measured at 31.1 °C are shown in black (adsorption $\circ$ and desorption $\times$). Error bars may be smaller than glyphs for some data points.

that accounts for the association interactions of hydrogen bonding.

The effect of the polyol bead interaction strength ϵ on the polyol–CO_2 properties is smaller and opposite the effect of σ, as seen in the center column of Figure II.S12. Because their effects are opposite, ϵ can be varied to "cancel out" the effect of varying σ, such that the same predictions for solubility and interfacial tension are made for a degenerate set of pairs of σ and ϵ. The effect on specific volume is not entirely opposite, however, because varying ϵ has a negligible effect

on the qualitative behavior of the specific volume with pressure and the quantitative effect of varying σ is significantly more than that of varying ϵ. Consequently, within this degenerate set of pairs of σ and ϵ, the predictions for specific volume can be adjusted while those for solubility and interfacial tension remain the same.

Finally, the effect of the molecular weight is negligible on the scale of 5% variations, as seen in the far right column of Figure II.S12. The model predictions for each value of N are almost indistinguishable at the scale at which they are shown. We believe that the reason for the small size of the effect of N is that its primary contribution to the free energy comes into the translational entropy of the polymer, which is proportional to $1/N$. At $N = 123$, a 5% change in N yield a roughly 5% change in $1/N$, which is already small. We expect that a significant decrease in N would increase the translational entropy of the polymer and drive greater mixing, *i.e.* greater solubility of CO_2 given that the CO_2-phobicity of the hydroxyl end groups is not accounted for in this model.

Alternative Parameters Increase Predicted Specific Volume, Leave Solubility and Interfacial Tension Unchanged

Given that the PC-SAFT model grossly underestimated the specific volume (see Figure II.12), we explored other model parameters that deviated more from the predictions of the group contribution method [9]. We found that by increasing both bead size σ and the interaction energy ϵ in proportion, we could increase the estimate for the specific volume to be closer to the experimental measurement without changing the estimates for solubility or interfacial tension.

II.S5 DFT Predicts Non-monotonic CO_2 Concentration Profile

In the main text, we only discuss the interfacial tension along the vapor–liquid interface predicted by our DFT model. This interfacial tension is computed from a complete density profile along the interface. An example of such a density profile predicted by our DFT model is shown in Figure II.S14. The plot shows the concentrations of CO_2 and PPG (2700 g/mol) at the interface between the CO_2-rich (left) and polyol-rich (right) phases. Interestingly, the CO_2 partitions similarly in both phases but accumulates at the interface. Such behavior is reminiscent of a surfactant and suggests that CO_2 may condense at the surface of bubbles that form at high pressure to mediate the drastic change in density from polyol-rich liquid to CO_2-rich vapor. This non-monotonic density profile of the volatile component was predicted with DFT for a binary mixture of liquid and gas by Talanquer and Oxtoby
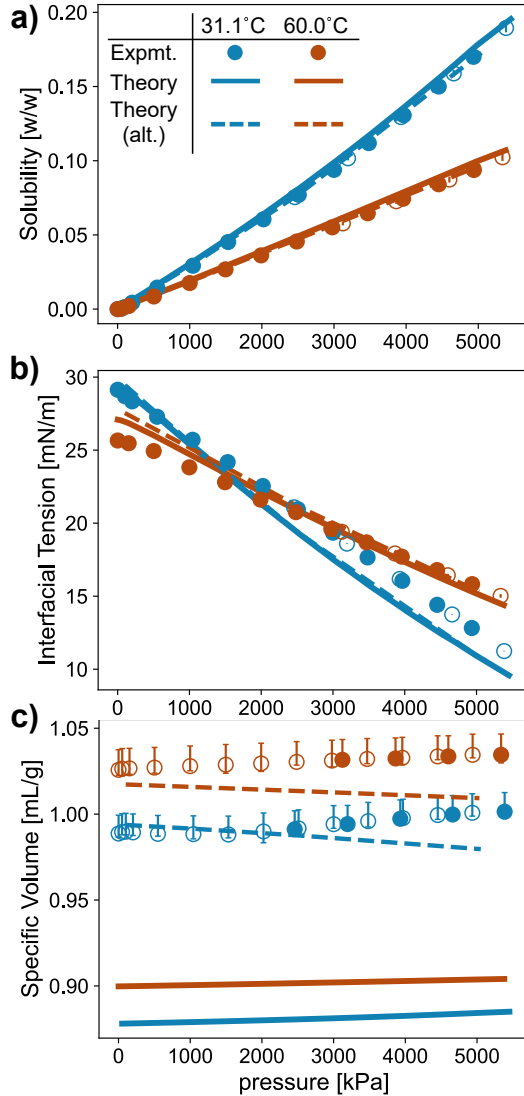
Figure II.S13: The agreement between the PC-SAFT model and measurements of a mixture of CO_2 and 2700 g/mol PPG is shown for two sets of PC-SAFT parameters. The predictions of the model using the parameters listed in Table II.2 is plotted in solid lines. The predictions of the model using $\sigma = 3.17$ Åand $\epsilon = 253$ k_B for the polyol (same N value) are shown with dashed lines (alternative theory). Data are plotted as a function of pressure [kPa] for two temperatures, 31.1 °C (blue) and 60 ° (red). a) Solubility of CO_2 [w/w] in polyol. b) Interfacial tension between polyol-rich and CO_2-rich phases [mN/m]. c) Specific volume of polyol-rich phase. The models are identical except in their prediction of the specific volume, for which the model represented by the solid line accurately models the qualitative trend but is inaccurate quantitatively while the model represented by the dashed line (alternative) is more quantitatively accurate but predicts the opposite qualitative trend with pressure.

[10] as well as for a binary mixture of CO_2 and PMMA [11–13] and CO_2 and P(MMA-*co*-EA) copolymer [14]. Talanquer and Oxtoby attribute the decrease in

the interfacial tension with pressure predicted by DFT (see Fig. II.11) to the increase in the amount of this enrichment of the volatile component along the liquid–vapor interface.
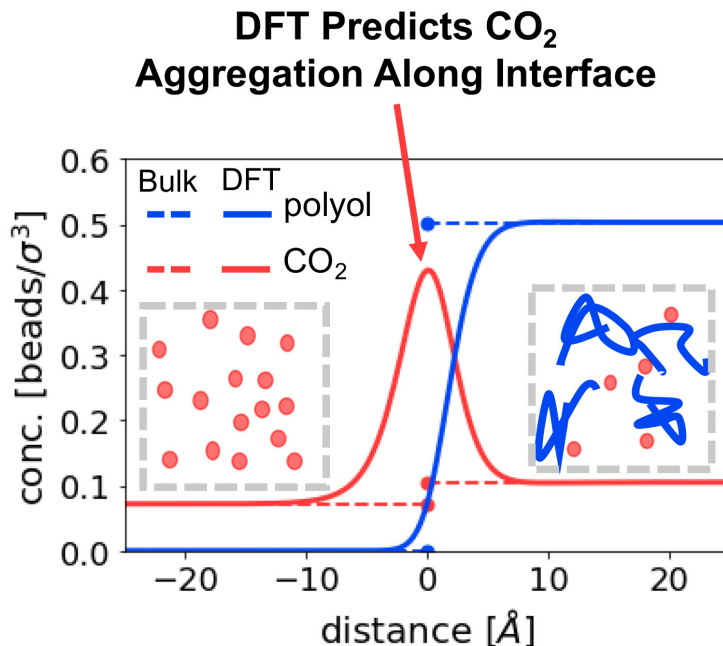
Figure II.S14: Density profiles of CO_2 and PPG (2700 g/mol) at the interface between CO_2-rich (< 100 Å) and polyol-rich (> 100 Å) phases at 5 MPa and 31 °C. Note that CO_2 has a similar partitioning in both phases but accumulates at the interface.

References

1. Ylitalo, A. S. *andylitalo/g-adsa: v0.1.0* 2022. https://github.com/andylitalo/g-adsa (2022).

2. NIST. *NIST Standard Reference Database Number 69* 2022. https://webbook.nist.gov/chemistry/ (2022).

3. Pastore Carbone, M. G., Di Maio, E., Iannace, S. & Mensitieri, G. Simultaneous experimental evaluation of solubility, diffusivity, interfacial tension and specific volume of polymer/gas solutions. *Polymer Testing* **30,** 303–309. ISSN: 01429418. https://linkinghub.elsevier.com/retrieve/pii/S0142941811000067 (May 2011).

4. Crank, J. *The Mathematics of Diffusion* 2nd Ed., 1–352 (Oxford University Press, London, 1975).

5. Song, B. & Springer, J. Determination of interfacial tension from the profile of a pendant drop using computer-aided image processing. *Journal of Colloid and Interface Science* **184,** 64–76. ISSN: 00219797 (1996).

6. Parks, K. L. & Beckman, E. J. Generation of microcellular polyurethane foams via polymerization in carbon dioxide. I: Phase behavior of polyurethane precursors. *Polymer Engineering & Science* **36,** 2404–2416. ISSN: 0032-3888. https://onlinelibrary.wiley.com/doi/10.1002/pen.10639 (Oct. 1996).

7. Guadagno, T. & Kazarian, S. G. High-Pressure CO 2 -Expanded Solvents: Simultaneous Measurement of CO 2 Sorption and Swelling of Liquid Polymers with in-Situ Near-IR Spectroscopy. *The Journal of Physical Chemistry B* **108,** 13995–13999. ISSN: 1520-6106. https://pubs.acs.org/doi/abs/10.1021/jp0481097%20https://pubs.acs.org/doi/10.1021/jp0481097 (Sept. 2004).

8. Yang, Z. *et al.* Effect of the properties of polyether polyol on sorption behaviour and interfacial tension of polyol/CO2 solutions under high pressure condition. *The Journal of Chemical Thermodynamics* **133,** 29–36. ISSN: 00219614. https://linkinghub.elsevier.com/retrieve/pii/S0021961419300643 (June 2019).

9. Tihic, A., Kontogeorgis, G. M., von Solms, N., Michelsen, M. L. & Constantinou, L. A Predictive Group-Contribution Simplified PC-SAFT Equation of State: Application to Polymer Systems. *Industrial & Engineering Chemistry Research* **47,** 5092–5101. ISSN: 0888-5885. https://pubs.acs.org/doi/10.1021/ie0710768 (Aug. 2008).

10. Talanquer, V. & Oxtoby, D. W. Nucleation of bubbles in binary fluids. *The Journal of Chemical Physics* **102,** 2156–2164. ISSN: 0021-9606. http://aip.scitation.org/toc/jcp/102/5%20http://aip.scitation.org/doi/10.1063/1.468737 (Feb. 1995).

11. Xu, X., Cristancho, D. E., Costeux, S. & Wang, Z.-G. Bubble nucleation in polymer–CO2 mixtures. *Soft Matter* **9,** 9675. ISSN: 1744-683X. www.rsc.org/softmatter%20http://xlink.rsc.org/?DOI=c3sm51477c (2013).

12. Xu, X., Cristancho, D. E., Costeux, S. & Wang, Z.-G. Density-functional theory for polymer-carbon dioxide mixtures: A perturbed-chain SAFT approach. *The Journal of Chemical Physics* **137,** 054902. ISSN: 0021-9606. http://aip.scitation.org/doi/10.1063/1.4742346 (Aug. 2012).

13. Xu, X., Cristancho, D. E., Costeux, S. & Wang, Z.-G. Discontinuous Bubble Nucleation Due to a Metastable Condensation Transition in Polymer–CO2 Mixtures. *The Journal of Physical Chemistry Letters* **4,** 1639–1643. http://pubs.acs.org/doi/10.1021/jz4005575 (May 2013).

14. Xu, X., Cristancho, D. E., Costeux, S. & Wang, Z.-G. Density-Functional Theory for Mixtures of AB Random Copolymer and CO 2. *Macromolecules* **48,** 6035–6046. ISSN: 0024-9297. https://pubs.acs.org/doi/10.1021/acs.macromol.5b01122 (Aug. 2015).

Chapter III

A Bubble Is Born (Nucleated): Microfluidic Flow Focusing Reveals Early Stages of Bubble Growth

> Time and space are modes by
> which we think and not conditions
> in which we live.

<div align="right">Albert Einstein</div>

The idea to use flow-focusing was first proposed by Prof. Julie Kornfield. The idea to perform flow-focusing with a capillary-based microfluidic device came from a chance lunch-time discussion with Prof. Stuart Prescott (UNSW, Australia). Dr. Orland Bateman led initial development of an acrylic-sheet microfluidic channel and assisted with the development of the final capillary-based design. Dr. Thomas Fitzgibbons (Dow) suggested the use of PEEK sleeves to maintain a high-pressure seal around the observation capillary. Dr. Valerie Scott was instrumental in loaning us the ISCO 260D high-pressure syringe pump from the Jet Propulsion Laboratory (NASA). Steve Weigand (Argonne) designed and set up the experiment to test the signal from SAXS.

While Chapter II focuses on the mother phase of polymer with dissolved CO_2, this Chapter and those that follow focus on the bubbles born by this mother phase upon reducing the pressure. If the pressure is reduced enough, bubbles may be born without the assistance of a surface by homogeneous nucleation, as discussed in Chapter I. Experimental measurements of homogeneous bubble nucleation in polymers have been limited by its stochasticity in space and time, its rapid depletion of dissolved gas, and the difficulty of eliminating heterogeneous nucleation, however. Here, we describe our experimental method for overcoming these challenges with a custom microfluidic channel and high-speed optical microscopy. To mitigate stochasticity in space, we localize supersaturation near the centerline of flow through a channel in a custom high-pressure (> 10 MPa) microfluidic flow-focusing apparatus. Due to the roughly linear decrease in pressure with distance from the inlet, there is a range of axial positions at which the supersaturation is sufficient to drive homogeneous bubble nucleation. We mitigate stochasticity in time by observing

those positions where homogeneous nucleation occurs often enough to detect many bubbles (several per second) and rarely enough that bubbles can be studied individually. Previously, it was thought that the stochasticity of bubble nucleation posed a fundamental limitation that "[did] not lend itself [nucleation] to generating large amounts of reliable, tightly bunched data" [1]. Because the flow is continuously replenished, we can observe bubble nucleation at a specific degree of supersaturation for as long as desired (at least, for several hours), making possible the generation of such data and overcoming the challenge of rapid depletion of dissolved gas by homogeneous bubble nucleation. Finally, the apparatus isolates the nucleating stream within a sheath of pure polymer, which prevents heterogeneous nucleation along walls (although there is still a possibility of small particles in the nucleating stream).

Although we designed the microfluidic channel for compatibility with small-angle X-ray scattering (SAXS) and light scattering, we determined that high-speed optical microscopy would offer the richest data source; the possibilities of measuring bubble nucleation with SAXS and light scattering are discussed in Section III.S6 of the Supplementary Information. Due to the diffraction limit of light, optical microscopy can only detect the early growth of bubbles larger than about 1 μm, whereas nucleated bubbles may be as small as 10 nm. Therefore, the method described in this Chapter does not directly observe bubble nucleation. How we fit a model to the observable period of bubble growth and use it to extrapolate the growth backward in time to the moment of nucleation is discussed in Chapter V.

III.1 Studying Homogeneous Bubble Nucleation: Challenges and Solutions

Have you ever seen something just as it disappeared? A shooting star? A bolt of lightning? Short, stochastic events like these can be as frustrating as they are fascinating. Because they are stochastic, we do not know where and when to look; because they are sudden, they disappear as soon as we do.

Single-Shot Studies of Bubble Nucleation Are Cluttered and Tedious

Homogeneous bubble nucleation is one such short, stochastic event. Techniques with the spatial resolution to distinguish nanoscopic bubble nuclei, such as small-angle X-ray scattering (SAXS) [2] or scanning electron microscopy (SEM) [3–20], lack the time resolution to capture them live, only reporting measurements of bubbles in a solidified matrix. Techniques that could achieve sub-microsecond time resolution to capture the nucleation event, such as optical microscopy of batch foaming [3, 9, 11, 14, 19, 21–34], lack the spatial resolution to distinguish the

nucleation event itself, only reporting micron-scale images of the early growth. As discussed in Section I.4, this dilemma has prevented direct experimental observation and quantification of homogeneous bubble nucleation, leaving us uncertain of the validity of the theoretical models available. The problem is further exacerbated by the rapid depletion of dissolved gas by homogeneous bubble nucleation relative to heterogeneous bubble nucleation due to the presence of nucleation throughout the bulk. Due to this challenge, measurements of homogeneous bubble nucleation in the literature are performed in batch processes and, therefore, require new sample preparation for each measurement, slowing down data acquisition. Measurement of homogeneous bubble nucleation also requires an exceptional degree of cleanliness and isolation from surfaces to prevent heterogeneous bubble nucleation from depleting the dissolved gas before homogeneous bubble nucleation is possible.

Nevertheless, given the challenges of direct observation, researchers have learned a tremendous amount about effects on bubble nucleation from indirect observations. Among the most common indirect observation methods is SEM analysis of the cell structure after foaming. While SEM achieves high spatial resolution, it is limited to analysis of the cells of the final solidified foam, using the number of cells as an estimate of the number of nucleation events despite the coalescence and ripening of bubbles during foaming. By counting cell number and size distribution of foams with SEM, researchers have elucidated how bubble nucleation is affected by photopolymerization [14], the addition of nucleant particles like talc [16], the rate of depressurization [15], wall effects [11], formulation [11], polymer glass transition temperature [4], polymer branching architecture [17], two-stage foaming [13], and polymer crystallization from the melt [7].

Other researchers have sought more direct observation at the expense of spatial resolution, observing the nucleation of bubbles upon depressurization of polymer–gas mixture in high-pressure cells with high-speed microscopy, which can capture bubble growth on the micron spatial resolution and millisecond time resolution. These batch foaming experiments, many of which were based on the apparatus designed by Guo *et al.* [21], have uncovered how bubble nucleation is affected by photopolymerization [14], depressurization rate [27], shear [29], extensional stretching [19, 20, 30], polymer crystallization [28, 30, 33], foaming agents (sodium bicarbonate [34], talc [19], and nano-clays [35]), temperature [33], physical blowing agent (*e.g.*, CO_2 [3, 9, 22, 24], N_2 [24], hydrocarbons like cyclopentane [3, 9], pentane [36], and isopentane [37], and alcohols [22]), wall effects [11], for-

mulation [11], and melt retraction [25]. While microscopy studies are limited to a two-dimensional field of view by significant light scattering from bubble surfaces, a study by Perez-Tamarit *et al.* acquired three-dimensional scans of early bubble growth during polyurethane foaming with X-ray tomography at a synchrotron X-ray source, which they used to study the nucleating effect of nanoparticles [38]. Scattering likewise probes a three-dimensional volume of the foam and allows for the estimation of the bubble size distribution, as demonstrated with Mie scattering [39], diffusing wave spectroscopy [11], and small-angle X-ray scattering [2], but the latter typically requires too long of acquisition times (seconds) to study nucleation directly.

Although the studies above have provided tremendous insight into bubble nucleation in polymer foaming, they are performed in batches, often requiring a waiting period to dissolve CO_2 into a highly viscous polymer sample to prepare for foaming [40]. Ando *et al.* offered an elegant method for repeated homogeneous nucleation of bubbles by local heating with a laser [41]. The heated region nucleates a single bubble in the bulk and quickly returns to equilibrium afterward for another measurement. This technique has not been applied to polymer foams, however. Within the context of polymer foaming, Tsujimura *et al.*, and later, Taki *et al.*, developed transparent, high-pressure continuous flow cells for observing the onset of foaming of polymer–gas solutions as it flowed through a channel between two thinly spaced glass plates [27, 42, 43] or in an injection molding cell [44]. Because the foaming fluid is in contact with the glass plates, however, much of the nucleation was likely heterogeneous along the glass surfaces, leading to a non-uniform foaming front and preventing study of homogeneous bubble nucleation due to the higher level of supersaturation that it requires.

Turning Time into Space

Almost all the studies discussed above suffer from the same dilemma between time resolution and spatial resolution; those that do not suffer from parasitic heterogeneous nucleation. This dilemma only exists for short, stochastic patterns in time; in space, we can thoroughly scrutinize short (in length), stochastic patterns like Turing patterns and glasses as long as we want. Is there a way to map a time sequence onto space to permit thorough scrutiny as well?

Novice jazz musicians like myself have long grappled with the same problem, particularly when studying "bebop." Only the most talented of musicians can

decipher a "lick" from this style of mid-century jazz known for its rebelliously fast tempos and unpredictable patterns [45]. Record it onto a vinyl disk, however, and even the novice can pick out the notes by slowing down playback and looping each section in her quest to play like the pros; the sudden and stochastic becomes intelligible.

Such a mapping of time onto space naturally exists for heterogeneous bubble nucleation, for which bubbles are continuously nucleated at the nucleation site with little effect on the bulk concentration. The bubbles then rise at a predictable velocity due to their buoyancy, allowing the observer to correlate each position to a point in the bubble's lifetime (see Figure I.2b). On the contrary, homogeneous bubble nucleation quickly depletes the bulk of excess dissolved gas necessary for further nucleation.

At the turn of the millennium, the Austin group demonstrated how to put kinetics "on repeat" with a microfluidic technique they called "flow-focusing" [46, 47]. The technique flows a fluid stream of interest inside another fluid stream, often studying the kinetics of reactions occurring along their interfaces. Due to the microscopic dimensions of their channels, the Reynolds number *Re* remained in the laminar regime despite low viscosities and high speed, so the fluid flowed along straight streamlines and maintained a constant speed [48]. Constant flow speed allowed the researchers to correlate the time that particular portion of protein was in contact with the buffer to the distance it had traveled along the channel by dividing that distance by the speed. The researchers could then scrutinize each millisecond in the timeline of the protein-folding kinetics for long periods of time by observing the corresponding location along the length of the capillary, allowing for observation with techniques that require long exposure times, such as small-angle X-ray scattering (SAXS) [47]. The design of similar devices took off as the fabrication of precise microfluidic channels polydimethylsiloxane (PDMS) with photolithography became more widely available [49] due to its small sample-size requirements and laminar flow. Unlike the original devices produced by the Austin group, focused on generating an unperturbed interface between nearly identical fluids, many of the devices that followed considered unlike fluids with an interfacial tension, such as oil and water. Even a small amount of interfacial tension drives the rapid formation of droplets due to the Plateau–Rayleigh instability [48]. The resulting droplet-based devices permitted the observation of millisecond-scale kinetics of processes like gelation [50], enzymatic reaction[51], and ice nucleation [52], often leveraging the

unique mixing behavior of droplets [53].

High-pressure Microfluidics

Due to the permeability of PDMS, experiments with these devices must be maintained near atmospheric pressure; an experiment performed at 50 psi is already considered "high pressure" [54]. The study of homogeneous bubble nucleation requires significantly higher pressures, however, both to achieve sufficient supersaturation and, in the case of polymer foams, to pump highly viscous fluids through microscopic channels. High-pressure microfluidics therefore faces its own dilemma: how does one design a design (1) strong enough to withstand high pressure (MPa-scale) and (2) transparent enough to allow optical observation? Glass and silicon became materials of choice due to their high pressure resistance (up to 40 MPa), compatibility with photolithography to etch precise microfluidic channels, and high optical transparency [55, 56]. To connect glass and silicon chips to laboratory devices while maintaining high pressures and small dead volumes, pressure-resistant connections from these chips to pumps and sampling devices were developed, some designing custom fittings [57, 58] and others adapting existing fittings [59]. To provide high pressure with precise flow control, these devices use high-pressure syringe pumps, such as those produced by Teledyne ISCO. Nevertheless, etching glass microfluidics requires a budget and resources not available outside dedicated microfluidics or photolithography labs.

An alternative, more accessible method for high-pressure microfluidics is capillary-based microfluidics, which flow fluids through capillary tubes instead of etched channels. Utada *et al.* initially pioneered the use of tapered microcapillaries to flow one fluid inside a sheath of another fluid, which we will refer to as "sheath flow" [60]. Marre *et al.* adapted this coflow microcapillary device to ensheath supercritical CO_2 with water at high pressure (8–18 MPa) [61], which was later modified to operate at higher temperatures and pressures [62]. Although the capillary walls are thin, the interior surface area is also smaller, reducing the force applied to the wall material, such that defect-free silica capillaries can withstand tens of MPa in pressure [63]. Leakage is most common at the connections between capillaries and other parts of the microfluidic device. Standard compression fittings such as Swagelok or VICI Valco fittings cannot be applied directly to silica due to its brittleness. Many methods for sealing these connections to withstand pressures over 10 MPa have been demonstrated in the literature, but most require irreversible chemical bonding [64, 65]. Some groups have achieved high pressure with remov-

able fittings. Maharrey and Miller reached pressures as high as 28 MPa using HPLC stainless steel compression fittings on a quartz capillary ensheathed by a polyether ether ketone (PEEK) sleeve [66]. Luther and Braeuer reported a pressure tolerance of 8.5 MPa for a connection between fused silica capillary epoxied in a sleeve and a reusable stainless steel port-connector [63]. Chen-Jolly *et al.* demonstrated that high pressures can be maintained in flexible perfluoroalkoxy (PFA) tubing in a slightly larger, millimeter-scale device [67].

III.2 High-pressure Microfluidic Hydrodynamic Focusing Localizes Supersaturation in Space and Time

By combining concepts from flow-focusing and high-pressure capillary microfluidics, we developed a continuous-flow microfluidic channel to observe homogeneous nucleation and early growth of gas bubbles in the polymer during rapid depressurization from industrially Trelevant pressures (about 10 MPa). Unlike many other capillary-based flow-focusing devices in the literature, which flow unlike fluids and thus generate droplets [68, 69], we consider fluids with sufficiently low interfacial tension and with high enough viscosities to suppress the breakup of the inner stream into droplets. We begin with a discussion of how the design of the apparatus produces sheath flow, followed by a discussion of its implications for the pressure along the flow and its role in localizing bubble nucleation. We then describe our fabrication method and some of the limitations of the device that were overcome by a careful balance of the operational parameters. We close this chapter with a discussion of the high-speed optical microscopy setup with which we captured the early bubble growth, whose measurement and modeling we will discuss in Chapters IV and V, respectively.

Flow-focusing Principle

One of the primary motivations behind flow-focusing is to surround the flow of the fluid of interest with a sheath of another fluid, isolating it from the inner walls of the flow channel. The microfluidic dimensions of the channels maintain this "sheath flow" throughout the apparatus. A schematic of the apparatus, expected flow, and principle behind taking measurements is shown in Figure III.1. An example validation of sheath flow is shown in Figure III.S2.

In capillary-based flow focusing [63, 68, 69], sheath flow is produced inside a tee junction by enveloping a capillary that extends across the tee junction (the "inner capillary") with the outer fluid before entering a transparent capillary for making
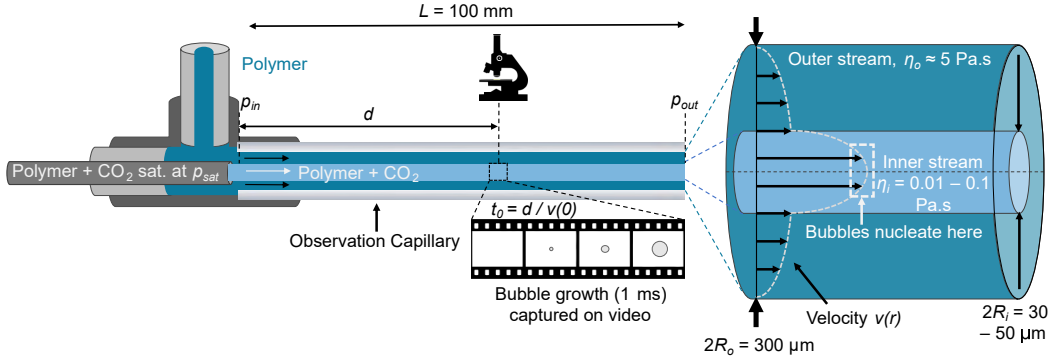
Figure III.1: Schematic of capillary microfluidic flow-focusing and flow profile for mapping timeline of kinetic process along length of a transparent capillary. Polymer with dissolved gas (CO_2) passes through a tee junction inside a narrow inner capillary to the entrance of the transparent observation capillary. Pure polymer enters through the top of the tee junction and ensheaths the inner stream before entering the observation capillary. Because of the high viscosities (up to 5 Pa.s) and narrow dimensions (300 μm inner diameter of observation capilary, 30–50 μm inner stream), the Reynolds number $Re < 10$, so the flow is laminar and the miscible inner and outer streams flow along straight streamlines with minimal mixing. On the right, the velocity profile predicted from Stokes flow is shown, with a higher velocity gradient in the inner stream due to the lower viscosity. Due to the loss of dissolved gas to the outer stream along the interface of the inner stream from diffusion, nucleation is most likely at the center, where the concentration of CO_2 is highest. The speed at the center $v(r = 0)$ is consistent and stable, so the time for a fluid element at the center to reach a distance d along the observation capillary is $t_0 = d/v(0)$. A microscope or other imaging device (eye schematic) can observe that location to watch the subsequent ≈ 1 ms of bubble growth immediately after t_0. By translating along the length L (100 mm), the average bubble behavior from the inlet pressure p_{in} to the outlet pressure p_{out} can be imaged. See Figure III.2 for the estimated pressure profile.

observations (the "observation capillary"), as shown schematically in Figure III.1. During operation of the instrument, a polymer–gas mixture flows from the left of the diagram through the inner capillary to the right end of the tee junction, where it exits the inner capillary near the entrance of the observation capillary. We considered mixtures of polyol and CO_2, but bubble nucleation could be studied in other viscous liquid–gas mixtures as well. Meanwhile, pure polymer flows from the top of the diagram around the inner capillary before flowing to the right into the observation capillary, where it ensheaths the polymer–gas mixture. At this point, the fluid pressure is p_{in}, which we kept at least 10% higher than the saturation pressure of the dissolved CO_2 p_{sat} to prevent heterogeneous bubble nucleation along the inside surface of the inner capillary. Once ensheathed, the inner stream is isolated from

the inside surface of the observation capillary, preventing heterogeneous nucleation (unless a solid contaminant enters the flow—see the discussion of this problem in Chapter VI). This sheath flow continues 100 mm to the end of the observation capillary where it reaches the outlet pressure p_{out}, which we kept at atmospheric pressure. Unlike droplet-based microfluidics [53], the inner and outer streams here are miscible, having the same composition besides a small fraction of gas in the inner stream. Given that we will show that the flow is laminar as well, the interface between them remains unperturbed in the absence of bubbles, only diffusing a small amount of gas a few microns into the outer stream.

In comparison to many microfluidic devices, the inner diameter of our observation capillary is large (300 μm) and the flow speeds are fast (up to 1 m/s), but the flow remains laminar due to the high viscosity of the outer stream polymer and the narrow dimension of the inner stream (30–50 μm), as shown in the flow diagram on the right of Figure III.1. We show that the flow is laminar by estimating the Reynolds number for the inner and outer streams, which have different flow due to the significantly lower viscosity of the inner stream as a result of the dissolved CO_2. The Reynolds number is defined as $Re = \frac{\rho U L}{\eta}$ for fluid density ρ, speed U, length scale L, and viscosity η. For the outer stream, $\rho \approx 1000$ kg/m^3, $U < 0.5$ m/s, $L = 300$ μm (ID of observation capillary), and $\eta \approx 5$ Pa.s (see polyol "1k5f" in Table II.1), yielding $Re < 0.1$, indicating Stokes flow ($Re \ll 1$). For the inner stream, $\rho \approx 1000$ kg/m^3, $U \approx 1$ m/s, $L < 50$ μm, and $\eta > 0.01$ Pa.s, yielding $Re < 5$, indicating laminar ($Re \ll 2000$) but not Stokes flow. While the inner stream may not always be in the Stokes flow regime, we assume Stokes flow and note that the polymers are Newtonian (see Figure III.S1 in the SI for measurement of viscosity in a shear rate sweep) to estimate the velocity profile as a function of the radial coordinate $v(r)$. This velocity profile is depicted in Figure III.1 and is similar to Poiseuille flow with a steepened gradient at the center due to the lower viscosity; see Section III.S1 for the derivation. While the velocity gradient is steep near the surface of the inner stream, bubbles generally nucleate at the center of the inner stream, where the velocity gradient is smallest, due to the loss of CO_2 to the outer stream along the edges. Consequently, when we observe a bubble nucleate at the center of the stream, we can estimate the time since that fluid element entered the observation capillary by dividing the distance d from the entrance of the observation capillary by the velocity at the center stream $v(0)$, giving $t_0 = d/v(0)$. The distance along the capillary therefore maps directly onto the timeline of the flow. We then capture around 1 ms of the growth of the bubble on high-speed video as it travels along the

field of view of our microscope, as discussed later in this Section. Once bubbles nucleate downstream, however, the viscosity drops significantly and the flow is no longer completely laminar.

Due to the small dimensions, the flow rates can be kept below 300 μL/min for the outer stream and 100 μL/min for the inner stream, such that a few hundred milliliters of fluid was sufficient for a full day of experiments.

Pressure

Relative to previous high-pressure capillary microfluidics [63], the fluid undergoes a steep pressure gradient along the observation capillary (about 100 MPa/m over 100 ms). This rapid rise in supersaturation of the dissolved gas drives a significant increase in the rate of homogeneous bubble nucleation over the range of our translation stage. Because of the high supersaturation required for homogeneous nucleation, we can set up experimental conditions under which bubbles do not nucleate before reaching the last third of the observation capillary. Most of the flow is thus bubble-free and, as discussed earlier, remains in or near the Stokes flow regime. Because the polymers are Newtonian (Section III.S1), we assume a roughly constant pressure gradient along most of the observation capillary, an example of which is shown in Figure III.2.

In this example experiment, CO_2 was dissolved into the polyol for the inner stream at a pressure of 7 MPa, just below the critical pressure (7.39 MPa [70]). The flow rates were chosen to keep the pressure at the inlet higher, p_{in} = 10 MPa, and prevent nucleation of bubbles along the walls of the inner capillary. Assuming a constant pressure gradient, we estimate the pressure profile with the plot in the lower half of the figure along the 100 mm length of the observation capillary. The polymer–CO_2 mixture remains below the saturation pressure for the first 30 mm, so no homogeneous bubble nucleation is observed. After, the pressure in the channel drops below the saturation pressure, supersaturating the solution. Because homogeneous nucleation requires high degrees of supersaturation, we do not observe bubbles until about 70 mm downstream, where the pressure is about 3 MPa. Within the field of view (about 1 mm), we observe a bubble grow to the width of the inner stream. The change in pressure during this growth is about 0.1 MPa, a decrease of about 3%, so we conclude that most of the growth is the result of the diffusion of CO_2 into the bubble rather than expansion of the gas due to the decreasing pressure (although we account for this change in pressure in our model of bubble growth in
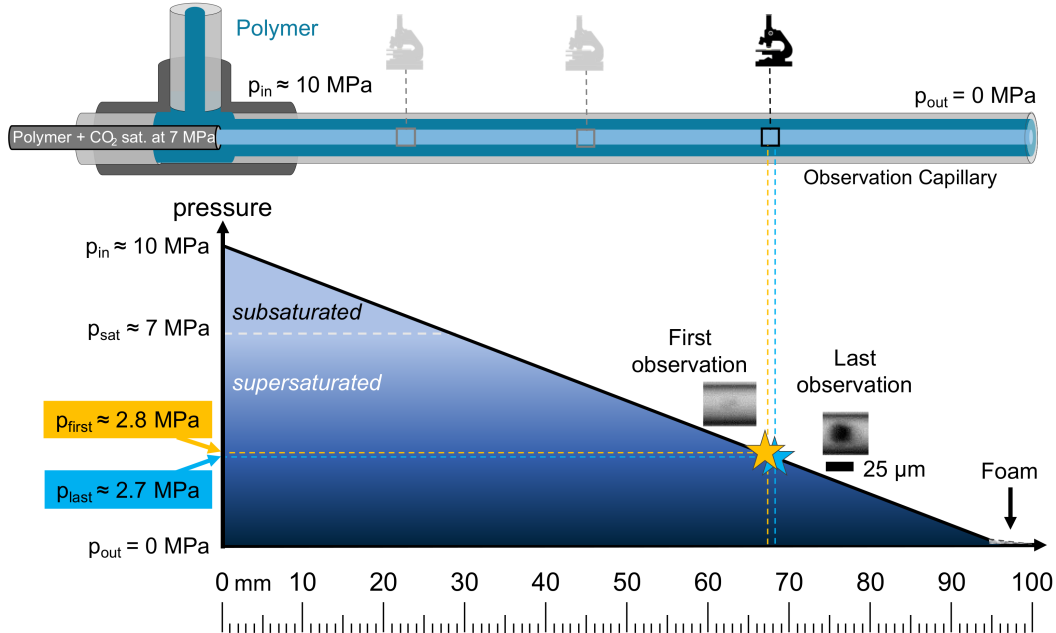
Figure III.2: Schematic of the pressure profile along the microfluidic capillary described in Figure III.1. In this example experiment, CO_2 is dissolved in polyol at a saturation pressure p_{sat} = 7 MPa. The inlet to the observation capillary is kept at a higher pressure (p_{in} = 10 MPa) to prevent heterogeneous bubble nucleation along the interior of the inner capillary before sheath flow. Because the fluids are Newtonian before bubbles nucleate (see Figure III.S1), we assume a constant pressure gradient. When a considerable number of bubbles has nucleated and produced a foam near the end of the capillary, the pressure gradient decreases signficantly and we can no longer assume Newtonian behavior. The estimated pressure profile is shown in the bottom plot. The fluid is subsaturated (light blue region) near the entrance of the observation capillary; bubbles are not observed (gray eye schematic). Once supersaturated (dark blue region), bubbles are not observed until reaching high supersaturation (black eye schematic), in this case, at p_{first} = 3 MPa (yellow star). The bubble can be observed over a field of view of about 1 mm, such that the pressure at the last observation has dropped only to p_{last} = 2.9 MPa (blue star). The distance along the observation capillary is shown at the bottom.

Chapter V). Near the end of the observation capillary, bubbles have grown large enough and nucleation is frequent enough that the inner stream becomes a foam. The location of this transition depends on the flow rates and concentration of CO_2 and can be varied anywhere along the observation capillary. Due to the significant reduction in viscosity upon foaming, we expect a significantly smaller pressure gradient here. This lower pressure gradient results in an error in our estimation of the internal pressure of the capillary. This error is usually on the order of only a few percent for most of the capillary, so we generally ignore this effect.

Device Fabrication

After exploring several designs to implement this flow-focusing principle (see Section III.S5 in the SI for their descriptions), we found the most success and simplicity with a design based on a tee junction machined out of a block of acrylic (see Figure III.S4 in the SI for dimensions). A digital image of the instrument built with this design mounted in a red, 3D-printed polylactic acid (PLA) case is shown in Figure III.3. The image at the top shows the inner and outer streams entering through stainless steel tubing (Restek 316 stainless steel tubing #27768, 1/16" OD, 0.040" ID) into the acrylic tee junction and meeting just before (to the left of) the entrance of the observation capillary (outlined in a white solid line). Due to the high viscosity of the outer stream, we did not insert the inner stream capillary into the observation capillary, as is done in some capillary devices for a more robust sheath [68, 69], which would have added significant pressure resistance at the entrance of the observation capillary. Rather, we extended the inner stream tubing with a small capillary (800 μm OD, 500 μm ID, Cynken #CKS1824, 304 stainless steel) that spanned across the entrance of the outer stream up to 1 mm from the entrance of the observation capillary, which we attached with silver epoxy. While the inner stream flowed slightly off center (see example snapshots in Figure III.3 due to the imprecision of this technique and the one-sided flow from the outer stream (better designs include flow from two sides [47] but require an additional pump), it was simple to assemble.

To withstand the high pressures inside the acrylic tee junction (up to 15 MPa), we connected the tubing to the tee junction with VICI Valco nuts and ferrules (316 stainless steel, 1/16", nuts #ZN1-10, and ferrules #ZF1S6-10). While they are rated to 10,000 psi (about 70 MPa) when used in stainless steel fittings, they permitted a gradual leak after about an hour of 10 MPa flow in the acrylic tee junction. This leak could have been prevented by epoxying the fittings into the acrylic, albeit at the expense of removability. Although the acrylic tee junction tolerated the high pressure as well, it showed some cloudiness from stress (seen faintly along its internal channels in Figure III.3). Additionally, the outer stream eventually indented a small cusp in the opposing wall (not seen in Figure III.3). We did not observe any effects on the flow as a result of these changes, however.

Because the observation capillary was too brittle to apply the VICI Valco ferrule directly, we inserted it into a hollowed-out extreme-pressure PEEK sleeve (McMaster Carr #51085K48, 1/16" OD, 0.03" ID) before applying the ferrule.
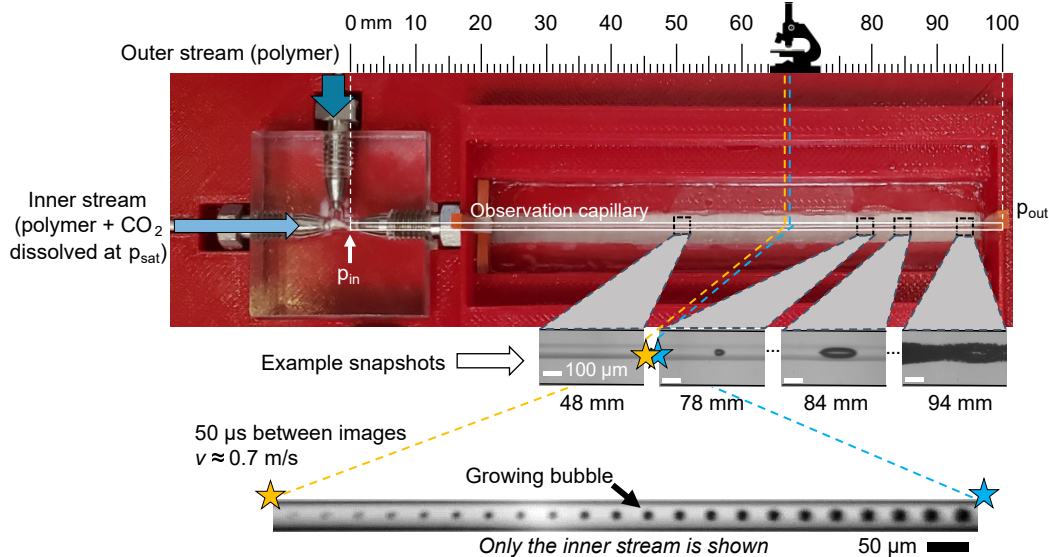
Figure III.3: Image of custom microfluidic capillary and acrylic tee junction in red 3D-printed microscope mount. A polymer–CO_2 mixture saturated at pressure p_{sat} enters from the left (light blue arrow) and travels through a narrow inner capillary to the entrance of the observation capillary (outlined in white). Pure polymer enters through the top (dark blue arrow) and ensheaths the inner capillary and inner stream of polymer–CO_2. This sheath flow enters the 100 mm observation capillary at pressure $p_{in} > p_{sat}$ and exits at p_{out}, atmospheric pressure. Behind the observation capillary is a transparent acrylic sheet that forms the base of an oil reservoir that reduces lensing from the curved surfaces of the observation capillary. The edges of the reservoir are sealed with orange silicone rubber at the left and right ends of the observation capillary. Micrographs taken at different points along the observation capillary (corresponding to different times and pressures) are shown below the image, showing how the inner stream (48 mm) nucleates bubbles (78 mm) that grow (84 mm) and ultimately generate a foam (94 mm). A set of collated images of bubble growth captured with a high-speed microscopy between 67 (yellow star) and 68 mm (blue star) is shown at the bottom (inner stream only).

While the literature recommends epoxying this PEEK sleeve onto the capillary [63, 71], we did not find epoxy necessary if the sleeve fit snugly, *i.e.* if the PEEK sleeve did not slide when the capillary was held vertically. Even with the PEEK sleeve, other compression fittings like Swagelok apply too much compression and fracture the capillary. The VICI Valco ferrule is unique in that it has a rim along the interior of the thinner end that "chomps" into the PEEK sleeve, providing a pressure-resistant fitting with less strain on the capillary. A similar technique has been used to observe underwater microbes at pressures relevant to the bottom of the ocean [71].

The observation capillary must withstand high internal pressure (up to 15

MPa) and light handling and have high optical transparency. We considered borosil-icate (Pyrex) and fused quartz due to their optical transparency, high flexural and tensile strength, and the availability of precision-manufactured capillaries. We suc-cessfully performed foaming experiments with an inexpensive borosilicate (Pyrex) observation capillary (Friedrich & Dimmock, Inc. #B100-50-100, ID = 500 μm, OD = 1000 μm); see Section III.S4 of the SI for estimation of the pressure rat-ings of these capillaries. Nevertheless, maintaining flow speeds near our target of 1 m/s under common operating conditions was easier with an inner diameter of 300 μm. We could only find fused quartz capillaries at that dimension (Molex #TSNC3001000/100, 300 μm ID, 1000 μm OD), although at almost one hundred times the cost, so we used them for the experiments discussed in this manuscript. Fused quartz also allows for compatibility with both X-ray scattering, because it is relatively featureless in the SAXS regime, and near-infrared imaging, due to rea-sonable transmission of wavelengths up to 3000 nm. We also tested PFA tubing for the observation capillary but found that it was too cloudy for precise optical measurement.

While the observation capillary is optically transparent, its curved inner and outer surfaces sharply refract much of the transmitted light, leaving all but the center portion of the flow dark. To prevent the refraction that causes lensing, index-matched material must fill in the curved surface such that light only passes between media of different indices of refraction orthogonal to the interface. The polyols tested (see Table II.1) have indices of refraction between 1.46–1.48, similar to the index of refraction of both borosilicate (1.47) and fused quartz (1.46). Therefore, the outer stream fluid will prevent lensing from the inner surface of the capillary. To prevent lensing from the outer surface, we submerge the observation capillary in Wesson vegetable oil, often used to turn borosilicate test tubes "invisible" due to its identical index of refraction (1.47) [72]. In Figure III.3, the oil (not shown) is contained in a reservoir between the orange strips of silicone rubber seen near the ends of the observation capillary and above a thin sheet of acrylic sealed with epoxy (not visible). Because the small silicone rubber seals at the extreme ends of the observation capillary are removable, they slowly leak oil, so oil must be replenished periodically during experiments. Refilling a reservoir with vegetable oil can be messy and tedious, so we also developed a technique for encasing the observation capillary in a square capillary filled with UV-cured optical adhesive (146H Norland optical adhesive, Edmund Optics #12-864), which we describe in Section III.S5 of the SI. This technique was prone to entrapping bubbles in optical

adhesive before curing and the accumulation of optical artifacts on the exterior of the square capillary, so we preferred the oil bath.

The red plastic mount for the microfluidic channel in Figure III.3 was 3D-printed from PLA using a CraftBot 3D printer at the Caltech Sherman Fairchild Library's TechLab. CAD designs can be found in the accompanying data in `data/3_bubble_birth/device_design/mf_mount.stl`. The bottom of the mount was designed to fit snugly around the translating fixture on the microscope translation stage (Zeiss #473356-9901). For added stability, the mount contains four cubbies along the location of this metallic fixture for 8 mm × 8 mm × 8 mm NdFeB magnets to provide a magnetic connection. A long ramp at the outlet of the observation capillary funnels waste away from the outlet into a waste container beyond the translation stage.

At four distances along the observation capillary, snapshots of the flow taken with high-speed optical microscopy are shown marked with their distance from the inlet. In each case, the inner walls of the observation capillary are highlighted with a solid black line. The inner stream of polymer–CO_2 is clearly visible due to the lower index of refraction than the pure polymer outer stream, which causes a slight lensing effect. Farther along the capillary, the flow transitions from laminar (48 mm) to rare bubble nucleation (78 mm) to elongated bubbles (84 mm) to frequent nucleation and flow instabilities (94 mm). Within the field of view of the microscope of about 1 mm, we can watch the early growth of just-nucleated bubbles, an example of which is shown around 67 mm at the bottom of the figure (only the inner stream is shown). The first and last images are the same as those shown for the first and last bubble observations shown in Figure III.2.

Not shown in Figure III.3 are the two high-pressure syringe pumps, Teledyne ISCO 100DM and ISCO 260D, which pumped the inner and outer streams, respectively. These pumps had enough capacity for hours of continuous operation at 50 μL/min and 300 μL/min (ISCO 100DM: 103 mL, ISCO 260D: 266 mL), provided precise, pulseless flow (ISCO 100DM: 0.3% of setpoint, ISCO 260D: 0.5% of setpoint), and were rated to pressures well beyond our requirements (ISCO 100DM: 69.5 MPa, ISCO 260D: 51.7 MPa). We connected these pumps to 1/16" ball valves (Swagelok #SS-41GS2) with rigid 304 stainless steel extreme-pressure tubing (McMaster Carr #51755K11) connected to the pumps by an internal reducing ferrule and nut (Valco Instruments #IZR21T). The rigid tubing could break from too much flexing, so we stabilized those connections with steel clamps. We filled

the ISCO 260D with pure polymer through wider, 3/32" inner diameter, 1/8" outer diameter nylon tube (Grainger #2VKT5) connected to the pump by a 1/8" ball valve (Swagelok #SS-41GS2), a high-pressure 1/8" OD tube (FreelinWade #1A-280-10, 0.073" ID), and 1/8" VICI Valco fitting (Valco Instruments, ferrule #ZF2S6-10 and nut #ZN2-10). The wider inner diameter was chosen to permit a faster refill rate of the viscous outer-stream polymer ("1k5f" in Table II.1).

While the pumps are expensive and the machining of the acrylic block must be precise, this microfluidic flow-focusing device offers a uniquely modular design allowing for use with a variety of different pumps, fluids, and observation capillaries to find the best for a given application.

Limitations

While this apparatus can provide unprecedented time resolution in measurements of early bubble growth in polymer foams, these design choices come at a cost that limits its measurement capabilities. Like all apparatuses, this apparatus operates best in a particular parameter range, which is discussed in greater depth in Section III.S2 of the SI. Outside this parameter range, certain assumptions about the flow are no longer valid. For example, if the viscosity difference between the inner and outer streams is too high, the interface may become unstable, as demonstrated in Section VIII.4. If the flow is too slow, whether due to high viscosity, a narrow observation capillary, or a low flow rate, the gas dissolved in the inner stream will diffuse into the outer stream, leading to a heterogeneous and low concentration profile of gas near the exit, where bubbles tend to nucleate.

Even inside the optimal parameter range, the apparatus does not always provide steady, consistent flow. As large bubbles grow and exit the observation capillary, they alter the effective length over which the pressure decreases to the outlet pressure because they cannot sustain a pressure gradient. These fluctuations in the pressure have little effect on the flow near the entrance, but near the exit, they can dramatically alter the local pressure and, consequently, the bubble nucleation and growth rates. The fluctuations can be so large near the exit that they can drive sudden, large-scale nucleation events, as shown in Figure VIII.S2. The limitations on the size of the inner stream (see Section III.S2 in the SI) place a fixed maximum size to which a bubble can grow before it is perturbed by the outer stream. Bubble growth measurements beyond this size no longer represent growth in an isotropic medium. When bubbles grow beyond this size, they elongate, speed up, and generate

significant convective currents along their sides and behind their tails, producing a wake that affects the growth of bubbles within it, as discussed in Section VIII.2. Near the exit, enough bubbles growth to a large enough size that they overlap and interact strongly, leading to complex behavior and flow instabilities. At this point in the observation capillary, much of the surrounding fluid is depleted of CO_2 by bubbles or by diffusion into the outer stream. Additionally, the large number and sizes of bubbles often results in bubble–bubble interactions, opacity of the inner stream, and uncertainty in our estimation of the internal pressure. For these reasons, we exclude these measurements from our discussions of bubble nucleation and growth.

III.3   High-speed Optical Microscopy Captures Early Bubble Growth

Initially, we intended to detect bubble nucleation directly with small-angle X-ray scattering (SAXS), which detects features on the scale of bubble nucleation (1–100 nm) [73], and light scattering, which can detect features much smaller than the wavelength of the scattered light [74]. We estimated the signal we would detect using SAXS by measuring the signal-to-noise ratio from various concentrations of nanoparticle solutions, but found that the signal from bubble nucleation in our apparatus would likely be too faint for reliable estimation of the nucleation rate, which we discuss in Section III.S6 of the SI. Light scattering could provide a signal for sub-micron bubble nuclei, but because the difference in index of refraction between the inner and outer stream would distort the scattering pattern from the bubble, we were not confident that we could accurately measure the object size or distinguish bubbles from debris; our suggestions for a light-scattering experiment to count the frequency of bubbles is discussed in Section III.S6 in the SI. We instead chose to use high-speed optical microscopy to capture the early bubble growth. Because optical microscopy is limited by the diffraction limit of light, it cannot detect bubble nucleation. Nevertheless, it can capture images of the early growth with high time resolution (20–50 μs), which we use to extrapolate the nucleation time with a model of bubble growth in Chapter V. Here, we describe the high-speed optical setup we developed to capture these images.

Microscope

We used a Zeiss optical microscope with a revolving nosepiece and objective lenses with magnifications of 4x, 10x, and 20x. See Table III.1 for their properties.

We found that these lenses allowed us to observe coarsely over a large field of view (4x) and finely over a small field of view (20x). Lower magnification

Magnification	NA	Res. @ 550 nm [μm]	WD [μm]	Corrections
4x	0.10	2.75	55.5	Plan
10x	0.22	1.25	10	None
20x	0.40	0.69	5.8	MSPlan ULWD

Table III.1: Table of properties of the objective lenses used in this study, classified by magnification. NA is the numerical aperture. Res. @ 550 nm is the spatial resolution of 550 nm light. WD is the working distance. "ULWD" stands for ultra-long working distance.

would likely be unable to discern bubbles narrower than the inner stream, and higher magnification would not be able to span the entire inner stream (and would have too small a working distance and depth of field to capture bubbles in focus). We used a translation stage (Zeiss, #473356-9901) to translate the microfluidic channel for viewing different points along the observation capillary. A condenser with an adjustable aperture (Zeiss, #465267) allowed us to balance brightness and contrast depending on the numerical apertures of the different objectives. The light source was collimated below the microscope and reflected upward through a field diaphragm before reaching the condenser.

Lighting

The key to successful high-speed imaging is bright, steady lighting. Bright lights are plentiful, but most rely on the high power provided by power outlets. Because this electricity is AC, the resulting light flickers noticeably under high-speed imaging. Until recently, halogen lamps powered by high-voltage DC power supplies provided the brightest, most stable microscope light sources. Due to their low cost, we began this project using such a light source, powering a 400 W halogen lamp (Osram HLX Xenophot EVD 36 V 400 W #64663) with a 30 V, 10 A power source purchased from eBay. At full power (400 W), this light was advertised to reach a brightness of 16 kilolumens (klm). Because we operated the light at about 80% power with our limited power source, we expect it produced a brightness of about 12 klm, most of which was radiated in directions not captured by the microscope. Furthermore, the halogen light source grew dangerously hot after extended use.

Nowadays, LED light sources provide brighter light with less heat than halogen sources, though they cost significantly more. For the experiments presented in this manuscript, we used a 3.3 W, 70 klm LED (ThorLabs, cool-white SOLIS-1C), which never caused a heat hazard. Its brightness could damage the eye, however, so we covered all eyepieces during experimentation and wore tinted safety glasses

while adjusting the lighting.

High-speed Camera

When purchasing a high-speed camera, the best camera provides a high-quality image with a high record rate and short transfer time. A high-quality image detects images over a high dynamic range with minimal readout noise. In light-starved applications, the dynamic range is best utilized by sensitive CMOS sensors with a high quantum efficiency (electrons generated per incident photon). A high record rate includes both a high frame rate and a high pixel count, and is measured in frames per second at 1 MP resolution. For a short transfer time, current state-of-the-art high-speed cameras use 10 Gb/s ethernet cables, either directly to a hard drive or connected through a Thunderbolt adapter—USB is not fast enough. The transfer protocol can usually be optimized significantly through adjustments to the software settings.

To accomplish these goals, we used a Photron Nova S6 (6400 fps @ 1 MP, 64 GB). This camera also allowed us to reach sub-microsecond exposures for use with the 20x objective, for which each pixel spanned less than 1 μm. While the camera recorded in 12-bit images, we typically compressed to 8-bit images for use with standard 8-bit image-processing methods (see Chapter IV for further discussion).

Experimental Setup

Briefly, we describe our procedure for saturating the polymer with CO_2 at high pressure, transferring the polymer–CO_2 mixture to a high-pressure syringe pump, and flowing the mixture through our high-pressure flow-focusing channel to drive bubble nucleation in the observation capillary.

First, slowly pour the desired polyol into the Teflon cup of a Parr reactor (Parr Instrument Company, #4760, 240 mL capacity), careful not to entrain bubbles. Mix in desired additives (*e.g.*, cyclopentane, surfactant—see Chapter VII). Seal Parr reactor top with 35 ft-lbs of torque, applied in three stages to the six bolts in a star-shaped pattern; if flammability is a concern, run a low-pressure flow of N_2 gas through the gas sampling valve until sealed. The Parr reactor is mixed with a brushless impeller at 5–10 RPM, which has been found to be slow enough not to entrain bubbles [3]. Gradually pressurize the Parr reactor by pumping CO_2 through the liquid sampling valve with an ISCO pump. Once the Parr reactor reaches the desired pressure or slightly higher, close the liquid sampling valve and let mix overnight, pumping in more CO_2 as needed.

Once the Parr reactor has equilibrated at the desired pressure, transfer its contents to the ISCO 100DM syringe pump through the liquid sampling valve. Throughout the transfer, the fluid must be kept above the saturation pressure to prevent bubble nucleation along the walls of the tubing. To pressurize the Parr reactor further, connect an N_2 gas tank (Airgas Industrial grade) equipped with a pressure regulator (Airgas CGA-580, 0–2500 psi #Y11N115H580-AG) to the gas sampling valve of the Parr reactor and increase the pressure by at least 100 psi (0.7 MPa). Because N_2 has a much lower solubility in polyol than CO_2 [75, 76], we assume that the additional partial pressure of N_2 will have a negligible effect on bubble nucleation. Before transferring the fluid to the ISCO 100DM, prime the tubing between the liquid sampling valve and the ISCO 100DM with pure polyol to maintain the pressure upon opening the valve. Next, open the liquid sampling valve and slowly fill the ISCO 100DM with the fluid, maintaining the pressure in the headspace with the N_2 pressure regulator. Once the ISCO pump has been filled with the desired amount of fluid, close its valve and the liquid sampling valve of the Parr reactor. Slowly depressurize the tubing between the Parr and the ISCO and between the N_2 cylinder and the Parr.

To perform the experiment, mount the microfluidic apparatus into the 3D-printed mount (see Figure III.3) and seal the ends of the oil reservoir with silicone rubber. Mount to the microscope translation stage with NdFeB magnets. Fill the oil reservoir with enough index-matched oil (Wesson vegetable oil) to submerge the observation capillary. Connect the ISCO 100DM pump (filled with the polyol–CO_2 mixture) to the inner stream tubing and the ISCO 260D (filled with the "1k5f" polyol—see Table II.1) to the outer stream tubing on the microfluidic apparatus. Prime and pressurize the apparatus and tubing with the ISCO 260D. Once the pressure in the tubing has reached the pressure in the ISCO 100DM, begin pumping the ISCO 100DM to provide the inner stream of nucleating fluid. After the inner stream forms in the observation capillary, adjust the flow until bubbles can be seen at the exit. Be careful not to let the pressure decrease so much that the entire apparatus fills with foam and depressurizes the ISCO 100DM. Different moments in the lifetime of the foaming flow can be captured by translating along the observation capillary.

With sufficient dissolved CO_2 and careful observation in the appropriate region of the observation capillary, we can capture the growth of bubbles immediately after they can be detected by optical microscopy, as seen in the image at the

bottom of Figure III.3. To our knowledge, no other group has captured the growth following homogeneous bubble nucleation from a polymer–gas mixture with comparable time resolution (compare ~ 20 *mu*s intervals between frames to the 20 ms intervals reported in Leung *et al.* [77]). Given that much of the nucleation in polymer foams occurs through homogeneous nucleation, we expect these data can help answer many unanswered questions in the field of polymer foaming, such as the wide variability in model estimates of the nucleation barrier (see discussion of the state of the literature in Section I.4).

III.4   Recommendations for Future Work

Our exploration of the capabilities of the instrument discussed in this Chapter has only been partial. Many improvements remain to be made, and many features have yet to be utilized. Here, we offer suggestions for both.

Improvements to Current Instrument

While the instrument successfully ensheaths in the inner stream with the outer, the inner stream does not run perfectly along the center of the observation capillary, as seen in the example snapshots in Figure III.3. The imprecision of the alignment of the smaller capillary silver-epoxied inside the inner stream tubing to extend it is one likely cause. We expect that the asymmetry of the tee junction, which receives the outer stream from only one side, also nudges the inner stream off center. A simple improvement might be to 3D-print a mount to align the smaller inner capillary inside the inner stream tubing while the silver epoxy is curing. If centering the inner stream is of high importance, a more invested researcher could machine an acrylic junction with symmetric inlets for the outer stream, both having the same length of tubing and fed by the same source.

The instrument in its current form also does not allow observation of the entire length of the observation capillary. While some obstruction of the entrance by the high-pressure fitting is inevitable, the region near the exit need not be obstructed. In the current iteration of the instrument, silicone rubber pieces are necessary at the ends of the observation capillary to slow leakage of the oil reservoir that reduces lensing. If done properly, the observation capillary can be encased in UV-cured optical adhesive (*e.g.*, Norland #146H) within a square capillary up just a few millimeters from the exit, as described in greater detail in Section III.S5 of the SI. The exit could then be supported on top of a transparent sheet before reaching the incline to the waste, which would allow observation at and beyond the exit of

the capillary. Fractionally, most of the pressure quench occurs in the final few millimeters before the exit of the observation capillary, so we expect significant foaming. Although we explored this modification to the instrument, we did not implement it because of the difficulty of discerning the size and shape of such tightly packed bubbles. Future studies of the behavior of the fluid near atmospheric pressure should also consider alternative observation techniques.

Additional Features to Consider

The initial motivation of the present study was the nucleation and growth of bubbles in high-pressure polyurethane foaming. We focused on only one aspect of polyurethane foaming, the pressure quench, but the unique properties of polyurethane foam depend on the effects of the chemical reaction between isocyanate and polyol and the heat this exothermic reaction releases as well. To study the reaction of isocyanate with polyol, the inner stream could be replaced with isocyanate (*e.g.*, pMDI) and the reaction along its interface observed. From the observations of the advancing reaction front by Machuga *et al.* [78], we expect that a thread of isocyanate within a sheath of polyol could be completely penetrated by polyol within common residence times in the observation capillary (≈ 100 ms). Another embodiment could first impinge the polyol and isocyanate streams in a tee junction at high pressure, as in industrial foaming nozzles [79]. The outlet of this tee junction would provide the inner stream for the tee junction in the current embodiment of the device, which would ensheath the reacting mixture with more polyol. For a diagram of how such a device with two flow-focusing tee junctions could be produced, see Figure 1 in the work of Hessberger *et al.* [68]. If the flow is fast enough, the reacting mixture could be ensheathed before causing fouling in the first tee junction the current embodiment. Isocyanate adds two additional challenges, however: (1) fouling and (2) exposure hazard.

The instrument presented in this Chapter is well suited to manage the first, fouling. First, the inner stream is completely isolated from the walls of the acrylic tee junction and observation capillary by the outer stream of polyol. Should some solid particles enter or form within the inner stream, they would be quickly flushed out by the overwhelming flow of the outer stream. Fouling may still occur along the walls of the tubing and inner capillary. In this case, they are both inexpensive and not too difficult to assemble, so the fouled part can be replaced. Pumping isocyanate directly with an ISCO pump is not recommended due to the difficulty of cleaning the interior in the case of following and high cost of repair. Instead,

isocyanate could be pumped from a tubular reactor with a piston driven by hydraulic fluid from another pump, as shown for providing pressure in the waste stream in the apparatus of Chen-Jolly *et al.* [67]. The piston in the tubular reactor would isolate the isocyanate from the pump and could be more easily cleaned in the case of fouling.

The instrument in its present form is not as well suited to managing the chemical hazards of isocyanate due to the open-air waste collection. If isocyanate is used as the inner stream, the experiment will ideally be performed in a chemical hood, or at minimum, under a snorkel/elephant trunk in a well-ventilated environment. The small volumes and significantly larger quantity of outer stream fluid than inner stream fluid would reduce the likelihood of exposure to or inhalation of isocyanate, but the severity of isocyanate exposure should not be taken lightly.

The study of the effect of temperature on bubble nucleation with the present instrument would be interesting scientifically, but less practically relevant to polyurethane foam. By studying the effect of temperature on the nucleation rate at a fixed degree of supersaturation, the nucleation energy barrier can be estimated using the second nucleation theorem [80, 81], which could be directly compared to theoretical models, as discussed in Chapter VI. The polyurethane reaction heats up slowly, increasing by only a few degrees Celsius before the cream time (usually around 1 minute) [9]. Consequently, we do not expect a significant increase in the temperature in industrial polyurethane foaming within the residence time of the present instrument. Temperature does provide an additional control of supersaturation, as seen by its significant effect on CO_2 solubility in Section II.2, and it can be controlled more precisely than the pressure. For example, bubbles could be nucleated on demand by local heating of the inner stream fluid by a laser, as in the study of homogeneous bubble nucleation in water by Ando *et al.* [41]. In this way, bubbles could be nucleated at precise locations upstream of the field of view of the microscope to capture precise periods of their growth. Bubbles could also be nucleated in rapid succession to study their interaction along the inner stream. Additionally, to prevent bubble nucleation upstream of the observation capillary, the inner stream fluid can be chilled with the cold water bath feature of the ISCO 100DM, maintaining the fluid well below saturation. The oil reservoir used to reduce lensing could be heated to supersaturate the fluid, even beyond the degree possible with depressurization.

While only briefly explored in Chapter VII, the present instrument is well suited for studies of bubble nucleation from formulations of polyols, including

physical blowing agents like cyclopentane and surfactants. These additives and others can be mixed with the polyol before dissolving CO_2 to explore their effect on bubble nucleation and foaming.

References

1. Lubetkin, S. D. Why Is It Much Easier To Nucleate Gas Bubbles than Theory Predicts? *Langmuir* **19,** 2575–2587. https://pubs.acs.org/doi/abs/10.1021/la0266381 (2003).

2. Terekhov, A. Y. *et al.* Small-angle X-ray scattering measurements of helium-bubble formation in borosilicate glass. *Journal of Applied Crystallography* **39,** 647–651. ISSN: 0021-8898. http://scripts.iucr.org/cgi-bin/paper?S0021889806025672 (Oct. 2006).

3. Brondi, C., Di Maio, E., Bertucelli, L., Parenti, V. & Mosciatti, T. Competing bubble formation mechanisms in rigid polyurethane foaming. *Polymer* **228,** 123877. ISSN: 00323861. https://doi.org/10.1016/j.polymer.2021.123877%20https://linkinghub.elsevier.com/retrieve/pii/S0032386121005000 (July 2021).

4. Costeux, S., Khan, I., Bunker, S. P. & Jeon, H. K. Experimental study and modeling of nanofoams formation from single phase acrylic copolymers. *Journal of Cellular Plastics* **51,** 197–221 (2015).

5. Doroudiani, S., Park, C. B. & Kortschot, M. T. Effect of the crystallinity and morphology on the microcellular foam structure of semicrystalline polymers. *Polymer Engineering and Science* **36,** 2645–2662. ISSN: 00323888 (1996).

6. Forest, C., Chaumont, P., Cassagnau, P., Swoboda, B. & Sonntag, P. Polymer nano-foams for insulating applications prepared from CO2 foaming. *Progress in Polymer Science* **41,** 122–145. ISSN: 00796700. https://www.sciencedirect.com/science/article/pii/S0079670014000689%20https://linkinghub.elsevier.com/retrieve/pii/S0079670014000689 (Feb. 2015).

7. Fu, L. *et al.* Improved cell nucleating effect of partially melted crystal structure to enhance the microcellular foaming and impact properties of isotactic polypropylene. *The Journal of Supercritical Fluids* **160,** 104794. ISSN: 08968446. https://doi.org/10.1016/j.supflu.2020.104794%20https://linkinghub.elsevier.com/retrieve/pii/S0896844620300450 (June 2020).

8. Krause, B. *et al.* Ultralow-k Dielectrics Made by Supercritical Foaming of Thin Polymer Films. *Advanced Materials* **14,** 1041. ISSN: 09359648 (Aug. 2002).

9. Minogue, E. *An in-situ study of the nucleation process of polyurethane rigid foam formation* PhD thesis (Dublin City University, 2000), 1–194. http://doras.dcu.ie/19076/.

10. Park, C. B. & Cheung, L. K. A study of cell nucleation in the extrusion of polypropylene foams. *Polymer Engineering and Science* **37**, 1–10. ISSN: 00323888 (1997).

11. Roberts, C. *et al.* Bubblescale observations of polyurethane foam expansion. *AIChE Journal* **68**, e17595. ISSN: 0001-1541. https://onlinelibrary.wiley.com/doi/10.1002/aic.17595 (May 2022).

12. Rizvi, A. & Park, C. B. Dispersed polypropylene fibrils improve the foaming ability of a polyethylene matrix. *Polymer* **55**, 4199–4205. ISSN: 00323861. http://dx.doi.org/10.1016/j.polymer.2014.06.014 (2014).

13. Rizvi, A., Chu, R. K. M. & Park, C. B. Scalable Fabrication of Thermally Insulating Mechanically Resilient Hierarchically Porous Polymer Foams. *ACS Applied Materials & Interfaces* **10**, 38410–38417. ISSN: 1944-8244. https://pubs.acs.org/doi/10.1021/acsami.8b11375 (Nov. 2018).

14. Taki, K. & Okumura, S. Production of Porous Polymeric Films with Unimodal or Bimodal Pore-Size Distributions via Depressurization- and Photopolymerization-Induced Bubble Nucleation in Low-Viscosity UV-Curable Monomer/High-Pressure CO2 Solutions. *Macromolecules* **43**, 9899–9907. http://pubs.acs.org/doi/abs/10.1021/ma101748c (Dec. 2010).

15. Tammaro, D., Iannace, S. & Di Maio, E. Insight into bubble nucleation at high-pressure drop rate. *Journal of Cellular Plastics* **53**, 551–560. ISSN: 0021-955X. http://journals.sagepub.com/doi/10.1177/0021955X17695094 (Sept. 2017).

16. Tammaro, D. & Di Maio, E. Early bubble coalescence in thermoplastic foaming. *Materials Letters* **228**, 459–462. ISSN: 0167-577X. https://www.sciencedirect.com/science/article/pii/S0167577X18309637 (Oct. 2018).

17. Wang, K. *et al.* A new strategy for preparation of long-chain branched polypropylene via reactive extrusion with supercritical CO2 designed for an improved foaming approach. *Journal of Materials Science* **51**, 2705–2715. ISSN: 0022-2461. http://link.springer.com/10.1007/s10853-015-9584-x (Mar. 2016).

18. Wang, G. *et al.* Role of elastic strain energy in cell nucleation of polymer foaming and its application for fabricating sub-microcellular TPU microfilms. *Polymer* **119**, 28–39. ISSN: 00323861. http://dx.doi.org/10.1016/j.polymer.2017.05.016 (2017).

19. Wong, A., Chu, R. K., Leung, S. N., Park, C. B. & Zong, J. H. A batch foaming visualization system with extensional stress-inducing ability. *Chemical Engineering Science* **66,** 55–63. ISSN: 00092509. http://dx.doi.org/10.1016/j.ces.2010.09.038%20https://linkinghub.elsevier.com/retrieve/pii/S0009250910005841 (Jan. 2011).

20. Zhao, J., Wang, G., Zhang, A., Zhao, G. & Park, C. B. Nanocellular TPU composite foams achieved by stretch-assisted microcellular foaming with low-pressure gaseous CO2 as blowing agent. *Journal of CO2 Utilization* **53,** 101708 (Nov. 2021).

21. Guo, Q., Wang, J., Park, C. B. & Ohshima, M. A microcellular foaming simulation system with a high pressure-drop rate. *Industrial and Engineering Chemistry Research* **45,** 6153–6161. ISSN: 08885885 (2006).

22. Hu, D. *et al.* Effect of additives on the dynamic bubble growth behavior of polymer foam evaluated with in-situ visualizations and simulations. *Polymer Testing* **105,** 107419. ISSN: 01429418. https://doi.org/10.1016/j.polymertesting.2021.107419%20https://linkinghub.elsevier.com/retrieve/pii/S0142941821003627 (Jan. 2022).

23. Leung, S. N., Wong, A., Wang, L. C. & Park, C. B. Mechanism of extensional stress-induced cell formation in polymeric foaming processes with the presence of nucleating agents. *Journal of Supercritical Fluids* **63,** 187–198. ISSN: 08968446. http://dx.doi.org/10.1016/j.supflu.2011.12.018 (2012).

24. Li, R., Lee, J. H., Wang, C., Howe Mark, L. & Park, C. B. Solubility and diffusivity of CO2 and N2 in TPU and their effects on cell nucleation in batch foaming. *The Journal of Supercritical Fluids* **154,** 104623. ISSN: 08968446. https://doi.org/10.1016/j.supflu.2019.104623%20https://linkinghub.elsevier.com/retrieve/pii/S0896844619303134 (Dec. 2019).

25. Shaayegan, V., Wang, G. & Park, C. B. Study of the bubble nucleation and growth mechanisms in high-pressure foam injection molding through in-situ visualization. *European Polymer Journal* **76,** 2–13. ISSN: 00143057. http://dx.doi.org/10.1016/j.eurpolymj.2015.11.021%20https://linkinghub.elsevier.com/retrieve/pii/S001430571530063X (Mar. 2016).

26. Shaayegan, V., Wang, G. & Park, C. B. Effect of foam processing parameters on bubble nucleation and growth dynamics in high-pressure foam injection molding. *Chemical Engineering Science* **155,** 27–37. ISSN: 00092509. http://dx.doi.org/10.1016/j.ces.2016.07.040%20https://linkinghub.elsevier.com/retrieve/pii/S0009250916304158 (Nov. 2016).

27. Taki, K., Nakayama, T., Yatsuzuka, T. & Ohshima, M. Visual Observations of Batch and Continuous Foaming Processes. *Journal of Cellular Plastics* **39,** 155–169. ISSN: 0021-955X. http://journals.sagepub.com/doi/10.1177/0021955X03039002005 (Mar. 2003).

28. Taki, K., Kitano, D. & Ohshima, M. Effect of Growing Crystalline Phase on Bubble Nucleation in Poly(L-Lactide)/CO2 Batch Foaming. *Industrial & Engineering Chemistry Research* **50,** 3247–3252. ISSN: 0888-5885. https://pubs.acs.org/sharingguidelines%20https://pubs.acs.org/doi/10.1021/ie101637f (Mar. 2011).

29. Wong, A. & Park, C. A visualization system for observing plastic foaming processes under shear stress. *Polymer Testing* **31,** 417–424. ISSN: 01429418. https://linkinghub.elsevier.com/retrieve/pii/S0142941811002169 (May 2012).

30. Wong, A., Guo, Y. & Park, C. B. Fundamental mechanisms of cell nucleation in polypropylene foaming with supercritical carbon dioxideEffects of extensional stresses and crystals. *The Journal of Supercritical Fluids* **79,** 142–151. ISSN: 08968446. http://dx.doi.org/10.1016/j.supflu.2013.02.013%20https://linkinghub.elsevier.com/retrieve/pii/S0896844613000740 (July 2013).

31. Wong, A., Wijnands, S. F. L., Kuboki, T. & Park, C. B. Mechanisms of nanoclay-enhanced plastic foaming processes: effects of nanoclay intercalation and exfoliation. *Journal of Nanoparticle Research* **15,** 1815. ISSN: 1388-0764. http://link.springer.com/10.1007/s11051-013-1815-y (Aug. 2013).

32. Wong, A., Mark, L. H., Hasan, M. M. & Park, C. B. The synergy of supercritical CO2 and supercritical N2 in foaming of polystyrene for cell nucleation. *Journal of Supercritical Fluids* **90,** 35–43. ISSN: 08968446. http://dx.doi.org/10.1016/j.supflu.2014.03.001 (2014).

33. Wong, A., Guo, Y., Park, C. & Zhou, N. A Polymer Visualization System with Accurate Heating and Cooling Control and High-Speed Imaging. *International Journal of Molecular Sciences* **16,** 9196–9216. ISSN: 1422-0067. http://www.mdpi.com/1422-0067/16/5/9196 (Apr. 2015).

34. Yang, J. *et al.* Experimental and numerical analysis of bubble nucleation in foaming polymer. *Materials & Design* **203,** 109577. ISSN: 02641275. https://linkinghub.elsevier.com/retrieve/pii/S0264127521001301 (May 2021).

35. Pardo-Alonso, S., Solórzano, E., Estravís, S., Rodríguez-Perez, M. A. & De Saja, J. A. In situ evidence of the nanoparticle nucleating effect in polyurethane-nanoclay foamed systems. *Soft Matter* **8,** 11262–11270. ISSN: 1744683X (2012).

36. Tuladhar, T. & Mackley, M. Experimental observations and modelling relating to foaming and bubble growth from pentane loaded polystyrene melts. *Chemical Engineering Science* **59,** 5997–6014. ISSN: 00092509. https://www.sciencedirect.com/science/article/pii/S0009250904004920%20https://linkinghub.elsevier.com/retrieve/pii/S0009250904004920 (Dec. 2004).

37. Reignier, J., Alcouffe, P., Méchin, F. & Fenouillot, F. The morphology of rigid polyurethane foam matrix and its evolution with time during foaming – New insight by cryogenic scanning electron microscopy. *Journal of Colloid and Interface Science* **552,** 153–165. ISSN: 00219797. https://linkinghub.elsevier.com/retrieve/pii/S0021979719305764 (Sept. 2019).

38. Pérez-Tamarit, S., Solórzano, E., Mokso, R. & Rodríguez-Pérez, M. In-situ understanding of pore nucleation and growth in polyurethane foams by using real-time synchrotron X-ray tomography. *Polymer* **166,** 50–54. ISSN: 0032-3861. https://www.sciencedirect.com/science/article/pii/S0032386119300618 (Mar. 2019).

39. Han, J. H. & Dae Han, C. Bubble nucleation in polymeric liquids. I. Bubble nucleation in concentrated polymer solutions. *Journal of Polymer Science Part B: Polymer Physics* **28,** 711–741. ISSN: 08876266. https://onlinelibrary.wiley.com/doi/10.1002/polb.1990.090280509 (Apr. 1990).

40. Leung, S. N., Park, C. B., Xu, D., Li, H. & Fenton, R. G. Computer Simulation of Bubble-Growth Phenomena in Foaming. *Industrial & Engineering Chemistry Research* **45,** 7823–7831. ISSN: 0888-5885. https://pubs.acs.org/doi/pdf/10.1021/ie060295a%20https://pubs.acs.org/doi/10.1021/ie060295a (Nov. 2006).

41. Ando, K., Liu, A. Q. & Ohl, C. D. Homogeneous nucleation in water in microfluidic channels. *Physical Review Letters* **109,** 044501. ISSN: 00319007 (2012).

42. Tsujimura, I. *et al.* A Study of Bubble Nucleation in Foam Extrusion Die. *Seikei-Kakou* **11,** 937–944. ISSN: 1883-7417. http://www.jstage.jst.go.jp/article/seikeikakou1989/11/11/11_11_937/_article/-char/ja/ (1999).

43. Shimoda, M., Tsujimura, I., Tanigaki, M. & Ohshima, M. Polymeric foaming simulation for extrusion processes. *Journal of Cellular Plastics* **37,** 517–536. ISSN: 0021955X (2001).

44. Shaayegan, V., Mark, L. H., Tabatabaei, A. & Park, C. B. A new insight into foaming mechanisms in injection molding via a novel visualization mold. *Express Polymer Letters* **10,** 462–469. ISSN: 1788618X (2016).

45. Deveaux, S. *The Birth of Bebop* 167–236. ISBN: 9780520922105. https://www.degruyter.com/document/doi/10.1525/9780520922105/html (University of California Press, Dec. 1997).

46. Knight, J. B., Vishwanath, A., Brody, J. P. & Austin, R. H. Hydrodynamic Focusing on a Silicon Chip: Mixing Nanoliters in Microseconds. *Physical Review Letters* **80,** 3863–3866. https://journals.aps.org/prl/pdf/10.1103/PhysRevLett.80.3863 (1998).

47. Pollack, L. *et al.* Compactness of the denatured state of a fast-folding protein measured by submillisecond small-angle x-ray scattering. *Proceedings of the National Academy of Sciences* **96,** 10115–10117. ISSN: 0027-8424. http://www.pnas.org/content/pnas/96/18/10115.full.pdf%20http://www.pnas.org/cgi/doi/10.1073/pnas.96.18.10115 (Aug. 1999).

48. Squires, T. M. & Quake, S. R. Microfluidics: Fluid physics at the nanoliter scale. *Reviews of Modern Physics* **77,** 977–1026. ISSN: 00346861 (2005).

49. Brody, J. P., Yager, P., Goldstein, R. E. & Austin, R. H. Biotechnology at low Reynolds numbers. *Biophysical Journal* **71,** 3430–3441. ISSN: 00063495. http://dx.doi.org/10.1016/S0006-3495(96)79538-3 (1996).

50. Seibt, S., With, S., Bernet, A., Schmidt, H.-W. & Förster, S. Hydrogelation Kinetics Measured in a Microfluidic Device with in Situ X-ray and Fluorescence Detection. *Langmuir* **34,** 5535–5544. ISSN: 0743-7463. https://pubs.acs.org/sharingguidelines%20https://pubs.acs.org/doi/10.1021/acs.langmuir.8b00384 (May 2018).

51. Song, H. & Ismagilov, R. F. Millisecond Kinetics on a Microfluidic Chip Using Nanoliters of Reagents. *Journal of the American Chemical Society* **125,** 14613–14619. ISSN: 0002-7863. https://pubs.acs.org/doi/pdf/10.1021/ja0354566%20https://pubs.acs.org/doi/10.1021/ja0354566 (Nov. 2003).

52. Stan, C. A. *et al.* A microfluidic apparatus for the study of ice nucleation in supercooled water drops. *Lab on a Chip* **9,** 2293–2305. ISSN: 14730189 (2009).

53. Song, H., Chen, D. L. & Ismagilov, R. F. Reactions in droplets in microfluidic channels. *Angewandte Chemie - International Edition* **45,** 7336–7356. ISSN: 14337851 (2006).

54. Hassanpour-Tamrin, S., Sanati-Nezhad, A. & Sen, A. A simple and low-cost approach for irreversible bonding of polymethylmethacrylate and polydimethylsiloxane at room temperature for high-pressure hybrid microfluidics. *Scientific Reports* **11,** 4821. ISSN: 2045-2322. https://doi.org/10.1038/s41598-021-83011-8%20http://www.nature.com/articles/s41598-021-83011-8 (Dec. 2021).

55. Marre, S. & Jensen, K. F. Synthesis of micro and nanostructures in microfluidic systems. *Chemical Society Reviews* **39,** 1183. ISSN: 0306-0012. http://xlink.rsc.org/?DOI=b821324k (Feb. 2010).

56. Martin, A., Teychené, S., Camy, S. & Aubin, J. Fast and inexpensive method for the fabrication of transparent pressure-resistant microfluidic chips. *Microfluidics and Nanofluidics* **20,** 92. ISSN: 1613-4982. http://link.springer.com/10.1007/s10404-016-1757-7 (June 2016).

57. Chen, C. F. *et al.* High-pressure needle interface for thermoplastic microfluidics. *Lab Chip* **9,** 50–55. ISSN: 1473-0197. http://xlink.rsc.org/?DOI=B812812J (2009).

58. Sell, A., Fadaei, H., Kim, M. & Sinton, D. Measurement of CO 2 Diffusivity for Carbon Sequestration: A Microfluidic Approach for Reservoir-Specific Analysis. *Environmental Science & Technology* **47,** 71–78. ISSN: 0013-936X. https://pubs.acs.org/doi/10.1021/es303319q (Jan. 2013).

59. Gerhardt, R. F., Peretzki, A. J., Piendl, S. K. & Belder, D. Seamless Combination of High-Pressure Chip-HPLC and Droplet Microfluidics on an Integrated Microfluidic Glass Chip. *Analytical Chemistry* **89,** 13030–13037. ISSN: 0003-2700. https://pubs.acs.org/doi/10.1021/acs.analchem.7b04331 (Dec. 2017).

60. Utada, A. S. *et al.* Monodisperse double emulsions generated from a microcapillary device. *Science* **308,** 537–541. ISSN: 00368075 (2005).

61. Marre, S., Aymonier, C., Subra, P. & Mignard, E. Dripping to jetting transitions observed from supercritical fluid in liquid microcoflows. *Applied Physics Letters* **95,** 134105. ISSN: 0003-6951. http://aip.scitation.org/doi/10.1063/1.3242375 (Sept. 2009).

62. Roig, Y., Marre, S., Cardinal, T. & Aymonier, C. Synthesis of exciton luminescent ZnO nanocrystals using continuous supercritical microfluidics. *Angewandte Chemie - International Edition* **50,** 12071–12074. ISSN: 14337851 (2011).

63. Luther, S. K. & Braeuer, A. High-pressure microfluidics for the investigation into multi-phase systems using the supercritical fluid extraction of emulsions (SFEE). *The Journal of Supercritical Fluids* **65,** 78–86. ISSN: 08968446. https://linkinghub.elsevier.com/retrieve/pii/S0896844612000782 (May 2012).

64. Trachsel, F., Hutter, C. & von Rohr, P. R. Transparent silicon/glass microreactor for high-pressure and high-temperature reactions. *Chemical Engineering Journal* **135,** 309–316. ISSN: 13858947 (2008).

65. Temiz, Y., Lovchik, R. D., Kaigala, G. V. & Delamarche, E. Lab-on-a-chip devices: How to close and plug the lab? *Microelectronic Engineering* **132,** 156–175. ISSN: 01679317. http://dx.doi.org/10.1016/j.mee.2014.10.013%20https://linkinghub.elsevier.com/retrieve/pii/S0167931714004456 (Jan. 2015).

66. Maharrey, S. P. & Miller, D. R. Quartz capillary microreactor for studies of oxidation in supercritical water. *AIChE Journal* **47,** 1203–1211. ISSN: 00011541. http://doi.wiley.com/10.1002/aic.690470526%20https://onlinelibrary.wiley.com/doi/10.1002/aic.690470526 (May 2001).

67. Chen-Jolly, H., Guillot, P. & Mignard, E. Supercritical continuous precipitation polymerization of acrylic acid in a droplet-based millifluidic device. *Chemical Engineering Journal* **334,** 389–399. ISSN: 13858947. https://linkinghub.elsevier.com/retrieve/pii/S138589471731745X (Feb. 2018).

68. Hessberger, T. *et al.* Co-flow microfluidic synthesis of liquid crystalline actuating Janus particles. *Journal of Materials Chemistry C* **4,** 8778–8786. ISSN: 2050-7526. http://xlink.rsc.org/?DOI=C6TC03378D (Sept. 2016).

69. Khan, I. U. *et al.* Microfluidic conceived drug loaded Janus particles in side-by-side capillaries device. *International Journal of Pharmaceutics* **473,** 239–249. ISSN: 18733476. http://dx.doi.org/10.1016/j.ijpharm.2014.06.035 (2014).

70. NIST. *NIST Standard Reference Database Number 69* 2022. https://webbook.nist.gov/chemistry/ (2022).

71. Bourges, A. C., Lazarev, A., Declerck, N., Rogers, K. L. & Royer, C. A. Quantitative High-Resolution Imaging of Live Microbial Cells at High Hydrostatic Pressure. *Biophysical Journal* **118,** 2670–2679. ISSN: 15420086. https://doi.org/10.1016/j.bpj.2020.04.017 (2020).

72. Brown, P. Investigating change using the invisible-test-tube demonstration. *Science Scope* **36,** 76–81. http://www.jstor.org/stable/43184272 (2013).

73. Schnablegger, H. & Singh, Y. *The SAXS Guide: Getting acquainted with the principles* 4th ed., 50–90. ISBN: 18012013. https://austria-forum.org/web-books/en/saxs00en2013iicm/000072 (Anton Paar GmbH, Austria, Graz, Austria, 2017).

74. Steen, H. B. Flow Cytometer for Measurement of the Light Scattering of Viral and Other Submicroscopic Particles. *Cytometry Part A* **57,** 94–99. ISSN: 15524922 (2004).

75. Aschenbrenner, O. & Styring, P. Comparative study of solvent properties for carbon dioxide absorption. *Energy Environ. Sci.* **3,** 1106–1113. www.rsc.org/ees (2010).

76. Wiesmet, V., Weidner, E., Behme, S., Sadowski, G. & Arlt, W. Measurement and modelling of high-pressure phase equilibria in the systems polyethyleneglycol (PEG)–propane, PEG–nitrogen and PEG–carbon dioxide. *The Journal of Supercritical Fluids* **17,** 1–12. ISSN: 08968446 (Feb. 2000).

77. Leung, S. N., Wong, A., Park, C. B. & Guo, Q. Strategies To Estimate the Pressure Drop Threshold of Nucleation for Polystyrene Foam with Carbon Dioxide. *Industrial & Engineering Chemistry Research* **48,** 1921–1927. ISSN: 0888-5885. https://pubs.acs.org/doi/10.1021/ie800079x (Feb. 2009).

78. Machuga, S. C., Midje, H. L., Peanasky, J. S., Macosko, C. W. & Ranz, W. E. Microdispersive interfacial mixing in fast polymerizations. *AIChE Journal* **34,** 1057–1064. ISSN: 15475905 (1988).

79. *The Polyurethanes Book* (eds Randall, D. & Lee, S.) ISBN: 0470850418 (Huntsman International LLC, Polyurethanes business, 2002).

80. Ford, I. J. Thermodynamic properties of critical clusters from measurements of vapour–liquid homogeneous nucleation rates. *The Journal of Chemical Physics* **105,** 8324–8332. ISSN: 0021-9606. http://aip.scitation.org/doi/10.1063/1.472687 (Nov. 1996).

81. Laaksonen, A. & Malila, J. in *Nucleation of Water: From Fundamental Science to Atmospheric and Additional Applications* 45–70 (2022).

III.S1   Flow in Microfluidic Sheath Flow

Newtonian Polyols
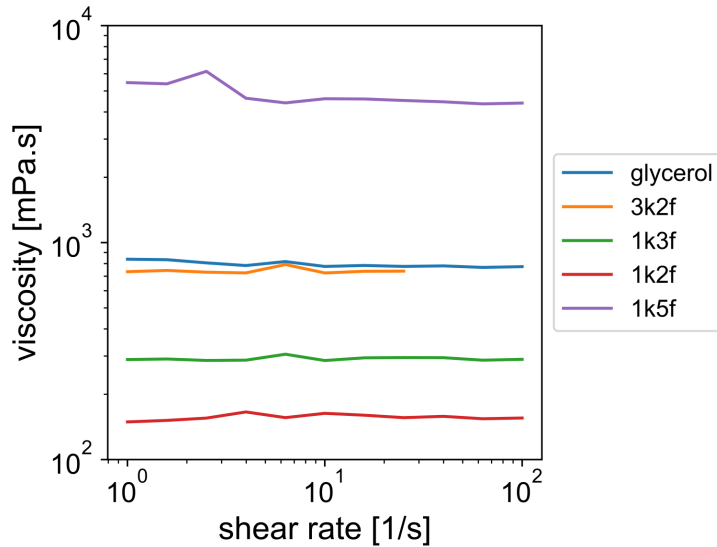
Figure III.S1: Viscosity measured in a shear rate sweep from 1 1/s to 100 1/s at a temperature of 25 degrees Celsius with 50 mm parallel plates and 0.7 mm gap size on an ARES RFS shear rheometer. Polyol names are encoded to conceal the identities of proprietary chemicals; for properties, see Table II.1.

Derivation of Flow Profile

Assumptions:

- Stokes flow ($Re \ll 1$)

- Incompressible fluid

- Newtonian fluid

- Axisymmetry about the flow axis (no θ dependence)

- Symmetric along the flow axis (no z dependence)

- Steady flow (no time dependence)

- No-slip boundary condition at the walls

- No-stress boundary condition at the interface between the inner and outer streams

- Effect of gravity is negligible

Because we assume that we are in the Stokes flow regime, the governing equation is the Stokes equation,

$$\nabla p = \eta \nabla^2 \vec{v} \tag{III.1}$$

where p is the pressure, η is the viscosity, and $\vec{v}$ is the velocity.

Because the flow is axisymmetric, there is no velocity component in the azimuthal (θ) direction. Additionally, because the flow is axisymmetric, symmetric along the flow axis, and incompressible, there is no velocity component in the radial (r) direction, either. Thus, we only need to consider the axial component of velocity (along the z-axis), which we will denote as w, according to convention. Then Stokes equation III.1 can be simplified to

$$\frac{1}{\eta} \frac{\mathrm{d}p}{\mathrm{d}z} = \frac{1}{r} \frac{\mathrm{d}}{\mathrm{d}r} \left(r \frac{\mathrm{d}w}{\mathrm{d}r} \right) \tag{III.2}$$

Because the system is translationally invariant in z, the pressure gradient is constant, $\frac{\mathrm{d}p}{\mathrm{d}z} \equiv -G$. Then the general form of the velocity profile is obtained by integrating equation III.2 twice to get

$$w = -\frac{Gr^2}{4\eta} + A \log r + B \tag{III.3}$$

However, since we are considering flow along a cylinder that includes $r = 0$ in the domain, a finite velocity requires that $A = 0$. This is true even for the outer stream's velocity profile because it may flow through $r = 0$ in the limit that the inner flow rate goes to 0.

We call the radius of the interface between the inner and outer streams R_i and the radius of the walls R. We also will denote the velocity profile of the inner stream as $w_i(r)$ on the domain $r \in [0, R_i]$ and that of the outer stream as $w_o(r)$ on the domain $r \in [R_i, R]$. Note that the inner and outer streams could have different viscosities, denoted by η_i and η_o. Because we assume no stress along the interface between the two streams, the velocity of the interface is the same on either side, which we will denote as V. Then the boundary conditions on the velocity profile $w_i(r)$ for the inner stream are

$$\begin{cases} \left. \dfrac{dw_i}{dr} \right|_{r=0} = 0, \text{(axisymmetry)} \\ w_i(r = R_i) = w_o(r = R_i) \equiv V, \text{continuous velocity} \end{cases} \tag{III.4}$$

The first boundary condition is satisfied because the coefficient of the logarithmic term $A = 0$. The second boundary condition determines the constant coefficient

$$B = V + \frac{GR_i^2}{4\eta_i} \tag{III.5}$$

Thus

$$w_i(r) = V + \frac{GR_i^2}{4\eta_i} \left[1 - \left(\frac{r}{R_i} \right)^2 \right] \tag{III.6}$$

The boundary conditions on the velocity profile $w_o(r)$ for the outer stream are

$$\begin{cases} w_o(r = R_i) = V, \text{continuous velocity} \\ w_o(r = R) = 0, \text{no slip along the walls} \end{cases} \tag{III.7}$$

Solving the second boundary condition for the constant coefficient B gives

$$B = \frac{GR^2}{4\eta_o} \tag{III.8}$$

Thus, the velocity profile of the outer stream is

$$w_o(r) = \frac{GR^2}{4\eta_o} \left[1 - \left(\frac{r}{R} \right)^2 \right] \tag{III.9}$$

Substituting equation III.8 into the first boundary condition gives the velocity at the interface between the inner and outer streams,

$$V = \frac{G(R^2 - R_i^2)}{4\eta_o} \tag{III.10}$$

By plugging in the expression for V from equation III.10 into the expression for the inner stream velocity profile in equation III.6, we find that the velocity profile of the inner stream is

$$w_i(r) = \frac{G(R^2 - R_i^2)}{4\eta_o} + \frac{GR_i^2}{4\eta_i}\left[1 - \left(\frac{r}{R_i}\right)^2\right] \tag{III.11}$$

The remaining unknown system parameters are the interfacial radius R_i and the negative pressure gradient G. These are set by the flow rates of the inner and outer streams, Q_i and Q_o, respectively.

Given that the inner stream's flow rate is Q_i,

$$Q_i = \int_0^{2\pi} \int_0^{R_i} w_i(r) r\, dr\, d\theta$$

Plugging in the result for the inner stream's velocity profile $w_i(r)$ from equation III.11 gives

$$Q_i = 2\pi \int_0^{R_i} \left\{\frac{G(R^2 - R_i^2)}{4\eta_o} + \frac{GR_i^2}{4\eta_i}\left[1 - \left(\frac{r}{R_i}\right)^2\right]\right\} r\, dr$$

$$Q_i = 2\pi \left[\frac{G(R^2 - R_i^2)R_i^2}{8\eta_o} + \frac{GR_i^4}{16\eta_i}\right]$$

which gives the following expression for the negative pressure gradient G,

$$G = \frac{8\eta_i Q_i}{\pi R_i^2 \left[2(R^2 - R_i^2)\frac{\eta_i}{\eta_o} + R_i^2\right]} \tag{III.12}$$

Next we enforce that the outer stream's flow rate be Q_o,

$$Q_o = \int_0^{2\pi} \int_{R_i}^{R} w_o(r) r\, dr\, d\theta$$

Plugging in the result for the outer stream's velocity profile $w_o(r)$ from equation III.9,

$$Q_o = 2\pi \int_{R_i}^{R} \left(\frac{GR^2}{4\eta_o} \left[1 - \left(\frac{r}{R} \right)^2 \right] \right) r \, dr$$

$$Q_o = \frac{\pi G}{8\eta_o} \left(R^2 - R_i^2 \right)^2$$

Plugging in the result for the negative pressure gradient G from equation III.12 gives that

$$Q_o = \frac{\pi}{8\eta_o} \left(R^2 - R_i^2 \right)^2 \frac{8\eta_i Q_i}{\pi R_i^2 \left[2(R^2 - R_i^2)\frac{\eta_i}{\eta_o} + R_i^2 \right]}$$

$$Q_o = \frac{\frac{\eta_i}{\eta_o} \left(R^2 - R_i^2 \right)^2}{R_i^2 \left[2(R^2 - R_i^2)\frac{\eta_i}{\eta_o} + R_i^2 \right]} Q_i$$

Solving this equation for R_i yields four solutions. The physical solution is that for which $0 \leq R_i \leq R$, which is

$$R_i = R \sqrt{\frac{(Q_i + Q_o)\eta_i - \sqrt{Q_o \eta_i (Q_o \eta_i + Q_i \eta_o)}}{Q_i \eta_i + 2Q_o \eta_i - Q_o \eta_o}} \tag{III.13}$$

Based on equation III.13, we predicted the stream width for a model system of glycerol inside glycerol. We fixed the flow rate Q_{out} of the glycerol in the outer stream and varied the flow rate Q_i of the glycerol in the inner stream. For low flow rates Q_{in}, the stream width grew roughly as the square root of the inner stream flow rate, as shown in Figure III.S2. For an inner stream width of $D_{in} > 20 \ \mu$m, the Stokes flow prediction for the inner stream width is consistent with the experimental measurements within experimental uncertainty. Therefore, we conclude that the Stokes flow solution can provide a useful estimate for the inner stream radius, although its accuracy may decrease when bubbles have nucleated in the inner stream.
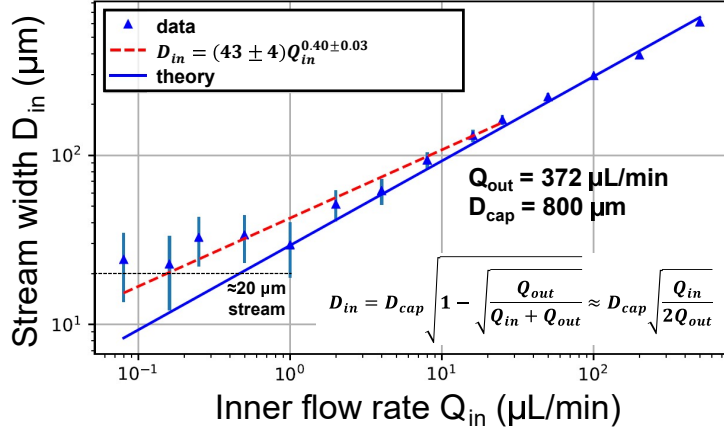
Figure III.S2: The width of the inner stream D_{in} [μm] is plotted as a function of the inner stream flow rate Q_{in} [μL/min] for an experiment flowing glycerol inside a sheath of glycerol (blue triangles with error bars indicating the experimental uncertainty in the measurement). The outer stream flow rate is fixed at Q_{out} = 372 μL/min. Based on Stokes flow of a fluid flowing inside a cylindrical shell of another fluid, the inner stream width D_{in} should follow the equation in the lower right, whose prediction is plotted (blue line) and agrees well with the measurements above 20 μm. Below 20 μm, the width of the inner stream plateaus, which could partially be the result of an optical effect. The theory simplifies to $D_{in} = D_{cap}\sqrt{\frac{Q_{in}}{Q_{out}}}$ for $Q_{in} \ll Q_{out}$, indicating that a 1/2 power-law is expected. A power-law fit is plotted (red dashed line), which has a power slightly lower than 1/2.

Lensing

Lensing is a major challenge of cylindrical capillaries. With square capillaries, lensing is eliminated because the light passes through no curved surfaces, but square capillaries and their fittings have only been shown to withstand high pressures when their dimensions are small (inner diameter of 50 μm [1]), which is not compatible with the width of the inner stream needed to prevent complete depletion of CO_2 before reaching the outlet (at least 50 μm). Lensing can occur on the inner and outer walls of the capillary, as shown in Figure III.S3. In panel (a), we show the effect of removing the lensing from the inner surface by filling the capillary with index-matched vegetable oil. In panel (b), we show the effect of removing the lensing from the outer surface by embedding the capillary in a square block of index-matched adhesive, but lensing still occurs on the inner walls, which are exposed to air. In panel (c), we show that by filling the capillary with index-matched oil and embedding it in index-matched adhesive, lensing is almost completely eliminated.
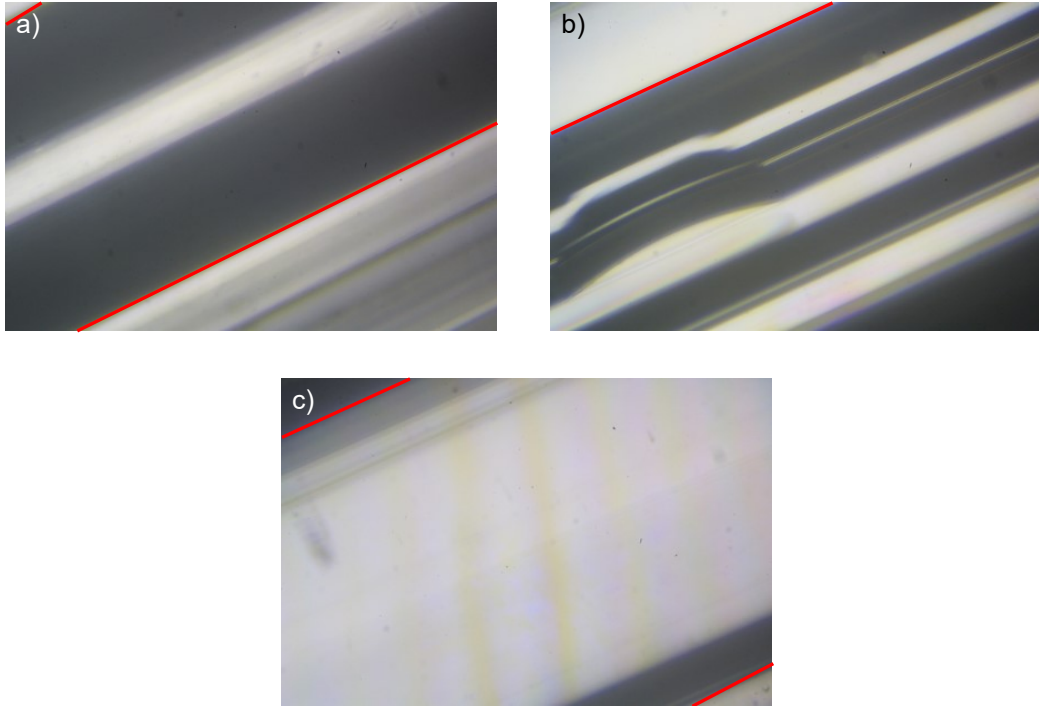
Figure III.S3: Images of borosilicate capillary (500 μm ID, 1000 μm OD) under 4x magnification with three treatments. Approximate location of inner walls of the capillary are shown with solid red lines. a) Capillary filled with index-matched oil (Wesson vegetable oil) shows lensing from a curved outer surface. b) Empty capillary embedded in square capillary filled with index-matched adhesive (146H Norland optical adhesive) shows lensing from the inner surface (slight distortion in lower right is residual oil droplet). c) Capillary filled with index-matched oil and embedded in square capillary filled with index-matched adhesive shows no lensing. Vertical streaks come from the image of the coils of the halogen light source.

III.S2   Parameter Selection

Parameter Selection

Briefly, we chose to focus on the saturation pressure of CO_2 near its critical pressure (7.39 MPa [2]) to explore the differences between supercritical and subcritical foaming. Therefore, we considered pressure quenches on the order of 10 MPa to ensure supersaturation was not reached until the fluid had traveled partway down the capillary. As discussed in Chapter IV, we ultimately focused on high-speed optical microscopy to observe bubbles. We wanted bubbles to flow at the highest speed without causing significant motion blur. The size of motion blur d_{blur} is the speed v times the exposure time τ_{exp}, $d_{blur} = v \times \tau_{exp}$. The best high-speed cameras can reach exposure times around 1 μs—shorter exposures typically are too dim to be useful. Ideally, the pixel size d_{pix} is around the diffraction limit of about

1 μm. Thus, to keep the motion blur d_{blur} smaller than the pixel size, we need $v < \frac{d_{pix}}{\tau_{exp}} \sim \frac{1\ \mu m}{1\ \mu s} \sim 1$ m/s. We chose the length of the capillary L to be roughly the length spanned by our microscope's translation stage ($\sim$ 100 mm). The residence time of the fluid in the capillary would be about $L/v \sim 100$ ms. We need the inner stream to be wide enough that it is not depleted of CO_2 before reaching the end of the observation capillary. Based on the data in Figure II.4, the maximum diffusivity we might expect is around 10^{-9} m^s/s. With that diffusivity, in 100 ms the diffusion boundary layer grows by $\sqrt{D \times t} \sim \sqrt{10^{-9}\ \text{m}^2/\text{s} \times 0.1\ \text{s}} \sim 10\ \mu$m. Therefore, the inner stream radius must be greater than 10 μm. At the same time, the inner diameter of the capillary must be small enough to maintain the $\sim 10^8$ Pa/m pressure gradient while keeping the speed of the flow below 1 m/s. In general, this requirement means that the inner stream radius must be less than 50 μm. We typically use an inner stream of 20–30 μm in radius.

We used the polyols listed in Table II.1. The most viscous polyol used was the "1k5f," which had a shear viscosity of 4820 mPa.s. Having observed that these polyols are Newtonian in the range of shear rates $\omega \in [1, 100]$ Hz, we can estimate the speed of the center of a stream of pure polyol $v_c = \frac{GR^2}{4\eta}$, where G is the pressure gradient [Pa/m], R_o is the inner radius of the capillary [m], and η is the viscosity of the fluid. As a strict upper bound, we can consider the case where the capillary is entirely filled with the most viscous polyol we will consider, which has a viscosity of about 5 Pa.s (see "1k5f" in Table II.1). The maximum inner radius of the capillary is then $R < \sqrt{\frac{4\eta v_{max}}{G}} \sim 450\ \mu$m. We ultimately considered inner radii of 100 μm, 150 μm, and 250 μm depending on the goals of the experiment. In general, we found a capillary with an inner radius of 150 μm to be most amenable to the experiments we were interested in.

To determine the wall thickness, we used the conservative form of Barlow's formula [3] to estimate the maximum pressure resistance of the capillary

$$p_{max} = \frac{2 \cdot T \cdot w}{OD} \tag{III.14}$$

where T is the tensile strength of the material [Pa], w is the wall thickness [m], and OD is the outer diameter of the capillary [m]. For tubes with a wall thickness comparable to the OD, this formula underestimates the maximum pressure resistance. Nevertheless, in case of sudden pressure spikes or imperfections in the capillary, we aimed for a pressure resistance 50% higher than the maximum pressure at which we

expected to operate (10 MPa), yielding p_{max} = 15 MPa. We considered capillaries made of borosilicate (Pyrex) or made of fused quartz. While the pristine tensile strength may be measured in excess of a GPa [4], most manufacturers report a tensile strength of 7 MPa for borosilicate and 49 MPa for fused quartz. With these values, we can estimate that, to have a borosilicate capillary with an inner radius of 150 μm (ID = 300 μm) safely withstand our target pressure, *i.e.* p_{max} > 15 MPa, its wall thickness w > 300 μm. We needed to keep the wall thickness thin enough that the observation capillary could fit inside a PEEK sleeve and the PEEK sleeve could fit inside a 1/16" VICI Valco fitting, which limited the outer diameter to about 1 mm. We ultimately used a fused quartz capillary with a wall thickness of 350 μm (Molex, ID = 300 μm, OD = 1000 μm), although we successfully performed experiments at 10 MPa without incident using a borosilicate capillary with an inner diameter of 500 μm and an outer diameter of 1000 μm (Friedrich & Dimmock).

Because we observed bubbles with optical microscopy, we set the length of the observation capillary L to match that of the range of a standard microscopy translation stage ($L \approx 100$ mm). We then determined the target flow speed to be as fast as possible without introducing motion blur. For digital imaging, motion blur occurs when an object moves more than one pixel during an exposure. To prevent motion blur, the product of the speed v and exposure time τ_{exp} must be smaller than the distance spanned by one pixel d_{pix}, so $v < d_{pix}/\tau_{exp}$. As discussed in Chapter IV, videos became too dim for exposure times $\tau_{exp} < 1$ μs, and pixels corresponded to about 1 μm with the magnification we used. Therefore, we aimed to keep the speed $v < 1$ m/s. As a result, the residence time of fluid in the channel was on the order of $L/v \sim 100$ ms.

For example, as common set of parameters in an experiment would be a pressure gradient G = 10 MPa / 0.1 s = 10^8 Pa/s, an inner stream radius R_i = 20 μm, an inner stream viscosity of η_i = 0.01 Pa.s (true for polyol with 20–30 % dissolved CO_2 by mass), and an outer stream viscosity of η_o = 5 Pa.s (polyol "1k5f'" in Table II.1), we calculate the speed along the center of the inner stream using equation III.11 for r = 0

$$w_i(r = 0) = G \left(\frac{(R_o^2 - R_i^2)}{4\eta_o} + \frac{R_i^2}{4\eta_i} \right)$$

$$\approx 1.11 \text{ m/s}$$

The predicted value of 1.11 m/s is sufficiently close to the 1 m/s desired.

For the tubing, we chose 1/16" OD because it was the smallest size for which standard high-pressure fittings and valves were available from major suppliers (*e.g.*, Valco Instruments, Swagelok). We used stainless steel because its pressure rating (10,000 psi, 69 MPa) far exceeded the pressures we considered (below 2500 psi, 17 MPa). The inner diameter was selected to be as large as possible while maintaining flexibility in the tubing—tubes with too thin of walls become inflexible. We choose Restek 1/16" stainless steel tubing with an inner diameter of 0.95 mm (measured). Finally, for the inner stream capillary, we choose the smallest stainless steel capillary available that could be silver-epoxied into this tubing, which was a CynKen 304 stainless steel tube of 0.5 mm ID $\times$ 0.8 mm OD.

III.S3 Materials for Fabrication of Flow-focusing Apparatus

We list the materials and equipment required to fabricate the flow-focusing channel shown in Figure III.3 in Table III.S1.

III.S4 High-pressure Microfluidic Flow-focusing: Device Fabrication
Machine Acrylic Tee Junction

First, we machine the 3/8"-thick acrylic block into a tee junction that can fit VICI Valco fittings. See Figure III.S4 for the dimensional drawing submitted to the machine shop.

Make Silicone Rubber Stoppers

To seal the oil or optical adhesive at the ends of the observation capillary, we use silicone rubber stoppers made in a custom mold using Smoothon Ecoflex 2-part cross-linking material. The size should match the inner dimensions of the square capillary.

Name	Quantity	Notes
Acrylic slab (3/8"-thick, at least 1" × 1")	1	To be machined for tee junction; check for crazing and strain
VICI Valco nut and ferrule	3 ea.	Nut: Valco Instr. #ZN1S6 Ferrule: Valco Instr. #ZF1S6
1/16" stainless Swagelok nut and front and back ferrule	2 ea.	Nut: Swagelok #SS-102-1 Ferrule: Swagelok #SS-100-SET
1/16" stainless steel tubing	1 m	Restek #27768 (0.040" ID, but measured to be about 950 μm)
Stainless steel capillary (0.5 mm ID × 0.8 mm OD)	> 1 cm	CynKen #CKS1824, 304 stainless steel (for inner capillary)
Silver epoxy	Pea size	MG Chemicals 8331-A & 8331-B; Paper clip works well for mixing and spreading
Extreme-pressure PEEK tubing 1/16" OD × 0.03" ID	> 0.5 cm	McMaster Carr #51085K48; drill out ID to fit observation capillary
Quartz or Pyrex capillary	100 mm	Quartz: Polymicro Molex (300 μm × 1 mm) #1068400902 Pyrex: Friedrich & Dimmock, Inc. #B100-50-100, (500 μm × 1000 μm)
NdFeB magnets	4	8 × 8 × 8 mm
3D printer	1	for printing mount (PLA filament recommended)
Steel file	1	Useful for cutting stainless steel tubing to desired length
Diamond-pointed pen	1	To score capillaries and break to right length
20 mL scintillation vial	1	For mixing 2-part silicone rubber
Wesson vegetable oil	> 5 mL	Index of refraction (1.47) matches quartz, Pyrex, and polyol
1.5 mm-thick acrylic sheet	1	Cut to 14.5 mm × 78.5 mm for base of oil reservoir
Silicone rubber	3 pcs.	one 2 × 15 mm and two 2 × 10 mm; seals oil reservoir
Loctite epoxy	≈ 1 mL	Enough to line the acrylic base
Two-part silicone rubber	5 mL	Smoothon Ecoflex 00-50
21-gauge needle	1	For boring rubber stopper

Table III.S1: Table of materials for fabricating flow-focusing channel shown in Figure III.3.

Prepare Tubing

Next, use silver epoxy to fix the inner capillary (0.5 mm ID × 0.8 mm OD stainless steel capillary) inside the stainless steel tubing (Restek). The inner capillary
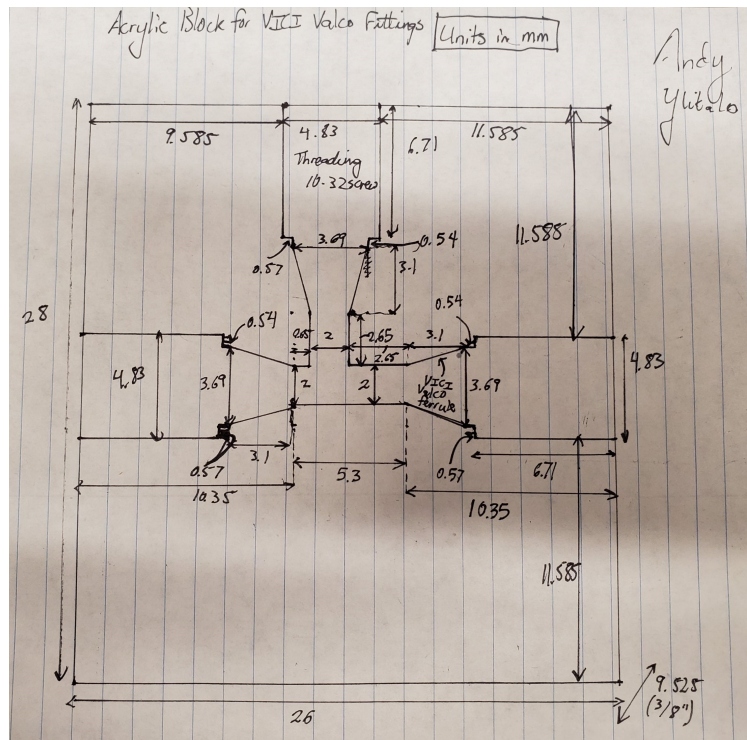
Figure III.S4: Hand-drawn dimensional sketch of acrylic tee junction to be machined from 3/8"-thick acrylic. Measurements are given in millimeters unless otherwise noted.

should extend far enough from the tubing that it clears the channel for the outer stream in the tee junction, promoting a complete and even sheath. Pump viscous polymer through the capillary before inserting it into the microfluidic apparatus to ensure that it will stay fixed under flow during experiments. The tubing should be long enough to allow for translation of the microfluidic apparatus up to 10 cm; bending the section between the ISCO pump and the apparatus into an "S" shape can provide this flexibility. The outer stream tubing is prepared similarly, but without the need for silver epoxy or as much flexibility.

Fit VICI Valco Fitting Around Observation Capillary

Next, fit a high-pressure VICI Valco fitting and PEEK sleeve onto the end of the observation capillary without breaking the capillary. The inner diameter of the PEEK sleeve may need to be bored wider with a drill to fit snugly around the observation capillary. Place the sleeve as near the end of the observation capillary as possible and thread the VICI Valco nut and ferrule over it so that a small section of the sleeve is visible beyond the end of the ferrule. Holding the pieces in their places, finger tighten into a VICI Valco fitting (HPLC fittings are suitable alternatives), then

tighten with a wrench until the fitting firmly holds the capillary in place.

3D-print Microscope Stage Mount

The design for the 3D-printed mount can be found with the data that accompanies this thesis in `3_bubble_birth/device_design/mf_mount.stl`. After 3D-printing and shaving off supports, laser cut a piece of acrylic to fit into the base of the oil reservoir and epoxy in place. Test for leaks.

III.S5   Other Device Designs

As mentioned in Section III.2, we tried to reduce lensing in the observation capillary by encasing it in a UV-cured optical adhesive (Norland #146H) instead of submerging it in an oil reservoir. This method is more consistent, is cleaner, and can allow for observation nearer the exit of the observation capillary. Nevertheless, the optical adhesive is prone to entrapping small bubbles when dispensed, which obstruct imaging. Any contamination or inhomogeneities in the optical adhesive are permanently fixed upon curing, so exquisite care is necessary for this design to provide images as clear as acquired with the oil reservoir, which is much easier to adjust. Therefore, we suggest the further development of this method as future work in Section III.4. The current, unrefined method is described below to be used as a starting point for such development.

Materials

In addition to the materials required for the fabrication of the device with the oil reservoir (excepting those used for the oil reservoir), the materials listed in Table III.S2 are required to encase the observation capillary in optical adhesive.

Fabrication

Cut the two lengths of heat-shrink tubing no more than 0.5 cm. Heat-shrink the smaller around the observation capillary about 2 cm from the top of the VICI Valco nut; repeat for the larger. Thread cylindrical observation capillary through a square capillary and mount vertically. Fill with optical adhesive very slowly, being careful not to introduce bubbles. If any adhesive enters the cylindrical capillary, clean it out and start over. Mount capillary inside an airtight vacuum chamber and apply a light vacuum to remove any remaining bubbles. After, thoroughly clean any spilled adhesive and fill the square capillary as near to the top of the observation capillary as possible without allowing any to enter the capillary. Cure with UV containing 325 nm and 365 nm wavelengths.

Name	Quantity	Notes
Optical adhesive (n = 1.46)	1 mL	Norland Optical Adhesive 146H (#12-864); index-matched to polyol (1.48), pyrex (1.47), and quartz (1.46)
Square glass capillary (2.0 mm ID × 0.3 mm wall thickness)	8–8.5 cm	Friedrich and Dimmock BST-2-30
Heat-shrink tubing	2 pcs	3 mm diameter, 5 mm length; for centering observation capillary
Two-part silicone rubber stopper	1	Smoothon Ecoflex 00-50
UV-cure chamber	1	Large enough to house observation capillary when mounted vertically (Thermal Spa used for curing nail polish works)
Vacuum chamber	1	large enough to house observation capillary when mounted vertically

Table III.S2: Table of materials for encasing observation capillary in square capillary filled with index-matched optical adhesive of flow-focusing channel shown in Figure III.3.

III.S6   Other Methods Considered for Observing Early Bubble Growth

The microfluidic channel shown in Figure III.3 was originally designed for compatibility with many imaging modalities due to the possibility of observation with long exposure times. In the present work, we focused on one, high-speed optical microscopy. Here, we describe two other imaging modalities considered and explain why they were not pursued.

Small-angle X-ray Scattering (SAXS)

The earliest microfluidic flow-focusing devices were designed for use with small-angle X-ray scattering (SAXS) [5] and bubble nucleation occurs within the dimensions it probes (1–100 nm [6]). Terekhov *et al.* used SAXS to measure the size distribution of nanometer-sized helium bubbles trapped in borosilicate [7]. While the size range of SAXS is appropriate for detecting bubble nuclei, detecting bubbles in dynamic systems has not been demonstrated due to the long exposure times required (seconds). Because the instrument designed in the present study allows for continuous observation of a particular point in the foaming timeline, it allows for longer exposure times. We could then estimate an average bubble distribution by averaging the signal over time, as demonstrated for the detection of the nucleation

of CO_2 particles under rapid cooling by Dingilian *et al.* [8]; additional applications of this technique were reviewed by Silva [9] and Ghazal *et al.* [10]. Furthermore, because the observation capillary can be made of fused quartz, which has a weaker background signal than borosilicate glass, the faint signal of the bubbles would not be overwhelmed by the background. The instrument is also easily portable to a beamline as long as two ISCO pumps, a Parr reactor, and gas cylinders are available. Nevertheless, we found that even a long exposure at the Advanced Photon Source at Argonne National Laboratory might not produce enough signal to detect bubble nucleation due to the low nucleation density observed and low density difference between bubble nuclei and polyol predicted.

SAXS detects differences in densities that cause small deflections of incident X-rays. Because the intensity of the signal is proportional to the square of the density difference [11], a solution of nanoparticles produces the same signal as a solution of bubbles even though nanoparticles are denser than the solvent while bubbles are less dense. We thus estimate the signal-to-noise ratio (SNR) of bubble nuclei with SAXS by measuring the signal from various concentrations of silica (SiO_2) nanoparticles in water (Nanocomposix #SISN50-25M, 50 ± 3 nm diameter) and converting to the equivalent number density of bubbles. The measurements were taken at beamline 5-ID-D of the Advanced Photon Source (APS) at the Argonne National Laboratory (Argonne, IL, USA). We pumped various dilutions of the nanoparticles into the quartz viewing cell of a Linkam stage (1.5 mm ID, 100 μm wall thickness) and scanned each concentration ten times with 3-second exposures. We repeated each measurement with deionized water to provide a background. Subtracting the background revealed a scattering signal, which is shown for different dilutions of aqueous SiO_2 nanoparticle solution in Figure III.S5. The wavelength of X-rays was 0.7293 Å and the sample–detector distance was 8.5028 m.

From Figure III.S5, we can see that the SAXS signal at 12.50 ppm of the nanoparticles follows the expected decreasing peaks and valleys of a solution of nearly monodisperse spheres (the slight polydispersity causes the valleys to be more shallow) [11]. At higher wave numbers q and lower concentrations of nanoparticles, the signal weakens and is drowned by noise, such that there is no discernible signal above the background at 0.78 ppm of nanoparticles. We want to determine the lowest weight fraction of nanoparticles that would give a discernible signal above the noise and estimate the number density of bubbles of CO_2 in polyol that would give a similar signal. If our microfluidic channel cannot produce a greater number density
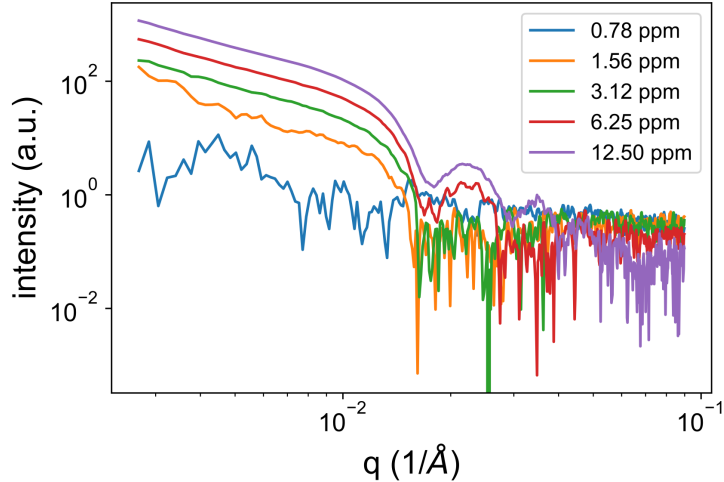
Figure III.S5: Intensity of small-angle X-ray scattering (SAXS) signal as a function of the wave number q of different concentrations of aqueous solutions of SiO_2 nanoparticles (concentrations given in ppm in legend). Signal is computed by subtracting background from water and quartz capillary. Measurements taken at beamline 5-ID-D of the Advanced Photon Source at Argonne National Laboratory (Argonne, IL, USA).

of bubbles, then we would not expect a discernible signal from bubble nucleation using SAXS.

To estimate the noise in the signal, we compute the statistical uncertainty in the signal computed by subtracting the background (water) from a scan (water and nanoparticles) σ_{signal}. We estimate this uncertainty by adding the standard deviation in the intensity of scans of water and nanoparticles (signal + background) σ_{scan} to the standard deviation in the intensity of scans of water (background) σ_{bkgd} in quadrature, $\sigma_{signal} = \sqrt{\sigma_{scan}^2 + \sigma_{bkgd}^2}$. Because the background drifts much more than the statistical uncertainty over the course of experiments (1 hour), as shown in Figure III.S6, we isolate the statistical uncertainty by computing the standard deviation of sets of ten consecutive scans and then averaging across each set of non-consecutive scans. This drift prevents the reduction in the noise level by averaging over more consecutive scans.

We compare our estimate for the statistical uncertainty to the background-subtracted signal of an aqueous solution of 1.6 ppm SiO_2 nanoparticles and the background signal in Figure III.S7. The signal-to-noise ratio (SNR) is roughly largest near the forward scattering peak $I(q = 0)$, where the signal is about 3.4 times larger than the noise $I(q = 0) \approx 3.4\sigma_{bkgd}(q = 0)$. We would therefore expect
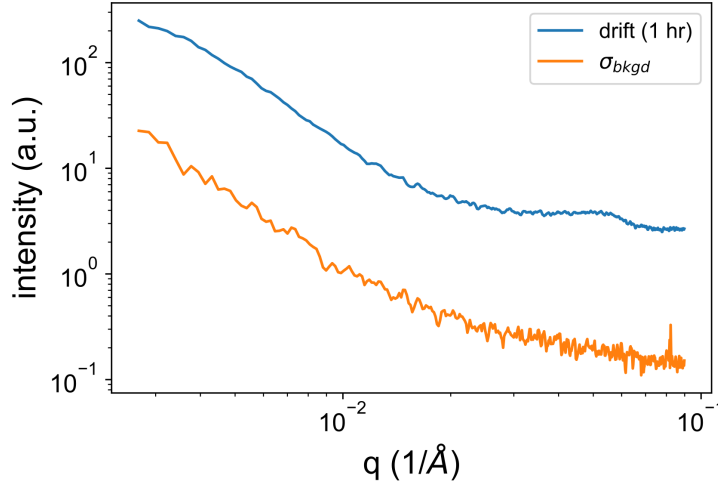
Figure III.S6: Comparison of drift in background signal (water and quartz capillary) over 1 hour and the standard deviation within ten consecutive background scans for scans shown in Figure III.S5.

no discernible signal at concentrations below 1.6 ppm / 3.4 ≈ 0.5 ppm. Indeed, we see in Figure III.S5 that while the signal at 1.56 ppm (orange) is discernible at low q values, the signal at 0.78 ppm is indistinguishable (blue) from the background, suggesting that our estimate of a discernible signal at 0.5 ppm is low.

Using 0.5 ppm as our estimate of the lowest concentration of SiO_2 nanoparticles that produce a SAXS signal discernible above the noise, we will estimate the number density of CO_2 bubbles in a polyol–CO_2 mixture that would produce a similar signal. Although we will show a model in Chapter VI that predicts bubbles nucleate with a diameter around 5–10 nm, these nuclei are much smaller and denser, so they will produce a significantly weaker SAXS signal than 50 nm bubbles; if we cannot detect a signal from 50 nm bubbles, neither will we detect a signal from bubble nuclei. For a fixed beam intensity, the forward scattering $I(q = 0)$ is proportional to the square of the total excess scattering length of a particle and the number density of particles. The total excess scattering length scales with the square of the product of the difference between the densities of the particles and the solvent $\Delta\rho = \rho_{part} - \rho_{solv}$ and the volume of each particle V [11]. Thus, the forward scattering $I(q = 0) \propto (\Delta\rho V)^2 n$. For $I(q = 0)$ to be equal for a solution of SiO_2 nanoparticles and a solution of bubbles,
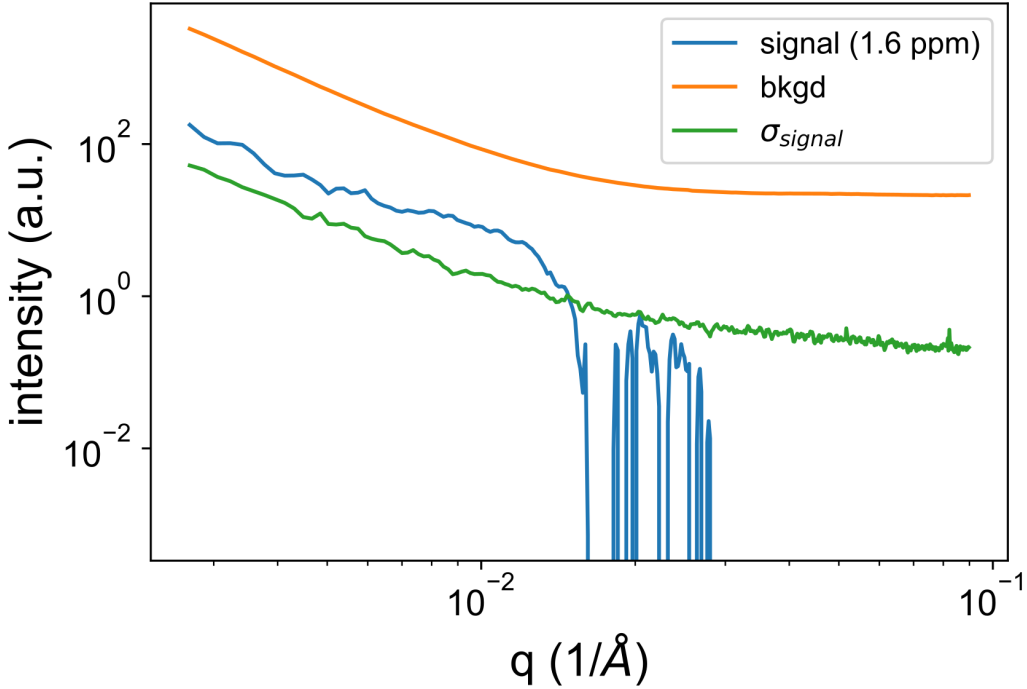
Figure III.S7: Comparison of small-angle X-ray scattering (SAXS) signal (blue) of a 1.6 ppm aqueous solution of 50 nm SiO_2 nanoparticles, the background (water and quartz capillary; orange), and the statistical uncertainty in the signal (σ_{signal}). Note that the signal becomes featureless when its intensity decreases below the statistical uncertainty.

$$I_{SiO2}(q = 0) = I_{bub}(q = 0)$$

$$(\Delta\rho_{SiO2}V_{SiO2})^2 n_{SiO2} = (\Delta\rho_{bub}V_{bub})^2 n_{bub}$$

Assuming bubbles of 50 nm in diameter, $V_{SiO2} = V_{bub}$, so

$$n_{bub}^{equiv} = \left(\frac{\Delta\rho_{SiO2}}{\Delta\rho_{bub}}\right)^2 n_{SiO2} \tag{III.15}$$

where $\Delta\rho_{SiO2} = \rho_{SiO2} - \rho_{H2O}$ and $\Delta\rho_{bub} = \rho_{CO2} - \rho_{poly}$. The densities of SiO_2 and H_2O are known to be $\rho_{SiO2} = 2.26$ g/mL and $\rho_{H2O} = 1.0$ g/mL, respectively. While our predictions suggest that CO_2 bubbles nucleate with a liquid-like density (see Figure VI.4), by the time they have grown from their initial size of around 10 nm to 50 nm, we estimate that the density of CO_2 inside would decrease to about $\rho_{CO2} \approx 0.1$ g/mL (see predictions of bubble growth model in Figure V.7). Finally, the density of polyol–CO_2 mixtures remain around $\rho_{poly} \approx 1.0$ g/mL based on the

G-ADSA measurements reported in Section II.2. Plugging in these values gives the relationship

$$n_{bub}^{equiv} \approx 2n_{SiO2} \qquad \text{(III.16)}$$

indicating that twice as many 50-nm bubbles of CO_2 in polyol as 50-nm SiO_2 nanoparticles in water are needed to generate the same SAXS intensity. In some cases, we expect the bubble to nucleate with a liquid-like density (see Chapter VII). If the density remains liquid-like when the bubble has grown to tens of nanometers, the signal will be much weaker than predicted in the following analysis as a result of the squared dependence on the difference in density from the solvent.

The concentration of SiO_2 nanoparticles in the aqueous solution was given in a parts per million weight fraction w_{SiO2}. Because of the low concentration, the density of the solution is roughly that of water, 1.0 g/mL, so the weight fraction in [g SiO_2 /g solution] is equivalent to the weight fraction in [g SiO_2 / mL solution]. Each SiO_2 nanoparticle has a mass of $m_{SiO2} = \rho_{SiO2} \left(\frac{4}{3}\pi R_{SiO2}^3 \right) \approx 1.5 \times 10^{-10}$ μg, where $R_{SiO2} = 25$ nm is the radius of a nanoparticle. The number density of nanoparticles is therefore $n_{SiO2} = w_{SiO2}/m_{SiO2}$, for w_{SiO2} in ppm and m_{SiO2} in μg. Thus,

$$n_{bub}^{equiv} \approx \frac{2}{1.5 \times 10^{-10} \ \mu\text{g}} w_{SiO2} \qquad \text{(III.17)}$$

We determined above that the lowest weight fraction of SiO_2 nanoparticles with a discernible signal is $w_{SiO2} \approx 0.5$ ppm, so the equivalent number density of bubbles is $n_{bub}^{equiv} \approx \frac{2}{1.5 \times 10^{-10}} \times 0.5$ bubbles/ mL $\approx 6 \times 10^9$ bubbles / cm^3. This density is equivalent to a lattice of bubbles separated by a distance of $(n_{bub}^{equiv})^{-1/3}$ cm ≈ 5.5 μm. Given that the closest we have observed bubbles nucleate is on the order of 10 μm (see Figure V.7) and that most of the observation capillary is filled with pure polymer, we concluded that our experimental method does not nucleate enough bubbles to be detected by SAXS at 50 nm diameter, let alone at 5–10 nm upon nucleation.

Light Scattering

Light scattering is another technique known for its ability to detect and measure the size of sub-micron objects [12], including bubbles [13]. Mie scattering of droplets of polyol supersaturated with CO_2 was explored as a complementary method for detecting bubble nucleation by Laccetti, although further work remains

to generate droplets from high-viscosity liquids, generate droplets with dissolved gas, and generate droplets while maintaining high pressure [14]. Light scattering could also be applied to the instrument presented in Figure III.3. While a laser could be coupled into the inner stream from upstream, such as through an optical window inserted into a bored hole in a 90° elbow junction, the laser would leak out of the inner stream upon ensheathing due to the higher index of refraction of the outer stream, leading to attenuation of the signal before reaching a bubble—see the schematic in Figure III.S8. Alternatively, a plane-wave laser could be directed along the length of the observation capillary and observed with a wide-angle camera to detect early nucleation events along the capillary.
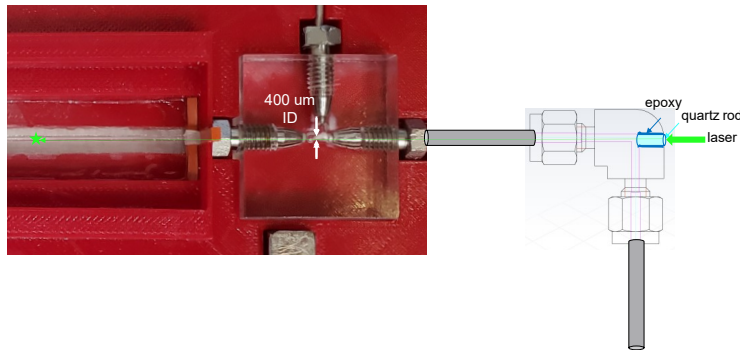
Figure III.S8: Schematic of an idea for laser scattering. A laser (green) could be coupled into an epoxied quartz rod aligned inside a 90° Swagelok elbow joint aligned along the inner stream tubing and observation capillary. The alignment is critical because the inner stream has a lower index of refraction than the outer stream due to the dissolved CO_2, so a laser signal will attenuate as it passes along it. If the alignment is precise, as could be achieved with an optical bench, the laser could be scattered by nanoscopic nuclei almost as soon as they nucleate along the observation capillary and the locations recorded with a wide-angle camera lens.

We anticipate that the most feasible application of light scattering would involve the focus of a laser directed perpendicularly to the observation capillary at a precise point along its length, ideally with a spot size less than 1 mm. While the matching of the indices of refraction of the outer stream, quartz observation capillary, and oil reservoir eliminates most lensing effects, the difference in index of refraction between the inner and outer streams due to the presence of high concentrations of dissolved gas or other additives (Chapter VII) in the inner stream would distort the background scattering. The detection of a bubble would therefore require that the signal from the bubble is distinguishable from these distortions as well as the fluctuations therein caused by disturbances in the inner stream. We have

not implemented this method, but offer it as a suggestion for future work.

References

1. Bourges, A. C., Lazarev, A., Declerck, N., Rogers, K. L. & Royer, C. A. Quantitative High-Resolution Imaging of Live Microbial Cells at High Hydrostatic Pressure. *Biophysical Journal* **118,** 2670–2679. ISSN: 15420086. https://doi.org/10.1016/j.bpj.2020.04.017 (2020).

2. NIST. *NIST Standard Reference Database Number 69* 2022. https://webbook.nist.gov/chemistry/ (2022).

3. Adams, A. J., Grundy, K. C., Kelly, C. M., Lin, B. & Moore, P. W. *The Barlow Equation for Tubular Burst: A Muddled History* in *IADC/SPE Drilling Conference and Exhibition* (SPE, Forth Worth, TX, USA, Mar. 2018). https://onepetro.org/SPEDC/proceedings/18DC/3-18DC/Fort%20Worth,%20Texas,%20USA/214112.

4. Holmquist, T. J. & Wereszczak, A. A. The Internal Tensile Strength of a Borosilicate Glass Determined from Laser Shock Experiments and Computational Analysis. *International Journal of Applied Glass Science* **5,** 345–352. ISSN: 20411286. https://onlinelibrary.wiley.com/doi/10.1111/ijag.12097 (Dec. 2014).

5. Pollack, L. *et al.* Compactness of the denatured state of a fast-folding protein measured by submillisecond small-angle x-ray scattering. *Proceedings of the National Academy of Sciences* **96,** 10115–10117. ISSN: 0027-8424. http://www.pnas.org/content/pnas/96/18/10115.full.pdf%20http://www.pnas.org/cgi/doi/10.1073/pnas.96.18.10115 (Aug. 1999).

6. Schnablegger, H. & Singh, Y. *The SAXS Guide: Getting acquainted with the principles* 4th ed., 50–90. ISBN: 18012013. https://austria-forum.org/web-books/en/saxs00en2013iicm/000072 (Anton Paar GmbH, Austria, Graz, Austria, 2017).

7. Terekhov, A. Y. *et al.* Small-angle X-ray scattering measurements of helium-bubble formation in borosilicate glass. *Journal of Applied Crystallography* **39,** 647–651. ISSN: 0021-8898. http://scripts.iucr.org/cgi-bin/paper?S0021889806025672 (Oct. 2006).

8. Dingilian, K. K. *et al.* Homogeneous nucleation of carbon dioxide in supersonic nozzles I: Experiments and classical theories. *Physical Chemistry Chemical Physics* **22,** 19282–19298. ISSN: 14639076 (2020).

9. Silva, B. F. B. SAXS on a chip: from dynamics of phase transitions to alignment phenomena at interfaces studied with microfluidic devices. *Physical Chemistry Chemical Physics* **19,** 23690–23703. ISSN: 1463-9076. http://xlink.rsc.org/?DOI=C7CP02736B (Sept. 2017).

10. Ghazal, A. *et al.* Recent advances in X-ray compatible microfluidics for applications in soft materials and life sciences. *Lab on a Chip* **16,** 4263–4295. ISSN: 1473-0197. http://xlink.rsc.org/?DOI=C6LC00888G (Nov. 2016).

11. Svergun, D. I. & Koch, M. H. J. Small-angle scattering studies of biological macromolecules in solution. *Reports on Progress in Physics* **66,** 1735–1782. ISSN: 0034-4885. http://stacks.iop.org/0034-4885/66/i=10/a=R05?key=crossref.536fbea0624dc0240270c53faac55ce5 (Oct. 2003).

12. Stetefeld, J., McKenna, S. A. & Patel, T. R. Dynamic light scattering: a practical guide and applications in biomedical sciences. *Biophysical Reviews* **8,** 409–427. ISSN: 18672469. http://dx.doi.org/10.1007/s12551-016-0218-6 (2016).

13. Han, J. H. & Dae Han, C. Bubble nucleation in polymeric liquids. I. Bubble nucleation in concentrated polymer solutions. *Journal of Polymer Science Part B: Polymer Physics* **28,** 711–741. ISSN: 08876266. https://onlinelibrary.wiley.com/doi/10.1002/polb.1990.090280509 (Apr. 1990).

14. Laccetti, B. J. *Therapeutic Microparticles and Biolistic Drug-Delivery to the Cornea* PhD thesis (California Institute of Technology, 2020). https://resolver.caltech.edu/CaltechTHESIS:10182020-133113205.

Chapter IV

Baby Videos: High-speed Optical Microscopy Observes Early Growth of Bubbles

You can observe a lot just by watching.

Yogi Berra

The question is not what you look at, but what you see.

Henry David Thoreau, August 5, 1851

An apparatus is useless without detection. A powerful mode of detection for humans is visual observation. Our eyes train our whole lives to see patterns: they are just missing patterns to look at. While X-ray or light scattering would have provided earlier detection of bubble nuclei, optical microscopy provided a powerful platform for our intuition. Just by watching, we learned a tremendous amount about this system. Unfortunately, our brains and eyes are slow: just watching all the recorded video generated for the present thesis would take weeks, let alone analyzing it. Here, we briefly describe the image-processing algorithms that watched and analyzed these videos. From these videos, the algorithms detect, track, and measure each bubble, and extract the size, speed, position, time, and other important measured properties into a reduced dataset. This dataset provides the input for fitting the bubble growth model presented in Chapter V that ultimately predicts the conditions of nucleation discussed in Chapters VI and VII.

IV.1 Image Processing Detects, Tracks, and Measures Bubbles

Amidst the many phenomena occurring in the flow-focusing channel, the image-processing algorithm detected, tracked, and measured bubbles observed under high-speed microscopy as they flowed down the flow-focusing channel. While it could not identify bubble nucleation due to the limited resolution of the microscope, the algorithms could measure the early growth precisely enough to fit a model that could predict the nucleation (Chapter V). The key components of this algorithm were background subtraction, image segmentation, and object tracking. These algorithms were primarily based on the OpenCV computer vision library [1]. The completed `CvVidProc` algorithm is available on github [2], as is its implementation for the present work `bubbletracking_koe` [3].

Background Subtraction

Among the most important steps of successful image processing is the distinction between objects of interest and background. Images are rich with detail, but often only a few of those details matters to the analysis. In this case, few frames in each video contained a bubble, and the bubble occupied a small fraction of the field of view. A simple technique for distinguishing the objects of interest is to generate an estimate for the parts of the image that are not interesting (the "background") and subtract it from each frame. In more complex measurements, this background may change over time. Here, we fixed the position of the observation capillary within the field of view of the microscopy during each recording, so the background remained static, excepting an instability in the inner stream (see Section VIII.4).

We considered three methods for background subtraction, which are compared in Figure IV.1: selecting a frame without any observable bubbles (usually the first frame), taking the mean of several frames, and taking the median of several frames. The median is typically recommended [4], but can be computationally more expensive due to higher memory requirements without a multithreaded algorithm like `CvVidProc` [2]. Indeed, taking the median provided the cleanest image of the background despite the presence of bubbles in some of the frames (*e.g.*, the first frame). The median algorithm fails, however, if there are pixels that are obstructed by objects in more than half of the frames sampled, which could occur in videos taken near the outlet of the observation capillary where a continuous foam (see Figure III.3) or fluid instability (see Figure VIII.11) had formed.

Using the median as the background, we subtracted the background from
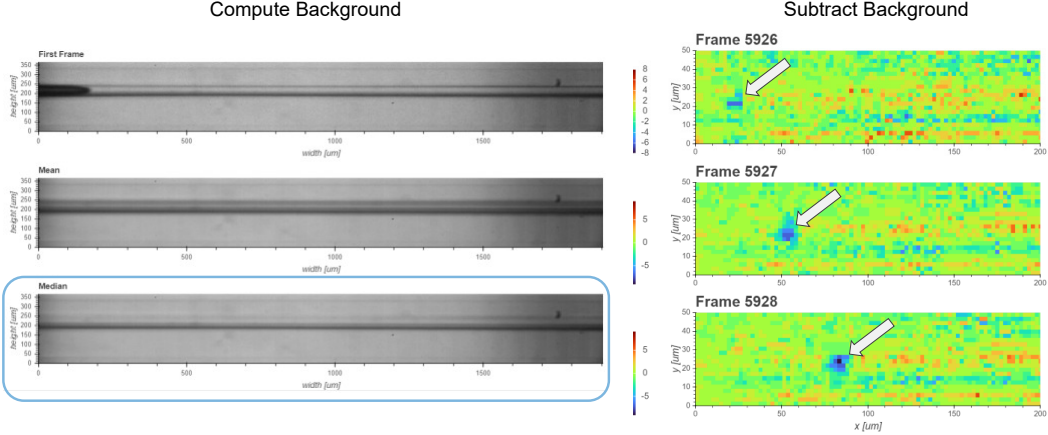
Figure IV.1: Left) Three background-subtraction methods are compared: selecting the first frame, taking the mean of the pixels in several frames, and taking the median of the pixels in several frames. Selecting an individual frame can sometimes include an anomaly or even an object, such as the bubble emerging from the left in the example shown. The mean is sensitive to objects in the foreground like bubbles, resulting in the darker pigment of the inner stream. The median provides the most accurate estimate of the background (circled in blue). Right) A sequence of three frames with the median-calculated background subtracted. The sign of the difference is kept and given a false coloring, in which red represents positive values (brighter than the background), blue represents negative values (darker than the background), and green represents values near 0. A bubble can be discerned as a blue spot growing in size from frame to frame.

each image in a high-speed video of the flow-focusing channel. Because bubbles are always darker than the background due to their strong scattering of light, we kept track of the sign of the image upon subtracting the background, which is not commonly implemented in background-subtraction algorithms due to the inconvenience and added memory of changing from an unsigned to a signed datatype. When detecting bubbles, we could ignore any positive differences from the background (brighter regions) and apply image segmentation only to the darker regions. On the right of Figure IV.1 are three example frames after applying background subtraction. False-coloring allows for the visualization of positive (red) and negative (blue) differences from the background. These frames show the first optical detection of a bubble (frame 5926) followed by its subsequent growth (bubble is blue spot indicated by white). Due to the partial volume effect resulting from the large pixel size relative to the initial bubble size, the first signal of the bubble is fainter than in later frames when the bubble has grown. Nevertheless, the signal from even the smallest bubble ($\sim 1~\mu$m) is easily distinguishable from the noise in the background, indicating that bubbles could be segmented almost at pixel scale.

Image Segmentation

Having removed the background and enhanced the signal from the bubbles, we perform image segmentation, in which pixels are classified as belonging to different objects or to the background. Image segmentation provides the basis for measurement because it reveals the spatial extent of each object. While the background has been subtracted, it has not yet been identified, so the first step of most image segmentation is the distinction between background and foreground. This distinction can quickly be made by applying a threshold to the image: pixels with values (after subtracting) beyond the threshold are classified as objects (foreground) while the rest are classified as background. The edges of bubbles tend to be fainter than the core, however. If applying a uniform threshold, a high threshold will exclude these dimmer edges while a low threshold will risk the inclusion of noise in the foreground; a useful compromise is not always feasible. Instead, we apply a hysteresis threshold, whose operation according to the `scikit-image` package [5] is depicted schematically in Figure IV.2a. After applying a high uniform threshold, a hysteresis threshold will apply a lower threshold to pixels contiguously connected to those pixels that exceeded the high threshold. The result is more accurate detection of edges with less detection of noise, and the resulting segmented shape more accurately represents the object (see Figure IV.2b).

In the present work, both a uniform and hysteresis threshold are combined. The thresholds are determined by performing the analysis at a sequence of threshold values for a few videos and identifying a value for which the number of true bubbles detected varies minimally under perturbations to the threshold value.

After separating foreground from background, accurate image segmentation relies on the application of processing steps that utilize the unique properties of the objects of interest. For example, because bubbles are generally round, we can apply erosion and dilation steps to smooth out the edges of objects and arrive at less noisy segmentations of bubbles. We also fill holes in our segmentation because the center of some larger bubbles may appear translucent and thus be counted as part of the background. Because we know that these regions are always surrounded by pixels classified as foreground, they can be added to the foreground by filling holes. Finally, because we cannot always distinguish the detection of a bubble the size of a single pixel and salt-and-pepper noise in the background, we require the foreground to include only objects larger than a minimum number of pixels (usually 4). Once segmented, area, dimensions, orientation, centroid, position, and other properties

a)

b)
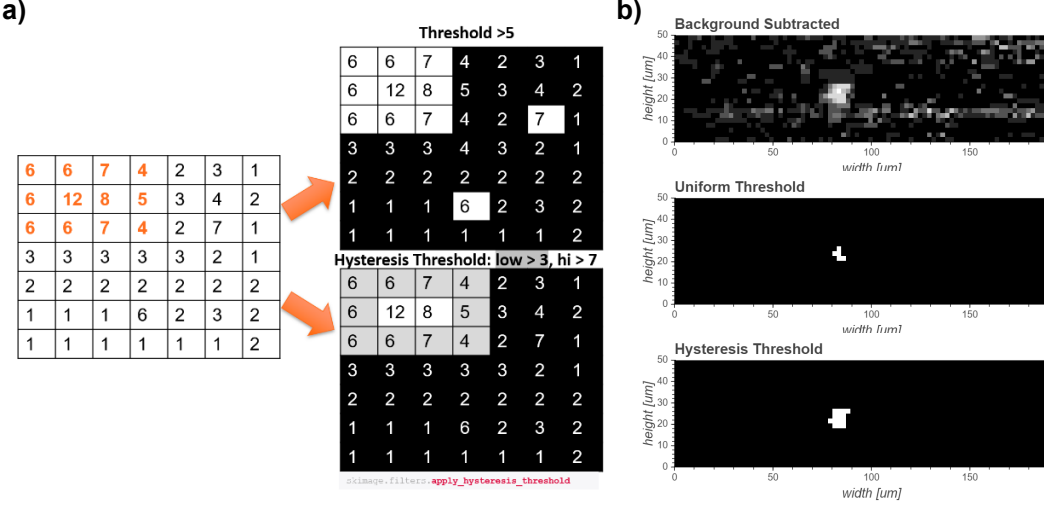
Figure IV.2: Schematic of hysteresis thresholding, as implemented by `scikit-image` [5]. a) The large array of pixels represents the pixel values following background subtraction. The values highlighted in orange are those representing the object (a rectangle), while the values in black text resulted from noise. Using a uniform threshold of 5 incorrectly segments the object and detects noise (follow orange arrow up and to the right). Perfect segmentation is achieved by using a hysteresis threshold, which first applies a high threshold of 7 followed by a threshold of 3 on pixels contiguously connected to those that passed the high threshold (follow orange arrow down and to the right). b) Top image shows a background-subtracted frame containing a small bubble (gray patch in the center). Applying a uniform threshold that does not pick up any noise poorly segments the object and the shape is unrecognizable (middle image). Applying a hysteresis threshold yields a better segmentation (bottom image).

of objects in the foreground can be measured. An example result of this image-segmentation algorithm and subsequent measurement is shown in Figure IV.3, in which an especially complex image is parsed into reasonable representations of bubbles. Further filtering by shape and dimensions can distinguish bubbles (round edges and less slender) from particles (jagged edges and often more slender).

Object Tracking

To track objects between frames, we adopted the "tracking-by-detection" paradigm, in which object detection and tracking are separate tasks, with tracking relying on the features and position of the objects detected (for a deeper discussion of this paradigm, refer to Chapter 2 of the thesis by Murray [6]). After segmenting the objects in two consecutive frames, we compared the distances between the positions of the objects. We used a custom distance metric to take into account that bubbles
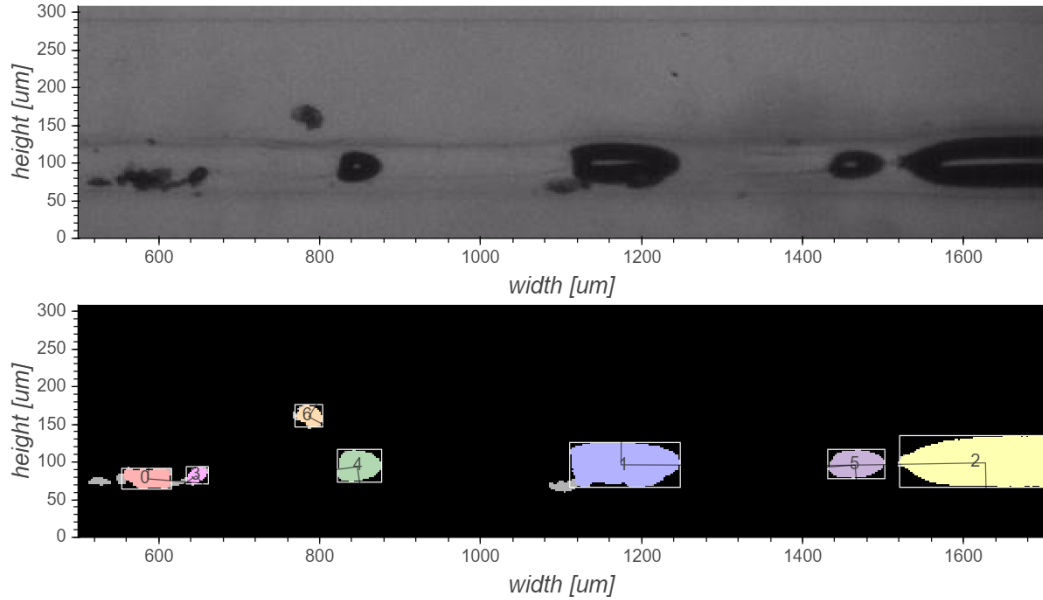
Figure IV.3: Example of the result of applying the image segmentation algorithm described in the text. Given a frame from a video recording of a foaming experiment (top image), the image segmentation algorithm identifies which pixels belong to which object, labels the objects (label drawn at centroid), and computes their orientation and dimensions, among other properties not shown (bottom image). Gray regions are those that passed the threshold but were excluded from the segmented object by the segmentation algorithm. Note that non-bubble features like the contaminant particle at the lower left of object 1 and the particles surrounding object 0 are removed by the algorithm.

tend to travel at a consistent speed along the flow direction. Distances off the flow axis were penalized more highly and distance along the flow axis was measured from the predicted position based on the estimated speed. An object that appeared upstream of an object in a subsequent frame was considered infinitely far away based on the assumption that bubbles only travel downstream. Using this distance metric, we applied the classic Hungarian algorithm to associate objects of the same identity in consecutive frames [7], as depicted schematically in Figure IV.4.

After evaluating the distance metric d between each pair of objects between the two consecutive frames, the resulting distance matrix is searched for the smallest value, which is 2 in this example (orange circle). Object 3 in the previous frame is then identified as the same object as object c in the new frame, and all entries in the corresponding row and column are removed from the matrix (indicated by orange lines). The algorithm repeats the process, looking for the smallest distance metric in the remaining matrix, which is 4 (blue circle). Note that, although the distance
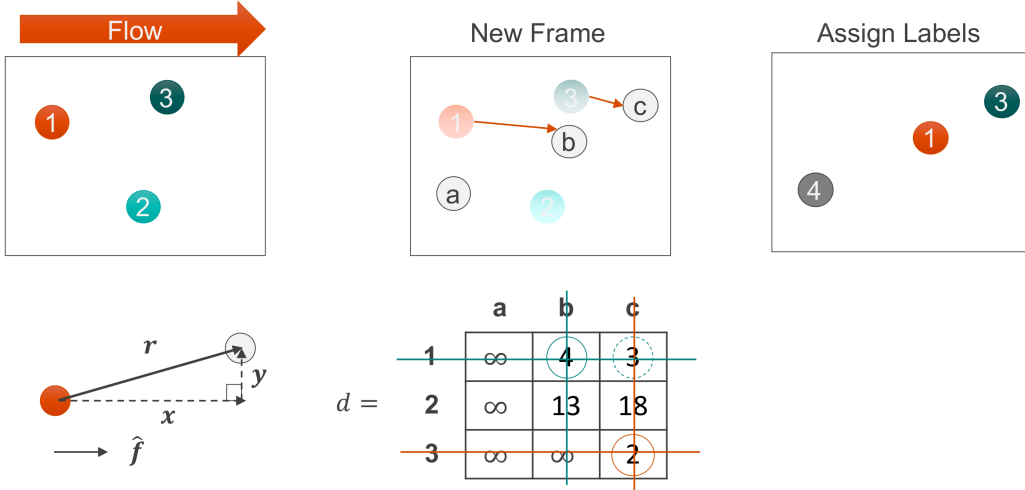
Figure IV.4: Schematic depicting the implementation of the Hungarian tracking algorithm [7] with a custom distance metric. Given a frame in which three objects have been segmented (1, 2, and 3 in the upper left) with flow from left to right, and given a second "New Frame" in which three other objects have been segmented (a, b, and c in the upper center), the distance metric is computed between each pair of objects between the frames by weighing the on- and off-flow-axis distances differently (depicted by triangle in lower left), where any bubble that is upstream of another bubble is treated as infinitely far away. The resulting distances are given in the matrix d (lower center). The algorithm successively identifies the smallest distance in the matrix, identifies the objects corresponding to its row and column, and removes that row and column from the matrix. Specifically, it first matches objects 3 and c (orange circle and omission of row and column crossed out by orange lines) and then matches objects 1 and b (same but in blue). Objects 2 and a are not matched because they are treated as infinitely far away, so object 2 is removed from the list and object a is registered as a new object, object 4. The new labels are assigned and can be used for tracking in the next pair of consecutive frames (upper right).

between object 1 and object c is smaller (3, blue dashed circle), because object c has already been assigned to object 3, this value is omitted from the search. Object 1 in the previous frame is then identified as the same object as object b in the new frame, and all entries in the corresponding row and column are removed from the matrix (indicated by blue lines). Because the only remaining distance is infinite (between object 2 and object a), we declare those two objects as distinct. Object 2 is then removed from our list of objects and object a is added as object 4 for the next frame. This process repeats until the end of the video is reached. In a more sophisticated implementation of this algorithm, "memory" can be implemented, in which case objects are not removed from the list of objects in the previous frame until

they have been absent for multiple consecutive frames. In this implementation, the object's position is extrapolated from its previous locations. While this strategy may improve the robustness of tracking some fainter bubbles through inhomogeneities in the background, it would also incorrectly assign a speck of noise that was registered in one frame to a true object a few frames later, so it was omitted from the final analysis.
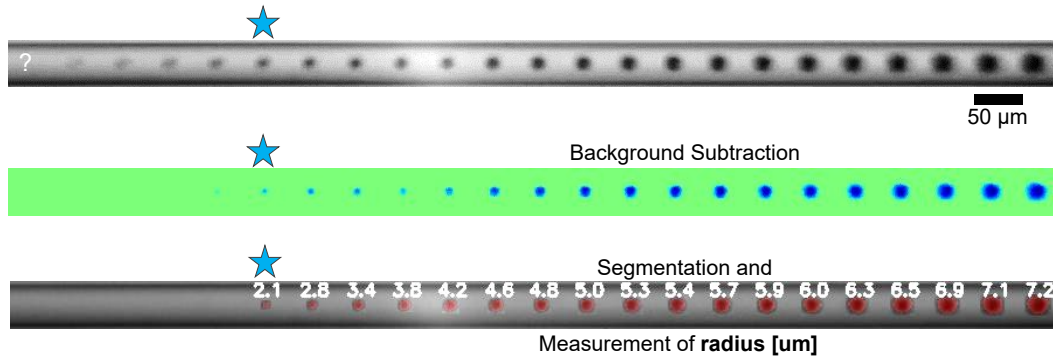
Figure IV.5: The result of image segmentation and tracking is applied to a bubble detected in an inner stream of PPG 2700 g/mol saturated with CO_2 at 7.0 MPa and 22 °C (same conditions as plotted in Figure V.7). Top) Superimposed images of bubble as it flows and grows along inner stream (outer stream outside field of view). Middle) Top frame after background subtraction of the median and application of a hysteresis threshold. Some images of the bubble are removed because they were too faint to pass the threshold. Bottom) Result of image segmentation highlighted in red with the estimated radius in μm listed above each observation of the bubble. While the first detection of the bubble by the algorithm is at the blue star, the bubble can be distinguished in earlier frames, but the algorithm can nevertheless not detect nucleation directly. Recorded with the 10x objective listed in Table III.1.

The result of the background subtraction, image segmentation, and object-tracking algorithms described above is the measurement of the size, shape, position, speed, etc. of a bubble over several frames. Given a bubble whose observations are superimposed in the frame shown in the top of Figure IV.5, background subtraction and thresholding can highlight the bubbles as shown in the middle panel, and segmentation and tracking identify the bubble (red highlights) and estimate properties like its radius (recorded in μm above each observation of the bubble). While false positives from fluctuations in the inner stream and other sources of noise must be filtered out based on position, speed, orientation, shape, and growth of the object, we can then estimate the number of true bubbles observed in an experiment. As shown in the Figure, even a blurry image can be processed to track a reasonable bubble size down to a radius of about 2 μm. Given that the human eye can still

detect the bubble four frames (corresponding to about 70 μs at 60,000 fps) before the first detection by the image processing (marked by a blue star in the Figure), the image processing could be fine-tuned further to capture the bubble at a smaller size. Nevertheless, image processing will never detect bubble nucleation, which occurs on the scale of less than 10 nm (see critical bubble volume predicted by the string method in Figure VI.4).

Instead of fine-tuning the image processing, we used a theoretical model to "see" smaller. In Chapter V, we discuss how we fit a model of bubble growth to the bubble radius measured by the image-processing techniques discussed in this Chapter. By extrapolating its predicted growth dynamics back to the critical radius, we estimated the point along the observation capillary at which the bubble nucleated.

A Comment on the Importance of Efficient Algorithms

The algorithm to performing the image-processing tasks described in this Chapter was originally developed in Python for its simplicity. While steps like object tracking were computationally cheap enough to continue running in Python, the calculation of the median to estimate the background and the loading and processing of images was prohibitively slow. Analyzing a single 6 GB video, of which over 100 were collected in a typical experiment, would take several minutes to an hour. The largest bottleneck was loading an entire image (an array of 10^4–10^6 pixel values) into memory and processing it. Relieving this burden required distributing the image across multiple threads so each would only need to load a fraction of the full image. Additionally, because Python is an interpreted programming language, every thing is compiled at run-time, slowing down computations.

To speed up this algorithm, Isaac Swanlund rewrote the computation of the background and image segmentation steps as a parallel-computed, multithreaded algorithm in C++ using optimized image-processing algorithms from the OpenCV computer vision library [1]. This backend was embedded in a Python frontend so it can be `pip` installed as a Python package (`CvVidProc` [2]; currently only available for Linux and Mac). By distributing computations among multiple threads (usually 8–12) and performing computations with optimized algorithms in C++, a compiled language, the analysis time was reduced by a factor of up to 100x. A 6 GB can now be analyzed in under a minute, and typically in under 5 seconds. The analysis performed to generate the plots in Chapters VI and VII would have taken at least hundreds of additional hours without this speed-up.

IV.2   Recommendations for Further Improvements

The image-processing pipeline used in the present work, while sufficient, can be improved by implementing a few additional steps. First, while images are recorded with 12-bit depth (2^{12} = 4096 pixel brightness values), the image processing was performed on an 8-bit compressed image (2^8 = 256 pixel brightness values) for simplicity and efficiency. This compression reduces both the sensitivity and the contrast in the images, limiting the smallest detectable bubble size and resulting in less precise boundaries during segmentation. Data storage and analysis of 12-bit images will be more memory-intensive, however. Second, threshold values are currently estimated manually by identifying the value for which the number of true bubbles detected is least sensitive to perturbations in the threshold value. This algorithm could be automated and made more quantitative to speed up the analysis and make it more robust. Third, true bubbles are currently distinguished from other detected features (contaminant particles, fluctuations of the inner stream, bubbles and particles in the outer stream, etc.) based on a heuristic set of requirements, including nearness to the center line, growth in size over time, range of velocities along the flow axis, maximum width, minimum number of frames observed, disappears from view upon reaching downstream side of field of view, and maximum aspect ratio. A machine-learning algorithm could identify more salient features and more precise parameter ranges for this classification if someone manually classified a few hundred objects as bubbles or not. Fourth, given the bubbles tracked with the current algorithm, the range of bubble growth could be extended by using that information to estimate the location of the bubble in frames prior to the first detection. In just the pixels near these locations, a more sensitive threshold and less erosive image segmentation could be applied to have a higher sensitivity without picking up noise. Finally, the object-tracking algorithm currently fails to detect merging and splitting events of bubbles. More complex algorithms like MHT-X [8] could be implemented to track objects properly through merging and splitting events, which would expand our ability to make quantitative measurements of ripening beyond our currently qualitative estimates (Section VIII.3).

References

1. Bradski, G. The OpenCV Library. *Dr. Dobb's Journal of Software Tools for the Professional Programmer* **25,** 120–123 (2000).

2. Swanlund, I. *CvVidProc: OpenCV Video Processing for Object-tracking: v1.0.0* 2022. https://github.com/UkoeHB/CvVidProc (2022).

3. Ylitalo, A. S. *bubbletracking_koe: v0.0.1* 2022. https://github.com/andylitalo/bubbletracking_koe (2022).

4. Liu, W., Cai, Y., Zhang, M., Li, H. & Gu, H. *Scene background estimation based on temporal median filter with Gaussian filtering* in *23rd International Conference on Pattern Recognition (ICPR)* (IEEE, Cancun, Mexico, 2016), 132–136. ISBN: 9781509048472.

5. Van der Walt, S. *et al.* scikit-image: image processing in Python. *PeerJ* **2,** e453. ISSN: 2167-8359. https://peerj.com/articles/453 (June 2014).

6. Murray, S. *Real-Time Multiple Object Tracking A Study on the Importance of Speed* PhD thesis (National Institute of Informatics, 2017). arXiv: 1709.03572. https://arxiv.org/pdf/1709.03572.pdf.

7. Kuhn, H. W. The Hungarian method for the assignment problem. *Naval Research Logistics Quarterly* **2,** 83–97. ISSN: 00281441. https://onlinelibrary.wiley.com/doi/10.1002/nav.3800020109 (Mar. 1955).

8. Zvejnieks, P. *et al.* MHT-X: offline multiple hypothesis tracking with algorithm X. *Experiments in Fluids* **63,** 1–18. ISSN: 14321114. arXiv: 2101.05202. https://doi.org/10.1007/s00348-022-03399-5 (2022).

Chapter V

Extrapolating Beyond the Limits of Optical Microscopy: Transport Model of Bubble Growth

> Time itself must come to a stop. You can't get to a time before the big bang, because there was no time before the big bang.
>
> _____
>
> Stephen Hawking

Prof. Richard Flagan of Caltech first proposed to me the idea of estimating the nucleation time of a bubble by fitting a model and extrapolating backward in time. Prof. John Brady stressed the importance of radial convection until I found out how to account for it. Dr. Valeriy Ginzburg and Dr. Irfan Khan of Dow, Inc. offered helpful feedback on the early drafts of the model presented in this Chapter.

Time marches forward—the opportunity to observe is lost forever. The opportunity to imagine, however, is always at hand. In our imagination, we can travel to any time we wish, future, past, or present. How much can we trust our imagination to illuminate the unseen? This is the question that challenges each scientific model; by repeated agreement between the newly seen and previously imagined, the imagined models gain our trust.

Likewise, this question challenges our ability to draw any conclusions about bubble nucleation from the method proposed in Chapter III. While we hope that X-ray or light scattering might someday permit nanoscopic bubble nuclei to be detected in the present apparatus, the optical microscopy used for the present work could not detect bubbles smaller than 1 μm, two orders of magnitude larger than a bubble nucleus based on the predictions of our nucleation model (Chapter VI). This challenge is depicted in Figure V.1, but so is our solution. Using image processing, we can measure the size of bubbles with high precision over the range of 1–10 μm. As Stephen Hawking traced the expansion of the universe back to the Big Bang based on a model fit to measurements of later growth, so do we hope to trace the growth of the bubbles we observe back to their nucleation—their "Little Bang," if

you will—using a model of bubble growth fit to our measurements of their later growth.
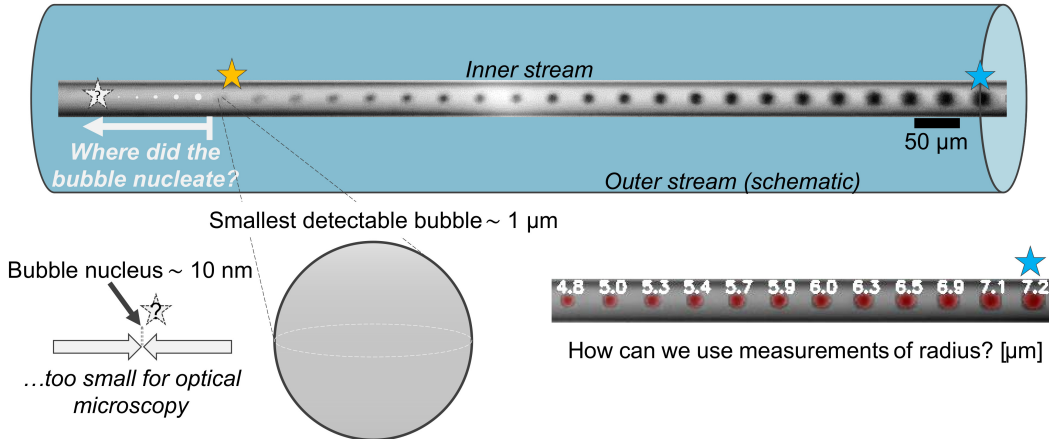
Figure V.1: Schematic of the limitations of optical microscopy in detecting bubble nucleation. Top: superposed images of the growth of a bubble from first detection inside the inner stream of polyol and CO_2 within a schematic of the outer stream (blue cylinder). The bubble was detected in an inner stream of 1k3f polyol (see Table II.1) saturated with CO_2 at 70 bar (7 MPa, 1015 psi) flowing at 50 μL/min inside a sheath of 1k5f polyol flowing at 230 μL/min inside a quartz capillary with an inner diameter of 300 μm and a length of 100 mm at 67 mm from the inlet under a 10x objective (see Table III.1). At the left side of the image of the inner stream, white dots of decreasing size indicate hypothetical bubble sizes too small to detect with optical microscopy, leading back to a hypothetical moment of bubble nucleation (star with "?"). Lower left: The size of the expected bubble nucleus of about 10 nm is shown relative to the size of the smallest bubble detectable with optical microscopy of 1 μm (bubbles are shown to the same relative scale). Lower right: segment of the same image of superposed bubble detections from the top but with image segmentation from the image-processing algorithm highlighted in red to show the quality of measurement and the estimated bubble radius in μm written in white above each bubble detection. The blue star at the right marks the same bubble observation as is marked by the blue star in the top image.

Here, we first explore the dominant physics driving bubble growth to motivate our decision to model it with the classic Epstein–Plesset model [1] in Section V.1. We consider several modifications to the original form of the model in Section V.2 and discuss how we fit these models to the data in Section V.3. The model that fits the data best assumes a diffusive flux as much as an order of magnitude larger than predicted based on the measured transport properties. We suggest that convection along the surface of the bubble steepens the concentration gradient at the surface to account for this enhanced flux and propose possible causes of this convection in Section V.3. In Section V.4, we estimate the time of nucleation during a bubble's

journey along the observation capillary by fitting the visible portion of its spherical growth (1–10 μm) to a model of bubble growth and extrapolating backward in time to the critical radius of nucleation. Finally, we close with recommendations for future work in Section V.5.

V.1   Models of Bubble Growth in Supersaturated Liquids

The growth of a bubble in a supersaturated liquid is governed by several coupled effects. In general, the primary driving force for growth is considered to be the diffusion of dissolved gas from the supersaturated liquid into the bubble. This problem was solved by Epstein and Plesset for the case of a single bubble in an infinite bath of incompressible liquid held at constant temperature and pressure with a uniform diffusivity constant and fixed interfacial tension [1]. The Epstein–Plesset model neglects the effect of radial convection, which was not incorporated until the work of Scriven, who noted the similarity of this problem to the growth of a bubble in a superheated liquid [2]. Scriven also noted that many of the other factors at play in bubble growth, such as viscous resistance, inertia, and interfacial tension become negligible early in the growth of the bubble, so he only considered the asymptotic growth of the bubble at times late enough that these factors could be safely neglected. Barlow and Langlois presented a model for bubble growth that include these factors yet decouples the diffusion from the hydrodynamics by a Lagrangian transform [3]. Due to the nonlinearity of the governing equation, however, a solution could only be obtained numerically, which they achieved by assuming that the concentration primarily varies within a thin shell much smaller than the size of the bubble, similar to the work of Plesset and Zwick on the problem of bubble growth in a superheated liquid [4]. Venerus and Yala later reported that this approximation is only valid in the case of rapid bubble growth [5]. While the growth of bubbles in a foam is limited by the finite supply of dissolved gas and competition with neighboring bubbles, first modeled using the "cell model" of Amon and Denson [6], the scope of this Chapter is limited to the growth of bubbles in isolation, however.

In the present analysis, we assume that the dominant driving forces for growth are diffusion and radial convection. We neglect the effects of inertia, viscosity, and interfacial tension. As noted by Scriven [2], these factors become negligible after a short time. Barlow and Langlois [3] estimated this time scale with the following equation,

$$\frac{\rho\gamma^2\mathcal{D}}{8p_at} + \frac{2\eta}{p_at} + \frac{2\sigma}{p_a\gamma\sqrt{\mathcal{D}t}} \gg 1 \qquad \text{(V.1)}$$

where ρ is the density of the fluid, γ is a coefficient that scales the rate of bubble growth to incorporate the effects of radial convection caused by the advancing boundary of the bubble ($\gamma = 2\beta$ for β described in equation 46 and Figure 5 of Scriven's work [2]), p_a is the pressure in the bulk liquid, η (written as μ is the original paper) is the viscosity of the bulk liquid (assumed to be constant), σ is the interfacial tension along the bubble surface (assumed to be constant), and t is the time. The first term indicates the time scale over which inertia is important, the second indicates the time scale over which viscous resistance is important, and the third indicates the time scale over which the interfacial tension is important. Inertia and viscous resistance become negligible for larger bubbles because the bubble decelerates as it grows unless there is an additional driving force (*e.g.*, decreasing pressure or raising temperature). The decreasing effect of viscous resistance was shown by Venerus *et al.* [5]. From the work of Szekely and Fang, it can be seen that increasing the importance of inertia (quantified by the dimensionless parameter B_I in their work) does not affect the rate of growth at later times, but appears just to extend the period of slower growth at the beginning [7]. Inertia may still affect bubble growth if the bubble expands extremely rapidly or takes place in a liquid metal with significantly higher density. Viscous resistance may still affect bubble growth in highly viscous media like polymer melts or viscoelastic media [8]. Interfacial tension becomes negligible for larger bubbles because the Laplace pressure decreases with the inverse of the bubble radius, as shown by Epstein and Plesset [1].

For the present work, the time scale over which these factors are important is negligible relative to the time scale of observation (hundreds of microseconds), so we neglect these factors in estimating the growth of bubbles. A rough time scale beyond which each factor becomes negligible is estimated by setting each of the three terms individually to 1 in the scaling from Barlow and Langlois (equation V.1), with the first term corresponding to inertia, the second term to viscous resistance, and the third to interfacial tension. Because each term decreases with time, times larger than this time scale will cause the terms to decrease well below one, which is the condition for these effects to be negligible according to Barlow and Langlois. To determine the maximum value for each time scale based on the properties of the system explored in the present thesis, we select the values of each parameter from

the relevant range that maximize the time scale. Those ranges are: $\rho \in [0.95, 1.01]$ g/mL between 31 °C and 60 °C (see Figure II.2), $\gamma \in [1, 100]$ (see discussion later in this Section), $\mathcal{D} \in [10^{-10}, 2 \times 10^{-9}]$ m^2/s (see Figure II.4), $p_a \in [5 \times 10^5, 10^7]$ Pa (see Figure III.2 and note that bubbles are not measured in foamed region), $\eta \in [10^{-2}, 0.3]$ Pa.s (see discussion of effect of CO_2 on viscosity and measurements of pure polyol viscosity for 3k2f in Figure III.S1), and $\sigma \in [0.005, 0.03]$ N/m (see Figure II.3a).

- **Inertia:**

$$t_\rho \sim \frac{\rho \gamma^2 \mathcal{D}}{8 p_a} < \frac{(1000 \text{ kg/m}^3)(100)^2(10^{-9} \text{ m}^2/\text{s})}{8(5 \times 10^5 \text{ Pa})} \sim 1 \text{ ns}$$

- **Viscous Resistance:**

$$t_\eta \sim \frac{2\eta}{p_a} < \frac{2(0.3 \text{ Pa.s})}{5 \times 10^5 \text{ Pa}} \sim 1 \text{ μs}$$

- **Interfacial Tension:**

$$t_\sigma \sim \left(\frac{2\sigma}{p_a \gamma \sqrt{\mathcal{D}}} \right)^2 < \left(\frac{2(0.03 \text{ N/m})}{(5 \times 10^5 \text{ Pa})(1)\sqrt{10^{-10} \text{ m}^2/\text{s}}} \right)^2 \sim 40 \text{ μs}$$

Therefore, even if these three effects were to completely halt bubble growth over the time period that they are relevant, a model that neglects them would result in a discrepancy from the true growth of no more than 100 μs, which would have a negligible effect on the estimate of bubble nucleation in Chapter VI.

The flow in the microfluidic flow-focusing channel used to induce bubble nucleation in the present work introduces two additional factors that affect bubble growth: decreasing pressure and depletion of CO_2 by diffusion into the outer stream. The decreasing pressure results from the shear stress along the inner walls of the

observation capillary, which leads to a roughly linear decrease in pressure along the capillary (see Figure III.2). As the pressure in the bulk fluid decreases, so does the pressure inside the bubble, though it is elevated by the Laplace pressure. As the pressure inside the bubble decreases, the gas inside expands, accelerating bubble growth. The time scale for this process is slow unless near the end of the channel relative to the field of view in experiments (about 1 mm, which corresponds to a change in pressure of about 1 bar, as in Figure III.2). Because the inner stream is ensheathed by an outer stream of pure polyol without CO_2, CO_2 dissolved in the inner stream gradually diffuses out into the outer stream. While the residence time of the fluid is typically around 100 ms and the fluids have a high viscosity—and, thus, low diffusivity—the loss of CO_2 can be significant because of the narrow dimension of the inner stream. The depletion boundary layer along the outer edge of the inner stream will grow roughly as $\sqrt{Dt} \sim \sqrt{10^{-9} \text{ m}^2/\text{s} \times 0.1 \text{ s}} \sim 10 \ \mu\text{m}$. Given that the inner stream radius is typically around 25 μm (see micrographs of flow channel in Figure III.3, for example), even the concentration of CO_2 at the center of the inner stream may decrease before reaching the end of the channel. The effect of depletion of CO_2 will slow bubble growth by reducing the effective bulk concentration of CO_2.

After diffusion, the most important factor affecting bubble growth is radial convection. Radial convection plays a significant role in bubble growth in the present system due to the fast growth relative to the diffusivity in the window of observation. In their review, Plesset and Prosperetti noted that the scale for the ratio of the diffusive to the convective term in the convection–diffusion equation is $\mathcal{D}/R\dot{R}$. As can be seen in the measured bubble radii in Figure V.7 (open black circles), a typical bubble might grow from 3 μm in radius to 10 μm in radius over about 1 ms. Fitting the asymptotic growth profile of $R(t) \approx a\sqrt{t - t_{nuc}}$ to these two points gives $a \approx 3 \times 10^{-4}\text{m}/\sqrt{\text{s}}$. The value $R\dot{R} \approx a^2/2 \approx 5 \times 10^{-8} \text{ m}^2/\text{s}$, while the diffusivity is at most $2 \times 10^{-9} \text{ m}^2/\text{s}$ (see Figure II.4). Thus, the ratio of the diffusive to the convective term is $\mathcal{D}/R\dot{R} < 0.04$, indicating that convection is more significant than diffusion in the convection–diffusion equation. To demonstrate the importance of convection, a model was constructed that incorporates all effects except for inertia and viscous resistance given that they become negligible within 1 μs. The model incorporates material properties measured using G-ADSA for the exact polyols involved and is discussed in greater depth in the SI. The model significantly underestimates the measured bubble growth, as seen in Figure V.2.
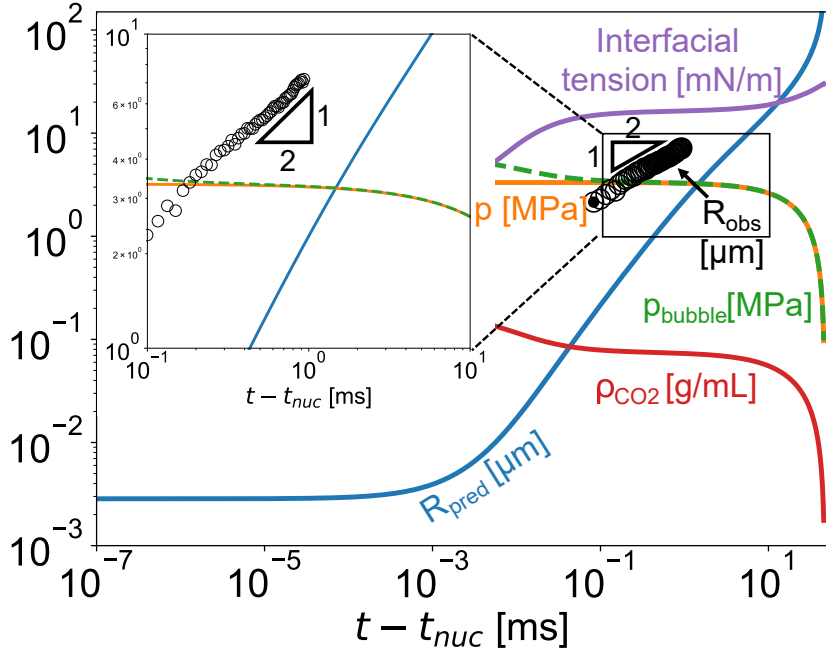
Figure V.2: Model of bubble growth excluding the effects of convection and accounting for the concentration dependence of the diffusivity plotted alongside measurements of the radius of a bubble (open black circles) over time since the estimated moment of nucleation $t - t_{nuc}$. The measurements were taken of the same bubble shown in Figure V.1. The model estimates several properties over time: the radius of the bubble R_{pred} [μm] (blue line), the density of CO_2 ρ_{CO2} [g/mL] (red line), the pressure estimated inside the channel p [MPa] (orange line), the pressure estimated inside the bubble p_{bubble} [MPa] (green dashed line), and the interfacial tension along the bubble surface [mN/m] (purple line). The inset zooms in on the region around the bubble radius measurements and highlights the underestimation of the bubble growth by the model, as well as the difference in power law behaviors (the data are matched a square root but the prediction is matched by a higher power).

Modeling the effect of radial convection explicitly can be challenging because it introduces a nonlinearity to the governing equation [3] and convection tends to introduce more numerical instability. Rather than model the effect of convection explicitly in the governing equations, we note that Scriven observed that the asymptotic solution to these equations is $R \propto \sqrt{t}$, just as in the static case modeled by Epstein and Plesset. Radial convection caused by growth in the radius of a bubble at a rate of $\dot{R}$ produces a velocity field $u = \frac{R^2}{r^2}\dot{R}$ by conservation of mass assuming spherical symmetry and an incompressible fluid. This velocity field decreases in speed with r, such that the advancing front of the bubble travels faster than the surrounding fluid. This velocity gradient causes the concentration profile of dissolved gas to be compressed into a smaller shell, increasing the concentration gradient and

the flux of gas into the bubble [9]. Because the asymptotic growth is the same with or without radial convection and the asymptotic growth regime is reached before we can detect bubbles (within about 10 μs based on the time scales estimated above), we choose to model the bubble growth using the simpler static model of Epstein and Plesset and lump all the effects of convection, as well as other neglected effects, into a coefficient C by which the concentration gradient is multiplied. We will refer to this coefficient C as the "convection coefficient." This coefficient is one of several modifications made to the Epstein–Plesset model in developing the model of bubble growth used in the present work, which is discussed in the next Section.

Loss of Dissolved Gas to Pure-polymer Outer Stream Decreases Diffusion
V.2   Modified Epstein–Plesset Model Fits Measured Bubble Growth

As mentioned in the previous Section, the Epstein–Plesset model of bubble growth applies Fick's Laws to model the concentration profile of gas outside the bubble and the flux of gas into the bubble that results from the gradient, all while the surface of the bubble expands. The system and model are shown schematically in Figure V.3.

The system is assumed to be spherically symmetric, quasistatic, with no convective effects, at constant temperature and pressure, and with uniform diffusivity. In a supersaturated system, the concentration of gas in the bulk fluid c_{bulk} is greater than the concentration of gas in equilibrium with the bubble at the surface $c_{sat}(p)$. As described by Fick's First Law, this concentration gradient at the surface of the bubble causes a total flux of gas into the bubble proportional to the surface area of the bubble ($4\pi R^2$ for bubble radius R), the diffusivity of the gas in the fluid $\mathcal{D}$, and the negative concentration gradient at the surface $-\left.\frac{\partial c}{\partial r}\right|_{r=R}$. As this flux depletes CO_2 at the surface of the bubble, Fick's Second Law describes how the CO_2 in the bulk diffuses toward the depleted area. Because we have assumed that the bubble is in an infinite bath with no other bubbles around it, the boundary conditions are that the concentration at infinite radius at the unreachable end of the bath is the bulk concentration c_{bulk} and the concentration at the surface of the bubble is the equilibrium concentration $c_s(p)$. The initial condition is a uniform fluid of concentration c_{bulk}. In the case of a static boundary, Fick's Laws can be solved with a similarity variable or integral transform. Because the surface of the bubble expands as CO_2 diffuses into the bubble to maintain a constant internal density, the geometry of the concentration profile changes with time. Epstein and Plesset solved this problem—ignoring convective effects—by transforming to a simpler coordinate
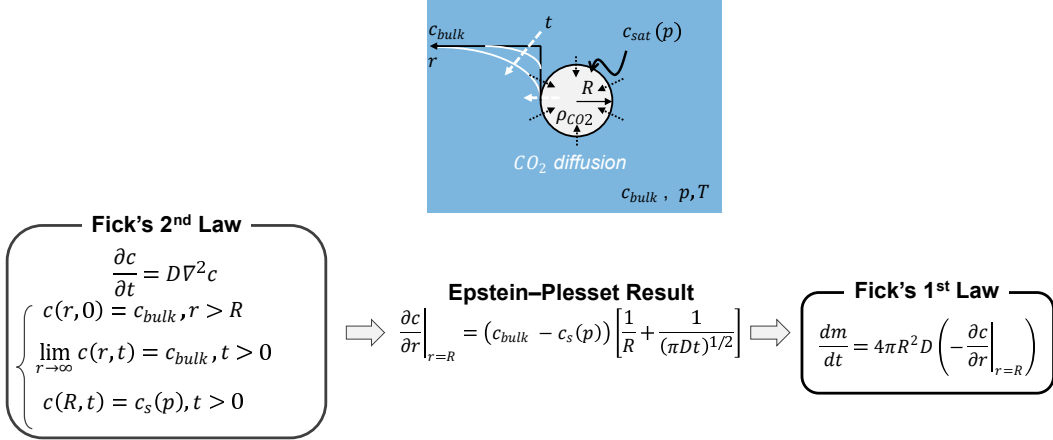
Figure V.3: Schematic showing the Epstein–Plesset model. Top: schematic of the system considered. A bubble (gray circle) with radius R and CO_2 density ρ_{CO2} is situated in an infinite fluid initially uniformly supersaturated with dissolved CO_2 (blue background) and fixed at a constant pressure p and temperature T. At the surface of the bubble, the concentration of CO_2 is fixed at the saturation pressure $c_s(p_{bub})$ for the bubble pressure p_{bub}, which is lower than the bulk concentration of CO_2 c_{bulk}. Consequently, CO_2 diffuses into the bubble (dashed black arrows), depleting CO_2 surrounding the bubble over time (white lines on the axes on the left). Bottom: flow of equations for computing bubble growth using the work of Epstein and Plesset [1]. First, Fick's Second Law (left) describes the diffusion of CO_2 outside the bubble. Next, the Epstein–Plesset result calculates the resulting concentration gradient at the surface of the bubble (middle). Finally, the flux of CO_2 into the bubble is calculated by substituting the Epstein–Plesset result into Fick's First Law (right).

system and solving for the concentration gradient at the surface of the bubble. The result is

$$\left.\frac{\partial c}{\partial r}\right|_{r=R} = (c_{bulk} - c_s(p)) \left[\frac{1}{R} + \frac{1}{\sqrt{\pi \mathcal{D} t}}\right] \tag{V.2}$$

which can be substituted into Fick's First Law to determine the change in mass of gas enclosed in the bubble.

Solving for Flow and Pressure

Unlike the Epstein–Plesset system, bubbles observed in the microfluidic flow-focusing channel experience a pressure that decreases over a time scale set by the flow speed of the inner stream. Although the change in pressure during the observable growth of a bubble has a negligible effect on the size, the pressure dictates the degree of supersaturation of the mother phase, which drives the diffusion of gas

into the bubble through a chemical potential gradient. We therefore must estimate the pressure at each point along the channel. Because the pressure results from the shear stress along the walls of the capillary, we must determine the properties of the flow to estimate the pressure. To determine the pressure profile and flow speed, we solved the Stokes equation for cylindrically symmetric sheath flow of two streams with different viscosities and flow rates, as shown in Figure V.4.
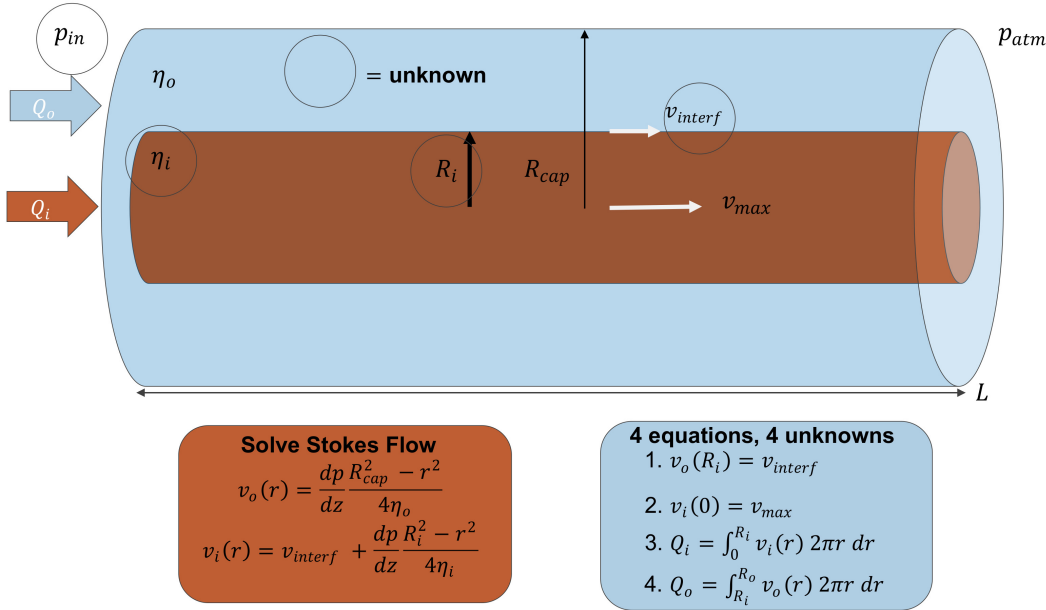
Figure V.4: Schematic showing a model of the flow in the microfluidic flow-focusing channel. Top: schematic of sheath flow with known parameters (not circled: inner stream flow rate Q_i, outer stream flow rate Q_o, outer stream viscosity η_o, inner stream center speed v_{max}, atmospheric pressure p_{atm}, inner radius of the observation capillary R_{cap}, and length of the observation capillary L) and parameters to solve for (circled: inlet pressure p_{in}, inner stream viscosity η_i, inner stream radius R_i, and speed along the interface of the inner and outer streams v_{interf}). Bottom left: axial velocity profiles as a function of radius r determined by solving pressure-driven Stokes flow in a pipe and assuming cylindrical symmetry. Bottom right: four conditions providing four equations to solve for the four unknown quantities.

We considered as known inputs the inner stream flow rate Q_i, the outer stream flow rate Q_o, the outer stream viscosity η_o, the outlet pressure p_{atm}, the length of the capillary L, the radius of the capillary R_{cap}, and the centerline speed v_{max} (since it could be measure by tracking a small bubble in a video). The inlet pressure p_{in}, the inner stream radius R_i, the velocity at the interface between the streams v_{interf}, and the inner stream viscosity η_i were unknowns to be solved for (although the inlet pressure could be compared to the pressure measured by the inner stream ISCO pump, which is close to the inlet pressure because the pressure

across the low-viscosity inner stream fluid is low and the inner stream radius could be compared to rough estimates from videos, although identifying the interface precisely was challenging). These four unknowns could be solved by solving Stokes flow equations in cylindrically symmetric coordinates under pressure-driven flow along the z axis (see orange box in lower left of Figure V.4) and applying four conditions: (1) continuity of velocity at the interface $v_o(R_i) = v_i(R_i) = v_{interf}$, (2) known centerline speed $v_i(r = 0) = v_{max}$, (3) inner stream flow rate Q_i passes through cylinder of radius R_i, and (4) outer stream flow rate Q_o passes through cylindrical shell from R_i to R_{cap}.

In solving for these flow properties, we have assumed that the viscosities of the inner and outer streams are uniform throughout their respective streams. In reality, the viscosity may change by an order of magnitude or more as CO_2 diffuses into or out of a region of fluid, an estimate we base on the strong sensitivity of diffusivity on CO_2 concentration in Figure II.4 and the inverse proportionality of diffusivity and viscosity based on the Stokes–Einstein–Sutherland relationship. We have also assumed that the flow remains in steady state and that the inlet pressure is constant. In reality, we have observed that the flow may fluctuate sometimes, typically as a result of the passing of bubbles, and the inlet pressure may vary over several minutes unless the flow rate is adjusted to counteract the changes.

We validate the estimates of the inlet pressure p_{in} and inner stream radius R_i against additional measurements. While η_i is not directly measured, we can vary its value until the model solves for values of the other parameters consistent with measurements. Having measured the dimensions of the tubing from the inner stream ISCO pump to the inlet of the observation capillary, we can estimate the inlet pressure by estimating the pressure drop from the measured pressure in the ISCO pump (reported by the ISCO pump's internal pressure transducer) using the formula for pipe flow. We can do the same with the ISCO pump for the outer stream. These estimates of the inlet pressure provide a range in which the value calculated from solving the flow equations shown in Figure V.4 should lie. We can also measure a range from the inner stream radius R_i by visual observation of the recorded videos. Often, the inner stream interface is blurred due to lensing caused by the gradient in index of refraction between the inner stream of polyol and CO_2 and the outer stream of polyol. Nevertheless, bounds can be placed on the radius in which the calculated value should lie. Finally, we measure the inner stream maximum speed v_{max} by tracking small bubbles, which we assume are traveling at roughly the same speed as

the flow (they do not seem to accelerate until reaching the width of the inner stream based on the data in Figure VIII.5). By measuring the speed of several bubbles, we can place a range on the input value of v_{max} as well. Because the inner stream viscosity η_i cannot be measured directly, we vary its value until the calculation for each of the measured values falls within the measured range. An example of the result of this estimation is shown in Figure V.5. At $\eta_i = 0.01$ Pa.s, the calculated values of the inner stream radius R_i, centerline velocity v, and the pressure drop across the observation capillary (Δp) are all in agreement with the measured ranges.
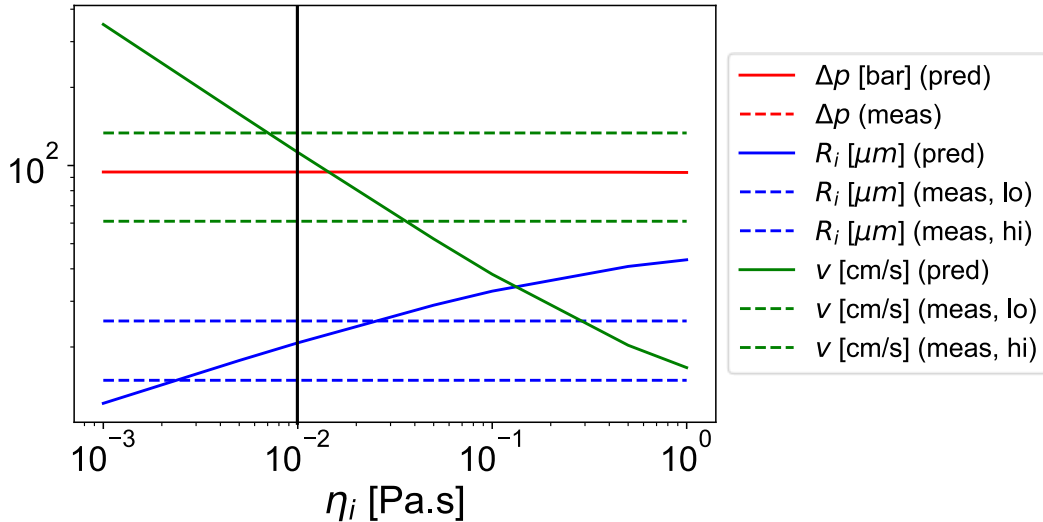
Figure V.5: Plot used to estimate the inner stream viscosity η_i [Pa.s]. Calculated values for the pressure drop across the observation capillary Δp [bar] (red), inner stream radius R_i [μm] (blue), and centerline speed v [cm/s] (green) are plotted as a function of the inner stream viscosity η_i as solid lines. Ranges of measured values are plotted as horizontal dashed lines. A value for η_i for which the calculated values are within the range of measured values is selected (0.01 Pa.s, marked by vertical black line). In this experiment, PPG 2700 g/mol saturated with CO_2 at 7.0 MPa and 22 °C was used as the inner stream.

Incorporating Material Properties

To improve the accuracy of our bubble growth model, we incorporate measured material properties of both CO_2 and polyol–CO_2 mixtures. Rather than assume that the gas inside the bubble is ideal, we determine its equation of state by interpolating pvT on CO_2 available from NIST [10]. We estimate the concentration of CO_2 at the bubble surface $c_s(p_{bubble})$, where p_{bubble} is the pressure inside the bubble, and the bulk concentration of CO_2 $c_{bulk}(p_{sat})$, where p_{sat} is the pressure at which CO_2 was saturated in the polyol–CO_2 mixture, by interpolating the solubility

data measured with G-ADSA (see Figure II.6. We then estimate the interfacial tension along the surface of the bubble with the measurements from G-ADSA at different pressures (see Figure II.3a). While we measured the diffusivity of CO_2 in polyol–CO_2 mixtures at a range of pressures and temperatures (see G-ADSA measurements in Figure II.4), the Epstein–Plesset model assumes a uniform diffusivity. We explored the effect of a concentration-dependent diffusivity $\mathcal{D}(c)$ based on the measurements made with G-ADSA and report our findings in the SI. Surprisingly, we found that assuming a constant diffusivity $\mathcal{D}$ and constant convection coefficient C leads to a good fit of the measured bubble sizes, so we focused on this empirical approach instead (see next Section).

We assume that the bubble begins at a radius similar to the critical radius predicted by the model of bubble nucleation based on the string method discussed in Chapter VI, which is about 3 nm. At such small sizes, the Laplace equation $p_{bubble} = p + 2\sigma(p_{bubble})/R$ predicts enormous Laplace pressures on the order of 1 MPa. These values are unphysical, however, because the extreme curvature of nanoscopic bubbles reduces the interfacial tension because the tension is applied with a radius of curvature comparable to the molecular size. This correction to interfacial tension for small droplets was derived by Tolman and is inversely proportional to an empirical "Tolman length" [11]. We considered Tolman lengths from 5–100 nm, but found that while it provides more physical bubble pressures at the early stages of bubble growth, it does not affect the radius of the bubble by more than 1% at any point during the growth for any of the Tolman lengths considered. We selected a Tolman length of 5 nm for consistency.

Numerical Algorithm

Because the pressure inside the bubble p_{bubble} in our model depends non-linearly on itself through the dependence of the interfacial tension in the Laplace pressure on p_{bubble} and the dependence of the radius of the bubble R on the density of CO_2 ρ_{CO2} on p_{bubble}, the modified Epstein–Plesset model in the present dissertation cannot be solved purely with finite difference methods. Instead, at each timestep, a system of self-consistent equations must be solved to determine p_{bubble} and R with a nonlinear solver (the `root` function was used from the `optimize` library of the `scipy` package [12]). A schematic of this procedure is provided in Figure V.6.

A bubble nucleus is used as the starting point for computing the bubble

a) Initialize bubble

1. Bubble
Nucleus

$$t^0 = t_{nuc} \text{ (guessed)}$$
$$R^0 = R_{nuc} \text{ predicted by string method}$$
$$p^0 = p_{atm} + (p_{in} - p_{atm})\frac{t^0}{v_{max}/L}$$
$$p^0_{bubble} = p^0 + \frac{2\sigma(p^0_{bubble})}{R^0}$$
$$m^0 = \frac{4\pi}{3}(R^0)^3 \rho_{CO2}(p^i_{bubble}, T)$$

b) Iterate through time

2. CO$_2$ diffuses into bubble

Epstein–Plesset Model
$$\frac{dm}{dt}\bigg|_{t^i} = 4\pi(R^i)^2 D\left(c_{bulk} - c_s(p^i)\right)\left(\frac{1}{R^i} + \frac{1}{\sqrt{\pi D t^i}}\right)$$

Euler Method
$$m^{i+1} = m^i + \frac{dm}{dt}\bigg|_{t^i}\Delta t$$

3. Equilibrate Radius

Update bulk pressure
$$p^i = p_{atm} + (p_{in} - p_{atm})\frac{t^i}{v_{max}/L}$$

Self-consistently solve for p^i_{bubble} and R^i

$$p^i_{bubble} = p^i + \frac{2\sigma(p^i_{bubble})}{R^i}$$

$$R^i = \left(\frac{3}{4\pi}\frac{m^i}{\rho_{CO2}(p^i_{bubble}, T)}\right)^{1/3}$$

Figure V.6: Schematic of the numerical algorithm used to compute bubble growth from the modified Epstein–Plesset model. a) The bubble is initialized at a guessed nucleation time t_{nuc}, estimated radius R_{nuc}, and estimated pressure p. The pressure inside the bubble p_{bubble} is solved self-consistently and used to estimate the mass of the bubble by using the equation of state of CO$_2$ to estimate the density ρ_{CO2} at that pressure. b) The bubble growth is estimated by iteratively advancing in time. Each timestep consists of two parts. First, the diffusion of CO$_2$ into the bubble is estimated by taking an Euler timestep according to the Epstein–Plesset result for the concentration gradient at the bubble surface. Second, the bubble radius and pressure are allowed to equilibrate by self-consistently solving for their values.

growth profile with the modified Epstein–Plesset model (see Figure V.6a). The time of nucleation t_{nuc} is guessed (the algorithm for fitting t_{nuc} is described in Section V.3) and used to calculate the pressure at the corresponding location along the observation capillary using the flow parameters from the flow calculations (Figure V.4),

$$p^0 = p_{atm} + (p_{in} - p_{atm})\frac{t^0}{v_{max}/L} \tag{V.3}$$

The radius of the nucleus R_{nuc} is taken from the prediction of our nucleation model based on the string method (described in Chapter VI). Next, the pressure

inside the bubble is solved self-consistently due to the dependence of the interfacial tension $\sigma(p_{bubble})$ in the Laplace pressure on the pressure in the bubble (see Figure II.3a),

$$p^0_{bubble} = p^0 + \frac{2\sigma(p^0_{bubble})}{R^0} \tag{V.4}$$

where the radius of the bubble R^0 is held fixed at R_{nuc} and the interfacial tension $\sigma(p^0_{bubble})$ is estimated by interpolating the values measured with G-ADSA (Figure II.3a). Finally, the pressure inside the bubble is used to determine the density of CO_2 ρ_{CO2} given the temperature T (held at laboratory temperature, $T \approx 22$ °C) and from that calculate the mass inside the bubble by multiplying by the bubble volume $\frac{4}{3}\pi(R^0)^3$.

Once the initial condition is set, the system is updated using an Euler timestep that assumes a first-order Taylor approximation of the dynamics as modeled by the Epstein–Plesset model in eq V.2 (Figure V.6b). The timestep is adapted to ensure that the discrepancy between a timestep of Δt and two timesteps of $\Delta t/2$ is below a tolerance (usually 1%). If the discrepancy is greater than the error tolerance, then the calculation for that timestep is rejected, the timestep Δt is halved, and the timestep is recalculated. If the discrepancy is smaller than the error tolerance, the calculation for that timestep is accepted and the timestep is increased by a small fraction (usually 30%). This adaptive timestep algorithm ensures that the fast dynamics at early times are calculated accurately with short timesteps while the slower dynamics at later times are calculated efficiently with larger timesteps.

Once a timestep is accepted, the properties of the bubble and the flow are updated in accordance with the increase in CO_2 in the bubble and the movement of the bubble down the observation capillary. The pressure is updated as in equation V.3 using the new time t^i instead of t^0. To calculate the pressure in the bubble p^i_{bubble} and the radius of the bubble R^i, the bubble pressure equation and the bubble radius equation must be solved self-consistently (step 3 in Figure V.6b), as mentioned earlier. The system is then ready to compute the next timestep. This process is repeated until the bubble reaches the end of the observation capillary, *i.e.* $t^i = L/v_{max}$.

V.3   Fitting Model to Data to Extrapolate Bubble Growth Back to Its Birth

The goal of this Chapter was to develop a model of bubble growth that could fit the observed bubble growth from about 1–10 μm in radius and extrapolate backward to the critical radius of nucleation to determine the time of nucleation. A similar technique was previously demonstrated by Leung *et al.* using the cell model of bubble growth [6] to model the growth of CO_2 bubbles in supersaturated polystyrene [13]. They explored the effects of other parameters like viscosity, interfacial tension, and the relaxation time of the polymer.

Here, the semi-empirical model used to model bubble growth has two fitted parameters: the nucleation time t_{nuc} and the "effective diffusivity" $\mathcal{D}_{eff}$. As discussed in the previous Sections, we chose to lump the effects of convection and other effects not included in the modified Epstein–Plesset model (Section V.2) into a convection coefficient C and fix the diffusivity to a constant value $\mathcal{D}$. Because both are arbitrary constants, their product is an arbitrary constant. We call their product the "effective diffusivity" $\mathcal{D}_{eff} \equiv A \times \mathcal{D}$ because although the diffusivity is unaffected by convection, convection ultimately leads to bubble growth that looks like an accelerated static diffusion problem.

Fitting Procedure for Nucleation Time

We first fit the nucleation time t_{nuc} using a bisection algorithm. We first guess a range for t_{nuc}, typically choosing the upper bound t_{nuc}^{hi} to be the time at which the bubble of interest was first observed and the lower bound as some fraction of that time (*e.g.*, 95%). We then take the average of the upper and lower bounds t_{nuc}^{lo} as our guess for t_{nuc} and calculate the bubble growth profile predicted by our modified Epstein–Plesset model (see Figure V.6).

The error between the model prediction for bubble growth and the measured bubble growth to determine if the guess for t_{nuc} should be improved. Because the effective diffusivity $\mathcal{D}_{eff}$ is not yet fit to the data, the slope of the model prediction may differ significantly from the slope of the measured bubble growth. Additionally, we want to know if the guessed nucleation time is too soon or too late. For these two reasons, we calculate the root mean *signed* squared fractional error (RMSSFE), meaning that we compute the square of the fractional error at each measurement of bubble growth and multiply by the sign of the error before taking the mean,

$$RMSSFE = \left\{ \frac{1}{N} \sum_{i=1}^{N} \text{sgn}[R_{pred}(t^i) - R_{meas}(t^i)] \left[\frac{R_{pred}(t^i) - R_{meas}(t^i)}{R_{meas}(t^i)} \right]^2 \right\}^{1/2}$$

(V.5)

where N is the number of measurements of bubble size, $R_{meas}(t)$ is the measured bubble radius at time t, $R_{pred}(t)$ is the bubble radius predicted by the modified Epstein–Plesset model (Section V.2) at time t, and t^i is the time of the ith measurement of the bubble radius. If the RMSSFE is within the tolerance (usually 0.3%), then the guessed nucleation time is accepted and the calculation proceeds to fit the effective diffusivity $\mathcal{D}_{eff}$ (see below). If the RMSSFE is not within the tolerance, the nucleation time t_{nuc} is updated. If the RMSSFE is negative, then the model underestimated the bubble growth, meaning that the nucleation time should be decreased to give the model more time to grow. The new guess for t_{nuc} is then $t_{nuc} \leftarrow (t_{nuc}^{lo} + t_{nuc})/2$ and the upper bound is updated to $t_{nuc}^{hi} \leftarrow t_{nuc}$. If the RMSSFE is positive, then the model overestimated the bubble growth, meaning that the nucleation time should be increased to reduce the time that the model grows the bubble before reaching the measurement times. The new guess for t_{nuc} is then $t_{nuc} \leftarrow (t_{nuc} + t_{nuc}^{hi})/2$ and the lower bound is updated to $t_{nuc}^{lo} \leftarrow t_{nuc}$.

Fitting Procedure for Effective Diffusivity

Once the nucleation time t_{nuc} is optimized, the effective diffusivity $\mathcal{D}_{eff}$ is optimized. As for t_{nuc}, $\mathcal{D}_{eff}$ is fit using a bisection algorithm: an upper bound $\mathcal{D}_{eff}^{hi}$ and lower bound $\mathcal{D}_{eff}^{lo}$ are selected by the user and a satisfactory fit is searched for by bisecting the interval based on the direction of the discrepancy of the model from the measurements. Because $\mathcal{D}_{eff}$ appears to affect the slope of the bubble growth on a log-log plot predicted by the model, the value is updated by comparing the slope on a log-log plot of the model to that of the measurements. Specifically, a line is fit on a log-log plot to the predicted values and another line is fit to the measured values (like a power-law fits), both at the times of measurement, and the ratio of the slope of the prediction divided by the slope of the measurement is sufficiently close to 1 (typically within 3%), the effective diffusivity $\mathcal{D}_{eff}$ is accepted along with the nucleation time t_{nuc} and the fit is complete. If the ratio is outside the tolerance from 1, the guess for $\mathcal{D}_{eff}$ is improved and the algorithm refits t_{nuc} using the new guess for $\mathcal{D}_{eff}$. If the ratio is greater than one, the effective diffusivity is too large, so it is decreased $\mathcal{D}_{eff} \leftarrow (\mathcal{D}_{eff}^{lo} + \mathcal{D}_{eff})/2$ and the upper bound is updated to $\mathcal{D}_{eff}^{hi} \leftarrow \mathcal{D}_{eff}$. If the ratio is less than one, the effective diffusivity is too small,

so it is increased $\mathcal{D}_{eff} \leftarrow (\mathcal{D}_{eff} + \mathcal{D}_{eff}^{hi})/2$ and the lower bound is updated to $\mathcal{D}_{eff}^{lo} \leftarrow \mathcal{D}_{eff}$.

The resulting nucleation time t_{nuc} can be used to estimate the location of nucleation along the observation capillary d_{nuc} and, from that, the pressure at which the bubble nucleated p_{nuc}. The location of nucleation d_{nuc} is calculated by multiplying the nucleation time t_{nuc} by the centerline flow speed v_{max} to get $d_{nuc} = v_{max}t_{nuc}$. The pressure of nucleation p_{nuc} can then be computed by assuming a linear decrease in the pressure from the inlet p_{in} to atmospheric pressure p_{atm} at the outlet, $p_{nuc} = p_{in} - (p_{in} - p_{atm})\frac{d_{nuc}}{L}$. The location and pressure of nucleation will be more relevant for the discussion of bubble nucleation in Chapter VI.

Epstein–Plesset Model Fits Bubble Growth when Multiplied by Empirical Factor

Upon completion of the algorithm described above, the fitted values of the nucleation time t_{nuc} and the effective diffusivity $\mathcal{D}_{eff}$ typically yield a surprisingly accurate fit to the measured bubble radius. The accuracy is surprising given that the diffusivity, effect of convection, effect of depletion of the inner stream by diffusion of CO_2 into the outer stream, and any other effects not incorporated into the model are lumped together into a single fitted coefficient $\mathcal{D}_{eff}$. This coarse-graining is only possible because many of the factors at play (*e.g.*, viscosity, inertia) are negligible or become so at times so early as to not affect the model prediction at the relevant scales and because the effect of convection is purely a quantitative increase in the concentration gradient in the asymptotic limit. An example fit of the modified Epstein–Plesset model to the growth of bubble measured in the microfluidic flow-focusing channel with image processing is shown in Figure V.7. The uncertainty in the measurements is smaller than the marker size (open circles), yet the predicted radius R_{pred} remains well within that margin for each measurement. Note that only measurements of the bubble for sizes smaller than the inner stream are considered to reduce the effects of confinement and depletion near the edge of the inner stream. Thanks to the 60,000 fps frame rate of the high-speed camera, this restriction still left a sufficient number of points to demonstrate a good fit to the data.

An advantage of incorporating the various material properties into the modified Epstein–Plesset model, as discussed in Section V.2, is that they, too, are estimated by the model. We therefore compare their trends with those of the bubble radius over time as shown in Figure V.7. The predicted bubble radius R_{pred} begins
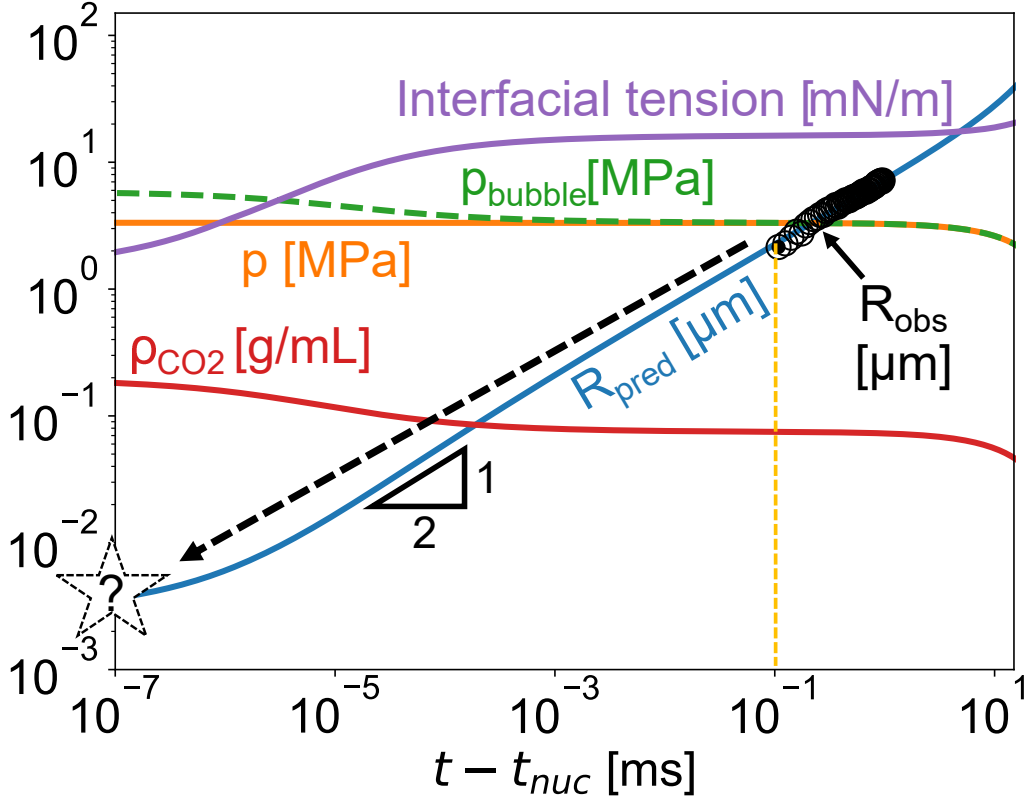
Figure V.7: Plot of the estimates of several bubble and flow properties by the modified Epstein–Plesset model fit to measured bubble radii (R_{obs} [μm], open black circles, same data as in Figure V.2) as a function of time since nucleation $t - t_{nuc}$ on a log-log plot. As in Figure V.2, the measured bubble radii grow with a 1/2 power law; the uncertainty in measurement is smaller than the marker size. The radius predicted by the model R_{pred} [μm] (blue line) passes within the uncertainty of each measurement. The moment of nucleation (star with "?") is estimated to be t_{nuc} due to the goodness of fit, which occurred about 100 μs before the first observation (marked by vertical dashed yellow line). As in Figure V.2, the interfacial tension (purple line), bubble pressure p_{bubble} (green dashed line), channel pressure p (orange line), and density of CO_2 in the bubble ρ_{CO2} (red line) are also plotted.

somewhat suppressed by interfacial tension, but quickly accelerates to the asymptotic limit of $R_{pred} \propto (t - t_{nuc})^{1/2}$ (indicated by slope triangle). At longer time scales (several milliseconds), the pressure in the bubble decreases enough that the growth accelerates beyond square-root growth, as seen by the uptick in R_{pred} at the end of the displayed trajectory. The interfacial tension is initially lower due to the Tolman correction for the effect of high curvature, then plateaus until slightly increasing as the density of CO_2 in the bubble decreases at longer time scales. The pressure in the channel decreases linearly, which appears to be slowly-then-quickly on a log-log plot. The pressure in the bubble follows the pressure in the channel once the bubble

exceeds 100 nm, but at smaller sizes the effect of interfacial tension is large enough that the Laplace pressure is a significant fraction of the channel pressure. Finally, the density of CO_2 inside the bubble is at first high (0.2 g/mL) due to the high pressure in the channel and the added Laplace pressure ($2\sigma(p_{bubble})/R$) due to the small bubble radius R. It later tracks the pressure inside the bubble p_{bubble} since CO_2 is not strongly non-ideal at lower densities.

Based on this model, the bubble would have nucleated at a radius around 3 nm about 100 μs before the first observation of the bubble at about 3 μm (marked by vertical dashed yellow line). While it is likely that the neglected effects of viscous resistance and inertia further hindered the earliest, invisible bubble growth relative to the model prediction, the discrepancy is likely comparable to the time scale at which the asymptotic behavior, $R \propto (t - t_{nuc})^{1/2}$ is reached, which is around 100 ns. Such errors are negligible relative to the measurement errors (*e.g.*, the precision with which I can estimate the time for the bubble to reach the point of observation from the entrance of the observation capillary).

In this particular example, the effective diffusivity $\mathcal{D}_{eff} \approx 2.75 \times 10^{-9}$ m^2/s. This value is roughly the diffusivity of CO_2 in PPG 2700 g/mol at the saturation pressure for this experiment of 7 MPa (70 bar, 1015 psi). Nevertheless, the diffusivity near the surface of the bubble, where the pressure is at most 3.3 MPa (33 bar, 480 psi), would be less than 10^{-9} m^2/s, and we would expect that the concentration gradient would be decreased by the depletion of CO_2 into the outer stream. Such a fit could not be achieved without incorporating this enhancement of the growth through what we call the effective diffusivity $\mathcal{D}_{eff}$ and attribute largely to convective effects unless a more sophisticated model were developed. Some values for the effective diffusivity exceeded 10 times the measured diffusivity for the saturated solution, suggesting a strong effect of convection, but a correlation between flow or convective effects and the effective diffusivity has not yet been found. These values are consistent with predicted enhancement of growth based on the work of Scriven [2].

V.4 Bubble Nucleation Can Be Estimated Accurately with $R \propto (t - t_{nuc})^{1/2}$

While we learn a lot about the state of the bubble during its growth from the modified Epstein–Plesset model, it is prone to numerical errors near the condensation pressure of CO_2. Even if the pressure is not physically achieved in the bubble, it may cause sudden changes in density while solving for the pressure self-consistently

when the pressure is near the condensation pressure. The model is also slow due to the need to solve for the entire growth profile for each guess of t_{nuc} and $\mathcal{D}_{eff}$, requiring hours to process the videos from a day of experiments, which amounts to a few minutes of real time recorded on high-speed video. Given that the growth quickly approaches the asymptotic behavior of $R \propto (t - t_{nuc})^{1/2}$ derived by Scriven [2], we compared the prediction of the nucleation time by fitting an asymptotic model $R(t) = a(t - t_{nuc})^{1/2}$ to the bubble growth to the prediction by the modified Epstein–Plesset model (Figure V.8). The asymptotic square-root model was fit to the data using the same bisection algorithm as used for fitting the modified Epstein–Plesset model, but because the bubble growth could be predicted by a function evaluation instead of a series of numerical timestepping and nonlinear equation-solving, the model could be fit to a day's experiments in minutes instead of hours. While the asymptotic square-root model does not provide other bubble properties like internal pressure and interfacial tension, it does model the growth as accurately as the modified Epstein–Plesset model (see Figure V.8a,b). The model fails at long times when the bubble growth is driven more by the decrease in pressure in the observation capillary, and the difference between its early predicted growth and that of the modified Epstein–Plesset model is relatively high. Nevertheless, the absolute difference between the models at early stages is small, on the order of microseconds typically. As a result, when converted to the nucleation location along the observation capillary d_{nuc} by multiplying the nucleation time t_{nuc} by the centerline flow speed v_{max} to get $d_{nuc} = v_{max}t_{nuc}$, the discrepancy in the prediction of the nucleation time between the models was below 100 μm for a population of 104 bubbles for all but one bubble, for which the discrepancy was about 1.2 mm, which is not catastrophically different (see Figure V.8c).

Because the asymptotic square-root model is faster and more stable numerically, while still agreeing closely with the predictions of nucleation time of the modified Epstein–Plesset model, we estimated the nucleation time for large populations of bubbles using the asymptotic square-root model fit. In the following Chapter, we discuss our analysis of the nucleation times and locations estimated with the bubble growth models presented in this Chapter for a large population of bubbles. In particular, we focus on the distribution of nucleation events over time and position along the observation capillary to estimate the nucleation rate at different degrees of supersaturation and demonstrate that nucleation is homogeneous.
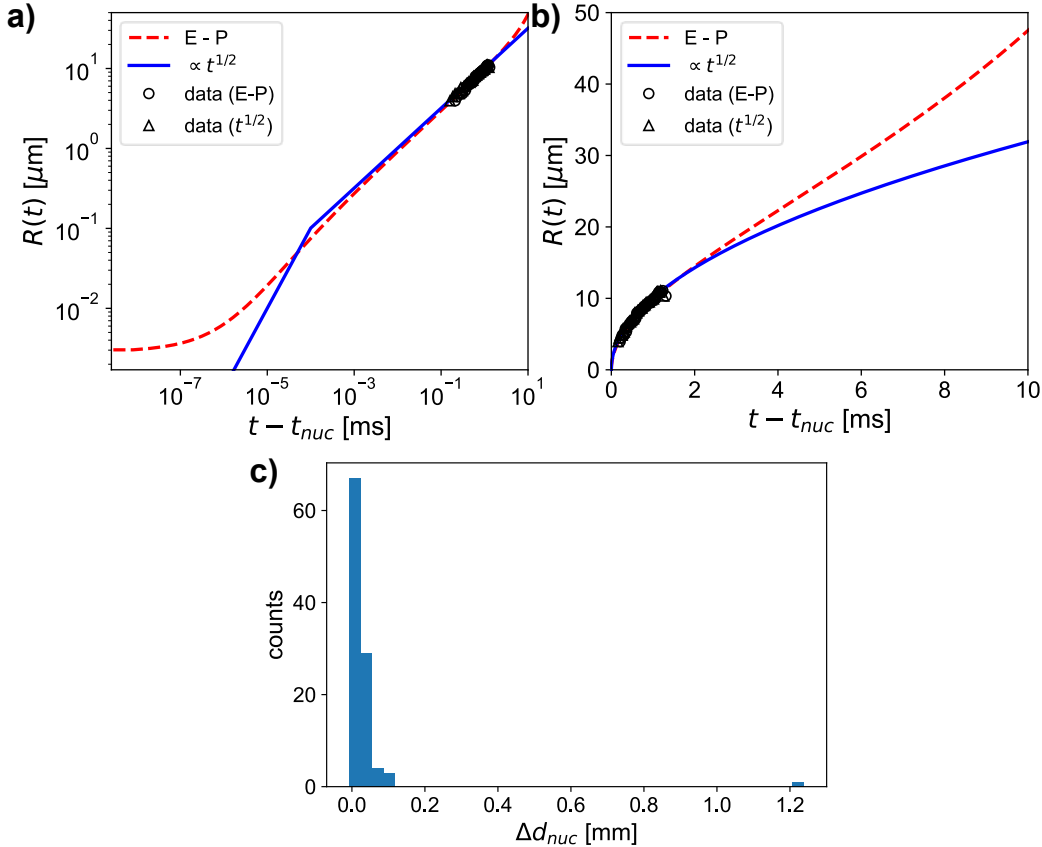
Figure V.8: a) The estimate of bubble growth using the modified Epstein–Plesset model (E - P, red dashed line) and the asymptotic square-root model ($\propto t^{1/2}$, blue line) are plotted as a function of time t since their respective estimates of the nucleation time t_{nuc}. The measured radius of a bubble observed in experiment is plotted as well. The measurements are plotted twice: once in open circles with the time measured relative to the t_{nuc} estimated with the modified Epstein–Plesset model and once in open triangles with the time measured relative to the t_{nuc} estimated with the asymptotic square-root model. The estimated values of t_{nuc} are so similar that distinguishing the two sets of markers for the measured data is difficult. b) Same as (a) but zoomed out to show the discrepancy at longer time scales due to the exclusion of pressure effects in the asymptotic square-root model. The bubble whose measured radii are plotted was observed in an inner stream of PPG 2700 g/mol and CO_2 saturated at 72 bar (7.2 MPa, 1045 psi) ensheathed in 1k5f polyol (see Table II.1) 83 mm along a 100 mm capillary with inner diameter 300 μm, at which point the pressure is estimated to be 23 bar (2.3 MPa, 335 psi). c) Histogram of the difference in the estimated nucleation location Δd_{nuc} [mm] between the two models for 104 bubbles (see Chapter VI for details on estimating the nucleation location based on the nucleation time).

V.5   Recommended Future Work

The bubble growth models presented in this Chapter provide sufficient precision in estimating the nucleation time of bubbles for us to draw conclusions about bubble nucleation in Chapter VI. Nevertheless, questions remain as to why the models we selected succeed and what underlying physics is lumped into the effective diffusivity. While we expect that the increase in the effective diffusivity relative to the true diffusivity is caused by convection, as demonstrated by Scriven [2], a study of how the addition of convection into the model affects bubble growth would be of interest. Specifically, to our knowledge, the literature lacks a clear comparison of the role of convection in accelerating bubble growth. As a suggestion, the model of Barlow and Langlois [3] could be numerically evaluated, as was done for the Epstein–Plesset model in this Chapter, but the convection term could be scaled by a dimensionless parameter $\epsilon \in [0, 1]$. A plot of the predicted bubble growth for values of ϵ in that range would provide useful insight into the extent to which convection accelerates diffusion. An extension of such a study would also solve for the concentration profile outside the bubble to test rigorously the idea that the increased bubble growth due to radial convection can be estimated by the steepening of the concentration gradient at the bubble surface. By quantitatively estimating the degree to which convection increases diffusive flux, one could elucidate the role of the other factors lumped into the effective diffusivity, such as the depletion of CO_2 or axial convection (which can also increase diffusive flux as demonstrated by the Sherwood number [14]). Another extension of such a study would explore the possibility of modeling the observed bubble growth with an Epstein–Plesset model adapted to consider a concentration-dependent diffusivity measured experimentally (*e.g.*, with G-ADSA, as in Chapter III), but scaled by a convection coefficient C. We hypothesize that the growth could be accurately modeled in this way, in which case the convection coefficient would more accurately represent the role of convection since it would be separated from the diffusivity. Such a model could also be extended to model the effect of depletion of CO_2 through diffusion into the outer stream, disentangling that factor from the effect of convection.

A study of the effect of the flow on bubble growth would also be useful in disentangling the various factors at play. We have so far assumed that the dominant form of convection is radial because the velocity gradient in the inner stream is small around small bubbles that nucleate at the center. When bubbles grow larger, or in the rare case that a bubble nucleates off-center, the bubble may no longer travel at the same speed as the surrounding fluid and, therefore, may experience non-

negligible shear convection along the surface of the bubble that might be expected to affect growth (see the work of Jae-Tack Jeong on the relative speed of a bubble in Hagen–Poiseuille flow to the surrounding fluid [15]).

Additionally, if an accurate estimate of the role of convection can be achieved, a survey of how various flow properties and bubble properties affect the role of convection would helpfully illuminate the mystery of why some bubbles have significantly higher effective diffusivities than others. While Scriven provides a formula and plot indicating the effect of different properties of the fluid on the enhancement of growth by convection, connecting that formula to measurable quantities in the experiments measuring bubble growth would extend the predictive power of Scriven's work to allow the experimentalist to estimate the role of convection under different flow or bubble conditions *a priori*.

Lastly, a convincing test of our mental model of how flow and bulk diffusion affect bubble growth would be to simulate the growth of an observed bubble with a computational fluid dynamics (CFD) simulation, such as with COMSOL or OpenFOAM. Ideally, such a model would incorporate the sheath flow profile, the radial convection caused by bubble growth, and the depletion of CO_2 from the inner stream through diffusion into the pure-polyol outer stream, as mentioned earlier, but it would also account for the effect of CO_2 concentration on the local viscosity of the fluid and the subsequent effect of viscosity variations on the flow and concentration profile in the bulk. Because measurements of the viscosity as a function of dissolved gas concentration are limited in the literature and challenging to perform due to the high pressures involved, a simple model based on the Stokes–Einstein–Sutherland relation that the viscosity $\eta \propto 1/\mathcal{D}$ could estimate viscosity as a function of the dissolved CO_2 concentration c_{CO2} using the diffusivity measurements $\mathcal{D}(c_{CO2})$ provided by G-ADSA (Figure II.4).

References

1. Epstein, P. S. & Plesset, M. S. On the Stability of Gas Bubbles in Liquid–Gas Solutions. *The Journal of Chemical Physics* **18,** 1505–1509. ISSN: 0021-9606. http://aip.scitation.org/doi/10.1063/1.1747520 (Nov. 1950).

2. Scriven, L. On the dynamics of phase growth. *Chemical Engineering Science* **10,** 1–13. ISSN: 00092509. https://linkinghub.elsevier.com/retrieve/pii/0009250959800191 (Apr. 1959).

3. Barlow, E. J. & Langlois, W. E. Diffusion of Gas from a Liquid into an Expanding Bubble. *IBM Journal of Research and Development* **6,** 329–337.

ISSN: 0018-8646. http://ieeexplore.ieee.org/document/5392374/ (July 1962).

4. Plesset, M. S. & Zwick, S. A. The growth of vapor bubbles in superheated liquids. *Journal of Applied Physics* **25,** 493–500. ISSN: 00218979 (1954).

5. Venerus, D. C. & Yala, N. Transport Analysis of Diffusion-Induced Bubble Growth and Collapse in Viscous Liquids. *AIChE Journal* **43,** 2948–2959. ISSN: 00011541 (1997).

6. Amon, M. & Denson, C. D. A study of the dynamics of foam growth: Analysis of the growth of closely spaced spherical bubbles. *Polymer Engineering and Science* **24,** 1026–1034. ISSN: 0032-3888. https://onlinelibrary. wiley.com/doi/10.1002/pen.760241306 (Sept. 1984).

7. Szekely, J. & Fang, S.-D. Non-equilibrium effects in the growth of spherical gas bubbles due to solute diffusionII. *Chemical Engineering Science* **28,** 2127–2140. ISSN: 00092509. https://linkinghub.elsevier.com/retrieve/ pii/0009250973850031 (Dec. 1973).

8. Arefmanesh, A., Advani, S. G. & Michaelides, E. E. An accurate numerical solution for mass diffusion-induced bubble growth in viscous liquids containing limited dissolved gas. *International Journal of Heat and Mass Transfer* **35,** 1711–1722 (1992).

9. Jones, S., Evans, G. & Galvin, K. Bubble nucleation from gas cavities a review. *Advances in Colloid and Interface Science* **80,** 27–50. ISSN: 00018686. https: //linkinghub.elsevier.com/retrieve/pii/S0001868698000748 (Feb. 1999).

10. NIST. *NIST Standard Reference Database Number 69* 2022. https:// webbook.nist.gov/chemistry/ (2022).

11. Tolman, R. C. The Effect of Droplet Size on Surface Tension. *The Journal of Chemical Physics* **17,** 758. https://doi.org/10.1063/1.1747247 (1949).

12. Virtanen, P. *et al.* SciPy 1.0: fundamental algorithms for scientific computing in Python. *Nature Methods* **17,** 261–272. ISSN: 1548-7091. arXiv: 1907.10121. http://www.nature.com/articles/s41592-019-0686-2 (Mar. 2020).

13. Leung, S. N., Park, C. B., Xu, D., Li, H. & Fenton, R. G. Computer Simulation of Bubble-Growth Phenomena in Foaming. *Industrial & Engineering Chemistry Research* **45,** 7823–7831. ISSN: 0888-5885. https://pubs.acs.org/ doi/pdf/10.1021/ie060295a%20https://pubs.acs.org/doi/10. 1021/ie060295a (Nov. 2006).

14. Takemura, F. & Yabe, A. Gas dissolution process of spherical rising gas bubbles. *Chemical Engineering Science* **53,** 2691–2699. ISSN: 00092509. https: //linkinghub.elsevier.com/retrieve/pii/S0009250998000943 (Aug. 1998).

15. Jeong, J. T. Axisymmetric slow viscous liquid flow around a spherical bubble translating in a circular tube. *European Journal of Mechanics, B/Fluids* **88,** 58–66. ISSN: 09977546. https://doi.org/10.1016/j.euromechflu.2021.01.001 (2021).

The Nucleation Nursery

The Lord took Abram [Abraham] outside and said, "Look up at the sky and count the stars—if indeed you can count them." Then he said to him, "So shall your offspring be."

The Book of Genesis, Chapter 15, Verses 3–5, New International Version

Understand, then, that those who have faith are children of Abraham.

St. Paul's Letter to the Galatians, Chapter 3, Verse 7, New International Version

Bubbles do not often nucleate homogeneously. As discussed in Chapter I, bubbles prefer to nucleate with the assistance of a surface or contamination through heterogeneous nucleation or grow from an existing microbubble when they have the chance to do so. A bubble that nucleates homogeneously has therefore avoided an easier pathway through a site that is seen until the mother phase can nucleate all bubbles at once through the unseen thermal fluctuations. At this moment, all bubbles emerge as children of the same mother phase and grow together in the same nursery of its mother. We cannot know the location or time of the nucleation of any

individual bubble, but through faith in the unseen workings of the mother phase, everywhere bubbles will gain life.

In this Chapter, these are the fingerprints by which we will distinguish homogeneous bubble nucleation from heterogeneous: randomness and rapid onset. They are also the features of homogeneous bubble nucleation that make it difficult to measure (as discussed in Section III.1). Homogeneous bubble nucleation results from thermal fluctuations, so nucleation events are independent of each other and uncorrelated. Such events are described by the Poisson statistical distribution. In Section VI.1, we show that the time interval between observations of bubble nucleation indeed follows behavior expected of Poisson distributed events, at least in the experiments for which sufficient bubbles were observed for meaningful statistics. Additionally, because homogeneous bubble nucleation occurs homogeneously, all nucleation "sites" can nucleate bubbles simultaneously. Given the high sensitivity of the nucleation barrier to the degree of supersaturation (see discussion of classical nucleation theory in Section I.4), the onset of an observable rate of bubble nucleation will be rapid in a system with an increasing supersaturation like the present apparatus (see pressure profile sketched in Figure III.2). We estimate the nucleation rate as a function of the supersaturation (estimated by the pressure) in Section VI.2 and show that the rate increases rapidly within a short window of the degree of supersaturation (pressure in the capillary).

We chose these fingerprints to distinguish homogeneous bubble nucleation because drawing the distinction from the observation of a single bubble is often not possible. In some cases, the distinction is obvious: a cluster of bubbles emanating from an oddly shaped particle is likely the result of heterogeneous nucleation from the cavities along with the contaminant particle. In most cases, however, an individual bubble that nucleates by homogeneous nucleation and a bubble that nucleates by heterogeneous nucleation appear the same. This similarity is even true in the apparatus described in Chapter III because, while the inner stream of polyol and CO_2 does not come into contact with the interior walls of the apparatus, it may contain sub-micron particles or metastable microbubbles not detectable with optical microscopy [1]. Bubbles can nucleate heterogeneously on sub-micron particles or emerge from microbubbles and leave no optically detectable trace of a particle, which often limits the experimentalist's ability to declare that a bubble nucleated by homogeneous nucleation (see Section 1.6 of [2]).

While we cannot ever prove that the bubbles observed nucleated homoge-

neously without more careful elmination of sub-micron nucleation sites, we can at least identify the bubbles whose behavior is consistent with homogeneous nucleation (which we will define as having the two fingerprints mentioned in the introduction: stochasticity and rapid onset with supersaturation) and estimate their rate of nucleation. We can then more meaningfully compare our experimental measurements to theoretical models of homogeneous bubble nucleation. Most models describe homogeneous bubble nucleation because heterogeneous nucleation is dependent on the microscopic geometry of the nucleating particles, which is often not known. In Section VI.3, we describe a model for estimating the nucleation energy barrier by applying the string method to the density functional theory described in Section II.4. We then show that this model of the nucleation energy barrier can be fit to the nucleation rates estimated from experiments in Section VI.4, while noting the limitations of modeling the nucleation rates with classical nucleation theory. Finally, we offer recommendations for the extension of this work in Section VI.5.

VI.1   Time between Nucleation Events Described by Poisson Statistics

The Poisson statistical distribution describes the occurrence of discrete, independent, and identically distributed probabilistic events. A classic example of such an event is the emission of a radioactive particle from an isotope undergoing radioactive decay because the emission of one particle has essentially no effect on the emission of the next. Under the proper circumstances, homogeneous bubble nucleation is also described by Poisson statistics. Given a collection of identical samples of fluid held at a fixed supersaturation, the nucleation of a bubble inside a sample is described by the Poisson distribution. This concept was used by Dr. Adam Olsen to estimate the nucleation rate of polyethylene oxide crystals in aqueous droplets at different activities of water [3]. In that case, the nucleation of crystals could take up to an hour and individual droplets could be held under fixed conditions and observed by Mie scattering inside a droplet levitation chamber. In the present apparatus (Chapter III), samples of polyol and CO_2 in the inner stream rapidly change in supersaturation as they flow down the observation capillary, so Olsen's experimental approach cannot be exactly replicated. Nevertheless, when the flow is stable, the degree of supersaturation at a particular location along the observation capillary remains constant. If we assume that the inner stream fluid is uniform, the segment of fluid observed at one moment has the same likelihood of nucleating as the segment of fluid observed at any other moment. Therefore, while the fluid particles themselves are not identical, the properties of the fluid under observation

are identical with respect to the factors relevant to bubble nucleation, so we treat the fluid within the field of view as the same sample over time.

One key property of Poisson-distributed events is that their occurrences are governed by first-order kinetics [4]. Consequently, given a collection of N_0 samples, the number of samples that has not yet nucleated decays exponentially with time $N = N_0 e^{-kt}$, where the decay constant k gives the frequency of nucleation events (see discussion on pp. 2-24 to 2-25 of [3]). In the present experiment, we do not continuously observe a sample of fluid, but although the fluid in the section of the flow observed is constantly replaced, its replacement is essentially identical throughout the experiment until a bubble appears. By assuming that the fluid in the section of the flow observed does not significantly change in properties, in particular, supersaturation of dissolved CO_2, we can treat the fluid in that section as a single "sample" in between bubbles.

The fluid within the field of view is not identical when it contains a bubble. A bubble reduces the volume of fluid in which another bubble can nucleate both by its volume and by the volume of fluid surrounding it from which it has collected its CO_2. Consequently, the fluid within the field of view is only identical in between observations of bubbles. Therefore, we treat the fluid within the field of view as if it is a single sample of fluid held at fixed supersaturation, neglecting the small variation in the pressure and, thus, the supersaturation along the field of view. From this perspective, the fluid within the field of view between bubble observations is like one of the droplets in Olsen's work, and the time between bubble observations is a reasonable estimate for the time that a single fluid sample would take to nucleate a bubble. However, bubbles are sometimes observed long after nucleation (see Chapter VIII). In these cases, we cannot consider the observable segment of fluid to have nucleated a bubble, but because it has been disturbed by the passing of a bubble, we also cannot consider it to be an identical sample. Consequently, we only consider segments of fluid observed between two bubbles that nucleated within the field of view, ignoring the rest of the experiment for this analysis.

Because we only consider segments of fluid between bubbles that nucleate within the field of view, the number of measured incubation times is few for most experiments. Nevertheless, in a couple of experiments, enough incubation times could be measured to compare N to exponential decay. Measurements from two such experiments are shown in Figure VI.1. In these experiments, the inner stream was composed of PPG 2700 g/mol (see Table II.1) saturated with CO_2 at 72 bar (7.2
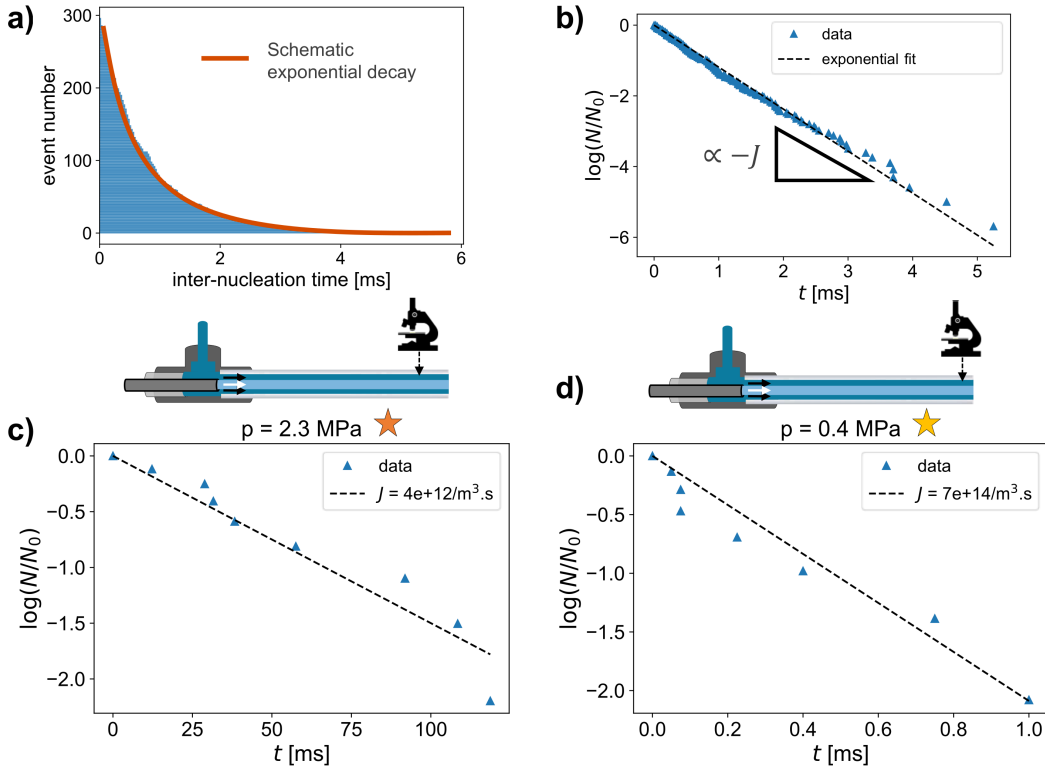
Figure VI.1: a) Time between consecutively observed nucleation events ("inter-nucleation time") plotted in decreasing order with schematic of an exponential decay fit. Data taken at 77 mm while flowing a 5:1 mixture of PPG 2700 g/mol polyol with cyclopentane saturated with CO_2 at 7.2 MPa with an inlet pressure of 13.4 MPa (too few bubbles without cyclopentane). b) The natural logarithm of the fraction of not-yet-decayed samples $\log(N/N_0)$ is fit to a straight line (dashed black) passing through the origin ($N(t = 0) \equiv N_0$), indicating exponential decay. The slope of the fit is proportional to the nucleation rate J. c) and d) Data were taken in an identical experiment in the absence of cyclopentane. The location of each measurement is depicted schematically above each plot. From exponential fits (dashed lines), the nucleation rate J is calculated (see legend for values). The measurements in (c) were taken at 83 mm along the observation capillary (2.3 MPa) with an inlet pressure of 13.4 MPa; the estimated nucleation rate will be represented by an orange star. The measurements in (d) were taken at 95 mm along the observation capillary (0.4 MPa) with an inlet pressure of 8.4 MPa; the estimated nucleation rate will be represented with a yellow star.

MPa, 1045 psi), and flowed at 50 μL/min inside a sheath of 1k5f polyol, within a quartz capillary of 300 μm inner diameter. For the data shown in Figure VI.1a,c, the outer stream was flowed at 320 μL/min, resulting in an inlet pressure of 134 bar (13.4 MPa, 1945 psi). For the data shown in Figure VI.1b,d, the outer stream was flowed at 210 μL/min, resulting in an inlet pressure of 84 bar (8.4 MPa, 1220 psi).

In the top row, the incubation time of each sample (horizontal axis) is plotted to give a visual depiction of the stochasticity. The number of samples that have not nucleated N is computed from the data in the top row by drawing a horizontal line at each time point on the vertical axis and counting how many bars it passes through. In the bottom row, the natural logarithm of the fraction of the number of samples that have not nucleated $\log(N/N_0)$ is plotted as a function of time. While fewer measurements were available in this experiment to draw a definitive conclusion about the quality of the fit, at both pressures considered, 2.3 MPa (Fig. VI.1a,c) and 0.4 MPa (Fig. VI.1b,d), the exponential decay fits reasonably well. Note that the incubation times differ by two orders of magnitude between the two pressures due to the significantly higher nucleation rate at the lower pressure. That the number of samples that have not nucleated decays exponentially suggests that the bubble nucleation observed is a Poisson process and thus is likely homogeneous. For stronger evidence of this conclusion, see Figure VII.2.

The decay of N is not always fit well by an exponential function. In some cases, $\log(N/N_0)$ contains clusters of nucleation times that follow different decay rates. We suspect that the different clusters correspond to variations in the flow conditions or supersaturation. Such variations may arise due to variations in the volume occupied by bubbles at the end of the observation capillary or other flow fluctuations. We have not explored the factors that correlate with these clusters, however. In other cases, a few fluid samples have a significantly longer incubation time than the others, such that most incubation times follow a single decay rate with a few outliers. Given that we only record $\sim$ 10 measurements per experiment, we suspect that these variations would be lessened by taking more measurements, as observed in Chapter VII where nucleation rates are higher.

As mentioned, the decay rate k is equal to the frequency of bubble nucleation in the sample volume. Therefore, the nucleation rate per volume J can be computed by dividing the frequency by the volume of the fluid sample k/V, where $V = \pi R_i^2 L_{FOV}$, with R_i as the inner stream radius and L_{FOV} as the length of the field of view within which we can detect bubbles during an experiment. This estimation method likely underestimates the nucleation rate because the cross-sectional area of fluid that is actually at the reported degree of supersaturation is smaller than the cross-sectional area of the inner stream due to depletion of CO_2 by diffusion into the outer stream (as discussed in Chapter V). Because we have not developed and validated an accurate estimate for this depletion of CO_2, we assume no depletion

for consistency. The reported nucleation rates J should thus not be interpreted as precise estimates of the true nucleation rate, but rather as rough estimates for comparison within the context of the present work. The nucleation rates estimated by this method are reported in the legends of Figure VI.1c,d. These nucleation rates are compared to the string method model in Figure VI.6. The ability to be described by the model gives further support for our hypothesis that the bubble nucleation is homogeneous and described by Poisson statistics.

VI.2   Estimation of Nucleation Rate vs. Pressure Indicates Rapid Onset of Bubble Nucleation

The other property we use to demonstrate that bubble nucleation is homogeneous is the rapid onset with increasing supersaturation. Heterogeneous bubble nucleation can occur at much lower degrees of supersaturation and is limited in rate by the rate at which bubbles leave the nucleation site. Homogeneous bubble nucleation occurs rapidly and throughout the bulk and is extremely sensitive to the degree of supersaturation. The sensitivity of homogeneous bubble nucleation to the supersaturation was demonstrated in the measurements of bubble nucleation in superheated liquids by Avedisian [5] (see Figure 2, in particular).

To demonstrate the onset of bubble nucleation, we count the number of nucleation events per time at points along the observation capillary, each corresponding to a different degree of supersaturation. As discussed in Section V.3, by fitting a model of bubble growth to a sequence of measurements of the radius of a bubble over time, we can estimate the nucleation time by extrapolating the model backward in time to the critical radius of nucleation. This time t_{nuc} can be converted into a distance along the observation capillary d_{nuc} by multiplying by the centerline flow speed v_{max} (since bubbles rarely nucleate away from the center of the inner stream). This distance can be converted to an estimate for the fluid pressure $p \approx [(L - d_{nuc})/L]p_{in}$ for capillary length L and inlet pressure p_{in}.

Because nucleation events can be rare, we count the number of nucleation events within a segment of the inner stream of length dL. The size of dL is chosen such that it is larger than the uncertainty in the capillary position (about $500~\mu$m) but smaller than the distance over which the pressure varies significantly ($p/(\mathrm{d}p/\mathrm{d}z)$, which depends on the local fluid pressure p). In general, we bin in segments of $\mathrm{d}L = 500~\mu$m, which corresponds to a volume of $V = \pi R_i^2 \mathrm{d}L$ for an inner stream width of R_i. Inside each bin, we count the number of bubble nucleation events over

the course of a video recording (or series of recordings) that lasts a length of time t. During the recording, bubbles may be observed that are larger than the width of the inner stream and have elongated (see Chapter VIII). Because we have only shown that our model for bubble growth is accurate for spherical bubbles, we cannot estimate the nucleation time for these elongated bubbles. Instead, we exclude these bubbles from the count of nucleation events. We show the number of nucleation events in each such bin in Figure VI.2a. The data were taken from the same set of experiments used to produce Figure VI.1a,c.
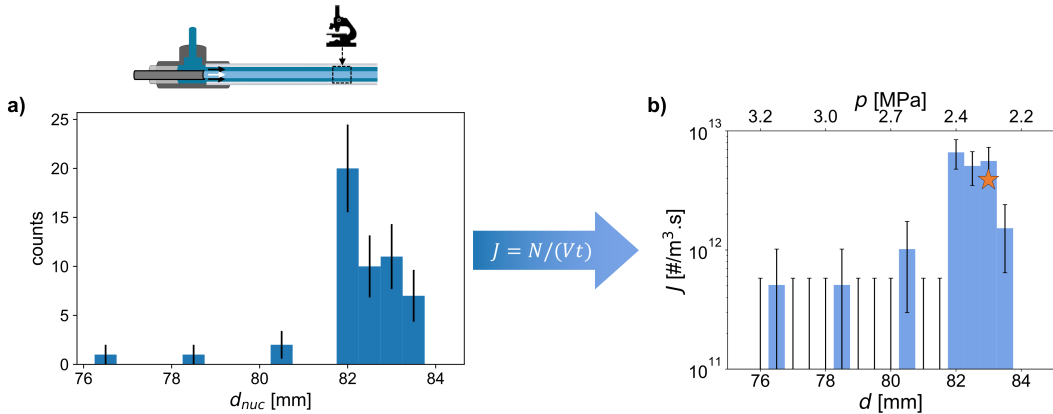
Figure VI.2: a) A histogram of the observed bubbles estimated to nucleate within the field of view of the microscope from video recordings taken at several locations along the observation capillary. Error bars represent one standard deviation of Poisson noise. Data were collected from the same experiment as Figure VI.1a,c. Location of the measurements is depicted schematically in the diagram of the microfluidic channel. b) By assuming that the number of nucleation events observed in a segment of the observation capillary is the number of observed nucleation events N in a volume V over a time t, the nucleation rate is calculated $J = N/(Vt)$ and plotted as a function of distance along the observation capillary (bottom axis) and estimated fluid pressure (top axis). Error bars are Poisson noise except in the case where no bubbles were observed (see text for explanation). The orange star represents the nucleation rate estimated by the exponential fit in Figure VI.1c.

Having shown that the nucleation events follow Poisson statistics in the previous Section, we plot error bars representing one standard deviation of the Poisson noise (proportional to the square root of the number of counts). From the counts alone, the rapid increase in bubble nucleation rate at 82 mm along the observation capillary is apparent. Nevertheless, different segments of the observation capillary may be observed for different amounts of time, so the relevant comparison is the nucleation rate. The nucleation rate is calculated by dividing the number of counts, which we assume is the expected number of counts $\langle N \rangle$, by the volume of the fluid

segment V and the time of recording t to get $J = \langle N \rangle / (Vt)$. The resulting nucleation rate is shown in Figure VI.2b. Note that the apparent decrease in the peak at 82 mm relative to the other values when converting from counts in (a) to nucleation rate in (b) is due to the longer time for which this location happened to have been observed.

While the Poisson noise offers a reasonable estimate of the uncertainty in the number of counts, it is zero for cases where no bubbles were observed. Nevertheless, a Poisson process may present no counts in an experiment even if it has an expected number of counts $\langle N \rangle > 1$. Given an expected number of counts $\langle N \rangle$ for a Poisson process, the probability of observing no counts is $e^{-\langle N \rangle}$. As a simple, first-order approximation of the uncertainty in a measurement of no counts, we assumed that a measurement of no counts is most likely an indication that the expected value was less than 1.15. We chose the cutoff of 1.15 because the probability of observing no counts given an expected value of 1.15 is $e^{-1.15} \approx 0.32$, which is the likelihood that a measurement of a Gaussian process is beyond one standard deviation from the mean. Therefore, the height of the error bars for measurements of zero counts in Figure VI.2b is the nucleation rate corresponding to the observation of 1.15 counts.

From Figure VI.2, we see that the nucleation rate rapidly increases with distance along the capillary d at $d = 82$ mm. For $d < 82$ mm, zero or one bubble nucleation events were observed during the experiment, while for $d = 82$ mm, 20 nucleation events were observed, corresponding to an increase in the nucleation rate of at least an order of magnitude over 500 μm of capillary or less than 0.1 MPa. While the increase may appear to be small on a log scale, an order of magnitude is a significant increase for such a small change in the supersaturation. This rapid rise also looks less rapid due to the apparent decrease in the nucleation rate for $d > 82$ mm. The nucleation rate appears to decrease because the inner stream becomes increasingly filled with elongated bubbles, which are not included in the count of bubble nucleation events. More measurements are needed to reduce the uncertainty enough to probe the possibility of a sharper increase in the nucleation rate.

In Figure VI.2b, an orange star is plotted at $p = 2.3$ MPa to show the prediction of the bubble nucleation rate by the exponential decay method shown in Figure VI.1c. The predicted rate is slightly below the lower bound of the error bar. Given that nucleation rates are notoriously imprecisely measured to their exponential dependence on the system properties, we consider this agreement reasonable between the two methods. Nevertheless, we note that the estimation of nucleation rate by counting nucleation events likely underestimates the true nucleation rate

due to the exclusion of elongated bubbles, leading to an underestimate of $\langle N \rangle$, and not accounting for the depletion of CO_2 along the edges of the inner stream, leading to an overestimate of V. Therefore, we do not comment on the possibility of inconsistencies between the methods.

In this Chapter, we used the asymptotic square-root model to model the bubble growth due to the greater efficiency and simplicity with little loss in accuracy, as discussed in Section V.4. In that Section, we showed in Figure V.8 that the error in the nucleation location d_{nuc} introduced by using the square-root fit instead of the modified Epstein–Plesset model is less than 100 μm, with one outlier out of 104 having an error of 1.2 mm. To demonstrate that this error is negligible for our analysis of bubble nucleation rates, we plot the nucleation rate estimated using each model in Figure VI.3. The conditions are identical to those used to produce Figure VI.1b,d. The estimated nucleation rate is identical for every segment except the four marked with a star above. In each of these four cases, the discrepancy is within the uncertainty. This Figure demonstrates another advantage of the square-root model inside the red dashed box. At these values of p and laboratory temperature ($T = 22$ °C), the bubble may reach the condensation pressure of CO_2 (6 MPa [6]) as a result of the Laplace pressure during computations. Near the phase change, the model becomes stuck in an infinite loop trying to correct for the resulting errors and no estimate for the nucleation time is found. With the square-root model, the properties of CO_2 are all lumped into the effective diffusivity, so the nucleation time can be estimated at these higher pressures. The accuracy cannot be evaluated relative to the modified Epstein–Plesset model in this regime, however.

In the preceding Sections, we demonstrated that we can identify bubbles that nucleate stochastically according to Poisson statistics (Section VI.1) and suddenly upon small changes in the supersaturation (Section VI.2). As described in the introduction to this Chapter, these two properties are unique to homogeneous bubble nucleation and are not expected for heterogeneous bubble nucleation. Showing that the bubbles observed have these properties is not sufficient to prove that the bubbles nucleated homogeneously. Jones *et al.* suggest that significantly higher supersaturation ratios (order 100 or greater) are necessary for homogeneous nucleation of bubbles from a supersaturated solution. They instead propose that bubbles that nucleate at lower supersaturation ratios, such as those considered in this Chapter, emerged from metastable microbubbles temporarily stabilized by trace surfactants in the solution at sizes smaller than the spatial resolution [1]. While we cannot
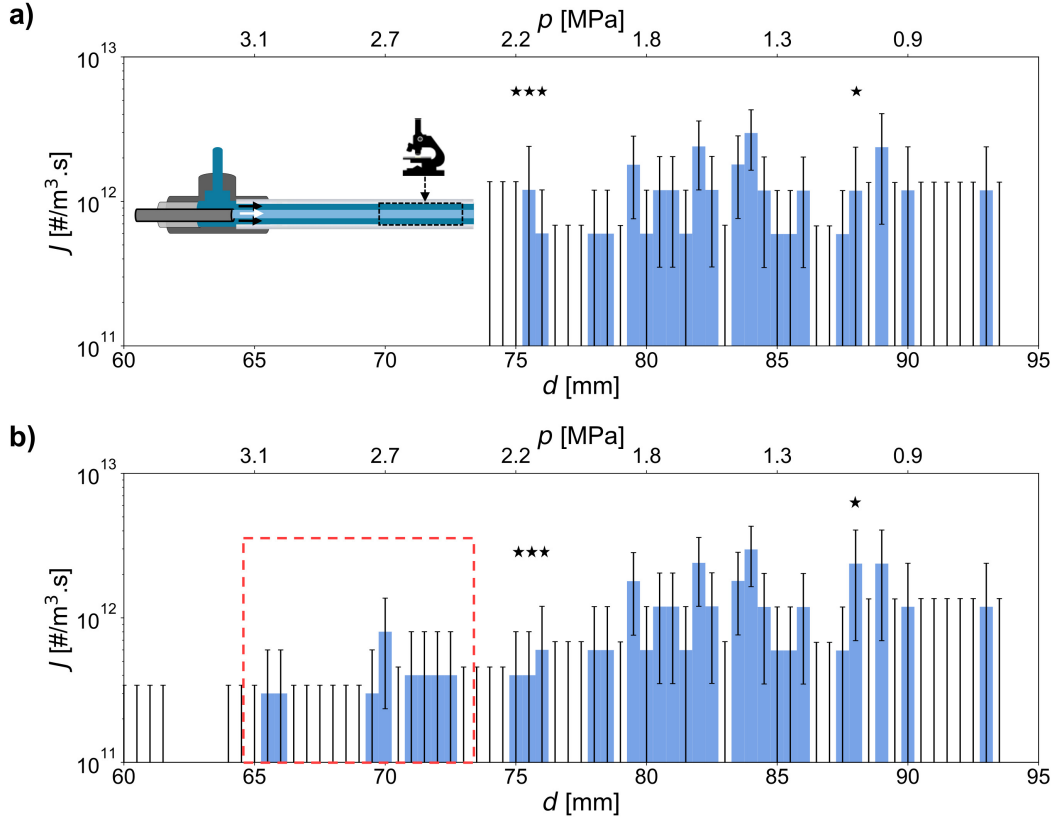
Figure VI.3: a) Nucleation rate J estimated as a function of distance along the observation capillary d (bottom axis) and estimated fluid pressure p (top axis) based on the prediction of the nucleation time from fitting the modified Epstein–Plesset model (see Section V.3). Error bars indicate Poisson noise except if no bubbles were observed (see main text for discussion). The location of the measurements is shown schematically with the diagram of the microfluidic channel. b) Same as (a), but the nucleation time is estimated from fitting the asymptotic square-root model (see Section V.4). This model permits the estimation of the nucleation rate at higher pressures (red dashed box). The four locations with different estimates for the nucleation rate between the models are marked with stars; all are within the statistical uncertainty.

completely rule out the possibility that the bubbles observed emerged from microbubbles or other sub-micron particles due to the limited spatial resolution of our optical microscope, we find that the behavior of the bubbles we observe to emerge from a sub-micron size is consistent with homogeneous bubble nucleation. Thus, we believe that they can be meaningfully compared to models of homogeneous bubble nucleation.

VI.3   Model of Bubble Nucleation Energy Barrier by Applying the String Method to a Density Functional Theory

Due to the limitations of classical nucleation theory, such as assuming an infinitesimal interface with constant interfacial tension (see discussion in Section I.4), we developed our own model of bubble nucleation. We wanted a platform that could incorporate the system-specific measurements of the mother phase provided by G-ADSA (Chapter II). Having demonstrated in Section II.4 that our density functional theory (DFT) could predict the interfacial tension between polyol-rich and CO_2-rich phases reasonably accurately, we built our model on this DFT. The string method [7] can find the minimum free energy pathway through the free energy landscape defined by the DFT, as demonstrated by Xu *et al.* [8]. A schematic of this process is shown in Figure VI.4a,b. Figure VI.4a shows the physical process of a bubble expanding from state A to state B to state C and, finally to state D. In Figure VI.4b, the same expansion is mapped along a two-dimensional projection of the free energy heatmap, with lines indicating system states with the same free energy. The initial guess for the nucleation pathway (straight black line with black circles directly from A to D) is pulled "taut" along the free energy landscape, shifting in the direction of the white left-pointing arrow until the minimum free energy pathway is found (pink line with pink circles tracing through each state). Based on the work of Xu *et al.*, collaborator Dr. Huikuan Chao applied the string method to the DFT he created for modeling the interfacial tension of the polyol–CO_2 mother phase to predict the nucleation energy barrier at different points along the observation capillary.

The output of the string method model is the density profile at each point along the minimum free energy path to nucleation. Using the DFT, the free energy of each density profile can be computed and plotted as a function of the volume of the bubble, where the surface of the bubble is usually estimated by the Gibbs dividing surface. An example of such a plot is shown in Figure VI.4c. The conditions were chosen to match those of the experiment analyzed to estimate the nucleation rates in the previous Section: PPG 2700 g/mol saturated with CO_2 at 7 MPa (70 bar, 1015 psi) and 24 °C. The free energy follows the qualitative behavior expected from the classical nucleation theory of a single nucleation barrier (marked by a star) followed by a steady decrease in the free energy. The string method assumes a quasistatic process that can partially equilibrate at each location along the string. In reality, equilibrium is only achieved at the nucleation barrier where the free energy reaches a saddle point, but the model is nevertheless valid if nucleation is slow enough
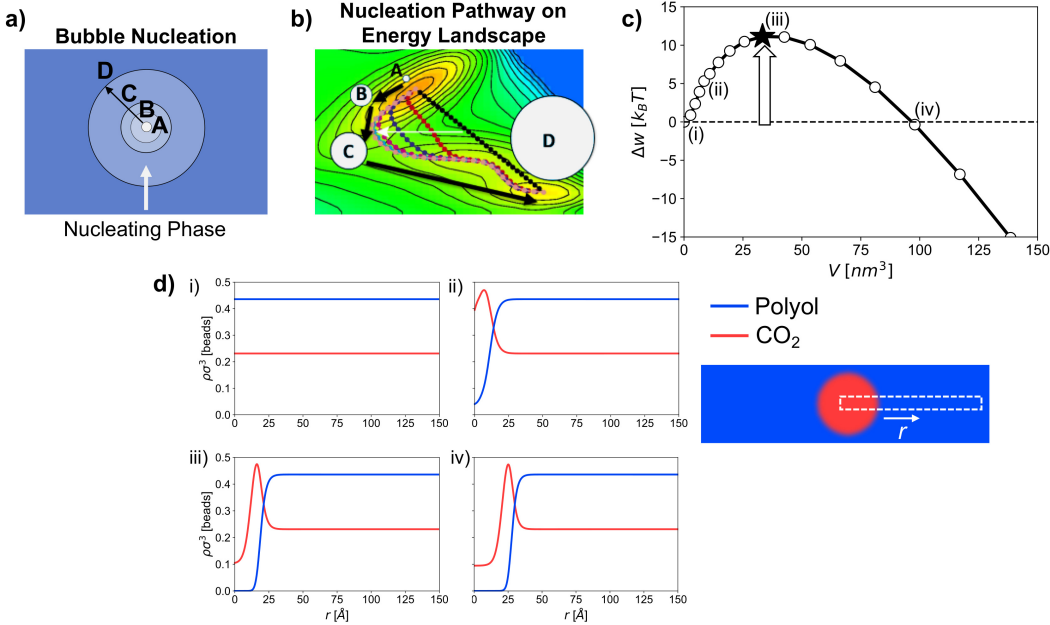
Figure VI.4: a) Schematic of bubble nucleation (light-colored circles) in a supersaturated mother phase (blue background) passing through states A, B, C, and D. b) Heatmap representing a free energy landscape for the different states passed through during nucleation (for schematic purposes only—not related to the present work). A pathway is guessed between the start (A) and end (D) states (black line with black circles). The string method then pulls the string connecting them "taut" (follow left-pointing white arrow) to find the minimum free energy path (pink line with pink circles). Adapted from Alberto Giacomello *et al.* *PNAS* 2016 113(3):E262 Copyright 2016 National Academy of Sciences. c) Prediction by the string method of the free energy along the string tracing the minimum free energy path for bubble nucleation. The conditions are: PPG 2700 g/mol polyol saturated with CO_2 at 7 MPa and 24 °C quenched to 0.1 MPa. The peak of the free energy (black star) is the nucleation energy barrier (height of white upward arrow). The indices (i)–(iv) indicate the points corresponding to the density profiles in (d). d) Density profiles from the DFT on which the string method is based of polyol (blue lines) and CO_2 (red lines) plotted in reduced units (number of beads of each compound per volume equal to the cube of the CO_2 bead size, which is 2.79 Åas given in Table II.2) as a function of radius r from the bubble center (in Angstroms). The free energy of each density profile (i)–(iv) is marked in c). The region between the bubble center and the mother phase plotted in (d) is shown schematically in the lower right with the radial direction r indicated.

that the state space can be explored before each nucleation event (see discussion in Section I.4). For more details on the formulation of the string method, refer to the presentation by Wang *et al.* [9].

While there is no evidence that the density profiles predicted by the DFT

along the path found by the string method are realized in physical systems, they provide insight into the nucleation process. Four density profiles from different points along the nucleation pathway are shown in Figure VI.4d, which are labeled (i)-(iv) with their size and free energy indicated by the same label in panel (c). In this case, the nucleation process begins from a uniform mother phase (i). To nucleate a bubble, CO_2 must be collected while expelling polyol, which costs free energy (ii). At the nucleation energy barrier, the bubble has grown to its largest size without achieving a bulk density inside. The high free energy cost is mostly driven by the large concentration gradients. Once the nucleation barrier is overcome, the bubble achieves a bulk density at its core (iv). Because the bulk phase inside the bubble is thermodynamically favorable (otherwise nucleation would not occur), the free energy cost decreases and the bubble continues to grow. Beyond this point, the predictions of the string method are not physically meaningful because they neglect diffusion limitations, convection and flow, and other macroscopic behaviors.

Because the string method is based on DFT, and the DFT is based on PC-SAFT (see Section II.4), the predictions of bubble nucleation by the string method depend on the selection of parameters for the PC-SAFT model. As discussed in Section II.4, an infinite set of PC-SAFT parameters can model the CO_2 solubility and interfacial tension measured with G-ADSA, but none can accurately model the specific volume. Rather, we found one set of parameters that accurately models the qualitative behavior of the specific volume (increases with pressure) and is similar to those predicted by the group contribution method [10]. Another set of parameters more accurately models the specific volume quantitatively (smaller discrepancy from the measurements) but predicts the opposite qualitative behavior (predicts that specific volume decreases with pressure instead of increasing). The nucleation energy barrier predicted by the string method with each of these sets of parameters is shown in Figure VI.5.

The conditions are the same as those used to generate the string method predictions shown in Figure VI.4c,d. The nucleation barrier (marked with a star) was calculated at four ambient pressures, each corresponding to a different point along the observation capillary: 4.0 MPa, 2.0 MPa, 1.0 MPa, and 0.1 MPa (outlet pressure) and plotted on the right. The prediction for the parameters that achieved a more *quantitative* fit of the specific volume (parameters listed in caption of Figure VI.5) is shown on the top; on the bottom is the prediction for the parameters that achieved a more *qualitative* fit (parameters listed in Table II.2). While these parameters lead to
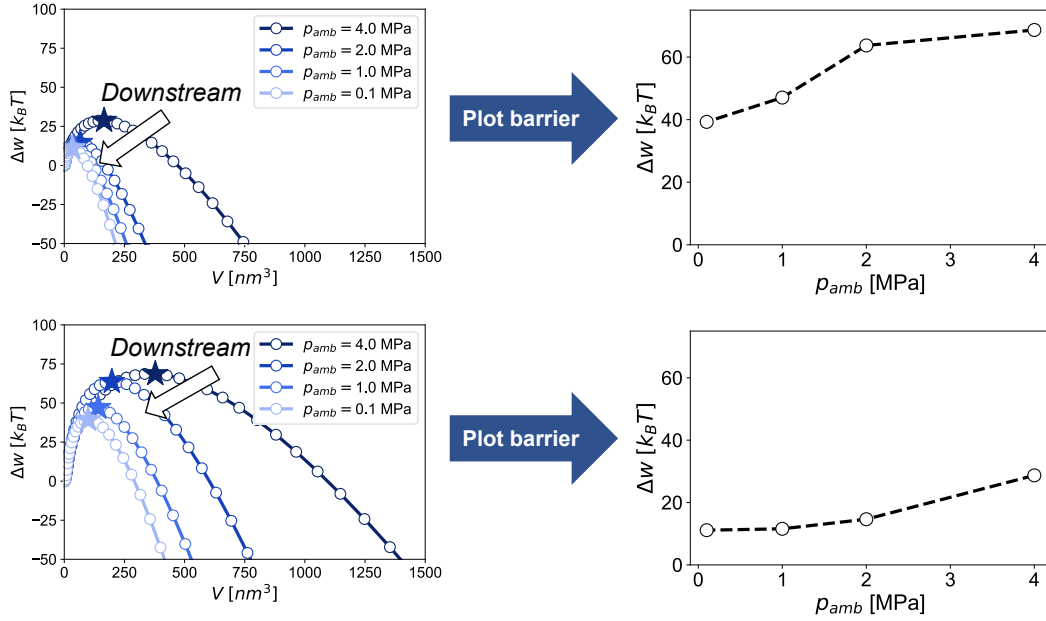
Figure VI.5: Left) Free energy Δw in units of thermal energy as a function of the bubble volume along nucleation pathways predicted by the string method for PPG 2700 g/mol polyol saturated with CO_2 at 7 MPa at 24 °C and quenched to p_{amb} = 4.0 MPa, 2.0 MPa, 1.0 MPa, and 0.1 MPa (in order of increasing lightness of blue), which corresponds to points further downstream along the observation capillary (marked by white arrow). Right) The nucleation energy barrier (marked by a star) is plotted as a function of the quench pressure p_{amb}. The model used for the top uses the PC-SAFT parameters listed in Table II.2. The model used for the bottom uses the PC-SAFT parameters that yield a better quantitative fit of the specific volume (see Figure II.2): $\sigma = 3.17$ Å and $\epsilon = 253$ k_B.

models that predict the same CO_2 solubility and interfacial tension, as well as specific volumes within 15% of each other, they caused differences in the prediction of the nucleation barrier by the string method of 20–40 $k_B T$. Given that the nucleation rate depends on the negative exponent of the nucleation energy barrier scaled by $k_B T$, these discrepancies correspond to multiplicative differences of 10^8–10^{17} in the nucleation rate.

Because of the extreme sensitivity of the string method's prediction of the nucleation rate on the PC-SAFT parameters, the value of the string method for quantitative predictions is limited without a more rigorous and precise method for estimating the PC-SAFT parameters. While the string method provides helpful qualitative insights into the nucleation pathway by estimating the density profiles along the way, the uncertainty in the nucleation energy barrier is likely too high to be useful. Furthermore, the string method does not provide an estimate of the

coefficient J_0 needed to estimate the nucleation rate $J = J_0 e^{-\Delta W / k_B T}$. The value of J_0 may vary by several orders of magnitude depending on whether nucleation is limited more by diffusion, interfacial tension, or viscosity [11], none of which is accounted for in the string method. Despite these limitations of the application of the string method, we explore the possibility of modeling the measured nucleation rates with the string method in the following Section.

VI.4 String Method Model Can Be Fit to Measured Nucleation Rate While Classical Nucleation Theory Cannot Be

Despite the extreme sensitivity of the string method predictions of the nucleation barrier to the PC-SAFT parameters used in the model, we attempt to use its predictions to model the data from Sections VI.1 and VI.2. Given that the PC-SAFT parameters that achieved a qualitative fit of specific volume (see Table II.2) led to reasonable nucleation barriers near 10 $k_B T$ (bottom right of Figure VI.5), we select that parameter set for our model. Because the string method does not treat the nucleation coefficient J_0, we treat it as a fitting parameter to the nucleation rates reported in Figure VI.2. We find that the value $J_0 = 10^{20}$ /m^3.s yields a reasonable model for the data, as shown in Figure VI.6, with the experimental measurements shown in panel (a) and the predictions of the fitted string method model in panel (b). While we cannot comment on why such a value yields a reasonable agreement, especially given the likelihood that the estimates of the measured nucleation rate are lower than the actual rate, the model qualitatively captures the observed behavior. In the experiment, an increase in the nucleation rate by a factor of 10 was observed from 2.5 MPa to 2.4 MPa. The model shows an increase in the nucleation rate by a factor of 10 from 10^{12} to 10^{13} / m^3.s from 2.6 MPa to 2.2 MPa (see inset). While the model predicts a steeper decrease in the nucleation rate at higher pressures, the uncertainty in the measurements is too large to determine if the nucleation rate decreased as rapidly in the experimental system.

We also compared the measured nucleation rate estimated using the fit to Poisson statistics from Section VI.1. The estimated nucleation rate J from Figure VI.1c for a pressure of 2.3 MPa is plotted with an orange star and that from Figure VI.1d for a pressure of 0.4 MPa is plotted with a yellow star. Surprisingly, both values are close to the model predictions. While the string method model is not robust to parameter selection, the model resulting from this particular set of parameters captures the measurements of nucleation rate available.
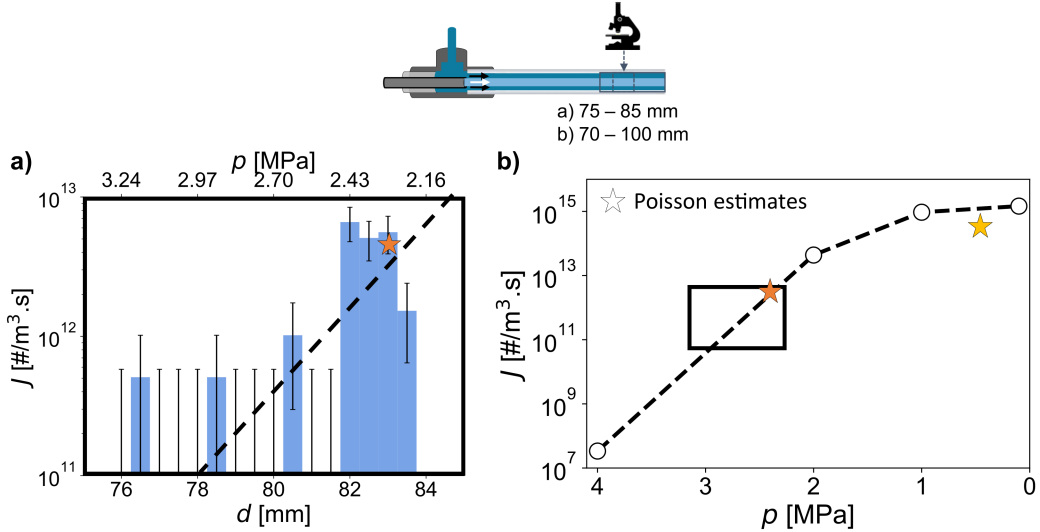
Figure VI.6: a) Same plot of estimated nucleation rate from experiments as a function of degree of supersaturation along the observation capillary as in Figure VI.2b, repeated for convenience, now with the fitted model from the string method plotted as a black dashed line. b) Model of bubble nucleation rate J using the string method model used to generate the top plots in Figure VI.5. Black box indicates the axis limits of (a) for more direct comparison. The orange star indicates the nucleation rate estimated from Figure VI.1c and the yellow star indicates the nucleation rate estimated from Figure VI.1d.

Classical Nucleation Theory

While we focused on the string method model, we want to address the limitations of classical nucleation theory (CNT) that persuaded us not to pursue it as a model of bubble nucleation. CNT assumes that (1) the interface between the bubble and the mother phase is infinitesimal and (2) the interfacial tension remains constant during nucleation. However, the present thesis has shown that (1) the interface between the bubble and the mother phase has a significant accumulation of CO_2 (see Figure II.S14) and (2) the interfacial tension varies significantly during bubble nucleation (see purple line in Figure V.7). Therefore, we do not expect CNT to model bubble nucleation in the present system accurately, although it is sometimes used to model bubble nucleation in polymer foams in the literature [12].

To give quantitative evidence of the poor suitability of CNT for modeling bubble nucleation in this system, we estimate the nucleation energy barrier predicted by CNT at the outlet of the observation capillary under the same conditions as used for the string method model in this Section. Based on the more convenient form of the nucleation energy barrier in equation I.6, the nucleation energy barrier

$$\frac{\Delta G^*}{k_B T} = \frac{16\pi}{3} \frac{\gamma^3}{(\Delta p)^2 k_B T}$$

where $\Delta p = p_{sat} - p$ with p_{sat} representing the pressure at which the gas was originally saturated into the fluid.

At the outlet of the observation capillary, the pressure is atmospheric pressure, 0.1 MPa. At this pressure, the interfacial tension between the polyol-rich and CO_2-rich phases is $\gamma \approx 30$ mN/m (see Figure II.3a), assuming equilibrium is rapidly attained. In our example, the saturation pressure was $p_{sat} = 7$ MPa. This formulation of CNT thus estimates the nucleation barrier to be

$$\Delta G^* \approx \frac{16\pi}{3} \frac{(0.03 \text{ N/m})^3}{(7 \times 10^6 \text{ Pa} - 10^5 \text{ Pa})^2 (10^{-23} \text{ J/K})(300 \text{ K})}$$
$$\sim 1000$$

A nucleation energy barrier of $1000\, k_B T$ is unphysically low and suggests that nucleation would be impossible, despite our observations that nucleation happens readily at higher pressures. While CNT could be adapted to achieve more physically relevant results, such as by adjusting the interfacial tension based on DFT predictions [8], we focused on the string method model due to the greater physical insight it provided.

In the present Section, we showed that some observations of bubble nucleation in a mixture of polyol supersaturated with CO_2 occur both stochastically and increase in nucleation rate sharply with supersaturation. We showed that the nucleation is stochastic by fitting the time between nucleation events, the "incubation time" of the inner stream, to an exponential decay, which is characteristic of the independent and identically distributed events of a Poisson process (see Figure VI.1). We showed that the nucleation rate sharply increases with supersaturation by estimating the nucleation rate at various locations along the observation capillary, which corresponds to various fluid pressures and thus degrees of supersaturation. The rate of bubble nucleation increased by at least an order of magnitude over a change in the pressure of about 0.1 MPa (see Figure VI.2). These two properties

provided support for our hypothesis that most of the bubble nucleation included in the analysis is consistent with homogeneous nucleation rather than heterogeneous. Therefore, we compared these estimates of bubble nucleation rate to a theoretical model that applied the string method to the density functional theory discussed in Chapter II. While the model was extremely sensitive to certain parameters (see Figure VI.5), it could reasonably model the estimated nucleation rates with the introduction of a fitted coefficient (see Figure VI.6). Classical nucleation theory, however, predicted extremely high nucleation barriers that would have suggested bubble nucleation were impossible under the conditions considered.

VI.5 Recommendations for Future Work

The most natural next step for future work on this topic is to take more measurements of bubble nucleation with the current method and perform the analysis presented on a larger dataset. By taking more measurements, the number of bubbles observed at each location increases, decreasing the relative size of the Poisson noise. By reducing uncertainty in the estimated nucleation rate, we can more precisely test our hypothesis that the bubble nucleation rate increases sharply with supersaturation, as is typical for homogeneous bubble nucleation. Taking more measurements can also expand the parameter space explored and reveal trends. For example, by varying the saturation pressure of CO_2, the assumption by classical nucleation theory that only the difference between the saturation pressure and the fluid pressure determines the bubble nucleation energy barrier (assuming a fixed interfacial tension; see equation I.6) could be tested. Additionally, by varying the flow speed, the role of depletion of CO_2 could be tested.

Another flow property that could be varied would the width of the inner stream. Because the number of nucleation events is proportional to the volume of the supersaturated fluid, for a given volume of fluid, only a limited range of nucleation rates will result in enough bubble nucleation events to be detected but not so many that they significantly deplete the available CO_2 and space to nucleate in. By increasing that volume, smaller nucleation rates can produce a detectable quantity of nucleation events; by decreasing that volume, larger nucleation rates will nucleate few enough bubbles to be measured. The width of the inner stream affects many other properties, however. The wider the inner stream, the faster the flow. Flow that is too fast will cause motion blur, reducing spatial resolution, and increase the distance traveled between frame captures, reducing time resolution. A wider inner stream will also lose a smaller fraction of CO_2 through diffusion into the

outer stream. In fact, in experiments, the number of observed bubbles dramatically increased with the increase in the inner stream flow rate despite a negligible change in the inlet pressure. If the inner stream is too narrow, it will lose its CO_2 more quickly both due to the smaller quantity of CO_2 contained and the longer residence time due to the slower flow speed. Within these limits, however, the variation of the inner stream radius can increase the range of bubble nucleation rates that can be probed with this method.

The conclusions of this Chapter could also be probed more rigorously through more careful and thoughtful analysis. In the present analysis, the entire inner stream is considered to be uniformly supersaturated based on the assumption that no CO_2 has been lost to diffusion and no bubbles are occupying space in the stream. In reality, a significant fraction of the inner stream has typically lost enough CO_2 that bubble nucleation is significantly suppressed. Additionally, not only can bubble nucleation not occur when a bubble is occupying a region of the inner stream, but it may also be suppressed in the wake of CO_2-depleted fluid it leaves behind (see discussion of the wake in Chapter VIII for more details). Accounting for the reduction in the volume of supersaturated fluid that can nucleate bubbles caused by these phenomena may significantly increase the estimated nucleation rate.

Another important part of the analysis is the accurate estimation of the fluid pressure. Because of the small dimensions of the capillary and the impossibility of machining ports into it, the pressure along the observation capillary cannot be directly measured with a pressure transducer. The introduction of mechanophores or compressible microbubbles could someday provide an estimate of the local pressure, assuming that they can be tailored to tolerate pressures over 10 MPa and adjust to the local pressure on the scale of milliseconds. Nevertheless, the pressure could also be estimated through indirect means. For example, given that we can estimate the inlet pressure reasonably accurately, we assume that deviations from a linear pressure drop are the result of bubbles in the inner stream, over which the pressure drop is negligible (see Figure 8 of Khandekar *et al.* [13]). By measuring the fraction of the time that the inner stream is occupied by a bubble along its length, one could estimate the reduction in the pressure drop across that portion of fluid by integrating this fraction from the outlet of the observation capillary.

While we showed reasonable agreement between a string method model and estimated nucleation rates from experiments, the high sensitivity of the string method model to the PC-SAFT parameters limits its utility without precise estima-

tion of these parameters. A more precise estimate of these parameters would thus increase the utility of the string method, although it may require the incorporation of association interactions (see discussion in Section II.5).

More precise comparison with the string method predictions of the nucleation barrier could also be achieved by estimating the nucleation barrier from measurements of the nucleation rate at different temperatures but fixed supersaturation using the second nucleation theorem, as originally presented by Ford [14] and further explained by Laaksonen and Malila [15]. The second nucleation theorem relates the derivative of the logarithm of the nucleation rate with temperature at fixed supersaturation to the nucleation energy barrier. Changing the temperature changes the degree of supersaturation, so to keep the degree of supersaturation consistent between measurements of the bubble nucleation rate taken at different temperatures, nucleation must be observed at higher pressures for higher temperatures. The pressure corresponding to the desired degree of supersaturation at a given temperature could be determined using the PC-SAFT model discussed in Section II.4. The distance along the observation capillary corresponding to that pressure could be estimated based on our assumption of a constant pressure gradient from the entrance to the exit of the observation capillary with a small correction for the reduced pressure gradient in the region near the exit of the capillary where a foam is formed.

References

1. Jones, S., Evans, G. & Galvin, K. Bubble nucleation from gas cavities a review. *Advances in Colloid and Interface Science* **80,** 27–50. ISSN: 00018686. https://linkinghub.elsevier.com/retrieve/pii/S0001868698000748 (Feb. 1999).

2. Brennen, C. E. *Cavitation and Bubble Dynamics* 1–290. ISBN: 0195094093. https://authors.library.caltech.edu/25017/5/BUBBOOK.pdf (Oxford University Press, New York, 1995).

3. Olsen, A. P. *Scanning Activity Gravimetric Analysis (SAGA) of Aqueous Polyethylene Oxide* PhD thesis (California Institute of Technology, 2006), 1–5–4.

4. Turnbull, D. Kinetics of solidification of supercooled liquid mercury droplets. *The Journal of Chemical Physics* **20,** 411–424. ISSN: 00219606 (1952).

5. Avedisian, C. T. The Homogeneous Nucleation Limits of Liquids. *Journal of Physical and Chemical Reference Data* **14,** 695–729. ISSN: 15297845 (1985).

6. NIST. *NIST Standard Reference Database Number 69* 2022. https://webbook.nist.gov/chemistry/ (2022).

7. E, W., Ren, W. & Vanden-Eijnden, E. String method for the study of rare events. *Physical Review B* **66,** 052301. ISSN: 0163-1829. https://link.aps.org/doi/10.1103/PhysRevB.66.052301 (Aug. 2002).

8. Xu, X., Cristancho, D. E., Costeux, S. & Wang, Z.-G. Bubble nucleation in polymer–CO2 mixtures. *Soft Matter* **9,** 9675. ISSN: 1744-683X. www.rsc.org/softmatter%20http://xlink.rsc.org/?DOI=c3sm51477c (2013).

9. Wang, Z.-G. *et al. Bubble Nucleation in Polymer-CO2 Mixtures* in *APS March Meeting 2020 Session S33: Physics of Foams: Fundamentals and Applications* (American Physical Society, 2020). https://absuploads.aps.org/presentation.cfm?pid=17459.

10. Tihic, A., Kontogeorgis, G. M., von Solms, N., Michelsen, M. L. & Constantinou, L. A Predictive Group-Contribution Simplified PC-SAFT Equation of State: Application to Polymer Systems. *Industrial & Engineering Chemistry Research* **47,** 5092–5101. ISSN: 0888-5885. https://pubs.acs.org/doi/10.1021/ie0710768 (Aug. 2008).

11. Blander, M. & Katz, J. L. Bubble nucleation in liquids. *AIChE Journal* **21,** 833–848. ISSN: 15475905 (1975).

12. Kim, K. I., Kang, S. L. & Kwak, H. Y. Bubble nucleation and growth in polymer solutions. *Polymer Engineering and Science* **44,** 1890–1899. ISSN: 00323888 (2004).

13. Khandekar, S., Panigrahi, P. K., Lefèvre, F. & Bonjour, J. Local Hydrodynamics of Flow in a Pulsating Heat Pipe: A Review. *Frontiers in Heat Pipes* **1.** ISSN: 2155-658X. https://www.thermalfluidscentral.org/e-journals/index.php/Heat_Pipes/article/view/103 (Nov. 2010).

14. Ford, I. J. Thermodynamic properties of critical clusters from measurements of vapour–liquid homogeneous nucleation rates. *The Journal of Chemical Physics* **105,** 8324–8332. ISSN: 0021-9606. http://aip.scitation.org/doi/10.1063/1.472687 (Nov. 1996).

15. Laaksonen, A. & Malila, J. in *Nucleation of Water: From Fundamental Science to Atmospheric and Additional Applications* 45–70 (2022).

Other Mothers: Effects of Additives to the Mother Phase on Bubble Nucleation

"With a Little Help from My Friends"

---

by John Lennon / Paul McCartney

High-pressure sampling experiments were performed at the Dow TXINN research facility in Lake Jackson, TX, with the tremendous help of Dr. Thomas C. Fitzgibbons, Marla Gilbert, and Dr. James Griffith. The experiment was designed by Dr. Bill Winniford, Dr. Steve Horvath, Dr. James Griffith, Dr. Thomas C. Fitzgibbons, and Prof. Julie Kornfield. Dr. Brenton L. Drake provided invaluable assistance with safety precautions to mitigate the risk of flammability when using cyclopentane. The discovery of the prediction of two-stage bubble nucleation with the string method, as well as the development of the PC-SAFT model of ternary phase behavior are the work of Dr. Huikuan Chao under Prof. Zhen-Gang Wang.

In Chapter I, we proposed to study a model system of polyurethane consisting of polyol and CO_2 instead of a complete polyurethane formulation. By studying a simple system, we could focus on a single driving force for the nucleation of bubbles—the supersaturation of dissolved CO_2—which simplified instrument development (Chapter III) and analysis of nucleation (Chapter VI). However, bubble nucleation in polyurethane is affected by the many other components involved, such as chemically reactive isocyanate, hydrocarbon-based physical blowing agents (PBAs), water (chemical blowing agent), surfactants, catalysts, and flame retardant, and the processing conditions, such as temperature increase and cross-linking reaction. While a high-quality polyurethane foam typically requires each of these aspects to work in concert, studying the effect of adding each one-by-one on bubble nucleation can elucidate the specific role of each in a way that previous work on complete formulations cannot.

In this Chapter, we present our first steps toward understanding the individual effects of these other aspects of polyurethane foaming, focusing primarily on the effect of adding cyclopentane, a hydrocarbon physical blowing agent (PBA) used to

replace ozone-depleting PBAs like CFCs and HCFCs (Section I.3). We focused on cyclopentane because its role in polyurethane foaming and, more specifically, in bubble nucleation during polyurethane foaming is not well understood. As discussed in Section I.3, the primary motivation to add cyclopentane in commercial polyurethane foam formulations is that the heat released by the exothermic polyurethane and urea synthesis reactions vaporizes the initially liquid cyclopentane early in the foaming process (the boiling point of cyclopentane is 49 °C, while the PU foam can reach 120 °C [1] to 190 °C [2]). Many studies have shown that the addition of cyclopentane increases bubble nucleation and decreases cell size in polyurethane foaming [3–5]. In all of these experiments, however, the polyurethane foam is heated above the boiling point of cyclopentane (49 °C), so the increase in bubble nucleation is explained as the result of vaporizing cyclopentane enough to nucleate on its own, independent of the CO_2 or other blowing agents involved.

Here, we will explore the role that cyclopentane plays in enhancing nucleation of CO_2-rich bubbles. This question has not been considered in the literature to our knowledge, but is motivated by findings in related systems. In a ternary mixture of polymer, solvent, and gas (like polyol, cyclopentane, and CO_2), a three-phase coexistence is both predicted [6] and observed [7] to be thermodynamically stable within a finite window of temperature and pressure. The significance of three-phase coexistence for nucleation behavior was highlighted by Müller *et al.* [8], who showed that, near a three-phase region, a solvent-rich liquid wets the interface of bubble embryos and may condense into a liquid-like phase in the bubble interior. This partial condensation reduces the interfacial tension along the bubble relative to a vapor-like bubble, which reduces the nucleation energy barrier, as first predicted in a binary mixture of polymer and gas by Talanquer and Oxtoby [9]. Bubble nucleation may proceed through this partially condensed state even if it is not thermodynamically favorable as a result of Ostwald's rule, which states that the nucleated phase may be that which is closer in free energy to the mother phase rather than the phase with the minimum free energy [10]. Such a low-barrier pathway to nucleation would not require the addition of heat. We show experimentally that the addition of cyclopentane significantly increases the bubble nucleation rate without the addition of heat in the vicinity of an experimentally demonstrated three-phase coexistence. We also present a theoretical model using string method based on DFT to show that the addition of cyclopentane opens up a two-stage nucleation pathway with a significantly lower nucleation barrier, something that classical nucleation theory cannot capture.

We also briefly discuss the effect of adding surfactant. Surfactants are added to polyurethane foams both to reduce the energy barrier to nucleate bubbles (by reducing the interfacial tension that opposes nucleation) and to stabilize bubbles as they grow [2].

Many other studies have explored the effects of adding solid particles to increase bubble nucleation. As discussed in Section I.3, solid particles are not typically included in rigid polyurethane foam (RPUF) formulations [11]. Given their limited use in industry and the challenges of thoroughly cleaning out nanoparticles between experiments, we did not explore their effects on bubble nucleation in the present work. Nevertheless, the addition of particles can provide unique insight into the role of particles in the current system, as discussed in Section VII.4.

Polyurethane foams also contain flame retardants and chemical catalysts that drive the polyurethane synthesis reaction. Their effects on bubble nucleation have not been thoroughly explored in the literature. These compounds are added in small quantities and are not intended to change the foam structure, but a study to verify the assumption that they have a negligible effect on bubble nucleation would be valuable.

VII.1   Adding Cyclopentane Dramatically Increases Bubble Nucleation in Polyol–CO_2 Foam

Estimating Nucleation Rate from Bubble Counts

We demonstrate that adding cyclopentane increases bubble nucleation by estimating bubble nucleation rates from a foaming experiment performed under identical conditions as that in Section VI.4. In this case, however, cyclopentane was mixed with the polyol (PPG 2700 g/mol) in a ratio of 1:5 by weight before dissolving CO_2 into the solution inside a Parr reactor. Based on the PC-SAFT model of this ternary mixture of PPG 2700 g/mol, cyclopentane, and CO_2 described in Section VII.3, under the saturation pressure of 7.2 MPa near laboratory temperature of 22 °C, the resulting mixture would be roughly 50% PPG, 10% cyclopentane, and 40% CO_2 by weight. Because few of the measurements of bubble nucleation in the PPG–CO_2 mixtures shown in Chapter VI contained enough data points to estimate the nucleation rate by the exponential decay in the incubation time (see Figure VI.1), we first estimate the nucleation rate in the PPG–cyclopentane–CO_2 mixture using the method of converting counts of nucleation events at a given supersaturation into a nucleation rate (as depicted in Figure VI.2). These estimates of the nucleation rate

for the mixtures with and without cyclopentane are shown in Figure VII.1.
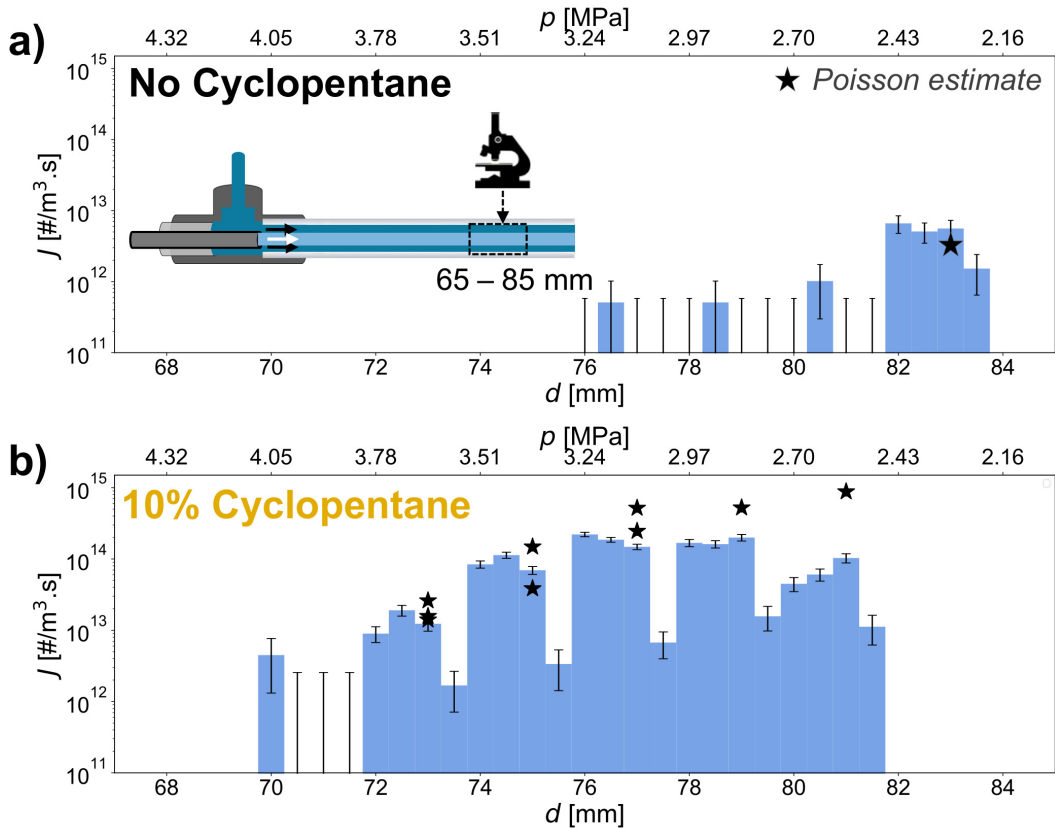
Figure VII.1: Comparison of bubble nucleation rate J vs. supersaturation estimated by counting nucleation events at different locations along the observation capillary d (lower horizontal axis), which corresponds to different fluid pressures p (upper horizontal axis). In both cases, the polyol is PPG 2700 g/mol, CO_2 is saturated at 7.2 MPa and 22 °C, and the inlet pressure was 13.ltd a) Mixture of polyol and CO_2 (same as in Figure VI.2b). b) Mixture of polyol, cyclopentane, and CO_2 prepared under the same conditions, for which polyol and cyclopentane were added in a ratio of 5:1 by weight. Stars indicate the estimates of the nucleation rate by fitting the inter-nucleation times to an exponential decay based on Poisson statistics described in Section VI.1; error bars are shown but are smaller than the markers.

Bubble nucleation in the mixture containing cyclopentane (C5) (Figure VII.1b) occurs at a lower degree of supersaturation (higher pressure) and at a faster rate than in the mixture without cyclopentane (Figure VII.1a). While the mixture without cyclopentane does not exceed an estimated bubble nucleation rate of $10^{13}/m^3$.s until the pressure is estimated below 2.4 MPa, the mixture with cyclopentane does so at an estimated pressure of 3.5 MPa. Once the pressure has dropped to 2.4 MPa, the nucleation rate in the mixture containing cyclopentane has increased by at least an order of magnitude. Because the current algorithm does not

exclude the volume occupied by elongated bubbles (see discussion in Section VI.5), which become more frequent at lower pressures, the true nucleation rate is likely higher. Interestingly, the bubble nucleation rate for the mixture with cyclopentane does not increase as abruptly as the measurements of the rate for the mixture without cyclopentane appeared to suggest. Rather, the bubble nucleation rate increases quickly but steadily, similarly to the prediction by the string method shown in Figure VI.6b. Last, it is possible that the increased number of bubbles in the inner stream in the mixture with cyclopentane results in a lower fluid pressure near the outlet of the observation capillary than in the mixture without cyclopentane, where there were fewer bubbles. Consequently, the estimated pressures may be lower for the mixture with cyclopentane than listed. Nevertheless, even if the pressure were overestimated for the mixture containing cyclopentane, the cause of the overestimation would be the increased amount of bubble nucleation relative to the mixture not containing cyclopentane. Therefore, we can still conclude that the addition of cyclopentane significantly increased bubble nucleation and reduced the supersaturation required to nucleate bubbles.

Estimating Nucleation Rate from Poisson Statistics

Because of the high rate of bubble nucleation in the mixture containing cyclopentane, enough bubbles could be detected in experiments to estimate the nucleation rate from the exponential decay of the incubation time (as depicted in Figure VI.1). Not only was the rate higher, but visual observation showed that small, spherical bubbles were less likely to be interrupted by elongated bubbles, leading to a higher proportion of consecutive bubble nucleation events. In fact, the number of consecutive observations of bubble nucleation was so much higher with cyclopentane that we could test for the exponential decay of the incubation time characteristic of a Poisson process much more rigorously than in Chapter VI. One example of the exponential fit to this decay is shown in Figure VII.2. Whereas fewer than ten nucleation events were available for the analysis of bubble nucleation in the PPG–CO_2 mixture in Figure VI.1, almost 300 were available for the analysis of bubble nucleation in the PPG–cyclopentane–CO_2 mixture in Figure VII.2. The distribution of the incubation times of these events is shown in panel (a) and the decay of the number of non-nucleated "samples" N (see discussion of this method in Section VI.1) is shown in panel (b). The exponential fit (dashed line) fits the data well, providing stronger support of our hypothesis that the bubbles we are observing nucleate according to a Poisson process, and thus behave as if they were nucleated

by homogeneous nucleation.
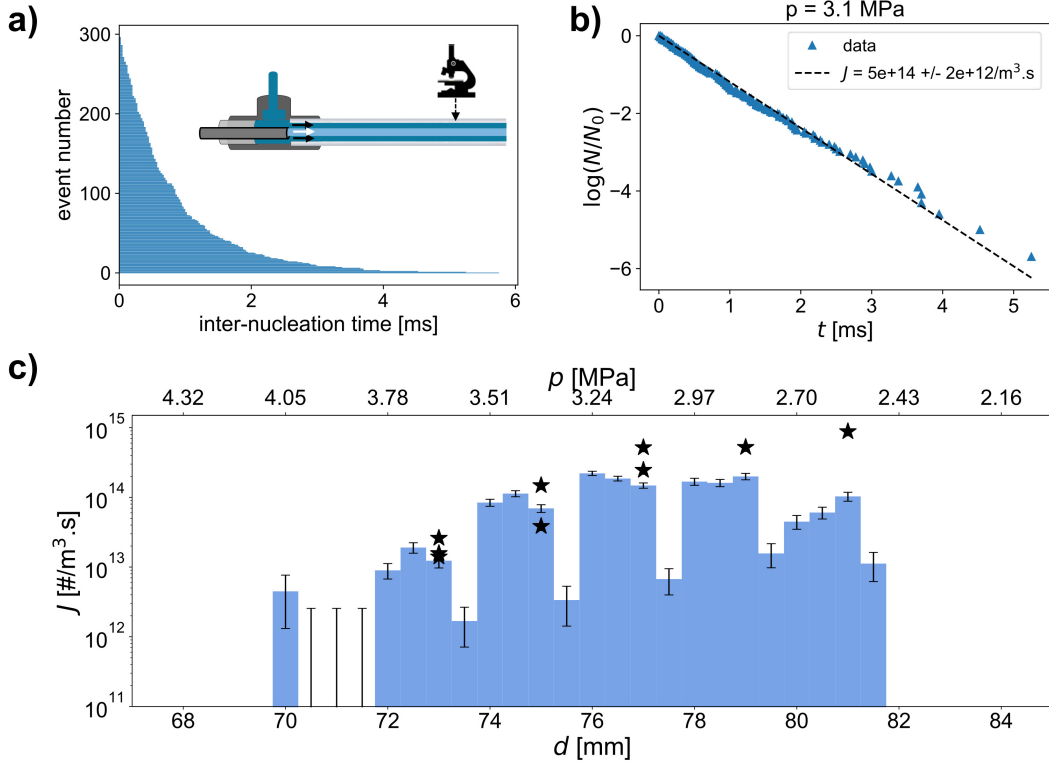
Figure VII.2: Exponential decay method for estimating nucleation rate of PPG–C5–CO$_2$ mixture under the same experimental conditions as in Figure VII.1. a) Inter-nucleation times as measured at 77 mm along the observation capillary (fluid pressure of $p = 3.1$ MPa, depicted schematically on diagram of microfluidic channel) according to the technique described in Section VI.1 for each nucleation event detected. b) The logarithm of the fraction of non-nucleated fluid samples $\log(N/N_0)$ (blue triangles) plotted as a function of time and fit to an exponential function (dashed line). A lower bound on the nucleation rate J is estimated by dividing the frequency (the decay constant of the exponential fit) by the volume of fluid (some of which is depleted of CO$_2$). c) Nucleation rate J as a function of distance along the observation capillary d (lower horizontal axis) and estimated pressure in the capillary p (upper horizontal axis). The bars represent the nucleation rate estimated by counting nucleation events in each segment of the capillary (same a Figure VII.1b). The bars decrease every 2 mm due to diminished detection of bubbles along the edges of the field of view caused by vignetting—we expect these rates to be similar to those nearby. The nucleation rate estimated from fits such as the one shown in (b) are superimposed (black stars). The nucleation rate was lower when the same measurements were performed a few hours later—these are omitted since we do not know how the system may have changed during this time.

As discussed in Section VI.1, the decay constant of the exponential fit to the decay of non-nucleated samples N gives the frequency of bubble nucleation,

which can be converted into the nucleation rate J by dividing by the observed volume. In Figure VII.2c, the nucleation rate estimated in this way is superimposed as stars on the bar chart of nucleation rate estimated by counting nucleation events (same bar chart as in Figure VII.1b). Note that the nucleation rate estimated with Poisson statistics upon the addition of cyclopentane is similar in Figure VII.2 as in Figure VI.1d without cyclopentane, yet the number of consecutive nucleation events was much higher for cyclopentane (compare with Figure VI.1b). This discrepancy is likely the result of having fewer interruptions of consecutive nucleation events by elongated bubbles, which become more common farther downstream, as was the case for the measurement in Figure VI.1b,d. Both methods of estimating the nucleation rate are within an order of magnitude of each other and show a similar rate of increase in the nucleation rate with decreasing pressure. We still expect that the volume of fluid by which we divide the frequency to obtain the nucleation rate J is overestimated, and thus, the nucleation rate is underestimated (see discussion in Section VI.5), but the rough agreement between the two methods suggests that the estimates of nucleation rate are consistent. This consistency further supports our conclusion that the addition of cyclopentane significantly increases the rate of bubble nucleation and allows for bubble nucleation at a lower supersaturation. In the next Section, we explore a possible explanation for this effect by adapting our string method model from Section VI.3 to a ternary mixture of PPG, cyclopentane, and CO_2.

VII.2   String Method Based on DFT Predicts Two-stage Bubble Nucleation with Cyclopentane

Using the string method based on DFT described in Section VI.3, we estimated the nucleation pathway of supersaturated mixtures of polyol–C5–CO_2 (where C5 represents cyclopentane) under depressurization. The DFT was extended to consider three components. Once again, the parameters describing each component were determined by fitting a PC-SAFT model to experimental measurements of the composition at different temperatures and pressures. These measurements are described in greater detail in the following section (Section VII.3).

Using this string method model, we estimated the nucleation pathway of supersaturated PPG–cyclopentane–CO_2 mixtures with different weight fractions of cyclopentane. In this case, we mean the weight fraction of cyclopentane in the saturated mixture of PPG, cyclopentane, and CO_2, which we will call w_{C5}. In the experiment analyzed in the previous Section, $w_{C5} = 0.1$. In Figure VII.3, we show

the nucleation free energy along the nucleation pathway found by the string method for $w_{C5} = 3.5\%$, 15%, 16%, and 17.8%. The polyol was modeled using the PC-SAFT parameters for PPG 2700 g/mol (see Table II.2) and was saturated with CO_2 at 8 MPa and 28 °C. The nucleation pathway was computed upon quenching the pressure to 0.1 MPa. As the weight fraction of cyclopentane increases, the peak value of the nucleation energy, the nucleation energy barrier, decreases significantly. While the nucleation barrier is about 20 $k_B T$ for $w_{C5} = 3.5\%$, it decreases to about 8 $k_B T$ upon increasing w_{C5} to 15%. The string method model's prediction of a significant decrease in the nucleation energy barrier upon the addition of cyclopentane is consistent with our observation of a significant increase in the nucleation rate in foaming experiments when the polyol is mixed with cyclopentane.

One possible explanation for the reduction in the nucleation barrier upon the addition of cyclopentane is the emergence of a two-stage nucleation pathway upon the addition of sufficient cyclopentane. Already at $w_{C5} = 17.8\%$ (red line in Figure VII.3a), the nucleation pathway has two peaks, each marked with a star. The presence of two peaks along the pathway indicates that the nucleation process is split up into two stages. Because the string method finds the pathway with the lowest nucleation energy, its selection of a two-stage nucleation pathway indicates that the two stages have a lower free energy than single-stage alternatives. Those two stages appear to be a liquid–liquid phase separation followed by a vaporization of the liquid droplet, as depicted in Figure VII.3b.

We present two forms of evidence that suggest that the two stages of nucleation are liquid–liquid phase separation and vaporization. The first evidence comes from an analysis that we refer to as "incipient phase analysis." In incipient phase analysis, we estimate the chemical potential of the mother phase immediately after quenching the pressure and solve for the composition of a phase with the same chemical potential. This phase is not in equilibrium with the mother phase because the pressures of the two phases are not set to be equal, so only chemical and thermal equilibrium are considered. Nevertheless, we propose that the composition of this phase might indicate the composition of the initial nucleus that forms upon supersaturation, even if the composition of the final phase at equilibrium is different. To estimate the chemical potential of the mother phase immediately after the pressure quench, we assume that the relative ratios of components remain fixed but allow the overall density to vary until the pressure matches the quenched pressure. Using the resulting composition, the chemical potential of the mother phase can be computed.
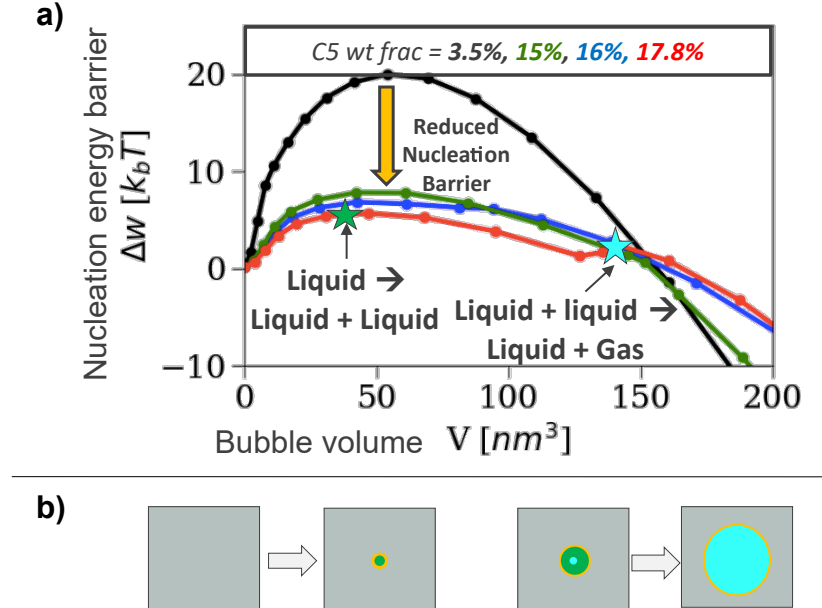
Figure VII.3: a) Nucleation energy barrier (normalized by the thermal energy k_BT as a function of the bubble volume (cubic nanometers) as a bubble nucleates in a mixture of 1k2f polyol (see Table II.1 for properties), cyclopentane, and CO_2. The mixture is saturated at 8 MPa and depressurized instantaneously to 0.1 MPa. The temperature is fixed at 28 °C. The string method identifies the minimum energy pathway, which is shown for four different weight fractions of cyclopentane: 3.5% (black), 15% (green), 16% (blue), and 17.8% (red). At the three highest concentrations of cyclopentane, the nucleation pathway has two peaks, meaning nucleation occurs in two stages: (1) liquid–liquid separation (dark blue star) and (2) vaporization of liquid (light blue star). b) Depiction of two stages of bubble nucleation. First, the uniform mother phase (gray) nucleates a bubble with a liquid-like density (green) surrounded by a high concentration of CO_2 and cyclopentane (yellow border) through liquid–liquid phase separation. Second, the liquid-like bubble vaporizes (light blue) and grows into a larger bubble with a vapor-like density. Plot produced by Dr. Huikuan Chao.

The result of the incipient phase analysis is shown in Figure VII.4a. The grand potential density g is plotted as a function of the weight fraction of cyclopentane in the mother phase w_{C5}. The analysis identified two classes of phases that are likely to nucleate upon a pressure quench from 8 MPa to 0.1 MPa. At low weight fractions of cyclopentane, a vapor-like phase (red line) is expected. Upon reaching a sufficiently high weight fraction of cyclopentane ($w_{C5} \approx 15$ %), a liquid-like phase (a phase with a liquid-like density) may nucleate (blue line). The liquid-like phase is less energetically favorable than the vapor-like phase until $w_{C5} > 42$ %, which is far beyond the relevant quantity for polyurethane foaming. While energetically less
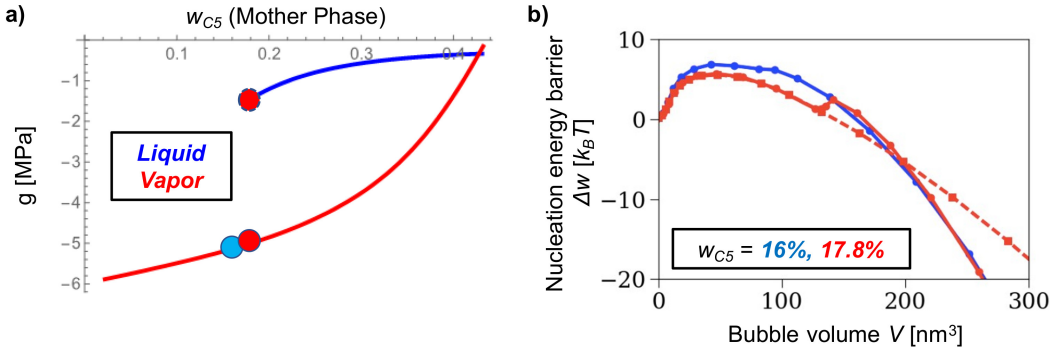
Figure VII.4: Nucleation behavior of mixtures of 1k2f polyol (see Table II.1), CO_2, and cyclopentane (C5) saturated at 8 MPa and depressurized to 0.1 MPa with temperature maintained at 28 °C. a) The free energy density of phases that can nucleate under supersaturation relative to the mother phase upon depressurization (g), as computed using the incipient phase analysis, plotted as a function of the weight fraction of cyclopentane w_{C5} in the saturated mother phase. For $w_{C5} < 0.17$, only a vapor phase (red line) can nucleate. At higher w_{C5}, a liquid phase (blue line) may nucleate. While it is less energetically favorable than the vapor phase for $w_{C5} \in [0.17, 0.43]$, it may still nucleate by Ostwald's phase rule [10]. The blue circle corresponds to the blue line in (b). The red circle with a solid outline corresponds to the solid red line in (b) and that with the dashed outline corresponds to the dashed red line in (b). b) Nucleation energy barrier nondimensionalized by the thermal energy $k_B T$ as a function of the bubble volume for different weight fractions of C5 (same as in Figure VII.3). The blue line ($w_{C5} = 16\%$) corresponds to a single-stage nucleation of a phase with a vapor-like density. The solid red line ($w_{C5} = 17.8\%$) corresponds to a two-stage nucleation of a liquid-like phase followed by a vaporization into a vapor-like phase. The dashed red line corresponds to a single-stage nucleation of a liquid-like phase. Note that the vapor-like phase of the solid red line soon becomes energetically favorable over the liquid-like phase of the dashed red line, indicating that, ultimately, a vapor-like bubble is preferred. Plots produced by Dr. Huikuan Chao.

favorable, the liquid-like phase has an energy more similar to the mother phase ($g = 0$), and the Ostwald rule predicts that such a phase is the more likely to nucleate [10].

To understand the difference between the vapor-like and liquid-like routes to bubble nucleation, we plot the free energy along the nucleation pathway predicted by the string method model for both conditions in Figure VII.4b. The blue line corresponds to $w_{C5} = 16\%$, marked by the light blue circle in panel (a). This pathway represents nucleation directly to a vapor-like phase and has a single peak, indicating a single stage. The red line corresponds to $w_{C5} = 17.8\%$ and has two peaks representing two stages of bubble nucleation. At this weight fraction of

cyclopentane, both vapor-like (marked by the red circle with a solid black outline in (a)) and liquid-like (marked by the red circle with a dashed black outline in (a)) phases can be formed. While the solid line in (b) represents the nucleation pathway predicted by the string method model, the dashed line represents the nucleation pathway taken if constrained to the liquid-like phase. These two pathways coincide up to the second peak, which suggests that the first peak corresponds to liquid–liquid phase separation. The pathways then diverge, with the liquid-like pathway (dashed line) having the higher free energy. While the string method model cannot be trusted beyond the peak, this discrepancy between the pathways suggests that the liquid-like bubble does not proceed with a liquid-like density. Instead, we assume that it transitions to a vapor-like density before reaching the vapor-like equilibrium phase.

The other form of evidence we present to show that the bubble undergoes liquid–liquid phase separation followed by vaporization at $w_{C5} = 17.8\,\%$ is the density profiles predicted by the DFT at different stages along the nucleation pathway. A handful of these density profiles is shown in Figure VII.5 with the corresponding points along the free-energy curve indicated by red arrows. Before bubble nucleation, the system begins at a uniform composition equal to the bulk composition seen on the right of the density profile plots in Figure VII.5. Upon nucleation (see panel (i)), the nucleating phase (left of the density profile) has acquired a higher concentration of CO_2 (blue line) and cyclopentane (green line) and pushed out polyol (blue line), and has a liquid-like density similar to the bulk fluid. Upon reaching the first nucleation barrier (ii), the cyclopentane concentration decreases in the center of the nucleating phase and almost all the polyol is expelled. Because the density of the nucleus remains liquid-like, however, we classify this stage as liquid–liquid phase separation. The interfacial tension between two liquids is typically much smaller than at an interface between a vapor and liquid, and because the primary energetic cost is the formation of a new interface, this lower interfacial tension is likely the reason for the lower nucleation energy barrier of this stage than the single-stage nucleation into a vapor. The composition remains similar between the two nucleation energy peaks (iii), but upon reaching the second nucleation energy peak (iv), the composition of the nucleus changes dramatically. While CO_2 and cyclopentane remain accumulated along the bubble surface, there is almost no cyclopentane in the core of the bubble and the CO_2 concentration is also much lower, resulting in a vapor-like density at the core. This vapor-like region expands beyond the second peak (v), so we classify this stage as the vaporization of the liquid bubble. Therefore,

we suggest that one reason why adding cyclopentane to the polyol dramatically increases the nucleation rate is that it can phase separate into a metastable liquid-like phase with CO_2 before vaporizing, which requires less energy than nucleating a vapor-like phase all at once.
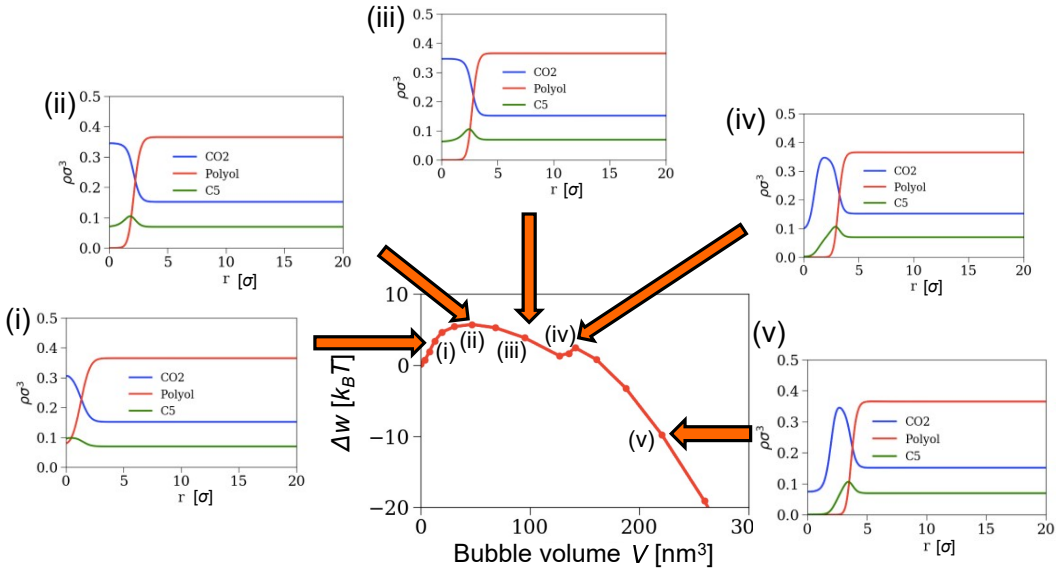

Figure VII.5: Center) Nucleation barrier in units of $k_B T$ as a function of the bubble size for a mixture of 1k2f polyol (see Table II.1), CO_2, and cyclopentane (C5) saturated at 8 MPa and depressurized to 0.1 MPa with temperature maintained at 28 °C, with initial C5 weight fraction of 17.8% (red line in Figures VII.3a and VII.4b). Around the nucleation barrier, the density profiles of the three components (CO_2 in blue, polyol in red, and cyclopentane (C5) in green) are plotted for different points along the nucleation pathway, indicated by orange block arrows. The densities are given in units of number of molecules per CO_2 bead diameter cubed (σ^3), and the radius measured from the center of the nucleus r is given in units of the CO_2 bead diameter σ ($\sigma = 2.79$ Åas shown in Table II.2). Before the second peak, the total density of the nucleating phase (small r) is similar to the mother phase (≈ 0.5 vs. ≈ 0.6), indicating a liquid-like embryo. Upon reaching the second peak (fourth plot of density profiles), the density at the core of the bubble embryo significantly decreases to about 0.1, indicating a vaporization to a vapor-like bubble, after which, the bubble grows while maintaining a roughly constant core density. Plots produced by Dr. Huikuan Chao.

This particular two-stage nucleation pathway has only been proposed theoretically for bubble nucleation; other factors may cause the increased bubble nucleation in formulations with cyclopentane. One possible alternative explanation for the enhancement of bubble nucleation upon the addition of cyclopentane was phase separation of cyclopentane into small droplets that provide additional nucleation sites. Similar droplets have been observed with SEM in polyurethane foams upon

the addition of isopentane to a polyol formulation [12], which has an even lower boiling point than cyclopentane (27.8 °C for isopentane vs. 49.2 °C). While light scattering could have revealed the presence of phase-separated microdroplets in the polyol–cyclopentane–CO_2 mixture, we examined the solubility of cyclopentane through another approach. First, we mixed cyclopentane with polyol under atmospheric pressure to determine its solubility. We found that cyclopentane is miscible at least up to 50% by weight in 1k2f polyol (see Table II.1, which is similar to the 3k2f polyol (PPG 2700 g/mol) used in this experiment, but with a lower molecular weight (the difference in molecular weight means cyclopentane is less soluble in 3k2f, but not significantly less so). Therefore, we only mixed in 17% cyclopentane by weight, well below the solubility. Second, we maintained the conditions far from those that lead to a three-phase coexistence at which cyclopentane-rich droplets will phase separate. These conditions are explored in the next Section.

VII.3   Adding Cyclopentane Opens Up Three-phase Region

First, see Section VII.S1 for some information on safety precautions to take when performing experiments with cyclopentane.

Why should the addition of cyclopentane open up a two-stage nucleation pathway with such a low nucleation barrier? We propose that the result is rooted in the thermodynamics of the mother phase, which we show reaches a three-phase coexistence under similar conditions. As shown by Müller *et al.*, under conditions near a three-phase coexistence, depressurization can drive the nucleation of bubble embryos whose surfaces are wetted by a solvent-rich liquid phase that may condense into a liquid-like phase in the bubble interior, just as is predicted by the string method to form in the first stage of bubble nucleation (Section VII.2). This partial condensation reduces the interfacial tension along the bubble surface relative to a vapor-like bubble, which reduces the nucleation energy barrier. While not thermodynamically favorable (see Figure VII.4), this liquid-like phase may still be preferred during nucleation because its free energy is more similar to that of the mother phase, as predicted by Ostwald's rule [10]. In this Section, we provide experimental evidence of a three-phase coexistence in the vicinity of the foaming conditions explored in Section VII.1 and fit the parameters of a PC-SAFT model for a three-component system to estimate the extent of this region. The parameters of this model also serve as the parameters of the DFT model that forms the basis of the string method used to predict the two-stage nucleation pathway in Section VII.1.

Tompa first presented a prediction that ternary mixtures of polymer, solvent, and vapor could yield a three-phase coexistence within a particular range of temperatures, pressures, and compositions [6], which Sundar and Widom elaborated upon [13]. Models have since been developed to predict the parameter range of three-phase coexistence in specific polymer–solvent–gas mixtures relevant to industrial processes, such as supercritical CO_2 extraction of solvent from polymer [7, 14]. Experimental measurements demonstrating three-phase coexistence are scarce, however. Most use some combination of cloud-point measurements—which can be imprecise and hysteretic for viscous polymers—and painstaking analysis of the compositions for each sample of polymer-containing phases [15, 16]. Bungert *et al.* showed a three-phase coexistence in a ternary mixture of polystyrene, cyclohexane, and CO_2, but at much higher temperature (170 °C) than is relevant for bubble nucleation in polyurethane foaming [15]. Nevertheless, we cannot be sure that a three-phase coexistence will occur for this mixture without measurement, and we cannot have confidence about the window of parameters that permit it without theory.

Before performing an experiment, however, we extended the two-component PC-SAFT model to treat three-component mixtures of polyol, CO_2, and cyclopentane. We determined the cyclopentane parameters by fitting a two-component model of cyclopentane and CO_2 to literature data on their binary phase coexistence [17, 18] . Because we could not obtain accurate measurements of the solubility of cyclopentane in polyol, we assumed that the interaction parameter k between polyol and cyclopentane was the same as that between CO_2 and polyol. We tested this crude approximation against experimental results shown later in this Section.

With the PC-SAFT model extended to ternary mixtures of polyol, CO_2, and cyclopentane, we could predict the conditions that might support a three-phase coexistence. These predictions are best presented on a Gibbs triangle, which we explain in Figure VII.6.

After searching through a range of pressures and temperatures, we found that the ternary PC-SAFT model predicted a three-phase coexistence at 37 °C and 6.7 MPa, as shown in Figure VII.7. Four types of phase coexistence are possible under these conditions, and a three-phase coexistence is only possible within a small range of compositions. First, a single-phase coexistence is predicted in the unmarked region at low concentrations of CO_2 (bottom of Gibbs triangle). At higher concentrations of CO_2 and lower concentrations of cyclopentane, a vapor–
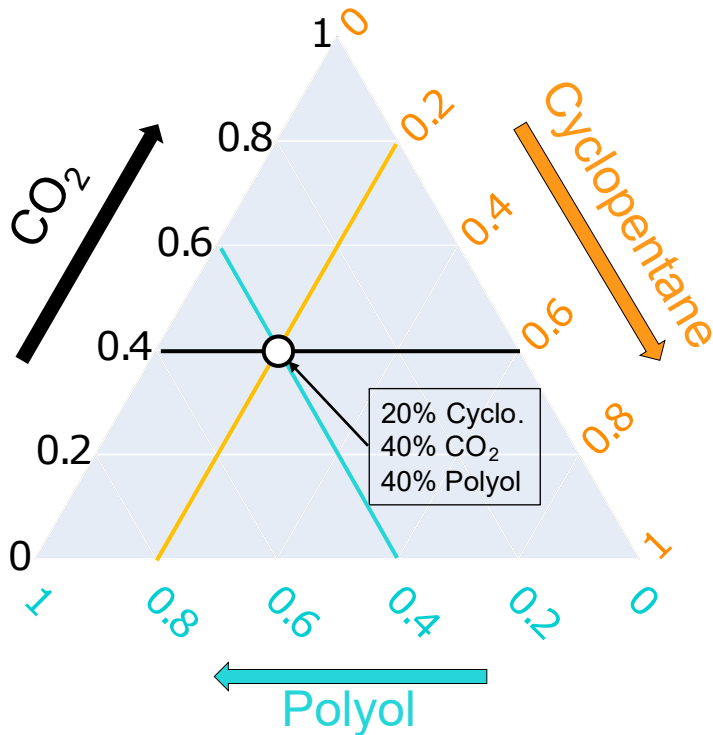
Figure VII.6: A Gibbs triangle is shown for indicating the weight fractions of each compound in a mixture of CO_2 (black, left axis), cyclopentane (gold, right axis), and polyol (light blue, bottom axis). A point (white circle) is plotted indicating a mixture with a composition of 20 % cyclopentane, 40 % CO_2, and 40 % polyol. Three lines indicating the corresponding composition of each phase are drawn intersecting the point.

liquid equilibrium (VLE) is possible between an almost purely CO_2 phase (upper tip of Gibbs triangle) and a polyol-rich, cyclopentane-poor liquid phase (bottom black line). Upon adding enough CO_2 and cyclopentane to enter the orange triangular region on the phase diagram, the system is predicted to separate into three phases, marked with stars: a CO_2-rich vapor (blue star), a polyol-rich liquid (green star), and a liquid-like phase of CO_2 and cyclopentane (pink star). For example, if the system composition were that indicated by the white circle in the Figure, it would separate into compositions marked by the three circles according to conservation of mass. Finally, at still higher concentrations of cyclopentane, the system is predicted to reach a liquid–liquid equilibrium (LLE), at which point the CO_2-rich vapor phase condenses into the liquid of CO_2 and cyclopentane.

Directly preparing a system with a composition in the three-phase region of Figure VII.7 at the pressure and temperature required can be challenging. Based on the PC-SAFT predictions of phase behavior, however, the system should pass
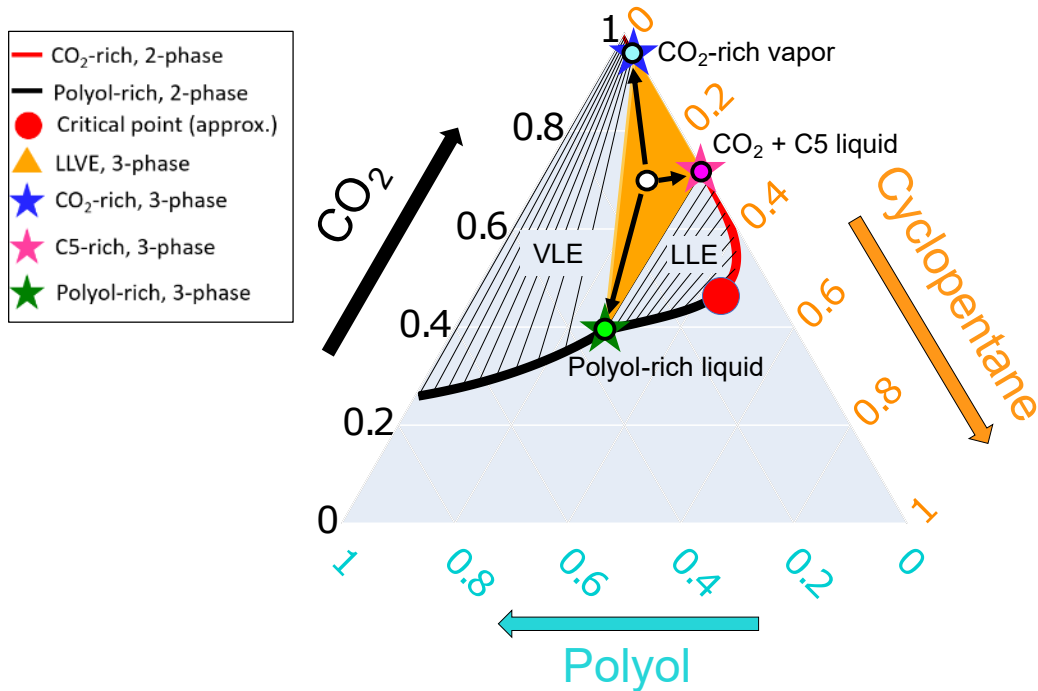
Figure VII.7: Prediction by PC-SAFT model of phase behavior of ternary mixture of 1k2f polyol (see Table II.1), CO_2, and cyclopentane at 6.7 MPa and 37 °C. In the left region of the Gibbs triangle, at low cyclopentane concentrations, the system achieves a vapor–liquid equilibrium (VLE) between a CO_2-rich vapor (red line near the top) and a polyol-rich liquid (black line). Tie lines are marked in between coexisting phases. In the right region, at high cyclopentane concentrations, the system achieves a liquid–liquid equilibrium (LLE) between a liquid of CO_2 and cyclopentane (red line) and a polyol-rich liquid (black line) with tie lines drawn between. At high enough cyclopentane concentrations, the system reaches a critical point (general location indicated by red circle) before becoming a single phase (lower region of Gibbs triangle). At intermediate concentrations of cyclopentane, the system achieves a liquid–liquid–vapor equilibrium (LLVE, orange triangle) among a CO_2-rich vapor (blue star), polyol-rich liquid (green star), and liquid of CO_2 and cyclopentane (pink star). If a system is prepared with the concentration indicated by the white circle, it separates into three phases with concentrations indicated by the light blue, light green, and pink circles consistent with mass conversation.

through the three-phase coexistence simply by pressurizing a vessel in gradual steps with CO_2, as shown in Figure VII.8. Therefore, to probe the possibility of a three-phase coexistence, we pressurized a Parr reactor filled with cyclopentane and polyol with CO_2 in steps. At low pressure (2.2 MPa), the system should only exist in a vapor–liquid equilibrium. Both phases can be sampled by the sampling apparatus, so this stage can be validated by comparing the sampled compositions to the predicted compositions. Upon adding CO_2 to reach higher pressure (7.0 MPa),

a three-phase coexistence opens up and the system will pass through it. At this point, the sampled compositions should match the liquid and vapor phases of the three-phase coexistence, but they will not account for all the mass in the system, some of which will be in the third phase of intermediate density (pink). Upon adding more CO_2 to reach still higher pressures (8.0 MPa), the system will reach a liquid–liquid equilibrium, at which point the gas-sampling valve should sample a liquid phase rather than a vapor phase.
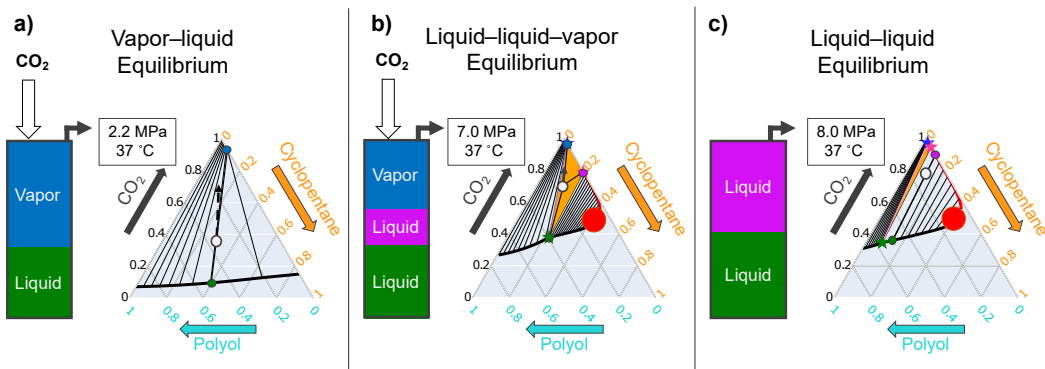

Figure VII.8: Schematic of experimental plan for demonstrating a liquid–liquid–vapor equilibrium by passing through three qualitatively distinct phase regimes simply by adding CO_2. In each panel, the high-pressure vessel is indicated by a vertical rectangle on the left with the predicted phase composition indicated. After sampling the composition of each phase in the mixture (indicated by green, blue, and pink circles in the theoretical phase diagram on the right), CO_2 is added (indicated by white block arrow), which raises the CO_2 weight fraction in the overall composition (white circle with increased CO_2 indicated by dashed arrow) and the pressure to reach the condition in the next panel to the right. Temperature is fixed at 37 °C for simplicity. a) vapor–liquid equilibrium (VLE) at 2.2 MPa, b) liquid–liquid–vapor equilibrium (LLVE) at 7.0 MPa, and c) liquid–liquid equilibrium (LLE) at 8.0 MPa.

To demonstrate three-phase coexistence in a mixture of polyol, cyclopentane, and CO_2, we developed a novel, high-pressure, gas- and liquid-sampling apparatus. The apparatus was constructed at the TXINN Research Facility at Dow, Inc. in Lake Jackson, TX. Its design and method of operation are discussed below.

High-pressure Liquid- and Gas-phase Sampling

The primary challenge of demonstrating a three-phase coexistence is to sample each phase at high pressure. This task requires that sampled volumes are small, increasing the variability, and that the components in the sample come out at high pressure. We developed a unique approach to estimate the composition of each phase by sampling only the liquid and vapor phases and using conservation of

mass to estimate the composition of any intermediate-density third phase that might phase separate. A schematic of the apparatus is shown in Figure VII.9.
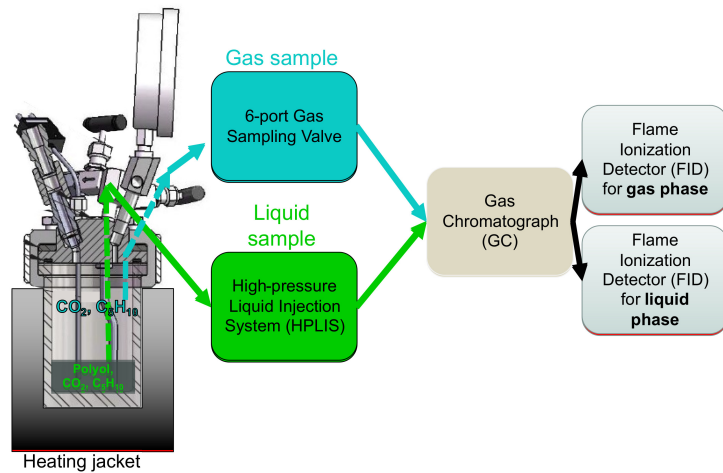

Figure VII.9: On the left, a Parr reactor (image obtained from the Parr Instrument Company's operating instruction manual of 4600 & 4700 models) contains a mixture of polyol, cyclopentane (C_5H_{10}), and polyol that has phase-separated into a denser phase (darker region at bottom) and polyol-free lighter phase. A heating jacket (black) surrounds it to maintain the temperature. The gas-like lighter phase is sampled from the gas-sampling valve (following the path of the blue arrows) at the top of the Parr reactor and flowed through a 6-port gas-sampling valve, which collects a small volume of that gas under pressure and sends it to a gas chromatograph (GC). The liquid-like denser phase is sampled from a dip tube (following the path of the green arrows) to a high-pressure liquid injection system (HPLIS), which vaporizes the CO_2 and cyclopentane and flows them to the same GC. Inside the GC, effluent from the gas and liquid samples are flowed through separate columns to separate flame ionization detectors (FIDs) with methanizers that measure the cyclopentane and CO_2 content.

The ternary mixtures of PPG 2700 g/mol, cyclopentane, and CO_2 were equilibrated in 1.2 L Parr reactor and are sampled from both the top through the gas-sampling port and the bottom through a dip tube. The headspace sample flows directly through a gas-sampling valve that is connected to the gas chromatograph (GC) at atmospheric pressure. The dense phase sample flows through a heated high-pressure liquid injection system (HPLIS), which vaporizes the volatile CO2 and cyclopentane out of the polyol before flushing these volatile components into the GC. The polyol composition is not directly measured; see Section VII.S3 in the SI for the method for estimating the polyol density in the liquid sample. The samples are prepared by first dissolving cyclopentane in polyol at roughly 50% by weight and adding the solution to the Parr reactor inside a nitrogen-atmosphere glovebox,

which reduces the risk of flammability. During the experiment, CO_2 is added at high pressure using an ISCO pump, which is fed through a dip tube from a liquid CO2 tank. The temperature is controlled using a temperature-control jacket around the Parr reactor. The components can be mixed using the mixing head built into the Parr reactor. Dead volumes were kept small to minimize loss of the contents of the Parr reactor when flushing the sampling valves to take a new measurement. A photo of the completed apparatus is shown inside a walk-in hood in Figure VII.10.

For details on the validation of the experimental method and data analysis, see the SI.

One major limitation of this design is that it cannot directly sample a third phase of intermediate density because it separates in between the low-density CO_2-rich phase and the high-density polyol-rich phase under the force of gravity, and we do not have a sampling port in that region (see Figure VII.11). We explore an indirect method for demonstrating the formation of such a third phase below.

Demonstration of Three-phase Coexistence

Following the plan outlined in Figure VII.8, we pressurized the vessel in steps and sampled the light and dense phases. The sample prepared in the Parr reactor was composed of 84 g PPG (2700 g/mol) and 79 g cyclopentane (48.5% by weight cyclopentane, which appeared to be soluble at room temperature). The total volume of 188 mL had a depth of 3.5 cm inside the 1.2 L Parr reactor chamber. The sample was kept at a temperature of 37 ± 4 °C by a heating jacket around the Parr reactor and mixed at 10 RPM between measurements. The phase behavior was changed by injecting CO_2 as outlined in Figure VII.8.

The compositions of the dense liquid phase and headspace were measured after each injection of CO_2. These compositions, along with the estimate of the overall composition (see Section VII.S3 for details of analysis), are plotted in Figure VII.12. The overall composition (white circles) increases in CO_2 concentration toward the CO_2 vertex after each injection (indicated by white arrow). The headspace composition (blue circles, see zoomed in CO_2 vertex on the right) initially increases in CO_2 concentration toward the CO_2 vertex as well. Upon increasing the pressure from 6.7 MPa to 7.0 MPa, however, the CO_2 weight fraction remained roughly constant. Upon increasing the pressure from 7.0 MPa to 7.5 MPa, the CO_2 weight fraction actually decreasesd (indicated by dark blue arrow). In the liquid phase sample (green circles), the addition of CO_2 likewise initially increased the CO_2
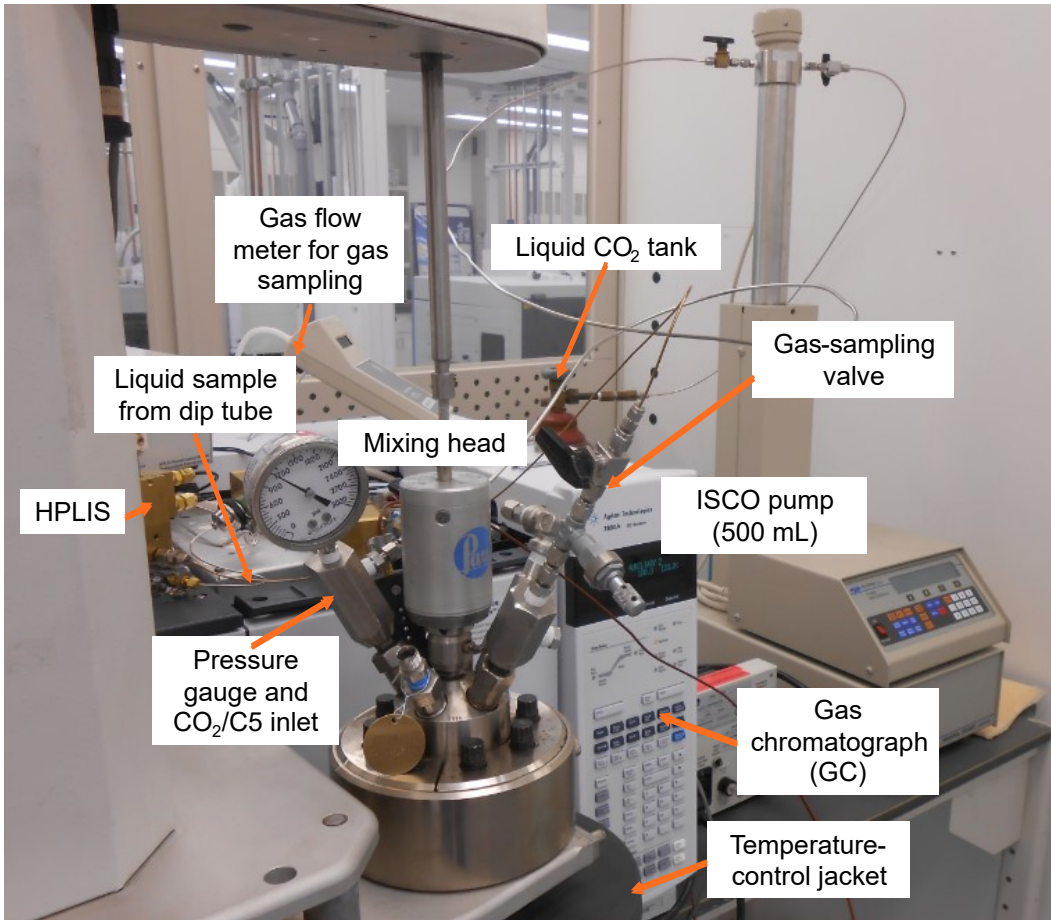
Figure VII.10: Image of the high-pressure sampling apparatus built at the TXINN facility at Dow, Inc., Lake Jackson, TX, based on the schematic in Figure VII.9. In the front left, a Parr reactor fixed into a mixing apparatus and temperature-control heating jacket holds the high-pressure mixture. Pressure is indicated by a pressure gauge attached to the inlet. The inlet is supplied with CO_2 or cyclopentane by a high-pressure ISCO syringe pump shown on the right, which receives liquid CO_2 from a tank in the back. The gas-like light phase is sampled through the valve on the right of the Parr reactor, from which it passes through a gas-sampling valve (not visible). A small sample then is flowed into the gas chromatograph (GC) and out throw a gas flow meter. The liquid sample collected from the bottom of the dip tube of the Parr reactor passes through the tubing indicated into the high-pressure liquid injection system (HPLIS), from which the vaporized CO_2 and cyclopentane flow into the GC (see Figure VII.S1 for alternative perspective). The apparatus is contained within a walk-in hood as an added safety measure in the unlikely scenario of the release of the pressurized contents.

composition. Upon increasing the pressure form 6.7 MPa to 7.0 MPa, the CO_2 weight fraction remained constant, the cyclopentane weight fraction decreased, and the polyol weight fraction increased. This trend continued upon increasing the
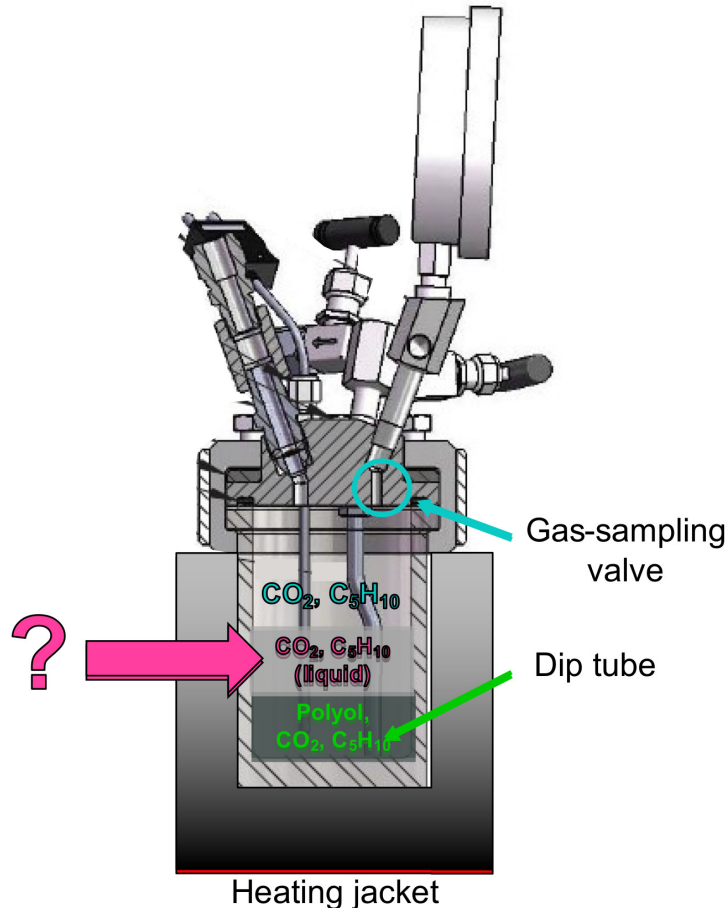
Figure VII.11: A schematic of a three-phase coexistence in a high-pressure mixture of polyol, CO_2, and cyclopentane (C_5H_{10}) in a Parr reactor (image obtained from the Parr Instrument Company's operating instruction manual of 4600 & 4700 models) with temperature maintained by a heating jacket (black). The dense, liquid-like phase of polyol, CO_2, and C_5H_{10} can be sampled by the dip tube that extends almost to the bottom of the Parr reactor (green). The light, gas-like phase of CO_2 and C_5H_{10} can be sampled by the gas-sampling valve at the top of the chamber (light blue). The intermediate, liquid-like phase of CO_2 and C_5H_{10} cannot be sampled (pink), so its composition is not directly measurable.

pressure from 7.0 MPa to 7.5 MPa after another injection of CO_2.

These anomalous changes in the composition of both liquid and vapor phases appear to violate the conservation of mass—how can the weight fraction of CO_2 decrease (vapor phase) or remain constant (liquid phase) upon adding CO_2? We suggest that the missing CO_2 has formed part of a CO_2-rich third phase of intermediate density, which cannot be sampled (as shown in Figure VII.11).

While the anomalous changes in composition upon injecting the Parr reactor
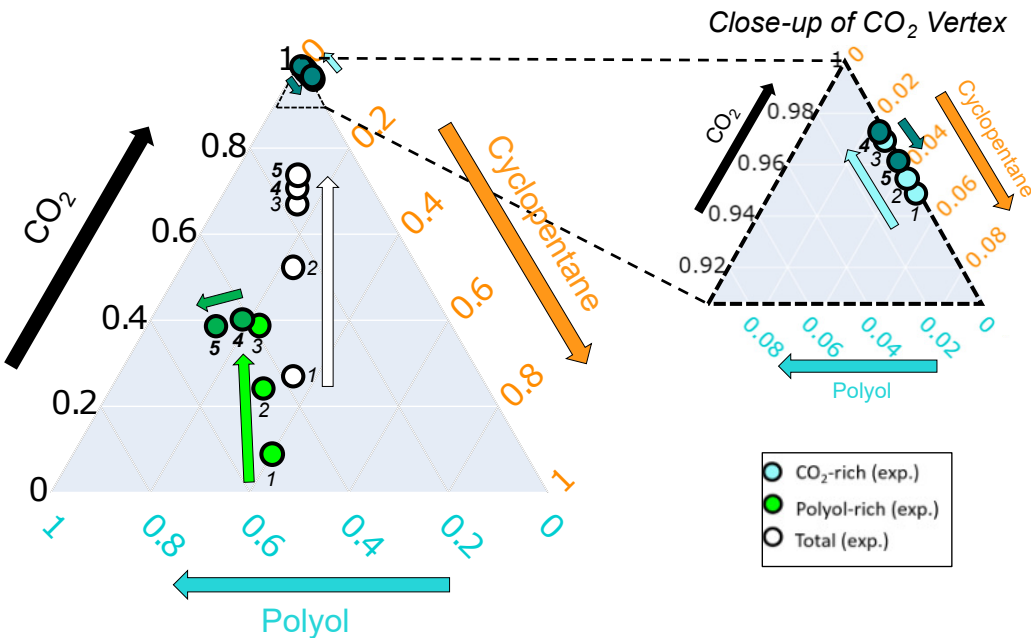
Figure VII.12: The composition of the overall system (white circle), sampled polyol-rich dense liquid phase (light and dark green circles), and sampled CO_2-rich light gas phase (light and dark blue circles) are plotted on a Gibbs triangle at 5 pressures: (1) 2.2 MPa, (2) 5.0 MPa, (3) 6.7 MPa, (4) 7.0 MPa, and (5) 7.5 MPa. Temperature is fixed at 37 °C. The region near the CO_2 vertex at the top is shown in greater detail on the right to distinguish the composition of the sampled CO_2-rich phase. While the overall CO_2 content increases (white circles), the CO_2 content plateaus at 0.4 in the polyol-rich phase (dark green circles) and decreases in the CO_2-rich phase (dark blue circles), suggesting that CO_2 is lost to the formation of a CO_2-rich third phase.

with CO_2 provide evidence for the formation of a third phase, it does not provide information about the validity of the PC-SAFT model that predicted a third phase under those conditions. To validate the PC-SAFT model quantitatively, we compared the measured and predicted compositions of liquid and vapor phases. The model was generally in agreement, but we only compare the theoretical predictions to one measurement taken at 7.5 MPa and 37 °C for brevity in Figure VII.12a. The measured compositions are plotted as circles outlined in black: the white circle represents the overall composition, the green circle represents the measured headspace composition, and the blue circle represents the measured liquid-phase composition. The overall composition (white circle) is in the range of compositions that the PC-SAFT model predicts will phase separate into three coexisting phases. The headspace composition (blue circle) closely matches the predicted composition of the CO_2-rich vapor-like phase (blue star; see zoomed in CO_2 vertex to the left). Likewise, the liquid-phase composition (green circle) closely matches the predicted

composition of the polyol-rich liquid-like phase (green star). While not shown, the densities are also in good agreement.
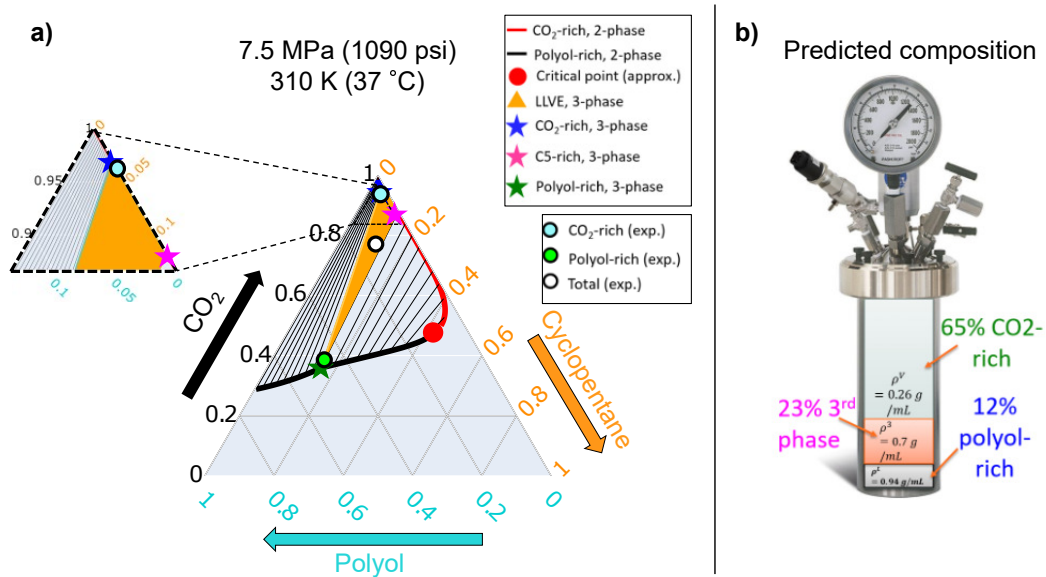

Figure VII.13: a) Measured composition (overall: white circle, CO_2-rich gas: blue circle, and polyol-rich liquid: green circle) superimposed on the PC-SAFT prediction of the phase diagram (see Figure VII.7 for details) at 7.5 MPa and 37 °C. The measured compositions are consistent with a three-phase coexistence, although the third phase (pink star) is not directly measured. b) Estimated volume and density of each phase depicted inside the Parr reactor (image obtained from https://www.parrinst.com/products/stirred-reactors/).

The overall composition does not lie along a tie line between the liquid and vapor compositions, however, indicating that a third phase must have formed to satisfy conservation of mass. To estimate the volume of this third phase relative to the other phases, we estimate the mass of cyclopentane that would be "missing" from the sample if such a third phase did not exist. To estimate this missing mass, we first measure the density of cyclopentane in the liquid ρ_{C5}^L and vapor ρ_{C5}^V phases. Next, we estimate the volume of the liquid phase V^L by assuming that all the polyol in the sample is in the liquid phase (because the vapor pressure is too low to be appreciably present in the vapor phase). Thus,

$$V^L = \frac{m_{poly}}{\rho_{poly}^L} \tag{VII.1}$$

where m_{poly} is the mass of polyol in the original sample (84 g) ρ_{poly}^L is the density of polyol in the liquid phase predicted by the PC-SAFT model. Next, we predict the

mass of cyclopentane assuming only a liquid and a vapor phase,

$$m_{C5}^{pred} = (V - V^L)\rho_{C5}^V + V^L \rho_C 5^L \qquad \text{(VII.2)}$$

where V is the internal volume of the Parr reactor (1200 mL) and $V - V^L$ is our estimate of the vapor phase density (because we assumed that there were only two phases).

We then compare this prediction for the mass of cyclopentane in the Parr reactor with the amount that should be remaining after sampling. We know the initial amount m_{C5}^0 = 78.5 g. By estimating the volume of each liquid sample and multiplying it by the measured density of cyclopentane, we can estimate how much is lost after N samples,

$$m_{sample}^N = \sum_{i=1}^{N} \rho_{C5,i}^L V_i^{sample} \qquad \text{(VII.3)}$$

The remaining cyclopentane after N samples is then $m_{C5}^N = m_{C5}^0 - m_{sample}^N$. The missing cyclopentane is then $m_{C5}^{missing} = m_{C5}^0 - m_{C5}^N$ and is assumed to have formed a third phase if the value is non-negligible. The volume of the third phase can then be estimated by dividing the mass of cyclopentane in the third phase by the density of cyclopentane in that phase predicted by PC-SAFT (pink star), $V^{(3)} = m_{C5}^{missing}/\rho_{C5}^{(3)}$, where a superscript (3) represents the third phase.

Three-phase Coexistence Can Be the Door to Low-barrier Nucleation

As discussed in the introduction to this Chapter, proximity on the phase diagram to a three-phase coexistence often opens up a two-stage nucleation pathway [8, 9]. Indeed, we observed a significant increase in the bubble nucleation rate upon the addition of cyclopentane to the foaming fluid while also demonstrating that a three-phase coexistence can be achieved in such a fluid, although under somewhat different conditions (higher temperature and higher cyclopentane fraction). Further-more, we showed with our string method model a probable pathway to nucleation through two stages: liquid–liquid phase separation followed by vaporization. Such two-stage nucleation occurs rapidly and nuclei remain in the liquid-like state for fleetingly brief periods of time because it is metastable. Our PC-SAFT model has shown, however, that a liquid-like phase of cyclopentane and CO_2 can be thermo-dynamically stable under some conditions. Here, we propose using such conditions

to drive low-barrier liquid–liquid phase separation followed by depressurization to drive the formation of vapor-like bubbles, as shown in Figure VII.14b. To stabilize the liquid phase, we heat the sample from 22 °C to 42 °C while maintaining the pressure at 8 MPa. This heating shifts the phase boundary such that the most stable phase behavior of a solution prepared with a composition of 40% polyol, 40% CO_2, and 20 % cyclopentane changes from a single phase to a liquid–liquid equilibrium. The liquid droplets that separate out of solution at this higher temperature will be thermodynamically stable aside from a drive to coalesce, which is reduced due to the low interfacial tension around liquid-like droplets. The low interfacial tension would also reduce the nucleation energy barrier, similar to the lower nucleation energy barrier for producing the metastable liquid phase predicted by the string method model and shown in Figure VII.4. We hypothesize that much more liquid droplets could be nucleated in this way than by a single-step nucleation into the vapor phase due to this lower nucleation barrier. The liquid-like droplets can then be vaporized by depressurizing the system to atmospheric pressure, which may also nucleate more vapor bubbles in the bulk if there is enough dissolved gas remaining.

VII.4   Future Work

Starting from this foothold, we intended to add in each of the key components in a polyurethane formulation—physical blowing agent, surfactant, isocyanate, heat, water, and catalyst—one at a time. Due to the complexity of the experiment, we have only just begun this process by exploring the effects of adding cyclopentane, just one common physical blowing agent used in polyurethane foaming. Exploring the effects of adding the remaining components of a complete polyurethane formulation in different combinations is therefore left to future work.

The next immediate step to explore would be to add surfactant to a mixture of polyol and CO_2. The effect of surfactant on polyurethane foaming has been explored before by Minogue [19], who found that surfactant reduces cell diameter in the final foam (see Fig. 3-25 in [19]). Minogue, however, suggests that the surfactant only stabilizes bubble nuclei and does not actually affect the nucleation process. This idea could be tested with the present apparatus by applying the techniques described in Chapters VI and VII to estimate the nucleation rate at different degrees of supersaturation. The apparatus could also watch the process of ripening and coalescence (ripening seems to be most common—see Chapter VIII) to see how its time scale is affected by the presence of surfactant. Additionally, these experiments could test recent findings of the favorability of nucleating bubbles from surfactant
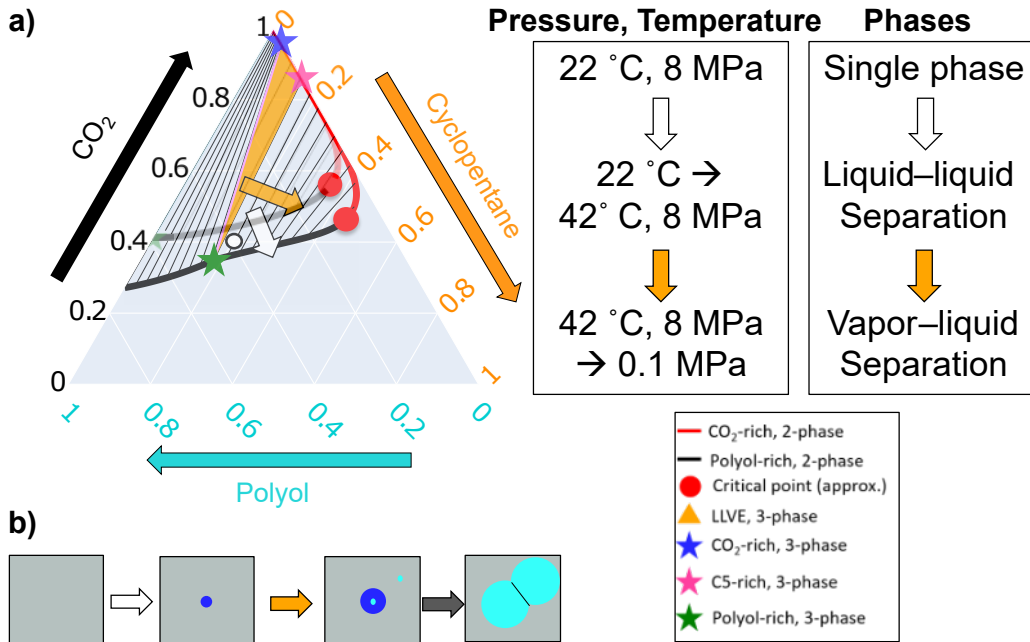
Figure VII.14: Depiction of method of two-stage foaming to enhance bubble nucleation. a) Predicted phase behavior. First, a mixture is prepared at low temperature (22 °C) and high pressure (8 MPa) at a composition that is predicted to form a single phase. The mixture is then heated to 42 °C, which widens the two-phase region enough that the mixture undergoes liquid–liquid phase separation, driving the formation of small, liquid-like bubbles with a low nucleation energy barrier due to the low interfacial tension. Finally, the mixture is depressurized to atmospheric pressure, causing the vapor–liquid equilibrium to widen and drive both the vaporization of the liquid-like bubbles and, if any excess CO_2 and cyclopentane remain, new vapor-like bubbles. b) Schematic of liquid–liquid phase separation followed by vaporization of liquid bubbles and nucleation of new vapor-like bubbles, which grow until they meet and form the cells of the foam.

micelles that form in ternary mixtures of polyol, PEO–PDMS surfactant, and CO_2 explored by our collaborator Dr. Sriteja Mantha (publication forthcoming).

A key component of polyurethane not explored in the present thesis is isocyanate. Without isocyanate, polyurethane cannot be produced. We did not perform experiments with isocyanate in the present work due to the complexity of its reaction and its high hazard as a sensitizer. The proper application of the work of this thesis to polyurethane foaming will require experiments involving isocyanate. Reacting isocyanate with a polyol formulation directly makes the isolation of the effects of the many simultaneous processes occurring during the reaction challenging. These processes are cross-linking, exothermic release of heat, generation of CO_2 upon reaction with water, and an advancing reaction front [20]. Isolating each of these

individually may not be possible, but we suggest a sequence of conditions to test before considering the complete polyurethane reaction to distinguish their effects more clearly in Figure VII.15.
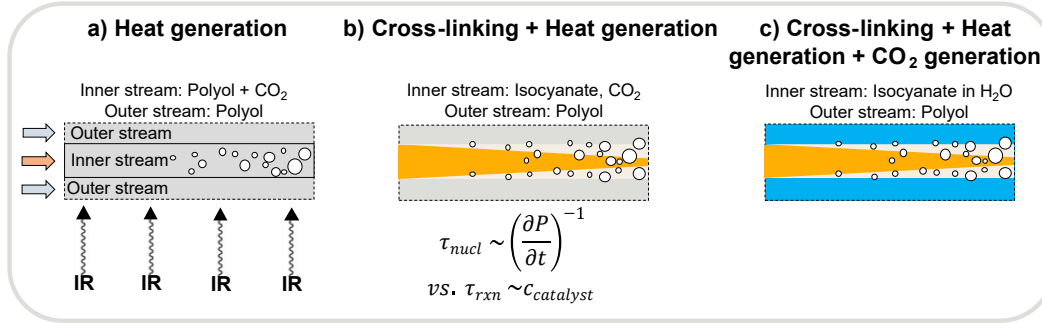

Figure VII.15: Sequence of experiments proposed for studying the effects of isocyanate on bubble nucleation in polyurethane foaming. In each diagram, a zoomed-in section of the sheath flow is shown. The flow enters from the left and exits to the right (see arrows on the left of (a)). The inner stream is at the center and sheathed by the outer stream at the top and bottom of the schematic images. The outer stream appears smaller than the inner stream because it is only partially shown—in general, the inner stream is significantly narrower than the outer stream. Bubbles are indicated by white circles of varying size. a) Focus on the effect of heat generation that would result from the exothermic reaction of isocyanate and polyol. The effect of heat can be decoupled from reaction by heating the inner stream directly, such as by infrared lamps. b) Add the effect of cross-linking to the effect of heating by studying the reaction of isocyanate with dissolved CO_2 inside an outer stream of polyol in the absence of water, which would generate CO_2. The time scale of the polyurethane synthesis reaction could be varied by the adjustment of the catalyst dissolved in the polyol phase. c) The full polyurethane synthesis reaction can be studied by adding water to the polyol phase (indicated by blue color of the polyol in the outer stream), which reacts with isocyanate to generate CO_2 *in situ*.

The effect of heat on bubble nucleation and growth can be studied independently of the isocyanate reaction. The same experiments as have been presented in the present thesis can be repeated while heating the inner stream to test this effect. Heat could be supplied by an infrared light source directed at the inner stream (keeping in mind the limited transmission of infrared by the quartz capillary). Heat could also be supplied through the oil bath used to reduce optical lensing effects, although, if kept at too high of a temperature, the index of refraction of the oil bath may change enough to cause lensing. The outer stream could also be heated directly, although controlling the temperature would be challenging due to the high rate of heat loss along the tubing from the ISCO pump to the microfluidic channel. At higher temperatures, nucleation would be expected to occur at higher pressures

(farther upstream in the observation capillary) because temperature drives supersaturation (see reduction in solubility at higher temperatures in Figure II.1). Increasing the temperature alone also increases bubble nucleation by increasing the frequency of "attempts" to nucleate, which is quantified in the scaling of the nucleation energy by $k_B T$. At higher temperature, however, the viscosities of the fluids will decrease, increasing the flow speed at a given inlet pressure and leading to greater instability. More viscous polyols may be needed to counteract this effect. Additionally, as discussed in Section VI.5, the nucleation energy barrier can be estimated from the temperature dependence of the nucleation rate using the second nucleation theorem [21, 22].

The effect of temperature ought to be studied before studying the effect of reaction because the reaction of isocyanate with polyol is highly exothermic, so the effects cannot be decoupled. By understanding the effect of higher temperatures on bubble nucleation, the effect of the cross-linking reaction alone would be more easily distinguishable. The effect of this reaction could be studied by flowing isocyanate in the inner stream and observing the reaction along the interface with the polyol in the outer stream (see Figure VII.15b). We hypothesize that the cross-linking reaction and heat will both increase the supersaturation of CO_2 because CO_2 is less soluble in polyurethane than polyol and at higher temperatures. The reacting front along the interface between isocyanate and polyol streams is expected to advance into the inner isocyanate stream based on the observations of polyol–isocyanate interfaces by Machuga *et al.* [20]. Based on their work, we might expect the reacting front to advance more than 50 μm within the estimated residence time of about 100 ms, which would consume the entirety of the inner stream. While flowing isocyanate may lead to concerns of fouling, the inner stream will be ensheathed in a much larger volume of polyol, which should react all of the isocyanate before reaching the outlet of the channel. The rate of this reaction τ_{rxn} can be varied relative to the depressurization rate τ_{nucl} by the addition of catalyst to the polyol in the outer stream. Note that the effect of a cross-linking reaction on foaming could be studied directly by using a photopolymer that cross-links under UV radiation, such as polymers with methacrylate groups.

Upon demonstrating the effects of heat and cross-linking on bubble nucleation, the effect of *in situ* CO_2 generation could be explored by adding water to the polyol in the outer stream, as shown in Figure VII.15c. This reaction may take seconds to occur, however, so a longer capillary or slower flow rate (through more

viscous polyol or a narrower inner diameter of the observation capillary) may be necessary. This reaction would be accompanied by a cross-linking reaction between polyol and isocyanate and the generation of heat by the exothermic reaction. By performing the other studies first, the effects of these processes on bubble nucleation could be more easily distinguished from those of the CO_2 generation itself.

While not commonly added to polyurethane formulations, microparticles, nanoparticles, and other solid nucleation sites could be added to understand how such particles would affect our results if they turned out to be present in the polyols. Because we did not filter the polyols used in the experiments, there could have been sub-micron particles providing sites for bubble nucleation. Instead of repeating these experiments with filtered polyols, which could be tedious due to the high viscosity of some of these polyols, the presence of particles could be estimated indirectly by *adding* more particles to the system. If adding a certain concentration of particles has a negligible effect on the degree of supersaturation at which bubble nucleation is observed, then we could conclude that the system must already have at least as many particles inside serving as nucleation sites. Talc [23] and fumed silica nanoparticles [24] have been added to enhance bubble nucleation in polymer foams in the literature, but an appropriate nucleant must not degrade the performance of the foam and must be miscible in the mother phase and not agglomerate. Chemical nucleation sites, such as oligomers with several CO_2-attracting functional groups, could also be used to collect CO_2 molecules and reduce the energy barrier to nucleate a bubble. Amines are generally good at capturing CO_2 and are often used in catalysts for polyurethane foaming [2], which suggests that they may be a compatible source of nucleation sites. Cyclodextrin has also emerged as an effective nucleation site for CO_2-blown foams due to its cage-like structure's hydrophilic exterior (which promotes miscibility) and hydrophobic interior (which can stabilize clusters of CO_2 molecules) [25]. Cyclodextrin does not agglomerate in the way that silica nanoparticles do, so while increasing the concentration of silica nanoparticles does not increase the amount of bubble nucleation above a certain concentration, the addition of cyclodextrin continues to increase bubble nucleation (see Figure 9 of [25]).

References

1. Tesser, R., Di Serio, M., Sclafani, A. & Santacesaria, E. Modeling of polyurethane foam formation. *Journal of Applied Polymer Science* **92,** 1875–1886. ISSN: 0021-8995. https://onlinelibrary.wiley.com/doi/pdf/10.1002/

`app.20170%20https://onlinelibrary.wiley.com/doi/10.1002/app.20170` (May 2004).

2. *The Polyurethanes Book* (eds Randall, D. & Lee, S.) ISBN: 0470850418 (Huntsman International LLC, Polyurethanes business, 2002).

3. Brondi, C., Di Maio, E., Bertucelli, L., Parenti, V. & Mosciatti, T. Competing bubble formation mechanisms in rigid polyurethane foaming. *Polymer* **228,** 123877. ISSN: 00323861. `https://doi.org/10.1016/j.polymer.2021.123877%20https://linkinghub.elsevier.com/retrieve/pii/S0032386121005000` (July 2021).

4. Choe, K. H., Lee, D. S., Seo, W. J. & Kim, W. N. Properties of Rigid Polyurethane Foams with Blowing Agents and Catalysts. *Polymer Journal* **36,** 368–373. ISSN: 0032-3896. `http://www.nature.com/doifinder/10.1295/polymj.36.368` (May 2004).

5. Kang, M. J. *et al.* Liquid nucleating additives for improving thermal insulating properties and mechanical strength of polyisocyanurate foams. *Journal of Materials Science* **45,** 5412–5419. ISSN: 0022-2461. `http://link.springer.com/10.1007/s10853-010-4594-1` (Oct. 2010).

6. Tompa, H. Phase Relationships in Polymer Solutions. *Trans. Faraday Soc.* **45,** 1142 (1949).

7. Bungert, B., Sadowski, G. & Arlt, W. Separations and Material Processing in Solutions with Dense Gases. *Ind. Eng. Chem. Res.* **37,** 3208–3220 (1998).

8. Müller, M., MacDowell, L. G., Virnau, P. & Binder, K. Interface properties and bubble nucleation in compressible mixtures containing polymers. *The Journal of Chemical Physics* **117,** 5480–5496. ISSN: 0021-9606. `http://aip.scitation.org/doi/10.1063/1.1497636` (Sept. 2002).

9. Talanquer, V. & Oxtoby, D. W. Nucleation of bubbles in binary fluids. *The Journal of Chemical Physics* **102,** 2156–2164. ISSN: 0021-9606. `http://aip.scitation.org/toc/jcp/102/5%20http://aip.scitation.org/doi/10.1063/1.468737` (Feb. 1995).

10. Ostwald, W. Studies on the Formation and Change of Solid Matter. *Z. Phys. Chem.* **22,** 289–302 (1897).

11. Golini, P. & Guandalini, M. *Polyurethane Rigid Foams* 2013. `https://patents.google.com/patent/WO2013030101A1/en`.

12. Reignier, J., Alcouffe, P., Méchin, F. & Fenouillot, F. The morphology of rigid polyurethane foam matrix and its evolution with time during foaming – New insight by cryogenic scanning electron microscopy. *Journal of Colloid and Interface Science* **552,** 153–165. ISSN: 00219797. `https://linkinghub.elsevier.com/retrieve/pii/S0021979719305764` (Sept. 2019).

13. Sundar, G. & Widom, B. Three-phase equilibrium in solutions of polystyrene homologues in cyclohexane. *Fluid Phase Equilibria* **40,** 289–303. ISSN: 03783812 (1988).

14. Xiong, Y. & Kiran, E. Prediction of high-pressure phase behaviour in polyethylene/n-pentane/carbon dioxide ternary system with the Sanchez-Lacombe model. *Polymer* **35,** 4408–4415. ISSN: 00323861 (Sept. 1994).

15. Bungert, B., Sadowski, G. & Arlt, W. Supercritical antisolvent fractionation: measurements in the systems monodisperse and bidisperse polystyrenecyclo-hexanecarbon dioxide. *Fluid Phase Equilibria* **139,** 349–359. ISSN: 03783812. https://linkinghub.elsevier.com/retrieve/pii/S0378381297001672 (Dec. 1997).

16. Seckner, A. J., McClellan, A. K. & McHugh, M. A. High-pressure solution behavior of the polystyrene-toluene-ethane system. *AIChE Journal* **34,** 9–16. ISSN: 0001-1541. http://doi.wiley.com/10.1002/aic.690340103 (Jan. 1988).

17. Eckert, C. J. & Sandler, S. I. Vapor-liquid equilibria for the carbon dioxide-cyclopentane system at 37.7, 45.0, and 60.0.degree.C. *Journal of Chemical & Engineering Data* **31,** 26–28. ISSN: 0021-9568. https://pubs.acs.org/doi/abs/10.1021/je00043a008 (Jan. 1986).

18. Shah, N. N., Zollweg, J. A. & Streett, W. B. Vapor-Liquid Equilibrium in the System Carbon Dioxide + Cyclopentane from 275 to 493 K at Pressures to 12.2 MPa. *J. Chem. Eng. Data* **36,** 188–192 (1991).

19. Minogue, E. *An in-situ study of the nucleation process of polyurethane rigid foam formation* PhD thesis (Dublin City University, 2000), 1–194. http://doras.dcu.ie/19076/.

20. Machuga, S. C., Midje, H. L., Peanasky, J. S., Macosko, C. W. & Ranz, W. E. Microdispersive interfacial mixing in fast polymerizations. *AIChE Journal* **34,** 1057–1064. ISSN: 15475905 (1988).

21. Ford, I. J. Thermodynamic properties of critical clusters from measurements of vapour–liquid homogeneous nucleation rates. *The Journal of Chemical Physics* **105,** 8324–8332. ISSN: 0021-9606. http://aip.scitation.org/doi/10.1063/1.472687 (Nov. 1996).

22. Laaksonen, A. & Malila, J. in *Nucleation of Water: From Fundamental Science to Atmospheric and Additional Applications* 45–70 (2022).

23. Tammaro, D., Astarita, A., Di Maio, E. & Iannace, S. Polystyrene Foaming at High Pressure Drop Rates. *Industrial and Engineering Chemistry Research* **55,** 5696–5701. ISSN: 15205045 (2016).

24. Pérez-Tamarit, S., Solórzano, E., Mokso, R. & Rodríguez-Pérez, M. In-situ understanding of pore nucleation and growth in polyurethane foams by using real-time synchrotron X-ray tomography. *Polymer* **166,** 50–54. ISSN: 0032-3861. https://www.sciencedirect.com/science/article/pii/S0032386119300618 (Mar. 2019).

25. Zhou, Y., He, L. & Gong, W. Effect of organic cage nucleating agent structure on nucleating efficiency and the structure-property relationship. *Polymers* **12,** 1–13. ISSN: 20734360 (2020).

VII.S1 Further Discussion of Experimental Apparatus

Safety Precautions Taken While Handling Cyclopentane

Because of the high flammability of cyclopentane and potential to ignite at small weight fractions in atmosphere (about 5 %), extra precautions were taken to keep oxygen sources low. Most importantly, the mixture of polyol and cyclopentane was poured into the Parr reactor and sealed airtight inside a nitrogen glovebox at the Dow TXINN. By keeping the pressure inside the Parr reactor higher than atmospheric pressure, we reduced the likelihood that any oxygen from the atmosphere would enter the Parr reactor during experimentation. As an additional precaution, we set up the experiment inside a walk-in chemical fume hood, which could safely contain a fire or explosion. If these resources are not available, the oxygen content in the Parr reactor can be minimized by running a slow flow of nitrogen gas through the gas-sampling valve of the Parr reactor while sealing the head to purge oxygen from the atmosphere.

High-pressure Liquid Injection System (HPLIS)

The high-pressure liquid injection system (HPLIS) used to vaporize liquid samples for GC analysis is shown in Figure VII.S1. The liquid sample is taken in through the upper port and expelled through a port on the other side to liquid waste, as indicated by the orange arrows. After purging the dead volume in the tubing, a sample can be injected into a stream of the mobile phase of the GC (composed of helium) upon activating a pneumatic piston (air provided at the top of the HPLIS) that injects 500 μL of the upper liquid stream into the lower stream of the mobile phase. At the same time, the piston is heated to 450 °C for 1.25 seconds.

VII.S2 Validation of Sampling Method

First, we calibrated the Agilent gas chromatograph (GC) equipped with two flame ionization detectors (FIDs) inside a Jetanizer (Advanced Research Company) operating at 400 °C, 35 sccm H_2, and 350 sccm air. To test the column used for sampling the headspace of the Parr reactor, which would take in a vapor-like sample, we prepared Tedlar bags of 1–10 L in size with various mixtures of CO_2 and N_2 as well as mixtures of cyclopentane and N_2. The volumes of gas were measured with a custom pump in the Dow TXINN gas chromatography lab. The contents of these Tedlar bags was fed into the GC column by connecting the inlet of the column to the nozzle on the bag and gently squeezing the bag to expel the gas inside. The CO_2 passed through the column more quickly and could thus be distinguished from the
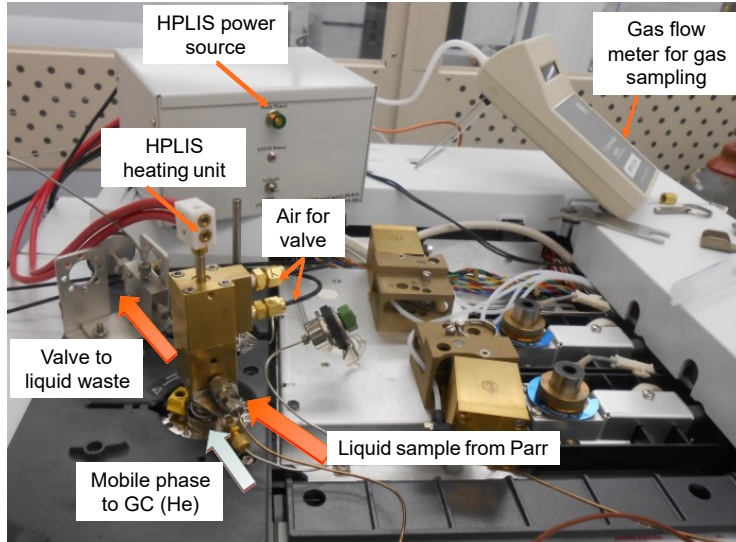
Figure VII.S1: High-pressure liquid injection system (HPLIS) is mounted on gas chromatograph (GC). It receives a liquid sample from the dip tube of the Parr reactor, which enters the HPLIS and exits through a valve to liquid waste normally. A pneumatic valve in the HPLIS pushes the heating unit into the flow of the mobile phase of the GC (helium) and the power source heats the tip to 450 °C to vaporize the cyclopentane and CO_2 so they can enter the GC while leaving behind the polyol.

cyclopentane peak in measurements. In Figure VII.S2, the known density of CO_2 and cyclopentane based on how much was added to the Tedlar bags is plotted on the horizontal axis, and the area under the peak detected by the GC is plotted on the vertical axis. The peak area is indeed proportional to the density for both CO_2 and cyclopentane, and the proportionality constant was used to convert GC peak area measurements into the composition.

To calibrate the GC column for measuring the liquid sample, we sampled CO_2 and cyclopentane differently. Liquid CO_2 was sampled from a dip tube in a liquid CO_2 tank at different split ratios. Cyclopentane samples of different composition were produced by mixing cyclopentane with heptane. In both cases, the liquid sample was passed through the high-pressure liquid injection system (HPLIS), which injected and vaporized a 500 μL sample into the mobile phase of the gas column for measurement.

Next, we used this apparatus to measure the solubility of CO_2 in polyol for comparison to the high-precision measurements of CO_2 solubility made using G-ADSA (see Section II.2). We measured CO_2 solubility at two pressures, 220 psi (1.5 MPa) and 740 psi (5.1 MPa), spanning the low and high end of the G-ADSA measurements. The pressure and measured CO_2 solubility over time are
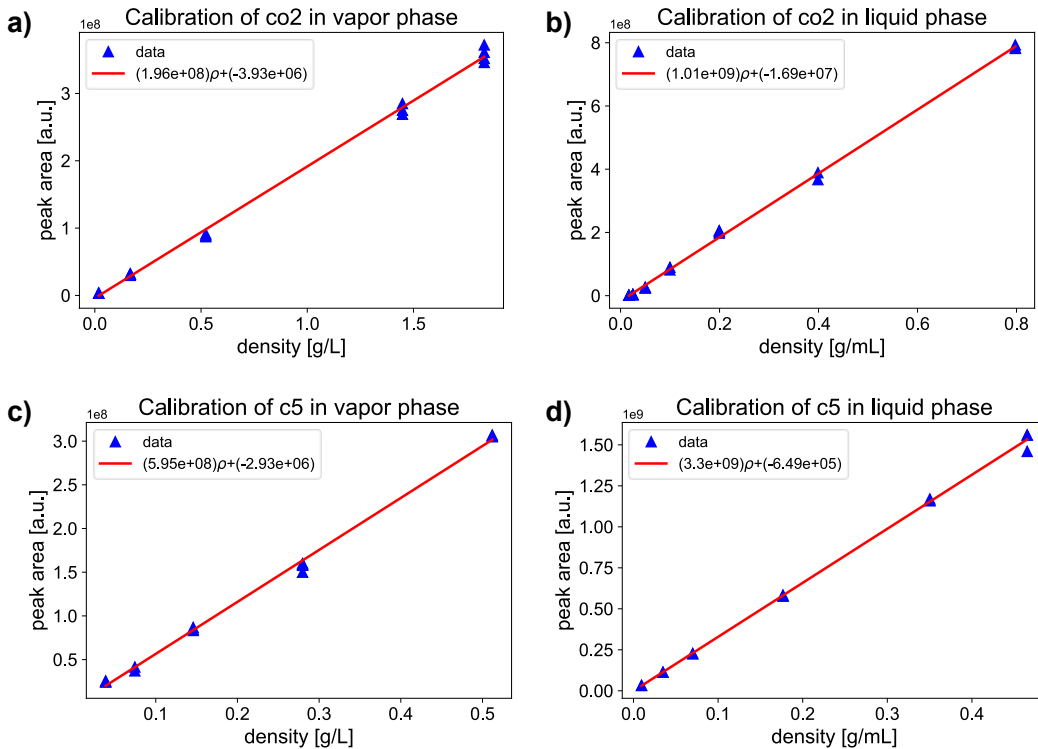
Figure VII.S2: Calibration curves of the gas chromatograph (GC) used to convert integrated peak area into a density. a) CO_2 in vapor phase flame ionization detector (FID). b) CO_2 in liquid phase FID. c) Cyclopentane in vapor phase FID. d) Cyclopentane in liquid phase FID.

shown in Figure VII.S3. The CO_2 solubility measured with GC in this experiment is compared to the measurements made with G-ADSA in Table VII.S1. Because we did not measure the solubility with GC under the exact same conditions as in G-ADSA, we interpolated the solubility values using the PC-SAFT model that successfully fit the measurements (see Figure II.9).

Pressure [MPa]	CO_2 Solub. (GC) [w/w]	CO_2 Solub. (G-ADSA) [w/w]
1.5 ± 0.1	$3.9 \pm 0.5\ \%$	$3.7 + 0.9\ \%$ or $-0.3\ \%$
5.1 ± 0.1	$15 \pm 1\ \%$	$14.4 + 2.8\ \%$ or $-2.1\ \%$

Table VII.S1: Estimated CO_2 solubility (weight fraction) at two pressures based on measurements using the high-pressure GC apparatus (Section VII.3) and G-ADSA (Section II.1).

We determined how long we would wait after changing conditions in the Parr reactor by measuring how the measured composition changed over time. Measurements shown in Figure VII.S4.
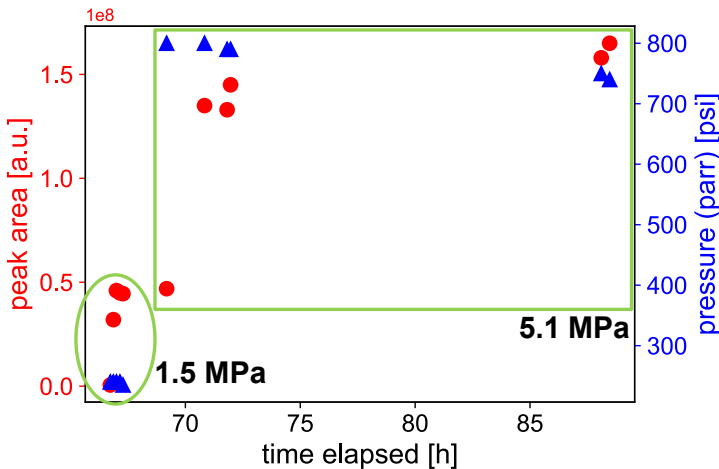
Figure VII.S3: Solubility of CO_2 in 1k2f polyol (see Table II.1) was measured at two pressures, first at 1.5 MPa then, after pressurization, at 5.1 MPa. Integrated area under the peak corresponding to CO_2 is plotted with red circles (left vertical axis), which is proportional to the density (see Figure VII.S2). The pressure inside the Parr reactor is plotted with blue triangles (right vertical axis). The horizontal axis gives the time since the start of the experiment in hours. The points corresponding to the 1.5 MPa pressure measurements are circled while those corresponding to the 5.1 MPa pressure measurements are boxed.
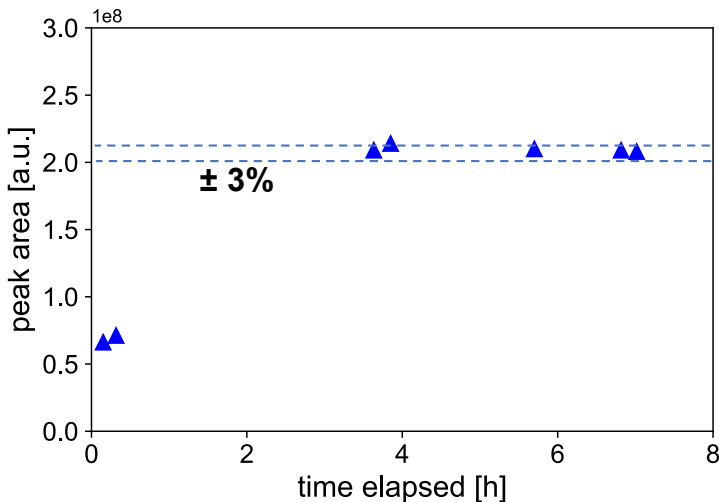

Figure VII.S4: The Parr reactor with about 188 mL (3.5 cm depth) of a 51.5:48.5 mixture of 1k2f polyol (see Table II.1) and cyclopentane is pressurized with CO_2 at time 0. The integrated area under the CO_2 peak measured with GC from samples of the dense liquid phase is plotted as a function of time while the Parr reactor is mixed at 10 RPM. The CO_2 concentration, as measured by the peak area, stabilizes to within 3 % after 4 hours.

VII.S3 Analysis for Estimating Composition of Each Phase from Sampling Measurements

Estimating the Volume of Samples

The volume of fluid sampled is important for many of the estimations of composition in this Section. An important distinction must be made between the volume of sample withdrawn from the Parr reactor and the volume of sample injected into the GC. The volume of sample injected into the GC is fixed by the sampling techniques: the six-port gas-sampling valve holds a sample of about 10 μL of the head space in its tubing for release into the GC and the HPLIS injects and vaporizes a 500 μL sample of the liquid sample into the mobile phase of the GC. The volume of sampled withdrawn from the Parr reactor is typically much larger in order to purge the dead volume between the Parr reactor and the sampling valves. The volume of fluid withdrawn from the head space was measured by a gas flow meter at the outlet. By assuming that the gas equilibrated to atmospheric pressure, we estimated the volume withdrawn $V^V_{withdrawn}$ by multiplying the estimated density $\rho^V_{tot}(p_{atm})$ by the volumetric flow rate Q^V and the time over which the sample was withdrawn t^V to get $V^V_{withdrawn} = \rho^V_{tot}(p_{atm})Q^V t^V$. The volume of fluid withdrawn from the liquid phase was measured by measuring the liquid volume in the waste container (about 2 mL per sample).

Estimating the Density of Polyol in the Liquid Sample

Because the HPLIS does not volatilize the polyol and the GC does not detect it, we do not directly measure the density of the polyol in the liquid sample. Instead, we must estimate the density based on the measurements of the cyclopentane and CO_2 densities and previous knowledge of the equation of state of polyol, cyclopentane, CO_2, and mixtures thereof. To perform this estimation, we make two major assumptions. First, we assume that cyclopentane in the liquid phase is incompressible, meaning that we assume that the density of cyclopentane in the liquid phase has the same density at a pressure $p \in [0.1, 8]$ MPa as at atmospheric pressure (0.1 MPa), $\rho^L_{C5}(p) = \rho^L_{C5}(p_{atm})$. Second, we assume that the polyol is both incompressible and has the same density as the CO_2 in the liquid phase, *i.e.* $\rho^L_{poly}(p) = \rho^L_{CO2}(p) = \rho^L_{poly}(p_{atm})$. We base this assumption on our measurements of the specific volume of polyol–CO_2 mixtures under pressure with G-ADSA, which showed that the density changes by less than 5 % (see Figure II.2). While the equality assumed may not be strictly true, we accept the error of 5 % that it incurs.

Because we assume that the polyol is incompressible, the density in the

liquid-phase sample is the density of pure polyol at atmospheric pressure $\rho_{poly}(p_{atm})$ scaled by the ratio of the volume of polyol V_{poly}^{samp} in the sample to the total sample volume V_{tot}^{samp}. The volume of polyol in the sample is

$$V_{poly}^{samp} = V_{tot}^{samp} - V_{CO2}^{samp} - V_{C5}^{samp} \tag{VII.4}$$

The volumes of CO_2 and cyclopentane in the sample can be estimated by dividing the density of each measured by GC ($\rho_{CO2}^{GC}(p)$ and $\rho_{C5}^{GC}(p)$) by density of the pure component estimated by the assumptions above. Specifically, $V_{CO2}^{samp}/V_{tot}^{samp} \approx \rho_{CO2}^{GC}(p)/\rho_{poly}(p_{atm})$ and $V_{C5}^{samp}/V_{tot}^{samp} \approx \rho_{C5}^{GC}(p)/\rho_{C5}^{L}(p_{atm})$. Therefore, the estimate for the density of polyol in the liquid sample is

$$\rho_{poly}(p) \approx \rho_{poly}(p_{atm}) \left(1 - \frac{\rho_{CO2}^{GC}(p)}{\rho_{poly}(p_{atm})} - \frac{\rho_{C5}^{GC}(p)}{\rho_{C5}^{L}(p_{atm})} \right) \tag{VII.5}$$

where each quantity in equation VII.5 is known from measurement. The weight fractions of each component can then be computed by dividing the density of that component in the sample by the total sample density $\rho_{samp}(p) = \rho_{poly}(p) + \rho_{C5}^{GC}(p) + \rho_{CO2}^{GC}(p)$.

Estimating the Vapor Density after Depressurization

Due to the challenges of maintaining pressure inside the sampling apparatus, the sample of vapor from the head space depressurized to atmospheric pressure inside the six-port gas-sampling valve. Consequently, the GC measured a much lower density of CO_2 and cyclopentane in the sample than expected. To correct the effect of depressurization on the densities, we assume that the head space can be treated as a binary mixture of CO_2 and cyclopentane and use a PC-SAFT model fit to such data [1] to estimate the total density $\rho_{tot}^{pc-saft}$ of the vapor phase under the known pressure and temperature of the Parr reactor. We assume that the weight fractions of CO_2 and cyclopentane remain the same under depressurization. Then we scale the measured densities by the ratio of the PC-SAFT prediction for the total density to the measured total density $\rho_{tot}^{GC(V)} = \rho_{CO2}^{GC(V)} + \rho_{C5}^{GC(V)}$ (where (V) indicates that the measurement is taken of the vapor-phase sample). Then the estimate for the true density of component i is

$$\rho_i^{true} \approx \left(\frac{\rho_{tot}^{pc-saft}}{\rho_{tot}^{GC(V)}} \right) \rho_i^{GC(V)} \qquad \text{(VII.6)}$$

Estimating Density of CO_2 in ISCO Pump

Initially, we believed that the amount of CO_2 in the Parr reactor could be estimated simply by using the CO_2 equation of state to calculate the density and multiply that by the volume dispensed by the ISCO pump into the Parr reactor. This method clearly overestimates the actual amount of CO_2 in the Parr reactor because a substantial amount of CO_2 leaked during the experiment. Additionally, the ISCO pump was likely partially liquid and partially vapor, so determining the overall density of the dispensed fluid was ambiguous. Therefore, we tried two other methods to estimate the amount of CO_2 in the Parr reactor. The first used the change in density of CO_2 in the vapor phase of a CO_2–C5 binary coexistence at the pressure and temperature before and after adding CO_2, assuming that CO_2 and C5 had equilibrated immediately after adding CO_2 or C5 to the Parr reactor or venting and that no CO_2 entered the liquid polyol-rich phase. The second used the PC-SAFT model developed by Dr. Huikuan Chao to estimate the composition of the vapor phase. This method is somewhat circular, however, because it relies on the model that the measurements attempt to validate. Nevertheless, it provided a rough estimate of the composition. In both of the latter cases, the estimates suffered from not accounting for the possible presence of a third phase, as depicted in Figure VII.11.

The first method used to estimate the mass of CO_2 in the Parr reactor was estimating how much CO_2 was dispensed from the ISCO pump into the Parr reactor based on the equation of state of CO_2 [2]. The volume and pressure were recorded from the sensor readouts on the ISCO pump both before and after injection of CO_2 into the Parr reactor. The temperature was assumed to remained constant at the lab temperature (about 21 °C). Based on the equation of state of CO_2, the beginning and final masses of CO_2 in the ISCO pump were estimated, and the difference was taken as an estimate for the amount injected into the Parr reactor.

This method assumed that:

1. The ISCO pump was liquid-full of CO_2 and therefore contained a single, homogeneous phase of CO_2 at all times

2. The Parr reactor did not leak

3. The temperature of the ISCO pump was constant and homogeneous throughout the reservoir

4. The pressure transducer of the ISCO pump did not drift

The first assumption was certainly false after the ISCO pump is refilled because the liquid CO_2 from the tank must expand to fill the dead volume. Additionally, the pressure of the tank is not sufficient to re-condense that vaporized CO_2. Whether the CO_2 became homogeneously liquid when pressurized to 1000 psi and above before injection was not clear and should be tested with another ISCO pump.

The second assumption was definitely false given the detection of a vapor leak through a needle valve on the gas-sampling port of the Parr reactor. The amount of leaked CO_2 was estimated based on differences in pressure betwee injections of CO_2 and C5, but these estimates have not been validated by other means.

The third (3) and fourth (4) assumptions are fairly robust, as the steel syringe of the ISCO pump conducts heat well enough to maintain thermal equilibrium with the laboratory and periodic checks of the pressure transducer reading when emptying the ISCO or loading with the liquid CO_2 tank at a known pressure did not show signs of drift beyond 10 psi, which would have a negligible effect on the estimated amount of CO_2 injected in the Parr reactor.

Overall, this first estimation method is likely an *overestimate* of the true mass of CO_2 in the Parr reactor because of the limitations of assumptions (1) and (2) discussed.

The second method of estimating the amount of CO_2 dispensed assumes that, because the amount of polyol in the vapor phase is negligible, the vapor phase can be approximated as the vapor phase of a CO_2–C5 binary coexistence. Under this assumption, a PC-SAFT model with parameters fitted to Eckert and Sandler's data [1] was used to compute the vapor–liquid equilibrium of CO_2 and C5 at the pressure and temperature in the Parr reactor both before injecting with the ISCO and immediately after. Next, the difference in density of CO_2 in the vapor phase was multiplied by the estimated volume of the vapor phase, which was estimated by subtracting the estimated liquid volume from the approximate interior volume of the Parr reactor (1200 mL). The liquid volume was estimated as $V_{liq} = m_{poly}/\rho_{poly}^{HPLIS}$, where $\rho_{poly}^{HPLIS} = \rho_{poly}^{atm}(T)v_{poly}^{HPLIS}$, where $\rho_{poly}^{atm}(T)$ is the estimated density of polyol under atmospheric pressure at the given temperature and v_{poly}^{HPLIS} is the volumetric

fraction of polyol in the HPLIS, inferred by estimating the volumes of CO_2 and C5 based on their masses measured by the gas chromatograph and their approximate densities at the given temperature.

This method makes the following assumptions:

1. There is no polyol in the vapor phase

2. The vapor-liquid equilibrium between CO_2 and C5 is achieved very rapidly (minutes)

3. The vapor-liquid equilibrium between CO_2 and C5 is not affected by polyol in the liquid phase (*e.g.*, the polyol does not enhance adsorption of CO_2 into the liquid phase)

4. No third phase forms

5. Fitting to Eckert and Sandler's data [1] yields accurate PC-SAFT parameters for the binary coexistence

The first assumption is likely valid because of the low vapor pressure of polyol given its molecular weight of 1000 g/mol and surface tension of almost 30 mN/m. A quick sniff assures the scientist that this is indeed the case.

The second, third, and fourth assumptions have limited validity. The vapor–liquid equilibrium will definitely be affected by the presence of polyol in the liquid as this will lower the diffusivity (hindering equilibrium between vapor-phase and liquid-phase CO_2 and C5) and will affect solubility in the liquid phase. This is made clear when the PC-SAFT estimates of C5 weight fraction in the vapor phase do not match the GC estimates. The fourth assumption is likely false by the sixth injection based on preliminary evidence of the formation of a third phase then, and it is likely that the third phase is present in later measurements as well.

The fifth assumption is probably trustworthy since the data are plentiful and precise.

The advantage of this method is that it only considers changes in CO_2 mass on the order of a few minutes, so we can neglect the leaking of CO_2 and actually use this method as an estimate for how much CO_2 leaked between injections from the ISCO.

Estimating Mass of Gas Lost through a Leak

We estimated the leak of CO_2 using the CO_2–C5 binary coexistence method's estimate of the mass of CO_2. Assuming that changes in the estimated mass are only due to the leaking of CO_2 or injections of CO_2 from the ISCO pump, we took the difference in mass (in general a decrease) between injections from the ISCO and divided by the elapsed time to estimate the rate of leak of CO_2. We noticed an increase in the rate later in the experiment, around the time that we began to notice leaking through the needle valve on the gas-sampling port of the Parr reactor.

VII.S4 PC-SAFT Model Details

The parameters of the PC-SAFT model are provided in Table VII.S2. The parameters of cyclopentane were fitted to literature data of the composition of binary mixtures of CO_2 and cyclopentane at different pressures and temperatures [1] while keeping the CO_2 parameters fixed to those values listed in Table II.2. The interaction parameter between cyclopentane and PPG 2700 g/mol was assumed to be the same as between CO_2 and PPG 2700 g/mol listed in Table II.2; this assumption was validated in the main text by the agreement between experimental measurements of the phase composition and the predictions of the PC-SAFT model using these parameters.

Species	N (beads)	σ [Å]	ε [k_B]	k
C5	2	3.92	290	CO_2: $-2.9 \times 10^{-6} T + 0.125$ Polyol: $10^{-4}(2T - 590)$

Table VII.S2: The parameters N (number of beads per chain), σ (bead diameter in Angstroms), ε (interaction energy parameter in units of Boltzmann's constant), and k (cross-interaction parameter between cyclopentane and CO_2 and cyclopentane and PPG 2700 g/mol, unitless, with T representing the temperature in Kelvin; identical for both species) that fit the solubility data for PPG (2700 g/mol) are listed.

References

1. Eckert, C. J. & Sandler, S. I. Vapor-liquid equilibria for the carbon dioxide-cyclopentane system at 37.7, 45.0, and 60.0.degree.C. *Journal of Chemical & Engineering Data* **31**, 26–28. ISSN: 0021-9568. https://pubs.acs.org/doi/abs/10.1021/je00043a008 (Jan. 1986).

2. NIST. *NIST Standard Reference Database Number 69* 2022. https://webbook.nist.gov/chemistry/ (2022).

C h a p t e r   V I I I

All Grown Up: Leaving the Nest

Your children are not your children. They are the sons and daughters of Life's longing for itself. They come through you but not from you, And though they are with you yet they belong not to you. You may give them your love but not your thoughts, For they have their own thoughts. You may house their bodies but not their souls, For their souls dwell in the house of tomorrow, which you cannot visit, not even in your dreams. You may strive to be like them, but seek not to make them like you. For life goes not backward nor tarries with yesterday.

Kahlil Gibran, *The Prophet*

"She's Leaving Home"

by John Lennon / Paul McCartney

Bubbles do not remain solitary and spherical forever. As they grow, they eventually come in contact with their environment, deforming upon brushing up against other bubbles and reaching the limits of their confinement. At this point, it

is time to get out. As bubbles deform under confinement, they also accelerate to the outlet, as if more fervently seeking escape. Others may find themselves squeezed against other bubbles along the way. The confinement may cause them to merge into one.

Typically, in the flow-focusing channel presented in Chapter III, bubbles first deform upon growing to the size of the diameter of the inner stream due to the higher viscosity of the outer stream than the inner. When bubbles span the width of the inner stream, additional interactions emerge, such as the formation of a "wake" with a different index of refraction behind the bubble (Section VIII.2). These differences in the index of refraction are caused by differences in CO_2 concentration, which affects where bubbles nucleate in the wake. As is often the case following such nucleation events in the wake, bubbles are squeezed against each other. In this case, coalescence is too slow to allow them to merge: ripening is the faster merging process (Section VIII.3). When enough bubbles have nucleated and grown large enough, the inner stream viscosity decreases significantly, which can lead to instabilities (Section VIII.4). While these instabilities preclude observation of bubble nucleation and growth, they are fascinating to watch and important to understand to determine the parameter ranges in which our flow-focusing method can be operated.

VIII.1   Bubbles Elongate Upon Facing Viscous Resistance from Outer Stream

Upon reaching the interface between between the inner and outer streams, bubbles face significant viscous resistance from the outer stream (viscosity almost 5 Pa.s; see Figure III.S1). The viscosity of the inner stream may be as low as 0.01 Pa.s, however, so the bubble can grow much more easily along the flow axis than radially into the outer stream. Consequently, the bubble elongates along the flow direction as if flowing inside a rigid tube rather than confined by a high-viscosity sheath, as shown in Figure VIII.1. The wake that the bubble later leaves behind as it elongates is discussed in the following Section (Section VIII.2).

Bubbles Elongate Exponentially in Time

The models of bubble growth presented in Chapter V no longer describe the growth of a bubble accurately after it reaches the surface of the inner stream and begins to elongate. At this point, the width of the bubble along the radial direction of the capillary remains roughly fixed at the width of the inner stream. The length of the bubble along the flow axis grows exponentially. The square-root growth characteristic of an isolated, spherical bubble and the exponential elongation of the
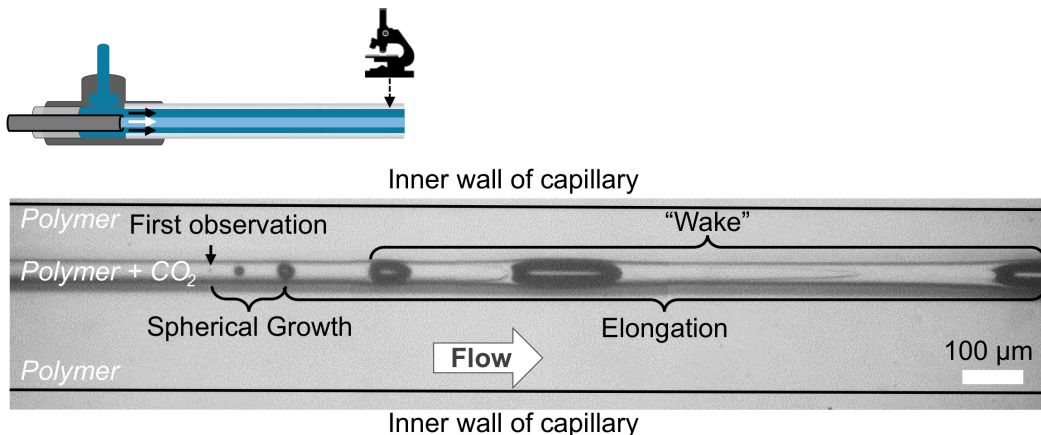
Figure VIII.1: Experimental conditions: PPG 2700 g/mol saturated with CO_2 at 7.0 MPa and 22 °C is flowed through a sheath of 1k5f polyol (see Table II.1) inside a quartz observation capillary with inner diameter 300 μm, length 100 mm, and inlet pressure of about 9.5 MPa, observed 94 mm along the observation capillary. Snapshots of a single bubble from first observation to exit from the field of view are superimposed to show the stages of bubble growth. Initially, the bubble grows spherically. Upon reaching the surface of the inner stream, the bubble elongates along the flow direction. During this elongation, the convection of fluid from the head to the tail of the bubble creates a "wake" behind the bubble (discussed in Section VIII.2). Location of measurement along observation capillary is shown schematically above figure.

bubble under confinement can be seen in the plots of bubble length L (distance from the head to the tail of the bubble), bubble diameter D (width along the radial dimension), and diameter of an equivalent sphere $D_{eq} = \left(\frac{6}{\pi}V\right)^{1/3}$ (where $V = \pi/6D^2L$ is the approximate volume of the bubble assuming an elliptical shape) in Figure VIII.2. The qualitative change in the growth rate can be seen in the linear plot in panel (a). Panel (b) plots the size along a logarithmic vertical axis, such that exponential growth appears as a straight line. Indeed, the growth of the length of the bubble L (blue line) matches the straight line shown for reference after the length exceeds the maximum diameter around 500 μs, indicating exponential growth. In this case, the time constant corresponding to the straight line is about 1 ms, meaning that the bubble grows by a factor of e every millisecond. Panel (c) plots both axes on a logarithmic scale, such that a power-law growth appears as a straight line with the power equal to the slope. Indeed, the growth of the bubble diameter D (orange line) grows with a power of 1/2, consistent with the observations in Chapter V. While the diameter of an equivalent sphere D_{eq}—an estimate of the diameter of the bubble if it were growing unhindered—appears in panel (c) to grow with a power

of 1/2 as well, even after the bubble has started elongating, the growth should be exponential since it is proportional to the cube root of the length. We suspect that this coincidence is the result of only observing a short segment of the exponential growth regime, which may look linear with a slope of 1/2 on a log-log scale for this brief period of time.
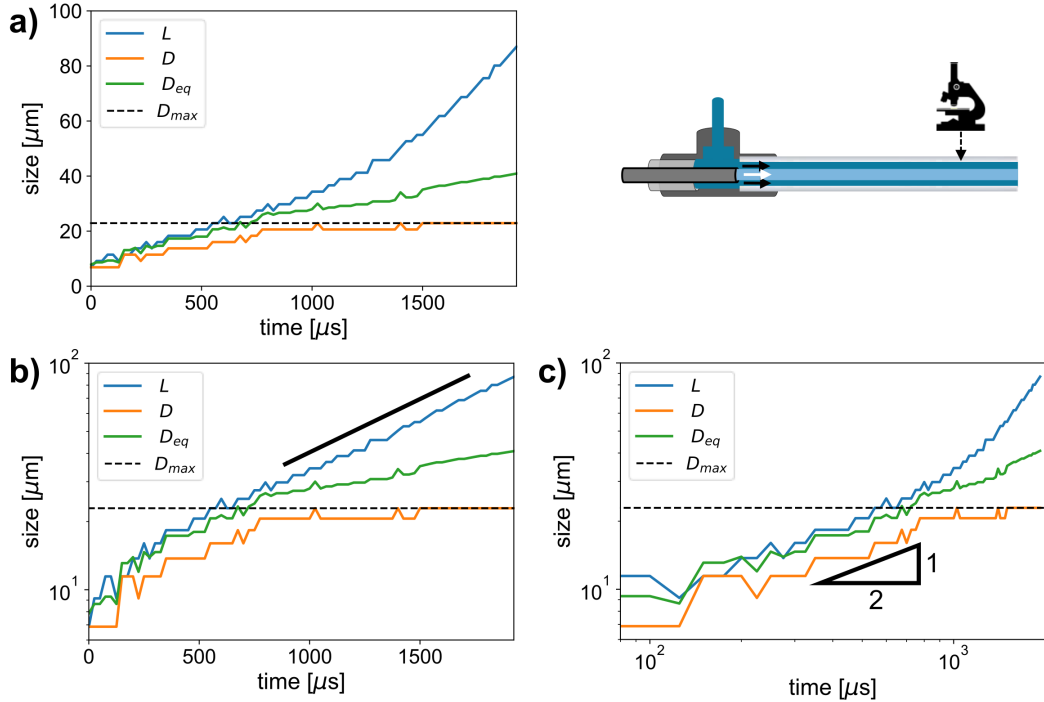

Figure VIII.2: A bubble's length L from head to tail (blue line), diameter D along the radial direction (orange line), equivalent diameter of a sphere of the same volume $D_{eq} = (D^2 L)^{1/3}$ (green line), and maximum diameter of the bubble (black dashed line) are plotted as a function of time. a) Linear scale for both axes. b) Logarithmic vertical scale. Black line provided as a reference to represent exponential growth with a growth constant of about 1 ms. c) Logarithmic vertical and horizontal axes. A slope of 1/2 is indicated by the triangle, which represents power-law growth $t^{1/2}$. The bubble analyzed comes from an observation taken during the experiment as in Figure VIII.1 but at 79 mm downstream.

The exponential elongation of bubbles under confinement has been observed before in the case of a vapor bubble in a boiling liquid flowing through a tube [1–3]. Exponential growth results from a growth rate of a dimension proportional to the size of that dimension. In this case, it suggests that $\frac{dL}{dt} \propto L$. Such growth is consistent with a flux that is constant when averaged along the length of the bubble, suggesting that CO_2 is not depleted significantly in the region immediately surrounding an elongated bubble, as if it is replenished. We explore this idea of replenishing CO_2

around elongated bubbles in Section VIII.2.

Bubbles Accelerate as They Elongate Due to Fluid Displaced by Growth

When a bubble elongates, it does so because it cannot push fluid around its lateral sides out of the way. Instead, fluid must be displaced at the head or tail of the bubble to permit the growth, assuming it is flowing in an incompressible fluid medium. Where does the fluid displaced by the elongation of the bubble go? While we cannot observe the flow field directly, nor can we place tracer particles into the inner stream because they would cause heterogeneous bubble nucleation, we can occasionally observe the flow indirectly by watching small bubbles.

In Figure VIII.3, we show that three small bubbles remain almost perfectly still as an elongated bubble passes by them. Two of the three bubbles can be seen in front of the elongated bubble in panel (a) (circled in yellow). The locations of the three bubbles are marked by yellow circles in three frames as the elongated bubble passes by them over the course of 440 μs (panels b–d). The right most edge of the marker circles in panel (d) is marked with a thin vertical yellow line to provide a guide to the eye for comparing the positions of the bubbles. Over the last 240 μs, the small bubbles translate less than 5 % of the distance traveled in the first 200 μs of the sequence of frames. This near-stagnation of the bubbles within the thin film between the bubble and the outer stream reveals that fluid at the head of the bubble ends up at the tail of the bubble as the bubble "slips past" the fluid. While in the laboratory frame of reference, the fluid in this film moves little, relative to the flow upstream and downstream, the fluid is moving upstream. A similar stagnation is observed in the outer stream, as shown in Figure VIII.S1 of the Supporting Information (SI).

Agostini *et al.* suggest that the fluid in the thin film between the bubble and the confining surface appears to flow upstream relative to the flow because it is the path of least resistance for fluid displaced by the growing bubble [2]. A schematic showing this process is presented in Figure VIII.4. In panel (a), at time t_i, a volume ΔV_b^i of the inner stream fluid surrounds the head of the bubble. This volume is equal to the volume by which the bubble will grow in a time step Δt, as shown in green in panel (b). The displaced fluid has nowhere to go but upstream to the tail of the bubble, as shown in panel (c), during which the fluid faces little resistance from the pressure upstream because the pressure along a bubble is negligible (see Figure 8 of Khandekar *et al.* [4]). Assuming that the bubble is incompressible, the fluid displaces the bubble, pushing the bubble farther downstream, as shown in panel (d).
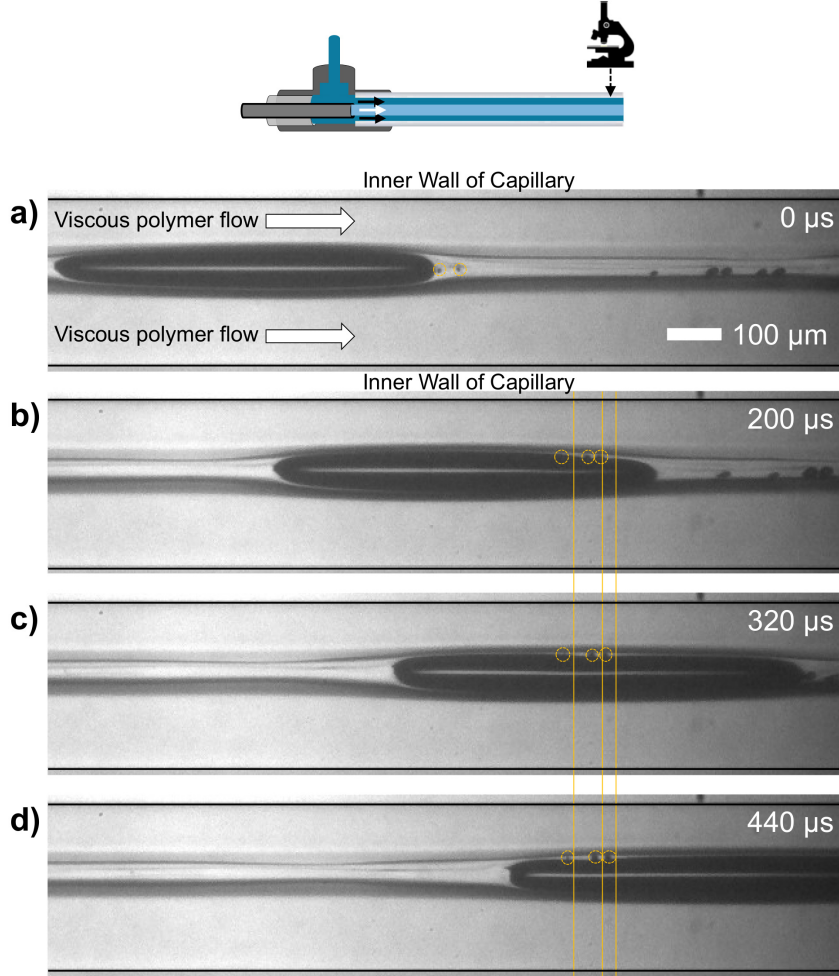
Figure VIII.3: a-d) Still frames of sheath flow show small bubbles stagnate in the thin film between an elongated bubble and the outer stream as the elongated bubble passes by them. Yellow dashed circles mark three small bubbles that act as tracers of the flow (one of these bubbles is not visible in (a)). The far-right edge of these circles in the final frame (d) is marked by vertical yellow lines. In the 240 μs between (b) and (d), the bubbles hardly move a few μm while they travel hundreds of μm in the 200 μs between (a) and (b). Top shows a schematic of where the observation was made along the observation capillary. PPG 2700 g/mol polyol (see Table II.1) saturated with CO_2 at 7.2 MPa and 22 °C flowed within sheath of 1k5f polyol in a quartz observation capillary of 300 μm inner diameter and 100 mm length with an inlet pressure of 13.4 MPa and observed at 95 mm along the length of the capillary.

During the time step Δt, the surrounding fluid has been flowing at a speed U_l and thus has traveled a distance $U_l \Delta t$, as shown in panel (e). Consequently, over a time step Δt, the bubble travels farther than the surrounding fluid medium.

This circulation of flow causes bubbles growing in confinement to accelerate with their length [1, 2]. We show this acceleration in Figure VIII.5. In panel (a), we
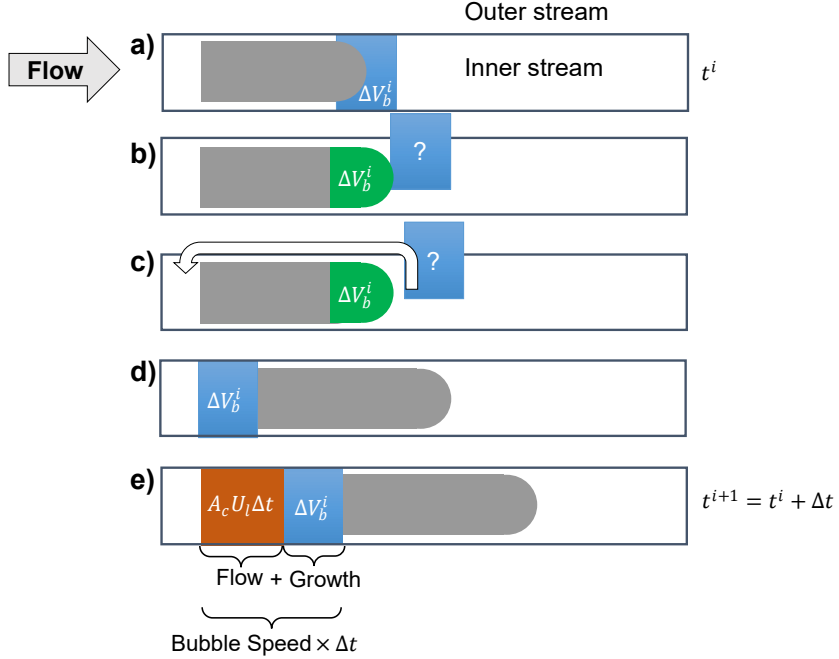
Figure VIII.4: Schematic showing that the displacement of fluid by an elongating bubble under confinement causes the bubble to accelerate faster than the surrounding medium. The black rectangle represents a segment of the inner stream; the area outside it represents the outer stream. Flow is left to right. a) At time t^i, a volume of fluid ΔV_b^i (blue) surrounds the head of the bubble (gray). b) The bubble grows by a volume ΔV_b^i (green) during the timestep Δt and the fluid around it must be displaced somewhere. c) The displaced fluid (blue) can only flow upstream to the tail of the bubble. d) Upon reaching the tail of the bubble, the displaced fluid (blue) displaces the bubble (gray) farther downstream. e) During the timestep Δt, the flow also travels a distance $U_l \Delta t$ (orange) which, when combined with the distance the bubble is displaced by the displaced fluid, results in the distance traveled by the bubble. The resulting bubble speed is larger than the flow speed.

plot the speed of the head (yellow) and tail (blue) of a large collection of bubbles observed at 88 mm and 90 mm along the length of the observation capillary. The data were collected from the same experiment as was used to estimate the rate of bubble nucleation in mixtures of PPG and CO_2 in Section VI.2: the inner stream is composed of PPG 2700 g/mol saturated with CO_2 at 7.2 MPa and 22 °C and the outer stream is composed of 1k5f polyol (see Table II.1), flowing through a capillary with an inner diameter of 300 μm and a length of 100 mm with an inlet pressure of 13.4 MPa. While the data do not perfectly collapse, some general trends are observed. When the bubble is smaller than the inner stream, the speed appears to decrease with length, possibly because the flow nearer the surface of the inner stream is slower. Once the bubble is longer than the width of the inner stream,

meaning that it is flowing under confinement inside the highly viscous outer stream, the speed increases with length. This increase is roughly linear until the bubble reaches a length of around 400 μm. Above 400 μm, further elongation of the bubble leads to little acceleration of the tail as the speed appears to plateau, while the head accelerates (as must be the case assuming an incompressible system) but less rapidly than for lengths below 400 μm.
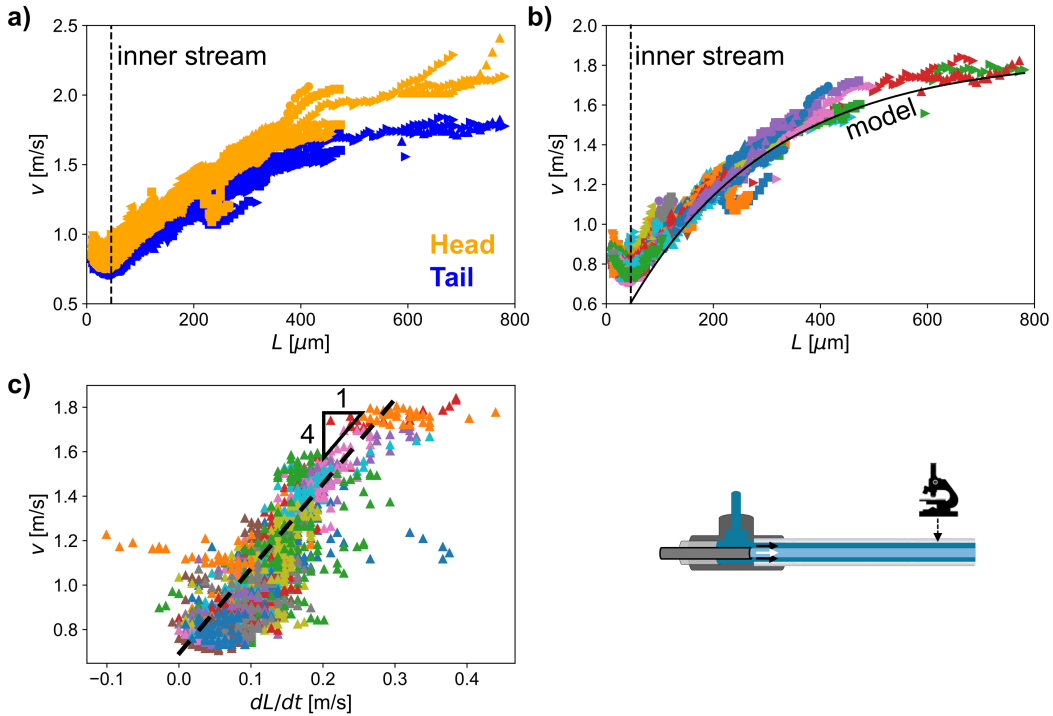

Figure VIII.5: Bubble speed as a function of length and elongation rate. a) The speed of the bubble head (yellow) and tail (blue) as a function of the length of the bubble. The vertical dashed line indicates the width of the inner stream; data points to the right of this line represent elongated bubbles. b) Only the data for the speed of the bubble tail from (a) are shown. Each color and symbol represents a different bubble as it grows. A fitted model based on the work of Agostini et al. [2] is shown (black solid line). c) Speed of the bubble tail as a function of dL/dt, the rate at which the bubble length L increases. The estimate for dL/dt is prone to noise due to limited spatial and time resolution and imperfect image segmentation. A linear fit with a slope of 4 is shown (black dashed line). Lower right indicates schematically where observations were taken along the observation capillary. PPG 2700 g/mol polyol (see Table II.1) saturated with CO_2 at 7.2 MPa and 22 °C flowed within sheath of 1k5f polyol in a quartz observation capillary of 300 μm inner diameter and 100 mm length with an inlet pressure of 13.4 MPa and observed at 95 mm along the length of the capillary.

Out of curiosity, we fit the collection of bubble speeds vs. lengths to a model

proposed by Agostini *et al.* for vapor bubbles flowing through a tube of boiling liquid refrigerant, as shown in Figure VIII.5b. The model assumes that the flux of gas into the bubble is proportional to the surface area of the bubble, that the fluid displaced by the bubble flows to its tail and pushes the bubble farther downstream, that the system is incompressible, and that the bubble feels an empirical friction force from flowing along the walls, which is responsible for causing the speed to plateau with length [2]. While we cannot comment on the validity of the assumption that friction causes the speed to plateau, but the model appears to capture the speed of the tail of the bubble well, suggesting that similar physics might be at play even though the systems are different. The model is least accurate when the bubble is smaller than the inner stream and not confined, indicating that different physics are dominant when a bubble is flow without the effects of confinement.

Out of further curiosity, we tested a hypothesis that the rate at which the bubble elongates is proportional to the speed of the bubble. This hypothesis was based on the assumption that the elongation of a bubble displaces fluid that flows to the tail of the bubble and pushes the bubble farther downstream, as depicted in Figure VIII.4. If this picture were true, the bubble would accelerate more the faster it grew because it would displace more fluid behind it, pushing it farther downstream in the same time period. To test this hypothesis, we plotted the bubble speed v as a function of the elongation rate dL/dt in Figure VIII.5c using the same collection of data as used to generate the plots in the other panels of the Figure. While the spread in the data is large, a general increase of speed with the elongation rate is observed having a slope of 4 (dashed black line). Therefore, while the bubble speed generally increases with the elongation rate, it does so at a rate four times faster. This difference in rate suggests that other physics than just the displacement of fluid by bubble growth depicted in Figure VIII.4 might be responsible for the acceleration of the bubble, such as the acceleration of the flow itself due to the decreased viscous resistance of longer bubbles.

VIII.2 Formation of the Wake

That fluid at the head of an elongated bubble ends up at its tail not only results in the acceleration of the bubble, but it also changes the concentration of CO_2 in the region behind the bubble. This change in concentration of CO_2 is seen behind the longer bubbles in Figure VIII.1, where a dark interface with the shape of a backward "C" is observed. An interface indicates a difference in the index of refraction, which could only be caused by a difference in the concentration of

CO_2 since there is no evidence that the outer stream polyol is mixing with the inner stream. We call the region between the tail of the bubble and this interface the bubble's "wake." Because the bubble accelerates as it grows under confinement, as discussed in the previous Section, the length of the wake increases with time, as seen in Figure VIII.1. The interface at the end of the wake also becomes stratified, likely due to the parabolic shape of the flow speed along the width of the inner stream. This interface indicates an inhomogeneous concentration of CO_2, but where is the CO_2 concentration greater and where is it lower? In the following discussion, we present a model of the wake to shed light on the relative CO_2 concentrations throughout it.

Wake's Anatomy

Why is it important to understand the wake's "anatomy"? Long bubbles can leave behind even longer wake regions, which may affect the likelihood that bubbles nucleate in these regions depending on the concentration of CO_2 (the "anatomy") within them. In experiments, we have observed the effects of different concentrations of CO_2 in the wake. For example, a bubble in the wake of another bubble often grows more slowly than the leading bubble. Additionally, we have seen under high contrast (achieved by narrowing the aperture on the condenser lens of the microscope) that the wake contains a narrow "trail" along its center, as seen in Figure VIII.6. Furthermore, when bubbles nucleate in the wake, they tend to nucleate near but outside this trail, as observed in the cluster of recently nucleated bubbles in the lower part of the Figure (outlined in a blue dashed rectangle).

To understand the wake's "anatomy," we begin where the fluid from the wake originates based on the discussion in Section VIII.1: the head of the bubble. We show a schematic of the thin film of the inner stream fluid between the head of an elongated bubble and the outer stream in Figure VIII.7. An example of an elongated bubble from an experiment is shown in the lower right with the region of interest outlined with a dashed white rectangle. We consider the reference frame of the bubble, so the acceleration of the bubble causes the inner stream to appear to be flowing toward the tail of the bubble (to the left in the Figure). As the inner stream "flows" at speed U to the left along the bubble, it is squeezed into a thin film with a width δ of a few microns. This film is significantly smaller than either the radius R or length L of the bubble, so we expand it for clarity (not to scale). The pressure inside the bubble is roughly the local fluid pressure (the Laplace pressure is negligible for bubbles larger than 1 μm as shown in Figure V.7), while the inner stream was saturated with CO_2 at a higher pressure. Thus, the equilibrium concentration of CO_2
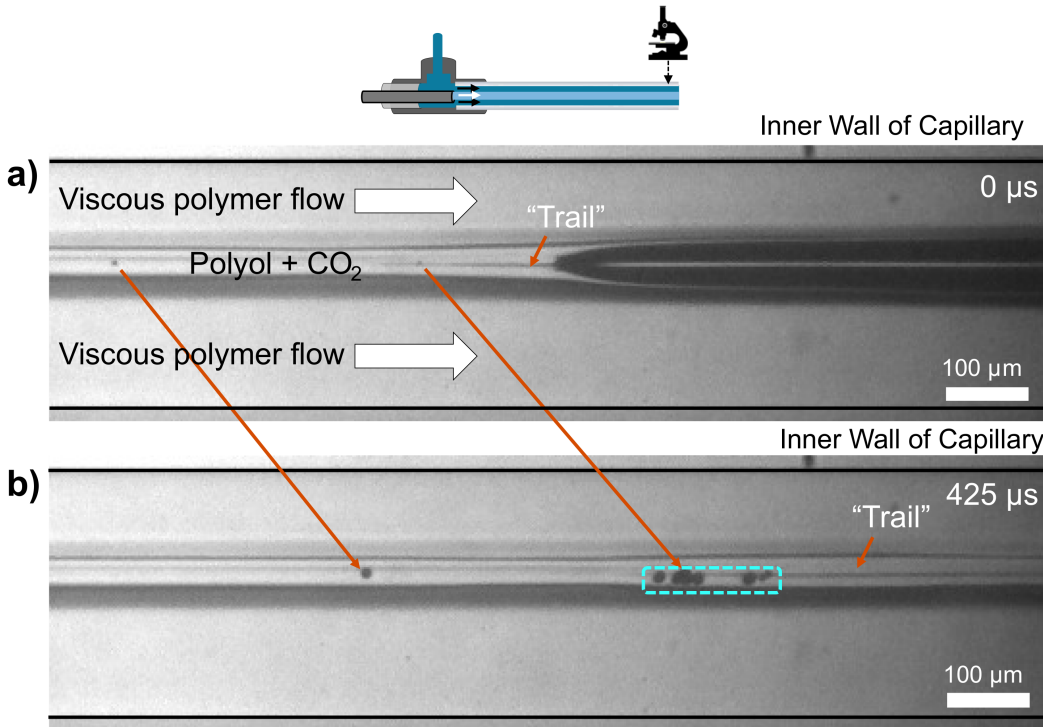
Figure VIII.6: a) Micrograph of the microfluidic sheath flow (location indicated in schematic at top). An elongated bubble is exiting the field of view and leaving behind a "trail" of different index of refraction within the inner stream. b) Micrograph of same location taken 425 μs later. In addition to the bubbles seen in the top image—indicated by orange arrows—many bubbles emerge along the "trail" left behind by the elongated bubble (light blue dashed rectangle). PPG 2700 g/mol polyol (see Table II.1) saturated with CO_2 at 7.2 MPa and 22 °C flowed within sheath of 1k5f polyol in a quartz observation capillary of 300 μm inner diameter and 100 mm length with an inlet pressure of 13.4 MPa and observed at 95 mm along the length of the capillary.

near the surface of the bubble is smaller than the concentration in the inner stream, driving diffusion of CO_2 from the inner stream into the bubble. The front of this diffusion of CO_2 expands into the thin film of the inner stream to have a width that grows as the square root of time since first contact of the fluid with the bubble τ and diffusivity $\mathcal{D}$, $\delta_D \sim \sqrt{\mathcal{D}\tau}$. At the tail of the bubble, the time since contact $\tau = L/U$. The width of the depletion layer at the tail of the bubble is thus $\delta_D \sim \sqrt{\mathcal{D}L/U}$.

Let's estimate the scale of width of this depletion layer. Based on the measurements of diffusivity with G-ADSA shown in Figure II.4, the diffusivity ranges between $\mathcal{D} \in [10^{-10}, 2 \times 10^{-9}]$ m²/s. Based on the sample of bubble lengths and speeds plotted in Figure VIII.5, $L \in [50, 800]$ μm and $U \in [0.7, 2.5]$ m/s. Lengths and speeds are correlated, however, so the ratio L/U ranges from 5×10^{-5}
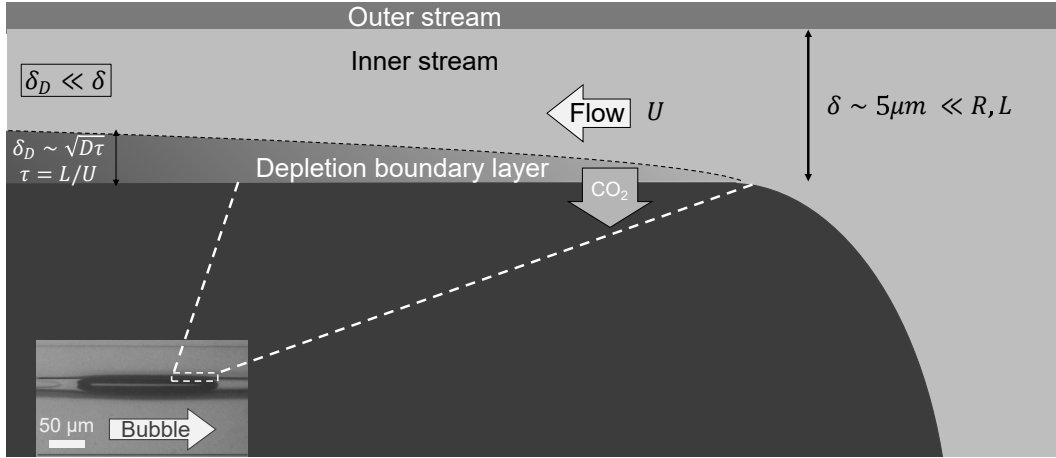
Figure VIII.7: Schematic of the depletion layer along the head of an elongated bubble (location indicated in micrograph in the lower left). The schematic is depicted in the reference frame of the bubble (dark gray region), so the inner stream (light gray region) appears to flow left along the bubble with speed U. The width of the thin film of the inner stream between the bubble and the outer stream (gray region at the top) $\delta \sim 5\ \mu$m, which is much smaller than the radius R or length L of the bubble. As the bubble passes the inner stream, CO_2 diffuses from the inner stream into the bubble, leading to a depletion boundary layer along the bubble (outlined with a dashed black line; darker shade indicates less CO_2). The width of this boundary layer δ_D scales with the square-root of the diffusivity of CO_2 $\mathcal{D}$ and the time for inner stream to pass along the full length of the bubble $\tau = L/U$. Not to scale.

m / 0.7 m/s $\approx 7 \times 10^{-5}$ s (shortest bubbles) to 8×10^{-4} m / 2.5 m/s $\approx 3 \times 10^{-4}$ s (longest bubbles). Therefore, $\delta_D \in [0.1, 0.6]$ μm, meaning that it is significantly thinner than the width of the thin film of inner stream (about 5 μm based on visual observation). Only a small fraction of the thin film nearest the bubble is depleted of CO_2.

How does the fact that the depletion layer along the bubble is much thinner than the film between the bubble and the outer stream affect the fluid in the wake? We show our hypothesis for the concentration of CO_2 in the wake of the bubble as a result of only partial depletion of the thin film along the bubble in Figure VIII.8. As the depletion layer is passed by the tail of the bubble, it is pulled into the center of the inner stream. The remaining volume around it is filled by the rest of the thin film around the bubble. This thin film has another depletion layer along the interface with the outer stream, however, because CO_2 diffuses out from the inner stream of polyol and CO_2 into the pure polyol outer stream. The result of this depletion is depicted by a gradient from dark (low CO_2 concentration) to light (high CO_2 concentration) from the outside to the inner part of the inner stream. The concentration of CO_2 is

thus highest in between these two depletion layers. Therefore, there is a gradient in the concentration of CO_2 along the edge of the depletion.
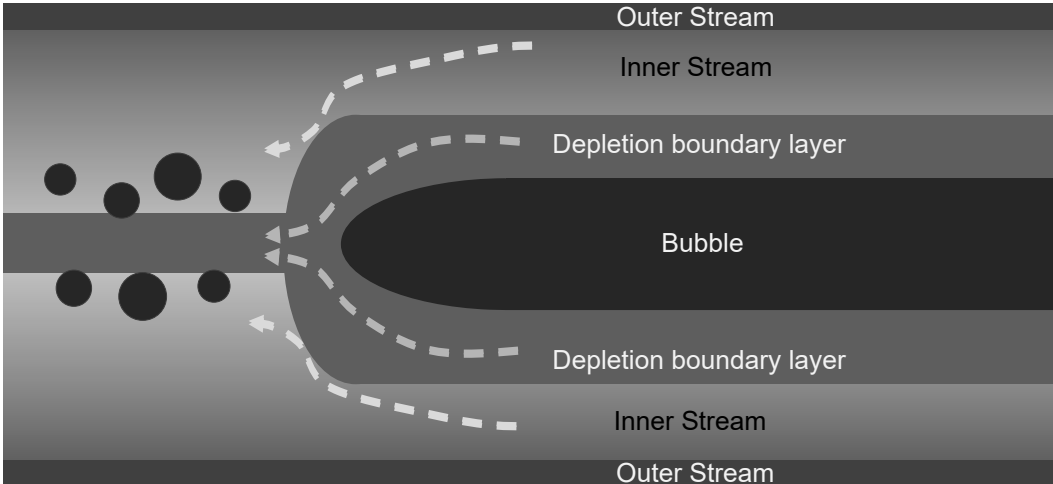

Figure VIII.8: Hypothesis for the explanation of the "trail" observed in Figure VIII.6. The depletion boundary layer at the tail of a bubble (compare with the depletion layer at the head in Figure VIII.7). Because the speed of the bubble scales with its length (see Figure VIII.5), the width of the depletion boundary layer δ_D is less than the width of the inner stream δ (see Figure VIII.7). At the tail of the bubble, the depletion boundary layer fills in the space behind the bubble. Due to the lower concentration of CO_2 (see Figure VIII.9), the index of refraction of the depletion boundary layer is lower than the rest of the inner stream, yielding a visible "trail" behind the bubble (darker gray region). The remainder of the inner stream also loses CO_2 through diffusion into the outer stream (dark gray, top and bottom), yielding a gradient in CO_2 increasing from outside in. This gradient is smoother because it has been formed since the inner and outer streams met at the entrance of the observation capillary. The greatest concentration of CO_2 in the "wake" region behind the elongated bubble is just outside the trail, which may explain why bubbles are often observed to nucleate in this region (see Figures VIII.6 and VIII.S2).

We hypothesize that this concentration gradient leads to a sufficient gradient in the index of refraction that an interface can be distinguished along it, which may be the interface observed along the "trail" observed in the wake (Figure VIII.6). The cause for the sharpness of the interface is not clear, however. Because bubble nucleation is highly sensitive to the degree of supersaturation, it is most likely to occur in the region of highest CO_2 concentration. Based on our hypothetical model, this region lies just outside the depleted trail at the center of the wake, consistent with the observation of bubble nucleation in clusters just outside the trail in Figure VIII.6.

Based on the hypothetical model for the concentration profile in the wake,
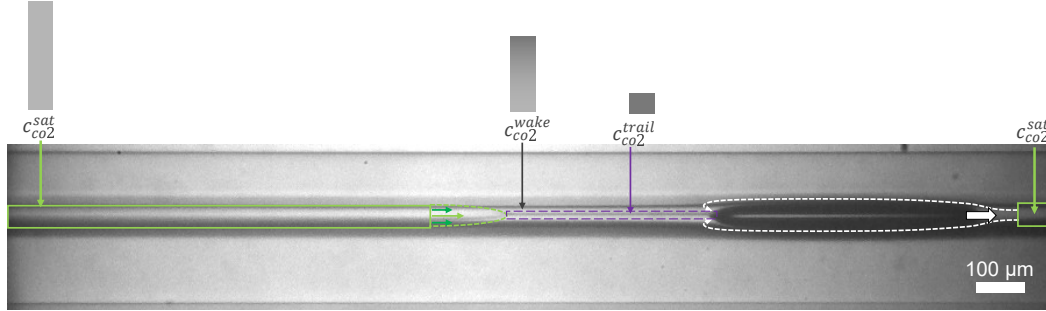
Figure VIII.9: An "anatomy" of the wake left behind an elongated bubble with hypothetical estimations of the relative concentrations of CO_2 in different regions. The bubble (dark object in the inner stream on the right) is moving to the right at a speed faster than the flow. Consequently, the inner stream will end up passing from head to tail of the bubble and filling the space in the back (dashed white arrows), forming a trail in the center of the inner stream (dashed purple box—see Figure VIII.8) with concentration of CO_2 c_{co2}^{trail}. Outside the trail, the concentration of CO_2 c_{co2}^{wake} is higher. Due to the velocity gradient within the inner stream (indicated by green arrows), the interface (green dashed parabola) between the wake and the unperturbed inner stream (outlined in solid green) becomes stretched over time into a parabolic shape. The higher concentration of CO_2 in the unperturbed region of the inner stream c_{co2}^{sat} leads to a difference in index of refraction along this parabolic interface and, therefore, a visible interface. PPG 2700 g/mol polyol (see Table II.1) saturated with CO_2 at 7.2 MPa and 22 °C flowed within sheath of 1k5f polyol in a quartz observation capillary of 300 μm inner diameter and 100 mm length with an inlet pressure of 13.4 MPa and observed at 95 mm along the length of the capillary.

we propose the "anatomy" of the wake shown in Figure VIII.9. In the region of the inner stream in front of the bubble (right side of the image), the concentration of CO_2 is the initial saturation concentration c_{CO2}^{sat}, excepting some depletion along the outside. As the bubble grows, it causes fluid previously near its head to end up at its tail. This fluid forms the wake. At the center of the wake is the trail, which has the lowest concentration of CO_2, c_{CO2}^{trail}. Outside this region, the concentration of CO_2 c_{CO2}^{wake} is greater, but still less than the initial saturation concentration due to depletion of CO_2 through diffusion into the outer stream. While the end of the wake (outlined in a dashed green parabola) begins flat, it becomes stratified due to the velocity gradient with radial distance from the center of the inner stream. Upstream from this interface, the concentration of CO_2 is once again near its saturation concentration c_{CO2}^{sat}.

VIII.3 Ripening and Coalescence

In general, the present thesis focuses on bubbles that grow in isolation so that the growth can be accurately modeled and extrapolated back to the point of nucleation (see Section V.4). Near the outlet of the observation capillary, however, enough bubbles nucleate and grow to a large enough size that they come into contact with each other. As the bubbles continue to grow, the confinement by the outer stream causes them to squeeze against each other. After enough time in close contact, the bubbles merge into one. Minogue recorded merging events in polyurethane foaming experiments (see pp. 130–131 of [5]) that he attributed to ripening in some cases and coalescence in others, but observations were made over the course of several seconds. Is ripening or coalescence dominant in the microfluidic flow-focusing channel?

To answer this question, we show an example of the merging of two bubbles in Figure VIII.10. After nucleating near each other along the trail of the wake of an elongated bubble, the bubbles (outlined by ellipses) squeeze against each other as they grow against the confinement of the outer stream (panel b), ultimately merging into one bubble (panel c). The bubbles merge about 500 μs after coming into contact with each other. Because we could not distinguish how the bubbles merged (ripening: one bubble grows at the expense of the other; coalescence: the liquid film between the bubbles breaks up), we distinguish the two processes by their time scale.

The time scale for ripening of a small bubble into a larger bubble is roughly the time for the fluid inside the smaller bubble to diffuse across the membrane between the bubbles. This time scale τ_{ripen} is therefore proportional to the mass of gas inside the smaller bubble m_1 and inversely proportional to the flux between the bubbles Φ and the area of contact A_c (see diagram in Figure VIII.10d). The mass inside the smaller bubble $m_1 = c_1 V_1$, where c_1 is the concentration of gas in the smaller bubble and V_1 is its volume. The flux of gas between the bubbles scales as the product of the diffusivity $\mathcal{D}$ and the concentration gradient, which can be estimated as the difference in concentrations divided by the thickness of the film between them, which scales as the critical film thickness of rupture h_c since the film thins quickly before reaching this thickness, so $\Phi \sim \mathcal{D}\frac{c_1-c_2}{h_c}$, where c_2 is the concentration of gas in the larger bubble ($c_2 < c_1$ due to the higher Laplace pressure in the smaller bubble 1). The critical film thickness between two bubbles in contact can be estimated from the work of Frostad *et al.* as $h_c \sim R_1 \bar{F}^{1/6} A^{1/3}$, where $\bar{F}$
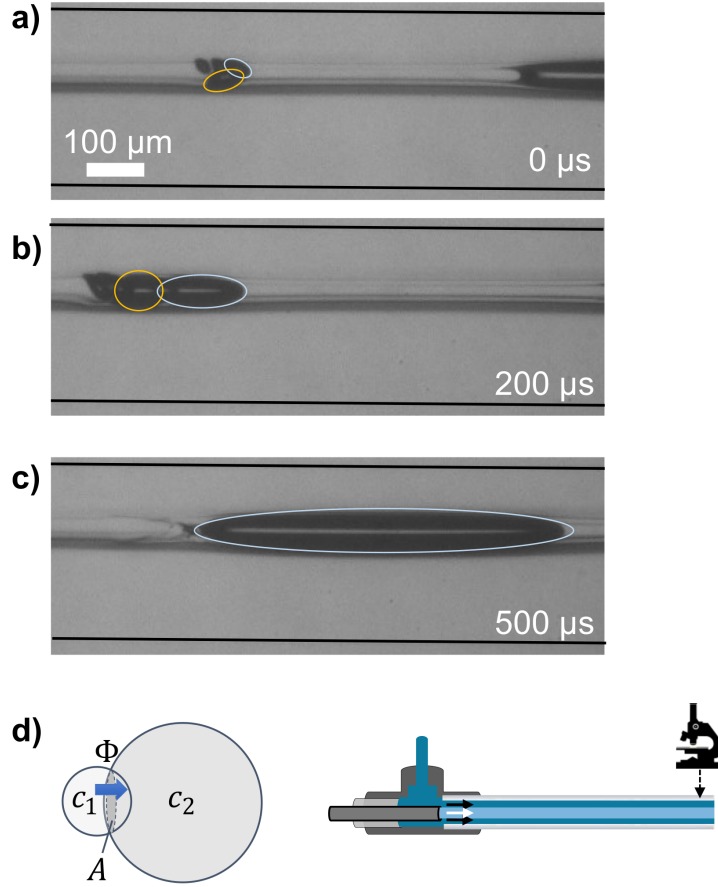
Figure VIII.10: Sequence of images shows two bubbles in contact merge through ripening (a-c). The two bubbles are outlined (orange and blue) until they merge in (c) (blue). d) Schematic of the geometry of two bubbles squeezed against each other. Inner stream of PPG 2700 g/mol saturated with CO_2 at 7.0 MPa and 22 °C was flowed at 50 μL/min in an outer stream of 1k5f polyol (see Table II.1) at 225 μL/min and observed with 4x magnification (see Table III.1) at 94 mm along the observation capillary. The inlet pressure of the observation capillary was 9.5 MPa.

is the force applied on the bubbles F scaled by the interfacial tension σ and the bubble radius R_1, so $\bar{F} = F/(\sigma R_1)$ and A is the dimensionless Hamaker constant $A = A_H/\sigma R_1^2$, where A_H is the Hamaker constant for the fluid [6]. Finally, the area of contact between the bubbles can be estimated from observation as $A_c = \pi R^2$. Thus, the ripening time scales as $\tau_{ripen} \sim \frac{c_1 R_1^3 h_c}{\mathcal{D}(c_1 - c_2) R_1^2}$. If we assume that the concentrations follow Henry's Law, then, Henry's constant cancels out and the ripening time scale can be written as

$$\tau_{ripen} \sim \frac{p_1 R_1 h_c}{\mathcal{D}(p_1 - p_2)} \tag{VIII.1}$$

where $p_1 = p + 2\sigma/R_1$ and $p_2 = p + 2\sigma/R_2$ are the pressures inside the two bubbles, equal to the local fluid pressure p plus the Laplace pressure.

In the experiment from which the images in Figure VIII.10 were taken, the following estimates were determined for these quantities. We consider the smaller bubble to have a radius between 5 μm and 10 μm while the larger bubble has a radius between 20 μm and 25 μm. The local fluid pressure is estimated as 0.7 MPa assuming a constant pressure gradient along the observation capillary, but it could be as well as 0.3 MPa if the unobservable last 5 mm of the observation capillary are completely filled with bubbles. The interfacial tension under these conditions is between 15 and 25 mN/m (see Figure II.3a). The diffusivity will be governed by the saturation pressure of 7 MPa, so it lies between 5×10^{-10} m^2/s and 1.5×10^{-9} m^2/s. From visual observation, the radius of the area of contact is somewhere between half to the full radius of the inner stream (25 μm), so $R_c \in [12.5, 25]$ μm. The Hamaker constant for glycerol is about twice that of water, which is 3.6×10^{-20} J, so we bound it between $A_H \in [3.6, 7.2] \times 10^{-20}$ J. We estimate the force between the bubbles as the Laplace pressure multiplied by the area of contact $F \sim 2\sigma/R_{bubble} \times R_c^2$. From these ranges, we can estimate the range for the ripening time to be $\tau_{ripen} \in [1, 25]$ ms. The value is slightly larger than observed, but is within the right order of magnitude, as expected for a scaling analysis.

We next compare this time scale with that of coalescence. Frostad *et al.* also estimated the time scale of coalescence and validated their scaling with experiments [6]. For that time scale, they gave the value $\tau_{coalesce} \sim \frac{\eta R}{\sigma} \bar{F}^{1/4} A^{-1/2}$, where η is the viscosity of the fluid and R is the scale for the radius of contact (the first factor is the capillary time). Noting that the estimate for the viscosity of the inner stream lies between 0.01 Pa.s and 0.03 Pa.s, the range for the coalescence time $\tau_{coalesce} \in [30, 2600]$ ms, which is far above the time scale observed. Therefore, between coalescence and ripening, we believe that ripening is the more common merging process at the short time scales over which merging can be observed in this apparatus.

VIII.4   Stream Instabilities

In the present work, the inner stream was kept stable to maintain a consistent environment for bubble nucleation. In some cases, however, the inner stream became unstable. While these instabilities prevented the accurate measurement of bubble nucleation for the purposes of this work, they yielded some fascinating flow patterns

that we discuss in this Section.
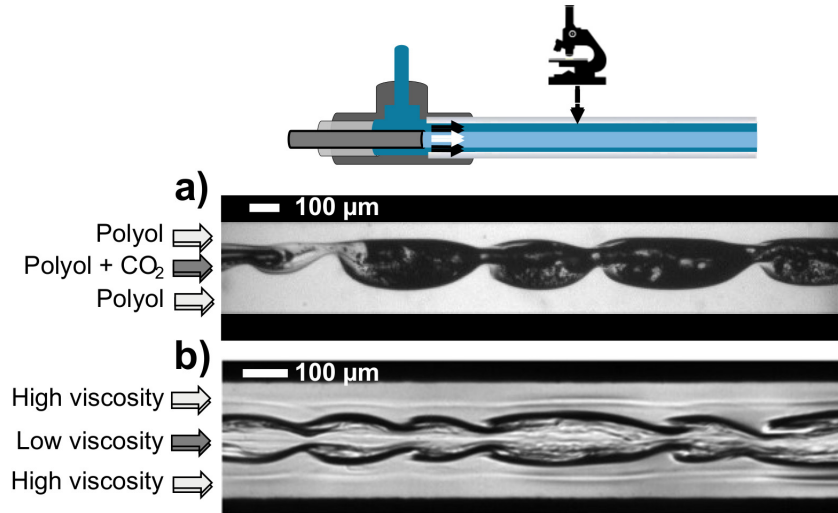
Figure VIII.11: Images of Kelvin–Helmholtz-like instabilities in microfluidic sheath flow. a) 1k3f polyol (see Table II.1) saturated with CO_2 at 8.8 MPa and 22 °C flowed within sheath of 1k5f polyol in quartz observation capillary of 300 μm inner diameter and 100 mm length at 55 mm along the length of the capillary. The opaque regions are bubbles that have nucleated inside the inner stream. Flow enters from the left. b) Low-viscosity (0.49 mPa.s) silicone oil flowing at 900 μL/min in a sheath of high-viscosity (485 mPa.s) silicone oil flowing at 100 μL/min. Adapted from X. Hu and T. Cubaud *Phys. Rev. Fl.* 2016 1:044101 Copyright 2016 American Physical Society.

One common instability was the formation of ligaments and vortices along the inner stream, as shown in Figure VIII.11a. In this experiment, the inner stream was composed of 1k3f polyol (see Table II.1) saturated with CO_2 at 8.8 MPa and 22 °C and the outer stream was 1k5f polyol. In this experiment, the inner stream had a low enough viscosity and a high enough rate of nucleation that nucleation was observed 55 mm along the observation capillary, where the image in Figure VIII.11a was taken, though the inlet pressure was in excess of 15 MPa. While the inner stream never broke up into droplets, as can happen for an immiscible inner stream, its interface developed oscillations and wave-like ligaments that folded in on themselves. The interior of the inner stream flowed much more quickly than these instability patterns at the interface as bubbles jetted along the winding path inside them. Such a pattern was observed in microfluidic sheath flow by Hu and Cubaud when flowing a low-viscosity silicone oil inside a silicone oil of much higher viscosity [7]. The instability is akin to the Kelvin–Helmholtz instability that arises when fluid flows more quickly past another, causing the patterns similar to

the crashing of waves along the interface. Indeed, the speed in the inner stream is significantly higher than that of the outer.

Hu and Cubaud found that the flow is significantly destabilized when the Reynolds number of the inner stream exceeds 90. Despite the small dimensions of the flow and low viscosity of the bubbly flow in the inner stream, such a Reynolds number is plausible given the high speed (several meters per second) and low viscosity of the inner stream apparent from the video. Nevertheless, the Reynolds number can be kept low enough to stabilize the flow by delaying the onset of bubble nucleation in the channel. Bubble nucleation can be delayed by maintaining a high inlet pressure through a high outer stream flow rate, limiting the flow rate of the inner stream, and limiting the saturation pressure of the polyol used for the inner stream. For a thorough depiction and discussion of the stabilization and onset of this instability, see the publication by Hu and Cubaud [7].

When polyol is mixed with cyclopentane the viscosity is lowered significantly due to the low viscosity of cyclopentane (about 0.5 mPa.s at room temperature and pressure [8]), especially after dissolving CO_2. Although the conditions would be suitable for a Kelvin–Helmholtz instability like that shown in Figure VIII.11, when not too many bubbles have nucleated, a different instability pattern emerges, shown in Figure VIII.12. In this experiment, 1k5f polyol (see Table II.1) was mixed with 15% cyclopentane by weight before saturating with CO_2 at 9 MPa. This fluid was flowed through the inner stream at a flow rate more than twice the flow rate of the outer stream of pure 1k5f polyol (70 μL/min vs. 30 μL/min). The fluids flowed through a quartz capillary of 200 μm in inner diameter and 100 mm in length, and were observed at 94 mm along the capillary. Bubbles would appear as opaque, but are not seen in this image, so we assume that bubbles had not yet nucleated despite the high degree of supersaturation, perhaps due to the narrow inner diameter of the observation capillary. Nevertheless, a difference in index of refraction can be distinguished, which reveals periodically spaced vortex-like patterns connected by what appear to be interwoven threads of fluid. We have not found such a flow instability in the literature, although the pearl and mushroom instability reported by d'Olce *et al.* is similar [9].

References

1. Revellin, R., Agostini, B. & Thome, J. R. Elongated bubbles in microchannels. Part II: Experimental study and modeling of bubble collisions. *International Journal of Multiphase Flow* **34,** 602–613. ISSN: 03019322 (2008).
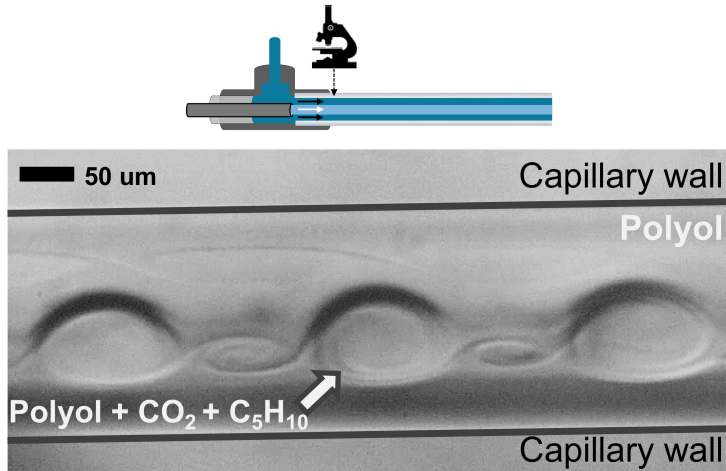
Figure VIII.12: Instability within inner stream of 1k5f polyol (see Table II.1) mixed with 15% cyclopentane by weight and saturated with CO_2 at 9 MPa flowed at 70 μL/min within a sheath of 1k5f polyol at 30 μL/min. The fluids flowed through a quartz capillary of 200 μm in inner diameter and 100 mm in length, and were observed at 20 mm along the capillary. Evenly spaced vortices appear to be linked by interwoven threads of fluid.

2. Agostini, B., Revellin, R. & Thome, J. R. Elongated bubbles in microchannels. Part I: Experimental study and modeling of elongated bubble velocity. *International Journal of Multiphase Flow* **34,** 590–601. ISSN: 03019322 (2008).

3. Yin, L., Jia, L., Guan, P. & Liu, D. Experimental investigation on bubble confinement and elongation in microchannel flow boiling. *Experimental Thermal and Fluid Science* **54,** 290–296. ISSN: 08941777. http://dx.doi.org/10.1016/j.expthermflusci.2014.01.004 (2014).

4. Khandekar, S., Panigrahi, P. K., Lefèvre, F. & Bonjour, J. Local Hydrodynamics of Flow in a Pulsating Heat Pipe: A Review. *Frontiers in Heat Pipes* **1.** ISSN: 2155-658X. https://www.thermalfluidscentral.org/e-journals/index.php/Heat_Pipes/article/view/103 (Nov. 2010).

5. Minogue, E. *An in-situ study of the nucleation process of polyurethane rigid foam formation* PhD thesis (Dublin City University, 2000), 1–194. http://doras.dcu.ie/19076/.

6. Frostad, J. M., Paul, A. & Leal, L. G. Coalescence of droplets due to a constant force interaction in a quiescent viscous fluid. *Physical Review Fluids* **1,** 1–14 (2016).

7. Hu, X. & Cubaud, T. Inertial destabilization of highly viscous microfluidic stratifications. *Physical Review Fluids* **1,** 044101. ISSN: 2469990X (2016).

8. Kurihara, K., Kandil, M. E., Marsh, K. N. & Goodwin, A. R. H. Measurement of the Viscosity of Liquid Cyclopentane Obtained with a Vibrating Wire Viscometer at Temperatures between (273 and 353) K and Pressures below 45

MPa. *Journal of Chemical & Engineering Data* **52,** 803–807. ISSN: 0021-9568. https://pubs.acs.org/doi/10.1021/je060416d (May 2007).

9. D'Olce, M., Martin, J., Rakotomalala, N., Salin, D. & Talon, L. Pearl and mushroom instability patterns in two miscible fluids' core annular flows. *Physics of Fluids* **20,** 024104. ISSN: 10706631 (2008).

VIII.S1 Stagnation of Bubbles

In the main text, small bubbles were seen to stagnate when an elongated bubble passed by them (Figure VIII.3). In Figure VIII.S1, we show that even bubbles in the outer stream slow down as elongated bubbles pass by. The reduction in speed caused by the passing of an elongated bubble is smaller in the outer stream than the inner stream due to the slower initial speed in the outer stream than the inner stream, so the effect is less obvious here. This slow-down indicates that the transport of fluid from the head to the tail of an elongated bubble occurs not just in the inner stream, but in the outer stream as well. It also shows that the significant reduction in the pressure drop along an elongated bubble is quickly felt throughout the inner and outer streams.
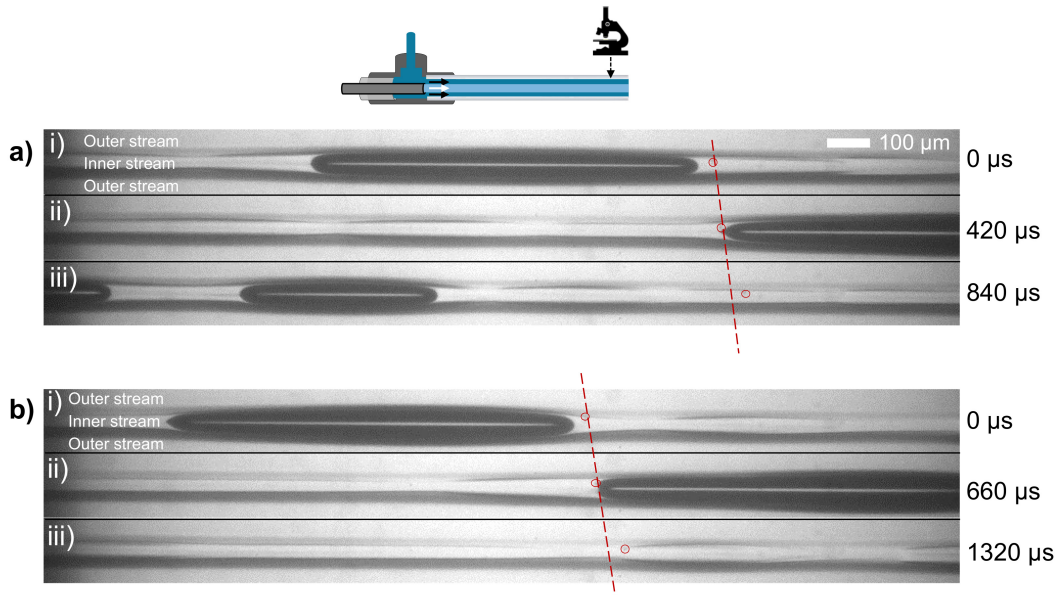

Figure VIII.S1: Still frames show how two small bubbles in the outer stream (circled in red) slow down almost to stagnation when an elongated bubble passes by them. In the top two frames of (a) and (b), the bubble in the outer stream moves minimally as an elongated bubble passes it. From the second to the third frame, the same time passes, but the bubble travels a farther distance, indicating that the passage of the elongated bubble slowed the flow even in the outer stream (although not to a complete stop). This difference in speed is demonstrated by the deviation from the extrapolation of the speed marked by the red dashed lines. Note that we determined that the bubble is in the outer stream due to its significantly slower speed and lack of growth.

VIII.S2 Nucleation of Bubbles in the Wake of an Elongated Bubble

In Figure VIII.S2, we show the nucleation of bubbles along the trail in the wake of an elongated bubble, followed by their growth, ripening, merging into a larger, elongated bubble, and subsequent nucleation of bubbles in the wake once again. The bubbles in the wake nucleate along the trail left behind the elongated bubble, which we suggest is the remnant of the depletion boundary layer formed as the bubble passed along the inner stream fluid (see Figure VIII.8). Bubbles likely nucleate around the same time due to a sudden decrease in the local pressure as a larger bubble reached the end of the observation capillary. The bubbles likely ripen instead of coalescing based on the time scale of merging (see discussion in Section VIII.3). This cycle may repeat many times as elongated bubbles exit the observation capillary and cause sudden decreases in pressure. These decreases in pressure are only significant near the end of the observation capillary where the pressure is on the order of atmospheric pressure.
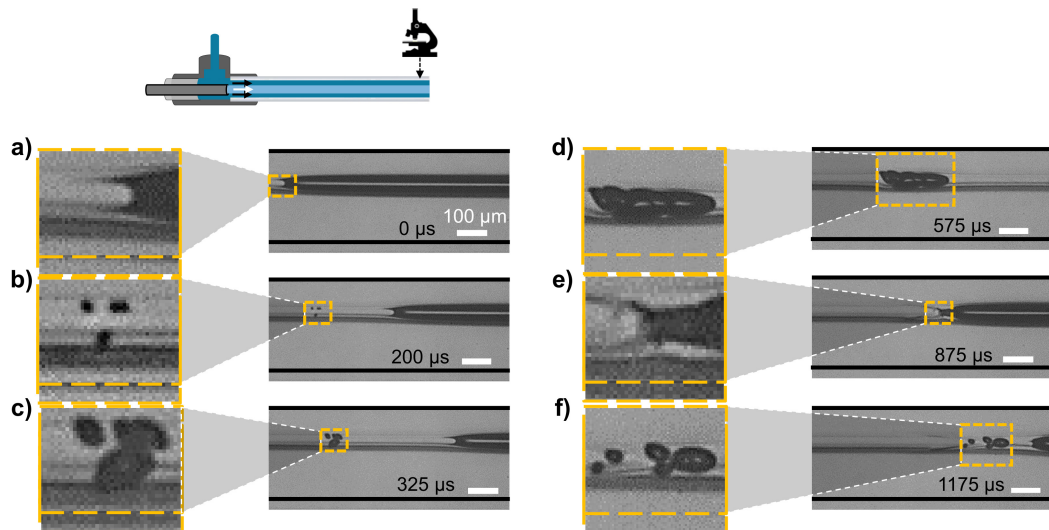

Figure VIII.S2: Depiction of bubble nucleation in the wake of an elongated bubble followed by merging and more nucleation in the wake. Images are zoomed in the panels on their left. Times from the first frame are recorded at the bottom. a) A wake is observed at the tail of an elongated bubble. b) Bubbles nucleate just outside the trail left in the wake of the elongated bubble, consistent with the schematic picture presented in Figures VIII.6 and VIII.8. c) The just-nucleated bubbles grow and come into contact with each other. d) The bubbles grow more and squeeze against each other, causing them to extend along the inner stream. e) The bubbles merge through ripening (see discussion in Section VIII.3) into another elongated bubble. f) The newly formed elongated bubble causes nucleation in its wake. This cycle repeats until CO_2 is depleted sufficiently in the wake.

Closing Thoughts

In closing, I wish to make the ill-advised shift back to the first person because the following are my personal reflections. When I began the work that forms the foundation for this thesis, I dreamed of measuring the rate of bubble nucleation precisely enough to show that the addition of cyclopentane leads to a qualitatively different pathway to nucleation, as predicted by the string method model developed by Dr. Huikuan Chao. While I have presented evidence in support of this prediction, I consider this dream unrealized. I still long to investigate further, to extend my personal pier of understanding ever farther out into the ocean of knowledge. The delight from fixing each new rock in place along the pier's perimeter continues to compel me to seek the next; the dream of discovery beckons me onward.

Why stop?

"To every thing there is a season, and a time to every purpose under the heaven: A time to be born, and a time to die; a time to plant, and a time to pluck up that which is planted."[1] My dream remains beyond arm's reach because God calls me to the next chapter in the story. He calls me not because the knowledge I had sought was not valuable, but because the understanding I have gained was *enough*.

But perhaps not for you. Perhaps your time to plant begins today. To that, I say, wonderful: the harvest truly is plenteous[2].

:)

---

[1] Book of Ecclesiastes Chapter 3, verses 1–2, King James Version.
[2] The Gospel of Matthew, Chapter 8, verse 37, King James Version.